

**UNIVERSITY OF NAPLES FEDERICO II**



Preparation and characterization of  
hyper-crosslinked resins and nanocomposites

Rachele Castaldo

PhD in Industrial Product and Process Engineering - XXIX cycle

Department of Chemical, Materials and Production Engineering

Tutor : Prof. Veronica Ambrogi

Co-tutor : Dr. Gennaro Gentile

April 2017

# Abstract

This thesis focuses on the preparation and the adsorption study of innovative hyper-crosslinked (HCL) polymers and nanocomposites.

New microporous nanocomposites were prepared including multi-walled carbon nanotubes (MWCNTs) in styrene/vinylbenzyl chloride/divinylbenzene hyper-crosslinked resins. In order to promote the embedding of the MWCNTs within the gel-type precursor, a proper surface modification strategy was set up, based on the grafting of a poly(vinylbenzyl chloride) (PVBC) resin, able to participate to the hyper-crosslinking step, onto the nanotubes surface. After dispersion of the MWCNTs into the monomer mixture, HCL nanocomposites were prepared by suspension polymerization followed by Friedel-Crafts reaction. Volumetric gas adsorption and adsorption from solution analysis revealed that, by addition of the modified MWCNTs, it was possible to modulate the pore size distribution and the adsorption properties of HCL polymers.

Then, a new synthetic strategy to obtain HCL polymers and nanocomposites was proposed, based on the bulk prepolymerization of a gel type precursor followed by the traditional Friedel-Crafts alkylation step. The obtained HCL materials showed comparable properties with respect to the corresponding resins obtained by suspension prepolymerization. Moreover, the versatility of the proposed process was demonstrated through the realization of two innovative classes of advanced materials: i) HCL microporous organic polymer nanocomposites (MOPNs) and ii) polymer composites containing HCL resins and nanocomposites as fillers.

In particular, MOPNs characterized by different porous structures and adsorption properties were prepared including graphene nanoplatelets (GNP) or surface modified graphene oxide (GO) into a styrene/vinylbenzyl chloride/divinylbenzene matrix. Using surface modified GO grafted with PVBC, microporous nanocomposites based on a styrene/divinylbenzene precursor, i.e. without the chlorinated monomer, were also realized. Their microporosity was only generated during the hyper-crosslinking occurring at the interface between the modified GO nanoplatelets and the styrene based matrix.

HCL resins and nanocomposites were employed as fillers in two type of composites, polysulfone membranes and chitosan hydrogels. The composite polysulfone membranes were tested for phenol adsorption from water solution, demonstrating that the addition of the functional microporous fillers within the polysulfone phase is able to induce significant enhancement of the equilibrium adsorption capacity. Adsorption tests of various dyes on the composite chitosan-based hydrogels proved that it

is possible to effectively combine the adsorption performances of the HCL resin with the chitosan matrix for the realization of new functional materials for broad-spectrum water remediation.

Finally, an in-depth study of the effect of the oxidation degree on the self-assembly and the surface area of graphene oxide is reported. Different self-assembly processes were used to prepare bulk and porous 3D GO structures, respectively based on water removal by evaporation at the liquid/air interface and by freeze-drying at the dynamic ice/water interface. Combination of morphological analysis, BET SSA analysis on cast and freeze-dried GO samples and SSA analysis through methylene blue adsorption on GO water suspensions allowed the evaluation of the effect of the oxidation degree on the processability and the adsorption properties of graphene oxide.

# Contents

1. Introduction .....	1
1.1 Microporous materials .....	1
1.1.1 Microporous organic materials .....	2
Metal-organic frameworks .....	2
Covalent organic frameworks .....	3
Conjugated microporous polymers .....	3
Polymers of intrinsic microporosity .....	4
Hyper-crosslinked polymers .....	4
1.1.2 Microporous inorganic materials .....	9
Zeolites .....	9
Activated carbons .....	9
Nanosized carbon allotropes .....	10
1.2 Adsorption .....	13
1.2.1 Physisorption and chemisorption .....	14
1.2.2 Gas adsorption .....	15
Modalities of adsorption .....	15
Thermodynamic of adsorption .....	17
From theory to practice: interpretation of physisorption isotherms .....	19
Specific surface area evaluation .....	23
Pore size distribution evaluation .....	25
1.2.3 Adsorption from solution .....	28
Specific surface area analysis through adsorption from solution .....	29
1.3 Aim of the work .....	31
1.4 References .....	33

2. Synthesis and adsorption study of hyper-crosslinked styrene-based nanocomposites containing multi-walled carbon nanotubes .....	39
Introduction .....	41
Experimental section .....	43
Results and discussion .....	46
Conclusions .....	59
Supplementary information .....	60
References .....	61
3. A new synthetic approach towards hyper-crosslinked styrene-based polymers and nanocomposites .....	64
Introduction .....	66
Experimental section .....	67
Results and discussion .....	72
Conclusions .....	87
Supplementary information .....	88
References .....	91
4. Chitosan hydrogels containing hyper-crosslinked resins as new broad-spectrum adsorbents for efficient water purification .....	94
Introduction .....	96
Experimental section .....	98
Results and discussion .....	101
Conclusions .....	107
Supplementary information .....	108
References .....	110
5. Effects of the oxidation degree on the self-assembly and the surface area of graphene oxide .....	112
Introduction .....	114
Experimental section .....	115
Results and discussion .....	119
Conclusions .....	132
References .....	134
6. Conclusions .....	136

Appendix A1 - List of Figures .....	139
Appendix A2 - List of Tables .....	141
Appendix B - Publications .....	142
Appendix C - Meeting contributions .....	143

# Chapter 1

## Introduction

### 1.1 Microporous materials

Research in the field of porous material have always attracted high scientific interest because of their outstanding performance and potential applications in various fields such as gas adsorption and separation,<sup>1,2</sup> energy storage,<sup>3</sup> air and water purification processes,<sup>4,5,6</sup> drug delivery,<sup>7</sup> catalysis,<sup>8,9</sup> sensing,<sup>10</sup> optoelectronics,<sup>11</sup> design of superhydrophobic surfaces.<sup>12</sup>

Several properties of the bulk materials depend on their porosity, and huge possibilities are offered by the analysis and the development of different porous structure. In particular, porous materials display extremely high specific surface area (SSA) and outstanding adsorption properties if nanosized porosity is present in significant amount. Pores have been classified by the International Union of Pure and Applied Chemistry (IUPAC),<sup>13</sup> in

- *micropores*, if the pores internal width is below 2 nm,
- *mesopores*, if the pores internal width is between 2 and 50 nm,
- *macropores*, if the pores internal width is over 50 nm.

Moreover, pores can be open or closed, slit-shaped, i.e. characterized by plane walls, or cylindrical, and the whole porosity can be composed of an ordered network or a disordered set of voids. Crystalline materials like zeolites and metal-organic framework, for example, are characterized by a regular and well-defined system of pores, while amorphous materials like activated carbons or hyper-crosslinked polymers possess an interconnected porosity irregularly shaped.

### 1.1.1 Microporous organic materials

Many types of organic porous materials have been synthesized, in recent years, using different molecular precursors. Their advantageous properties include low density, large surface area, and the possibility to control composition, surface functionalities and pore size. In fact, microporous organic polymers (MOPs) offer the possibility of designing and building specific porous structures, to compose either crystalline (covalent organic frameworks - COFs, metal-organic framework - MOFs) or amorphous (hyper-crosslinked polymers - HCPs, conjugated microporous polymers - CMPs, polymers of intrinsic microporosity - PIMs) materials. Moreover, their organic nature allows significant functional diversification, as through the introduction of specific chemical functionalities into the pores.<sup>14,15</sup>

#### Metal-organic frameworks

Metal-organic framework are a class of hybrid materials composed of polydentate organic linkers coordinated to transition metal cations to form highly ordered and porous structures. There are ever-growing possibilities to create different metal ions-organic linkers combinations, designing their specific surface area, porosity, and chemical interactions.<sup>16,17,18</sup> Thousands of MOFs have already been synthesized, and SSA values up to  $\sim 7000 \text{ m}^2/\text{g}$  have been reached.<sup>19</sup> Changing the length of the linkers and maintaining the same shape of the structure a series of so-called *isoreticular* metal-organic frameworks (IRMOF) may be designed.

The network connectivity in MOFs largely determine their properties, in the same way a monomer determines the polymer characteristics. MOF synthesis does not only requires the selection and/or the preparation of desired modules, but also some foresight on how they will be assembled in the final product. In fact, a key factor in MOFs synthesis is the preservation of their building blocks. It is important to find conditions mild enough to preserve the organic moieties functionalities and yet sufficiently reactive to establish the metal-organic bonds. Early synthetic approaches involved techniques previously used to grow simple inorganic salts crystals. These involved the slow introduction of the building blocks to reduce the rate of crystalline nucleation, or the slow evaporation of the precursors solution, or again the slow diffusion of one component solution into another through membranes or immobilizing gels. Where ligands needed to be deprotonated, like carboxylic acid, a volatile ammine was gradually added via vapour diffusion. Following approaches introduced solvothermal methods, that were found conveniently faster and effective in the construction of more robust frameworks. According to this new strategy, the precursors are to be combined in polar solvents, sealed in vessels and heated, generating autogenous pressure.

MOFs are ideal candidate for gas adsorption and for removal of toxic chemicals, due to their high microporosity and the possibility of tailoring their selectivity by proper functionalizations. They

usually show a type I adsorption isotherm, presenting high uptake at low pressure, and no hysteresis, demonstrating the reversibility of the phenomenon.<sup>20,21</sup> Furthermore, the strength of the adsorption interaction has been proved for various complexes, showing gas uptake by occlusion of the gas molecules, rather than just surface adsorption.<sup>22,23</sup> Moreover, their proper functionalization lead the way to applications as highly selective molecular sieves, sensors, or catalysts.<sup>24,25,26</sup>

### **Covalent organic frameworks**

Covalent organic frameworks (COFs) are crystalline polymers analogue to MOFs in structure. Since they are made of lightweight elements connected by strong covalent bonds, COFs have low mass densities, possess high thermal stabilities, and provide permanent porosity. They have, as MOFs, wide structure tailoring possibilities. The first successful example of COF was proposed by Yaghi and co-workers in 2005, demonstrating the utility of the topological design in their synthesis of porous organic frameworks connected via covalent bonds.<sup>27</sup>

COFs can be categorized in two- or three-dimensional COFs (2D and 3D COFs). In 2D COFs, the covalent bound framework is restricted to 2D sheets, interacting among each other through  $\pi$ -interactions and forming layered structures containing aligned porous columns. 3D COFs, containing  $sp^3$  carbon or silane atoms, extend the covalent bound framework to the third dimension. To obtain such ordered and controlled structure, the typical synthesis follows the principle of dynamic covalent chemistry (DCC), involving the reversible formation of covalent bonds, which can be formed, broken and reformed.<sup>28</sup> Unlike conventional covalent bond formation, DCC is thermodynamically controlled and provides reversible reaction systems, producing structures with “error checking” characteristics, and thus leading to the obtainment of defect free stable structures.

COFs main properties arise from their porosity and molecular skeletons. Their frameworks can be further functionalized, for example, to contain catalytic sites for use in heterogeneous catalysis. COFs have been demonstrated being able to load many molecules/ions in their nanopores to form heterogeneous catalytic systems.<sup>29,30</sup> Furthermore, 2D COFs are characterized by a diffused  $\pi$ -coupling which facilitates the transport of charge carriers and photoexcited states, giving them potential to develop new molecularly designed semiconducting and photoconducting materials.<sup>31,32,33</sup> 3D COFs, on the other way, with their three-dimensional framework structure, are characterized by very high SSA and very large amount of open sites, making them very good candidates for gas storage.<sup>34,35,36</sup>

### **Conjugated microporous polymers**

Conjugated microporous polymers (CMP) are a particular class of MOPs exhibiting extended  $\pi$ -conjugation. For the interesting combination of typical high surface area polymers properties and

their unique electronic and electroluminescent properties,<sup>37,38</sup> they find application in the sensing, electrical, and optical fields. Their micropore size distribution and SSA can be controlled by varying the length of the organic linkers. CMPs have been prepared in diverse range of architectures, such as linear polymers, dendrimers, hyper-branched polymers, and networks.<sup>39,40,41</sup> Similarly to MOFs and COFs, also CMPs porosity and surface area can be finely tuned by varying the strut length in the network.<sup>42,43</sup>

### **Polymers of intrinsic microporosity**

Polymers of intrinsic microporosity (PIMs) are amorphous polymers displaying high SSA due to their highly rigid and contorted molecular structure, which provides inefficient macromolecular packing. In particular, due to their fused ring structures, PIMs do not possess rotational freedom along the polymer backbone, which ensures that the macromolecular components cannot rearrange their conformation, so that their highly contorted shape is fixed during synthesis. The first strategy to obtain a microporous rigid polymer raised from the idea of McKeown et al. of connecting extended aromatic molecules, miming the graphene sheets of activated carbons, to a linking group that would ensure inefficient packing and prevent structural relaxation and loss in microporosity, for which he choose a spiro compound. The spirocyclic crosslinks efficiently prevent a close packing of the polymeric chains, giving an amorphous microporous structure with SSA in the range of 500-1000 m<sup>2</sup>/g and with very significant adsorption at low pressure, indicating microporosity.<sup>44</sup> PIMs may be prepared either as insoluble networks or soluble polymers, with both types giving solids that exhibit analogous behaviour to that of conventional microporous materials such as activated carbons.

### **Hyper-crosslinked polymers**

The word hyper-crosslinked polymers (HCPs) groups a variety of polymers prepared through the extensive crosslinking of a linear or lightly crosslinked precursor polymer. Before the introduction of this approach, high specific surface area macroporous poly(styrene-co-divinylbenzene) was prepared by suspension polymerization, provided that high levels of crosslinker (divinylbenzene – DVB) were present (estimated as more than 50 vol%), together with a suitable porogenic solvent. However, in this polymerization process, as the reaction proceeds, the high level of DVB induces steric congestion, preventing the continuation of the reaction. As a result, many vinyl groups remain unreacted at the end of the procedure and this limitation in the extent of crosslinking is unavoidable.<sup>45</sup>

In 1969, a new method for the production of porous polystyrene (PS) was introduced by Davankov, based on the crosslinking of linear polystyrene by an *external crosslinker* through Friedel-Crafts reaction.<sup>46</sup> The external crosslinker proposed is a bifunctional electrophilic compound that, upon activation by a Friedel-Crafts catalyst, installs structural bridges between neighbouring aromatic

rings whilst the PS is in a highly swollen state. PS acquires, in this way, a *hyper-crosslinked* structure characterized by high specific surface area and micropore volume.

This procedure was further developed by Jeràbek<sup>47</sup> and Sherrington<sup>48</sup>, who proposed the introduction of an *internal electrophile*, more specifically a reactive co-monomer, the vinylbenzyl chloride (VBC). The VBC chloromethyl groups, upon activation by the Friedel-Crafts catalyst, act as crosslinkers when the polymer is in the swollen state, promoting the formation of HCPs. The typical HCP structure is a rigid expanded three-dimensional network, characterized by spatially non-planar cycles formed by crosslinking bridges and very short segments confined between the branching points (see Figure 1.1).

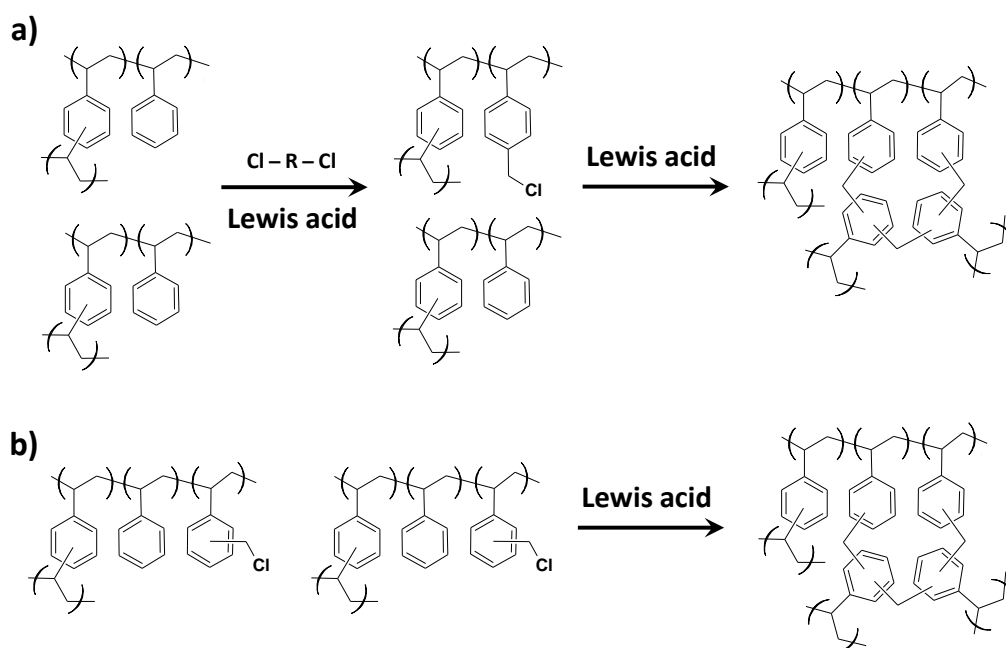


**Figure 1.1** Hyper-crosslinking reaction scheme through external (a) and internal (b) electrophile

#### *Precursor monomers*

The effect of the precursor monomers on the final HCPs was studied extensively by many research groups. Ahn et al. characterized different hyper-crosslinked DVB-PS-VBC polymers, assessing that the amount of DVB introduced is crucial for the porosity of these hyper-crosslinked materials. They found that a low DVB content, such as  $\sim 2$  mol%, allows obtaining a microporous polymer characterized by high SSA, while higher amounts of DVB, such as  $\sim 20$  mol%, lead to obtain a lower surface area polymer showing bimodal pore size distribution. In the latter case, meso- and macroporosity are induced by DVB and the microporosity is formed in the hyper-crosslinked step.<sup>48</sup> Ahn et al. also showed that the reaction employing internal electrophiles is extremely efficient. The reaction was found to reach almost completion after 15 min (determined by steep decrease in Cl content from  $\sim 19\%$  to  $\sim 2\%$  and SSA increase from  $\sim 0$  to  $1200 \text{ m}^2/\text{g}$ ) and achieve conclusion after 2

hours, when the values of SSA and residual Cl reached a plateau, with SSA =1800 m<sup>2</sup>/g and Cl ~2%. They suggested that the internal electrophile is so efficient because the last step of the reaction is particularly favourable, being the aromatic ring to be substituted already doubly alkylated and thus electron rich.

Fontanals et al. tested different VBC isomers finding that polymers prepared by p-VBC (para-VBC) and mix-VBC (mixture of 70:30 = meta:para VBC isomers) differ in chlorine content. This is ascribable to preferential hydrolysis of p-VBC under the used synthesis conditions. Moreover, the properties of VBC-derived HCPs, prepared through suspension polymerization of the precursor polymer, depend strongly from the VBC isomers used. They reported that the hydrolysis of the VBC chloromethyl group would be expected to proceed through a SN1 mechanism, thus involving the formation of a stabilized carbocation intermediate followed by nucleophilic attack of water. Therefore, p-VBC forms a more stable carbocation with respect to m-VBC, leading to a more favourable p-VBC hydrolysis. The HCPs based on p-VBC or mix-VBC show, respectively, either higher hydrophilic character or either higher SSA. The p-VBC-derived HCP contained 4wt% of oxygen and displayed 900 m<sup>2</sup>/g BET SSA and the mix-VBC-derived HCP contained 1.5wt% of oxygen and showed 1900 m<sup>2</sup>/g BET SSA.<sup>49</sup>

The use of different DVB isomers for the production of materials with enhanced H<sub>2</sub> adsorption was explored by Wood et al., finding that o-DVB (ortho-DVB) was detrimental to the production of high SSA materials, with respect to p-DVB and m-DVB. This fact was associated with the lower degree of condensation of o-DVB.<sup>50</sup>

Frèchet and Svec groups investigated the effect of polyaniline and polypyrrole as precursors in HCPs on the H<sub>2</sub> adsorption capacity of the hyper-crosslinked resin. Polyaniline was previously reported as a potential H<sub>2</sub> storage material, but they found that the protonation of HCPs containing polyaniline diminishes the polyaniline ability to adsorb hydrogen. Aromatic rings, which contain electron-donating functionalities, adsorb H<sub>2</sub> more readily than those bearing electron-withdrawing groups but, while the aniline functionality is highly electron-donating, protonated anilines are electron-withdrawing, diminishing the hydrogen sorption capacity.<sup>51</sup> Polypyrrole instead, was found, through various synthetic techniques, to lead to higher H<sub>2</sub>-polymer interactions when introduced in HCPs.<sup>52</sup>

Dawson et al. prepared a series of HCPs based on benzene and aniline as precursors in different relative ratios to enhance the CO<sub>2</sub> adsorption capacity of the resin, since aniline was reported to adsorb preferentially CO<sub>2</sub>. They found, as expected, that SSA decreased as the aniline amount in the polymer increased, and a good compromise was found when aniline was included as the 40% (SSA ~200 m<sup>2</sup>/g and CO<sub>2</sub> uptake ~1.2 mmol/g). Furthermore, the difference between the SSA and the CO<sub>2</sub> decreasing rates suggested that these materials could have good selectivity for CO<sub>2</sub>/N<sub>2</sub> adsorption.

Finally, Chaikittisilp et al. prepared HCPs characterized by SSA of ~2500 m<sup>2</sup>/g, using benzyl chloride terminated double-four-ring cubic siloxane cages as precursors. The realization of such high

SSA values was attributed to the simultaneous polymerization of the organic functional groups and the destruction of the siloxane cages during synthesis.<sup>53</sup>

### *Synthetic routes*

Davankov synthesised the first HCPs starting from dissolved PS, obtaining a rigid monolithic block. Moved by the objective of producing spherical particles, the PS precursor was then lightly crosslinked with DVB and spherical beads were obtained. These beads swelled in a good solvent but did not dissolve, thus maintaining the spherical shape after hyper-crosslinking.<sup>54</sup> HCPs prepared through suspension polymerization are usually polydisperse (mean diameter  $\sim 10\text{-}500\mu\text{m}$ ), which can limit their application in certain fields. In this view, emulsion polymerization was introduced, obtaining nearly monodisperse beads with medium diameter of  $\sim 420\text{ nm}$ .<sup>55</sup> Non-aqueous dispersion polymerization (NAD) and precipitation polymerization (PP) have also been employed to obtain more homogeneous particle sized, giving as results, respectively, beads with  $4\text{-}10\mu\text{m}$  diameter range, and monodisperse  $4\mu\text{m}$  beads. Apart from size and shape, the precursor polymerization synthesis was found to also influence the HCPs final SSA and porosity. In particular, it was found that for NAD and PP an amount of VBC higher than 50 % was required in order to obtain HCPs with SSA higher than  $1000\text{ m}^2/\text{g}$ .<sup>56</sup> In contrast, for suspension polymerization the 20 % of VBC in the monomer feed was sufficient to obtain HCPs with SSA over  $1000\text{ m}^2/\text{g}$ . The highest SSA HCPs obtained by suspension polymerization showed SSA of up to  $2090\text{ m}^2/\text{g}$  and was prepared using DVB, ST and VBC in the molar ratio  $\text{DVB:ST:VBC} = 2:49:49$ .<sup>48</sup> Finally, another synthetic approach was proposed by Fréchet and Svec, who prepared HCPs in the form of monolith performing in situ hyper-crosslinking in capillary columns in presence of organic porogens (toluene and 1-dodecanol) obtaining a material with SSA of  $663\text{ m}^2/\text{g}$ .<sup>57</sup>

### *External crosslinkers, catalysts and solvents*

Initially, the most commonly used external crosslinker was chloromethyl ether (CME), however, due to its carcinogenic properties it was progressively replaced by various other reagents, such as carbon tetrachloride, monochlorodimethyl ether, dichloroxylylene. Recently, Li et al. proposed the use of a new crosslinker acting through a new strategy consisting in “knitting” building blocks with a more environmentally friendly crosslinker, formaldehyde dimethyl acetal (FDA), which gives methanol as a by-product instead of chlorinated compounds. The procedure proposed allows preparing the HCPs in a one-step procedure, dissolving the aromatic monomers, the FDA and the Friedel-Crafts catalyst in the proper solvent. By adjusting the type of monomers and the amount of FDA, the largest SSA value achieved was  $\sim 1400\text{ m}^2/\text{g}$ .<sup>58</sup>

The Friedel-Crafts catalysts employable in hyper-crosslinking reactions are Lewis acids or protonic acids. In principle, all Lewis acids are suitable to the use, but some differences in the HCPs obtained are ascribable to the catalyst. In particular, poor solubility and steric bulk are the primary factors limiting an extensive hyper-crosslinking. The latter is a particularly relevant issue considering that, after the first crosslinks form, larger catalyst may be obstructed from accessing the chloromethyl moieties to activate the formation of more crosslinks.<sup>59</sup>

Hyper-crosslinking is typically performed in a thermodynamically good solvent for the polymer, in which the precursor resin may dissolve or swell, depending on his linear or crosslinked structure. The extensive crosslinking leaves the polymer chains locked while they are in an expanded form, preventing them from collapsing after solvent removal, thus creating a three-dimensional structure made of interconnected pores. Dichloroethane (DCE) is one of the most widely used solvents for hyper-crosslinking, although various solvents have been experimented, such as nitrobenzene, chlorobenzene, cyclohexane, hexane and different mixtures of them. Surprisingly, also bad solvent for PS as hexane and chlorobenzene are effective in the reaction, leading to high surface area HCPs.<sup>46,54</sup> Moreover, the HCPs are able to swell in a broad spectrum of solvents, regardless of their thermodynamic affinity with the precursor polymer. For example, despite of their hydrophobicity, PS-based HCPs are able to absorb almost at the same level polar protic solvents such as water and methanol and good solvent for the precursor polymers as toluene and THF.<sup>48</sup>

### *Chemical modification*

Hyper-crosslinked polymers were originally based on polystyrene, therefore they did not possess any functional specific group besides aromatic cycles and were, in case, functionalized to broaden their potential application in adsorption. HCPs can be functionalized by post-polymerization chemical modification, either before or after the hyper-crosslinked process.

For VBC-based polymers, a very efficient and practical functionalization strategy is to exploit the residual chloromethyl groups after hyper-crosslinking: Li et al. followed this route to modify HCPs with dimethylamine obtaining amine modified HCPs with enhanced adsorption properties towards polar compounds;<sup>60</sup> Fontanals et al. adopted this strategy using acetyl sulfate or lauroyl sulfate to produce sulfonated HCPs and improve the resin ion-exchange properties;<sup>61</sup> also, an HCP synthesised from Friedel-Crafts alkylation between carbazole and  $\alpha,\alpha'$ -dibromop-xylene was subjected to modification via sulfonation and transformed in a very efficient material for solid acid catalysis for the production of biodiesel.<sup>62</sup>

Another fundamental approach to tune the adsorption properties of the hyper-crosslinked polymers may be considered the selection of precursor monomers that already contain the proper functionality.

## 1.1.2 Microporous inorganic materials

Inorganic microporous materials typically display, with respect to their organic counterparts, higher chemical, thermal, and mechanical resistance. Some examples of high surface area inorganic materials are the highly ordered zeolites, the inert activated carbons and some nanosized allotropic forms of carbon, such as carbon nanotubes and graphene.

### Zeolites

Zeolites are crystalline hydrated aluminosilicates, which contain regular discrete pores and cavities extending into three dimensions. Zeolites consist of fully interconnected framework of corner-sharing  $\text{SiO}_4$  and  $\text{AlO}_4$  tetrahedra.<sup>63</sup> The dimensions of zeolites cavities are dependent on the structure, with the sizes of the openings ranging from 3 to 7 Å across various zeolites.

Zeolites were first commercialised in 1954, where they were used, for their hydrophilic nature, as refrigerant desiccants and in the drying of natural gas.<sup>64</sup> The first exploitation of the molecular sieve properties of zeolites occurred in 1959 with the ISOSIV process, which separates branched and linear hydrocarbons on the basis of their molecular cross-sectional areas, with branched isomers having a larger cross sectional area than linear isomers. The smaller pore openings allow the passage of linear hydrocarbons, but prevent the entry of the bulkier branched and cyclic structures. This property can be used to separate other hydrocarbons, and to separate metallic impurities from water.<sup>65,66</sup> Zeolites are also applied to gas separation processes. A large number of zeolites are prepared as nanocrystals since the early 90s. Synthesis in a closed system allows adjusting the ultimate crystal size via the control of the nucleation process. The number of viable nuclei in the system determines the ultimate crystal size, since the growth process stops after the conversion of the amorphous precursors into crystals. Therefore, more nuclei in a system result in smaller crystals in the final product.<sup>67</sup> Zeolites are also produced in the form of membranes, through the formation of seed layers by techniques such as manual assembly and Langmuir-Blodgett trough deposition, followed by secondary growth methods such as gel-free growth and minimization of twinning. Recent developments have enabled the formation of zeolite membranes as thin as 100-200 nm, which are promising advances for their commercial viability.<sup>68,69</sup>

### Activated carbons

Activated carbons are amorphous carbons undergone to chemical or physical activation. The activation process gives rise to very high SSA ( $\sim 500\text{-}3000\text{m}^2/\text{g}$ ) and sometimes to well-developed microporosity. They are also generically called *porous carbons*. The morphology of activated carbons consists of graphene layers with varying degrees of perfection randomly stacked within the

structure. The varying gaps between the stacks give rise to the microporous nature of the material, which has a pore size distribution of macropores, mesopores and micropores.<sup>70</sup>

Activated carbons are typically obtained from coals, cokes, wood, coconut shells and pecan shells, along with other carbonaceous agricultural by-products. Chemical activation involves the addition of compounds such as  $\text{ZnCl}_2$ ,  $\text{H}_3\text{PO}_4$  and  $\text{H}_2\text{SO}_4$  to the precursor feedstock prior to carbonization, and later removal. These compounds act as dehydrating agents, preventing the formation of tars and increasing the yield of activated carbon. Physical activation consists in the treatment of the carbon material by gases such as carbon dioxide and steam in the temperature range 700-1100 °C.<sup>71</sup> Although chemical activation often yields higher surface areas than physical activation, this process is currently not favoured because of environmental considerations.

The microporous nature, high specific surface area and chemical inertness of activated carbons lead to their use in industry as adsorbents for applications including trace impurity removal, gas separation and removal of  $\text{CO}_2$  from flue gas.<sup>72</sup> The adsorption potential of activated carbons is modified by the presence of functional groups, which are usually at the edge of the graphene layers, where carbon atoms are unsaturated. The most important functional groups are the oxygen based, which give hydrophilic nature in addition to the hydrophobic nature of the graphene layers. The dual nature of activated carbons allows a wide range of chemical species to be adsorbed onto the material.

### **Nanosized carbon allotropes**

Elemental carbon exists in nature in three allotropes, graphite, diamond and fullerene. Graphite is formed by layers of  $\text{sp}^2$  hybridized carbon atoms. Within a layer (a *graphene* layer), each carbon atom covalently bonds to three others, forming a planar array of fused hexagons. The un-hybridized  $2p_z$  orbital that accommodates the fourth electron forms a delocalized orbital of  $\pi$  symmetry that further stabilizes the in-plane bonds. The weaker van der Waals force keeps the layers stacked together, 3.354 Å apart.<sup>73</sup> This particular structure confers graphite the characteristic exfoliability, and the outstanding in-plane electrical and thermal conductivity. In the diamond allotropic form, the carbon atoms are  $\text{sp}^3$  hybridized and arranged tetrahedrally. Each carbon atom is attached to four other carbons with a C-C-C bond angle of  $109.5^\circ$ , forming a strong, rigid three-dimensional structure. This accounts for diamonds hardness, extraordinary strength and durability and gives diamond a higher density than graphite. Fullerenes, the more recent allotropic form of carbon discovered, were observed for the first time in 1985 by Kroto et al.<sup>74</sup> They are molecular carbon allotropes, consisting in spherical networks of  $\text{sp}^2$  hybridized carbon atoms composed in hexagons and pentagons (see Figure 1.2). The smallest stable and most prominent is the *buckminsterfullerene*, or  $\text{C}_{60}$ , made of sixty structurally equivalent carbon atoms connected in 12 pentagons and 20 hexagons. The discovery of fullerenes marked the beginning of an era of synthetic carbon allotropes, including the synthesis of carbon nanotubes (CNTs) in 1991<sup>75</sup> and the discovery of graphene in 2004.<sup>76</sup>

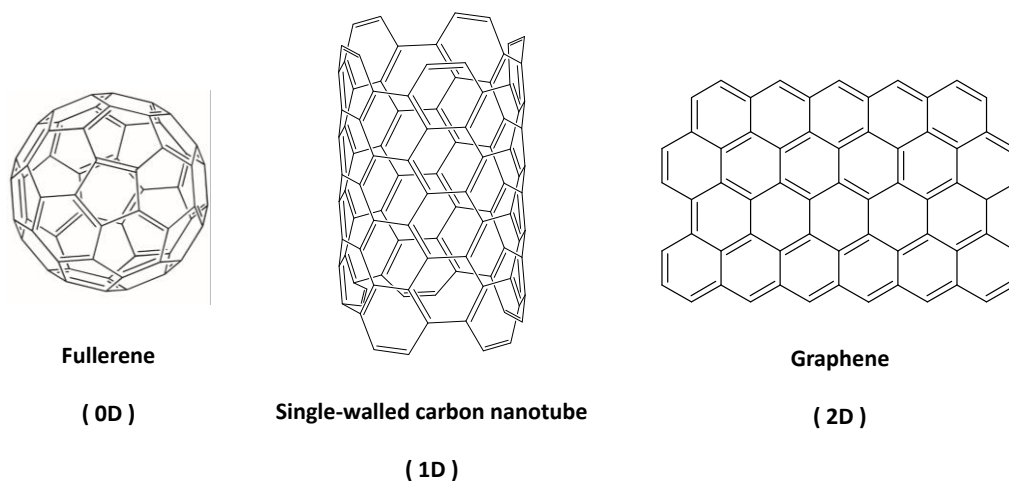


**Figure 1.2** Nanosized carbon allotropes

Carbon nanotubes are nanosized tubes made of seamless rolled-up graphite sheets. Depending on the preparation conditions, either single-walled or multi-walled carbon nanotubes (SWCNT or MWCNT) are obtained, with different chiralities (degree of twist).<sup>77</sup> These tubular networks of bent  $sp^2$ -hybridized atoms are characterized by a pronounced one-dimensionality because of a very high aspect ratio: typical diameters of single-walled carbon nanotubes are around one or two nanometres, but their lengths can easily reach millimetres and above. Graphene is a flat monolayer of carbon atoms tightly packed into a two-dimensional honeycomb lattice.<sup>78</sup> It was considered for a very long time a theoretical material, and was prepared for the first time by means of mechanical exfoliation of graphite by Andre Geim and Konstantin Novoselov. Geim and Novoselov also headed the team behind the investigation of the electronic properties of graphene.<sup>79</sup>

Carbon nanotubes have been subjected to increased research interest especially because of their electronic and mechanical properties. CNTs conductivity has been shown to be a function of their chirality, so that they can be either metallic or semi-conducting in their electrical behaviour. As concerning the mechanical behaviour, since each atom is connected via strong chemical bonds to the neighbouring atoms, they show very high tensile strength and Young's modulus. CNTs have also been studied for applications as hydrogen storage medium. Initial very promising results have been discouraged later by doubts on the initial reports but, more recently, some careful studies have reported storage capacities up to 3–4 wt% (under specific conditions), which could generate renewed interest in the field.<sup>80</sup> An upcoming application domain of CNTs is water purification. Portable filters containing CNT meshes are commercialized for purification of contaminated drinking water, and tangled CNT sheets have been proven to provide mechanically and electrochemically robust networks with controlled nanoscale porosity. These are used to electrochemically oxidize organic contaminants, bacteria, and viruses.<sup>81</sup> Moreover, membranes containing aligned encapsulated CNTs have demonstrated unprecedented low flow resistance for both gases and liquids flowing through the

interior of the CNTs.<sup>82</sup> This allowed, in the case of SWCNTs with very low diameter, water desalination by reverse osmosis with enhanced permeability, enabling lower energy costs in comparison to commercial polycarbonate membranes.<sup>83</sup>

Graphene, since its discovery, has attracted tremendous interest in a variety of fields, due to its outstanding electronic, thermal, and mechanical properties.<sup>84</sup> Furthermore, it is associated with high specific surface area, the predicted value being  $\sim 2630 \text{ m}^2/\text{g}$ .<sup>85</sup> Three-dimensional graphene-based aerogels have been reported in many research studies to combine ultralow density with high surface area and good conductivity, in order to improve adsorption, catalytic, and electrochemical performances. Besides, graphene-based aerogels can be easily restored by a simple heat treatment.<sup>86,87,88,89</sup> Another interesting field of application for graphene is microelectronics. In fact, since materials with high electrical conductivity and accessible surface area can achieve high electrical double layer capacitances, in this context, graphene sheets are widely regarded as a promising electrode material. Yu et al. described a hierarchically structured carbon microfiber made of an interconnected network of aligned SWCNTs with interposed nitrogen-doped reduced graphene oxide sheets. The obtained structure is mesoporous, with large specific surface area ( $396 \text{ m}^2/\text{g}$ ) and high electrical conductivity ( $102 \text{ S/cm}$ ).<sup>90</sup>

## 1.2 Adsorption

Adsorption is the phenomenon occurring between a liquid or a gas and the surface of a solid material generating enrichment of the fluid density at the interface. The understanding of adsorption is very important for the comprehension of many physical, chemical and biological phenomena based on adsorption, taking place at interfaces.<sup>91,92</sup> In fact, adsorption is exploited as fundamental principle of various technologies in the field of gas separation, purification and storage,<sup>93,94</sup> liquid purification,<sup>95,96</sup> controlled drug delivery<sup>97</sup> and catalysis.<sup>98,99</sup> Moreover, adsorption techniques have become fundamental in the evaluation of specific surface area and porosity of various fillers, pigments, fine powders and highly porous natural or synthetic materials. Many technologic advances on nanostructured materials have been possible thanks to their adsorption capacity characterization.

The study of the adsorption phenomena evolved by a series of fundamental steps over the years. Various phenomena now associated with adsorption were already known in the antiquity; for example, Egyptians, Greek and Romans employed clay, sand and wood for desalination of water, clarification of fat and oil and for the treatment of many diseases.<sup>100</sup> The first scientific studies about gas adsorption of some forms of charcoal came out between 1773 and 1777 by Scheele, Priestley and Fontana.<sup>101,102</sup> The exothermal nature of adsorption was noted for the first time in 1814 by de Saussure,<sup>103</sup> and in 1843 Mitscherlich suggested that the amount of gas adsorbed in a porous carbon was such that it should be probably in the liquid state.<sup>104</sup> The heat of adsorption of porous materials was studied only by means of calorimetry until 1879-1881, when Chappuis and Kayser related for the first time the gas adsorbed to the pressure, starting measuring the adsorption isothermal curves in different solid-gas systems.<sup>105</sup>

Advances in gas adsorption studies were accompanied by progresses in the field of liquid adsorption, too, signed by the observation for the first time of the heat of adsorption for solid-liquid systems by Leslie in 1802. Investigations on different solid-liquid isotherms of adsorption succeeded, with the formulation of one of the first mathematical models for this phenomenon by Freundlich, in 1907.<sup>106</sup>

From then on, the most significant advances in gas adsorption study in the past century were made by Zsigmondy, Polanyi and Langmuir. Zsigmondy, in 1911, noting the large uptake of water vapour of a porous silica, pointed out that the condensation of a gas in narrow pores could occur at lower pressure than the bulk liquid normal vapour pressure, basing its consideration also on an original concept of Lord Kelvin.<sup>107</sup> This concept is now generally recognized as *capillary condensation*. Polanyi, in 1914, formulated the fundamental theory that the adsorption of molecules on a surface depends on a potential, i.e. the intensity of the adsorption interaction decreases with increasing the distance from the surface.<sup>108</sup> This theory provided the basis for the definition of a *characteristic curve of adsorption*, refined and modified by Dubinin and co-workers in their theory of micropore filling.

In 1916, Langmuir's idea that the gas adsorption proceeded by constitution of a *monolayer* attracted enormous interest.<sup>109</sup> When Brunauer-Emmett-Teller, in 1938, published the BET theory,<sup>110</sup> centred on an S-shaped isotherm and *multi-layer* adsorption, Langmuir's concept of a monolayer coverage was really helpful to ascertain the stage at which monolayer coverage completed and from this evaluate the surface area of the adsorbent. BET theory, although being reliable under certain specific assumptions, became a standard procedure for the evaluation of the specific surface area of porous materials. Langmuir's paper was also of great influence for Dubinin and co-workers, who revised their adsorption theory considering diverse adsorption mechanisms for pores of different dimensions.

These and more speculations led finally to surface area and porosity analysis by adsorption techniques based on volumetric or calorimetric approaches, producing results comparable with other acknowledged techniques, such as microscopic, scattering and computational analysis. The International Union of Pure and Applied Chemistry (IUPAC) have established some guidelines for the adsorption field definitions and measurements. In according to IUPAC definitions, the material on which adsorption occurs is defined *adsorbent*, the gas or liquid in the adsorbed state is the *adsorbate*, while the same component in the fluid state is referred as *adsorptive*. Adsorption takes place in an interfacial phase between adsorbent and adsorbate, in which the adsorbate molecules are bond to the adsorbent through physical or chemical interaction defining, respectively, *physisorption* or *chemisorption*. Adsorption can also occur through a combination of the two but, in all cases, it is a surface phenomenon, in opposite to *absorption*, which is the diffusion of a mass through a solid or liquid material (bulk phenomenon). When it is difficult or impossible to distinguish between adsorption and absorption, it is convenient to use the term *sorption*, and the derivative *sorbent*, *sorbate* and *sorptive*. The reverse process of adsorption is defined *desorption*.<sup>111</sup>

### 1.2.1 Physisorption and chemisorption

Distinguishing between physisorption and chemisorption is, basically, as distinguishing between physical and chemical interactions. When adsorption occurs by physical interactions, the forces acting are long-range interactions, based on van der Waals forces and, as such, they are weak forces. Physisorption is analogous with vapour condensation within the pores and, in fact, the enthalpy of adsorption is the same as for condensation, except for the cases in which adsorption is enhanced by very narrow pores. The phenomenon is not specific, the adsorbed species are chemically identic in the adsorbate and adsorptive state, and it does not require an activation energy. Since the adsorbate molecules become more ordered in the adsorbed state, physical adsorption involves a decrease in the entropy of the adsorbed phase. It is a spontaneous process, therefore the variation in the Gibbs free energy ( $\Delta G$ ) is negative. Being

$$\Delta G = \Delta H - T\Delta S \quad (1.1)$$

where  $\Delta H$  and  $\Delta S$  are the enthalpy and the entropy of adsorption and  $T$  is the temperature of the phenomenon, and being  $\Delta S$  also negative, it is implied that  $\Delta H$  is also negative, defining adsorption as an exothermic process. For this reason, physisorption is favoured at lower temperatures, according to Le Cathelier's principle, except when adsorption shows activated diffusion effects. Physical adsorption is completely reversible by furnishing heat to the adsorption system, can occur in multi-layers and rapidly reaches equilibrium.<sup>112</sup>

Chemical adsorption, on the other side, is due to the formation of chemical bonds between adsorbate and adsorbent. Hence, it is a short range interaction, characterized by higher values of enthalpy with respect to physisorption, that are of the same order of magnitude of the energy change in a comparable chemical reaction. Chemisorption occurs on precise adsorption sites, and can only take place between specific adsorbates and adsorbents. For this reason, chemisorption can only occur in monolayer, it often requires an activation energy and is favoured at higher temperatures.<sup>113</sup> Chemisorption is irreversible, unless severe conditions are used. Moreover, chemical adsorption may be dissociative, leading to the fragmentation of the adsorbed molecules on the surface of the adsorbent, which acts as a catalyst.<sup>114</sup> Combined cases of physisorption and chemisorption exist, and physisorption may occur on top of a chemisorbed layer.

## 1.2.2 Gas adsorption

### Modalities of adsorption

The modalities through which adsorption occurs strictly depend on the morphology of the characteristic porosity. The interactions between the adsorbed gas molecules and the adsorbent surface are of electromagnetic nature, and involve the electronic densities surrounding the interacting molecules. For neutrally charged molecules, the Lennard-Jones potential is considered a satisfactory model for representing the adsorbate-adsorbent interactions.<sup>115</sup> If the adsorbate molecules have a permanent dipole or a quadrupole moment, the system cannot be described by just the Lennard-Jones potential and electrostatic interactions also have to be taken into account. The Lennard-Jones potential, instead, takes into account the energy associated with the long-range attractive forces (London dispersion forces) between the adsorbate and adsorbent molecules and the short-range repulsive forces generated by the overlapping of their electron clouds. With  $\sigma$  indicating the radius of the assumed spherical adsorbate molecule and  $\varepsilon$  indicating the depth of the potential well, the energy of the adsorbate-adsorbent interaction ( $E$ ) as a function of the adsorbate-adsorbent distance ( $r$ ) can be expressed by equation 1.2:

$$E = 4\varepsilon \left(\frac{\sigma}{r}\right)^{12} - \left(\frac{\sigma}{r}\right)^6 \quad (1.2)$$

The term to the twelfth power of (1.2) is related to the repulsive forces and the term to the sixth power is representative of the attractive forces. As represented in Figure 1.3, equilibrium between the two factors is reached for a certain distance  $r_e$ , with the potential assuming the lower possible value and the occurring of the adsorption.

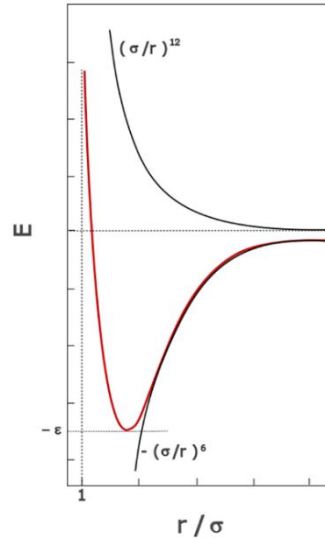


**Figure 1.3** The Lennard-Jones potential

When adsorption occurs on curved surfaces, a modification of the potential may follow. In *micropores*, for which the internal width is comparable with the molecular dimensions, the adsorbate molecules come to interact with all the faces of the pore. Hence, the potential energy function of a single adsorptive molecule interacting with different adsorbent molecules will depend on more adsorbate-adsorbent interactions than in the case of a molecule adsorbing on a flat surface. This effect was studied by Everett and Powl considering a model based on slit-shaped micropores.<sup>116</sup> They found that the adsorption potential of the adsorptive molecule is more complex in the case of a molecule adsorbed in a micropore with respect to the same molecule adsorbing on a flat surface of the same material; depending on the pore walls distance with respect to the adsorptive molecule radius, the interaction potential of the adsorptive molecule changes, as shown in Figure 1.4. As the pore walls distance ( $\delta$ ) approaches the dimension of the adsorptive molecular radius ( $\sigma$ ), the minimum energy levels for the adsorption potentials related to both faces of the pore decrease, and for  $\delta$  equal to  $\sigma$  the two combining potential merge in a unique curve with the lowest minimum. Consequently, the adsorption in micropores is favoured, and occurs at lower pressure than on flat surfaces. The mechanism of micropore adsorption is called pore-filling.

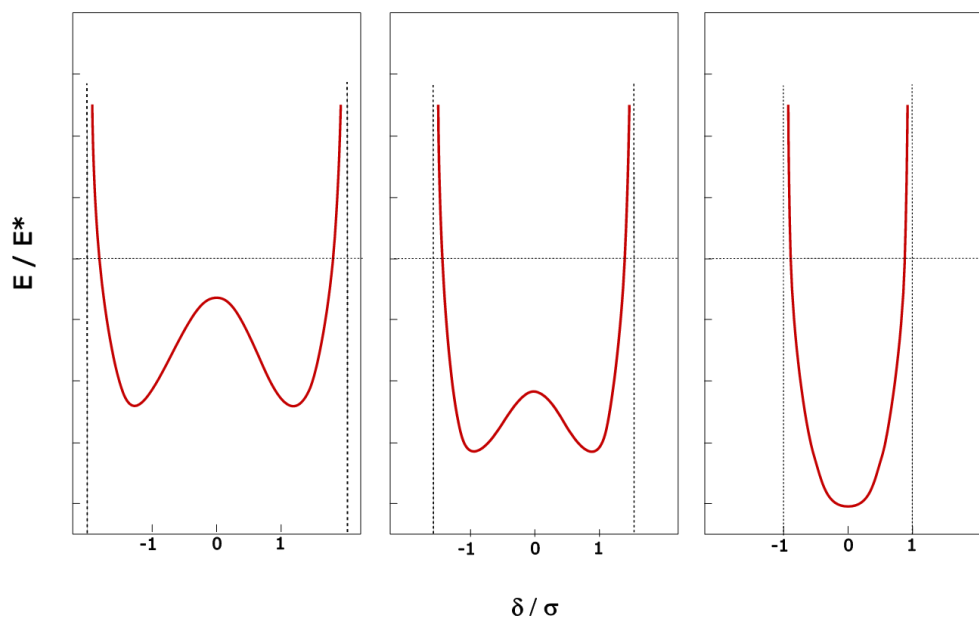


**Figure 1.4.** Interaction potential in a slit-shaped pore, simplified to a bi-dimensional system

In *macropores*, instead, no particular enhancement of the adsorption with respect to the surfaces is showed. Macropores and mesopores are usually considered transport pores for the micropores adsorption, and they influence the kinetic of the phenomenon. With *mesopores*, furthermore, is often associated the phenomenon of *capillary condensation*, with the gaseous adsorbate condensing at lower pressure than the saturation pressure of the bulk liquid. When capillary condensation occurs *hysteresis* arises between the adsorption and the desorption branches of the isotherm, computing the exercise of a lower pressure to desorb a condensed fluid than the pressure necessary to adsorb it from the gaseous phase.

### Thermodynamic of adsorption

As previously discussed, physisorption is an exothermic process. The differential *energy* or *enthalpy of adsorption* (for an ideal gas  $\Delta\dot{H}_a = \Delta\dot{U}_a - RT$ ) gives information about the energetics of surface coverage or micropore filling. The enthalpy of adsorption can be assessed by calorimetric methods and, involving some thermodynamic considerations, through the analysis of the isotherms of adsorption.<sup>111</sup>

Considering an isothermal and isochoric process, the *energy of adsorption*  $\Delta U_a$  can be expressed as

$$\Delta U_a = -Q_{T,V} \quad (1.3)$$

where  $Q_{T,V}$  is the amount of heat evolved at constant temperature and volume.

Since in physisorption the adsorbent is considered non-reacting with the adsorbate, the energy of adsorption depends only on the adsorptive molar internal energy in the adsorbed ( $u_a$ ) and in the gaseous ( $u_g$ ) states, that is:

$$\Delta U = u_a - u_g \quad (1.4)$$

The *chemical potential*, or *partial molar free energy* ( $\mu$ ) of a species in a gas mixture is defined as the change in Gibbs free energy with respect to the change in amount of the species at constant pressure, temperature and constant amount of other components. At equilibrium, the total sum of the chemical potential of all the species in the mixture is zero, thus the adsorptive chemical potential is equal in the gaseous ( $\mu_g$ ) and the adsorbed phase ( $\mu_a$ ). For the gas phase, the change in chemical potential energy  $d\mu_g$  is given by:

$$d\mu_g = -S_g dT + V_g dP \quad (1.5)$$

Where  $S_g$  ( $\text{J K}^{-1} \text{mol}^{-1}$ ) and  $V_g$  ( $\text{cm}^{-3}$ ) are the entropy and the volume of the gas phase, and  $P$  is the equilibrium pressure. For the adsorbed state, the change in chemical potential  $d\mu_a$  is given by:

$$d\mu_a = -\dot{S}_a dT + \dot{V}_a dP + \left(\frac{\delta\mu_a}{\delta n_a}\right)_{T,p} dn_a \quad (1.6)$$

Where  $\dot{S}_a$  and  $\dot{V}_a$  are the differential entropy and molar volume of the adsorbed phase, and  $n_a$  is the number of moles adsorbed. Being  $\mu_g = \mu_a$ , for a given amount of gas adsorbed ( $n_a$  constant), the combination of (1.5) and (1.6) gives:

$$(S_g - \dot{S}_a) dT = (V_g - \dot{V}_a) dP \quad (1.7)$$

that rearranged is

$$\left(\frac{dP}{dT}\right)_{n_a} = \left(\frac{S_g - \dot{S}_a}{V_g - \dot{V}_a}\right) \quad (1.8)$$

Assuming that  $V_g$  is much greater than  $V_a$ , and assuming the gas obeys the ideal gas law,  $V_g = RT/P$  and (1.8) becomes

$$\left(\frac{dP}{dT}\right)_{n_a} = \frac{P (S_g - \dot{S}_a)}{RT} \quad (1.9)$$

where  $(S_g - \dot{S}_a)$  represents the total change in entropy ( $\Delta \dot{S}_a$ ). At equilibrium  $\Delta \dot{H}_a = T \Delta \dot{S}_a$  and the latter expression can be formulated as

$$\left(\frac{dP}{dT}\right)_{n_a} = -\frac{P \Delta \dot{H}_a}{RT^2} \quad (1.10)$$

that, for integration, through separation of variables, gives the Clausius Clapeyron equation:

$$\ln P = -\frac{\Delta \dot{H}_a}{RT} + \frac{\Delta \dot{S}_a}{R} \quad (1.11)$$

The Clausius Clapeyron equation represents the relation between pressure and temperature for a given amount of gas adsorbed. Obtaining isotherms at different temperature, and plotting  $\ln P$  against  $1/T$ , the value of the *isosteric enthalpy* and *entropy of adsorption* can be calculated from the gradient and the intercept of this plot. Extrapolation of the enthalpy of adsorption at zero coverage provides a fundamental measure of the adsorbate/adsorbent interaction.<sup>117</sup>

### From theory to practice: interpretation of physisorption isotherms

The equilibrium relation between the quantity of adsorbed species and the pressure or concentration of the adsorbate in the bulk phase at constant temperature is known as the *adsorption isotherm*.<sup>118</sup> Much information about the porosity of the adsorbent and the modality of adsorption is given by the adsorption isotherm. This curve is an intrinsic characteristic of the adsorption system, depending on all its elements, i.e. the nature of the adsorbent and the adsorbate, the temperature of measurement and the range of pressure covered. Adsorption isotherms may be determined through *direct measurement*, by the manometric measurement of the amount of gas removed by the gaseous phase, and *indirect measurement*, via the gravimetric analysis of the adsorbent gas uptake.

Adsorption isotherms report the *surface excess amount* of gas adsorbed as a function of the equilibrium pressure. To correctly interpret them, one should distinguish between *excess adsorption* and *absolute adsorption*. An adsorption system is composed of three regions delimitating the adsorbent, the gas and the *adsorption space*, whose content is the *amount of adsorbed moles* ( $n_a$ ). Evaluation of  $n_a$  depends on the volume of the adsorption space  $V_a$ , which is usually an unknown quantity. Gibbs proposed a model for the calculation of the adsorbed gas based on the assumption of the adsorption space being bidimensional ( $V_a = 0$ ). Introducing an imaginary surface of adsorption (Gibbs Dividing Surface, GDS) that delimits the volume  $V_g$  available for the gas phase, the amount of adsorptive in the gas phase  $n_g$ , in equilibrium with the adsorbent, is then calculated by application of the appropriate gas laws. The difference between the total amount of adsorptive introduced into the system,  $n$ , and  $n_g$  is the adsorptive *surface excess amount* ( $n_\sigma$ ). The surface excess amount can be considered almost identical to the adsorbed amount  $n_a$  for adsorption of vapours up to 1 bar, if calculated considering a Gibbs dividing surface very close to the adsorbent surface. Therefore, much attention should be addressed to the determination of the dead volume in manometric measurements and the buoyancy in gravimetric analysis. For the adsorption of vapours at pressure higher than 1 bar the difference between  $n_a$  and  $n_\sigma$  cannot be ignored. In this case, provided that the volume of the adsorption space and the adsorbent are known, in the simplest case of GDS coinciding with the actual adsorbing surface,

$$n_a = n_\sigma + c_g V_a \quad (1.12)$$

Where  $c_g$  is the concentration of the gas.

Adsorption isotherms at temperatures below the adsorptive critical point are usually plotted as the amount of gas adsorbed ( $n_a$  or  $n_\sigma$ ) versus the relative pressure  $p/p^0$ , where  $p^0$  is the saturation pressure at the adsorption temperature, so as to easily compare different isotherms. If the analysis temperature is above the critical one, and no  $p^0$  exists, one must necessarily use the equilibrium pressure  $p$ .<sup>111</sup>

Five fundamental types of physisorption isotherms were originally proposed by Brunauer, Deming, Deming and Teller in the usually referred as BDDT or Brunauer classification.<sup>119,120</sup> Ever since, new characteristic isotherms have been identified and shown to be closely related to the pore size distribution of the adsorbent. The original five isotherm types, together with a sixth one later added by the IUPAC are reported in Figure 1.5.

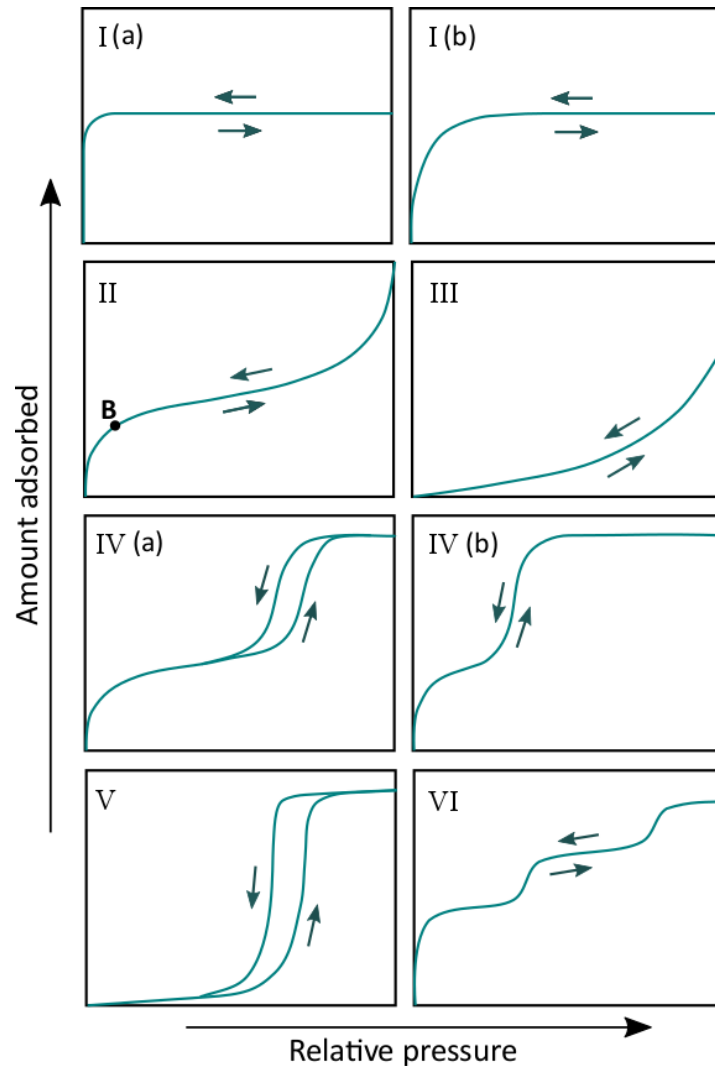


**Figure 1.5.** Classification of adsorption isotherms

The Type I isotherm is concave to the relative pressure axis. The curve rises steeply at low relative pressure and reaches plateau adsorption. The steep uptake at very low  $p/p^0$  is indicative of a strong adsorbent-adsorptive interaction, due to narrow micropores (pore filling). Therefore, this isotherm is characteristic of materials having only a limited range of micropore size; the I(a) isotherm is showed by microporous adsorbents having very narrow pores ( $< \sim 1$  nm), the I(b) is given by microporous materials having broader pore size distribution including wider micropores and possibly narrow mesopores ( $< \sim 2.5$  nm).

The Type II isotherm is concave to the relative pressure axis at low  $p/p^0$  and convex at higher  $p/p^0$ . It is indicative of multilayer adsorption, the point B corresponding to the monolayer coverage.

The Type III isotherm is convex to the relative pressure axis over the complete range of adsorption. This is characteristic of non-porous or macroporous solids, having weak adsorption interactions. There is no point recognizable as of monolayer coverage; in fact, in these cases the adsorbed molecules do not even form a uniform layer, instead they aggregate in clusters around the most favourable adsorption sites.

Type IV(a) and IV(b) isotherms are closely related to the Type II isotherm, with the difference that at high relative pressure they reach a characteristic saturation plateau, although this might be short and reduced to an inflexion point. They are characteristic of mesoporous adsorbents. In IV(a) isotherm, the typical hysteresis associated to the capillary condensation is showed. This behaviour is more frequently showed with respect to Type IV(b), although for adsorbents having mesopores of smaller width, completely reversible isotherms like Type IV(b) are possible.

The Type V isotherm shape is very similar to that of Type III (thus implying weak adsorbent-adsorbate interactions), except that at higher  $p/p^0$  the curve show a steep adsorption increase, suggesting a pore filling mechanism.

The reversible stepwise Type VI isotherm is representative of layer-by-layer adsorption on a very high uniform surface. The sharpness of the steps depends on the adsorbent-adsorptive system and the temperature of the process, while the height of the steps represents the capacity of each adsorbed layer.

The hysteresis shape also hinder much information about the porous structure of the adsorbent. The main types of hysteresis are showed in Figure 1.6.

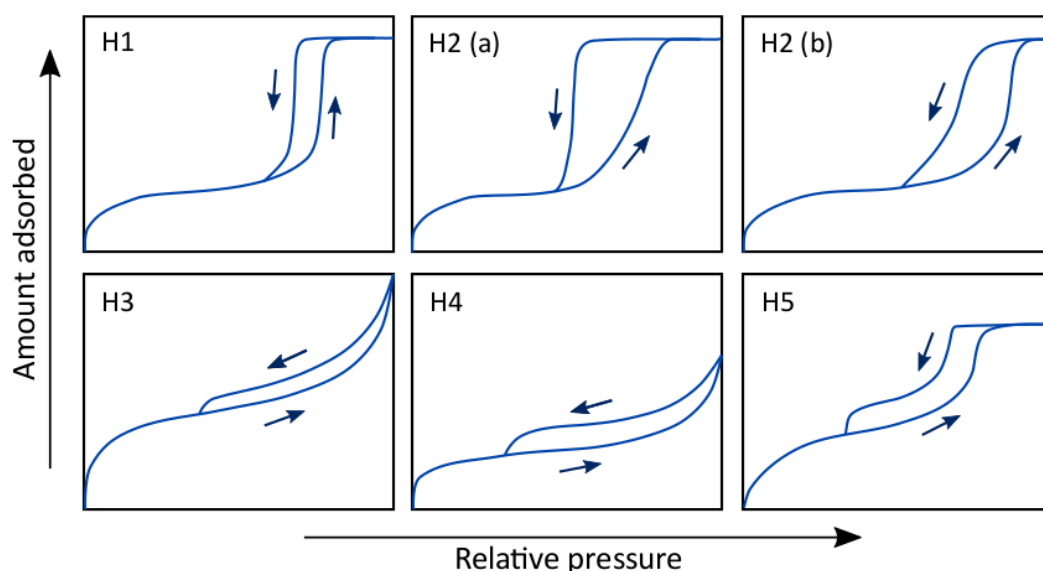


**Figure 1.6** Classification of adsorption isotherms hystereses

The Type H1 hysteresis is characteristic of adsorption isotherms of materials that exhibit a narrow range of uniform mesopores.

Hysteresis loops of Type H2 are revealing of more complex pore structures in which network effects are very important. The very steep desorption branch in H2(a) can be attributed either to pore-blocking/percolation in a narrow range of pore necks or to cavitation-induced evaporation. The Type H2(b) loop is also associated with pore blocking, but in this case the size distribution of neck widths is larger.

In Type H3, associated to a Type II isotherm, the sharp step-down of the desorption branch is normally located at the cavitation-induced  $p/p^0$ .

The H4 hysteresis is similar to H3, but the adsorption branch is now a combination of Types I and II, the more pronounced uptake at low  $p/p^0$  being associated with the filling of micropores. H4 loops are often found in micro-mesoporous materials.

The Type H5 hysteresis shape is associated with certain pore structures containing both open and partially blocked mesopores. Together with Type H3 and H4, it is characterized by a sharp step-down of the desorption branch. Generally, this is located in a narrow range of relative pressure for a particular adsorptive and analysis temperature ( $p/p^0 \sim 0.4 - 0.5$  for nitrogen at 77K).

## Specific surface area evaluation

On the basis of physisorption isotherms, the Gibbs excess adsorption amount can be evaluated through fitting of the curve with an appropriate model. The first attempt to fit adsorption isotherms was made in 1888 by Bemmelen, who introduced what is now known as the *Freundlich equation*:

$$\frac{n}{m} = K_F P^{1/\eta} \quad (1.13)$$

where  $n$  is the adsorbed gas moles number,  $m$  is the mass of the adsorbent,  $P$  is the equilibrium pressure and  $K_F$  and  $\eta$  are adsorbent-specific parameters.<sup>121</sup> This equation is only empirical and does not purport to capture or contain the physics of adsorption. Nonetheless, it displays key behaviours that are common to fit functions for Type I isotherms. The gas adsorption behaviour, at relatively low pressure, follows Henry's law:

$$n = K_H P \quad (1.14)$$

where  $K_H$  is the Henry's constant. Henry's law can be derived from ideal gas assumptions. If we assume that the adsorbed phase takes the form of a two-dimensional ideal gas following

$$P_a A_a = nRT \quad (1.15)$$

where  $P_a$  and  $A_a$  are respectively the spreading pressure and the area of the adsorbed gas, and also assume that the equilibrium spreading pressure is proportional to the equilibrium bulk gas pressure  $P$  ( $P_a = cP$ ), then

$$\frac{P_a A_a}{RT} = \frac{c P A_a}{RT} = n = K_H P \quad (1.16)$$

Accordingly, the low-pressure regime of an isotherm, where uptake is proportional to applied gas pressure, is commonly referred to as the Henry's law regime. This model does not fit the higher adsorption range, in which the isotherm reaches a plateau.

Irving Langmuir, in 1918, derived a model for gas adsorption that incorporates both the Henry's law regime and the saturation regime behaviour.<sup>122</sup> He supposed that the adsorbate would form a monolayer above the surface of adsorption and took a number of simplifying assumptions, as follows:

- i. the adsorbent surface is perfectly flat
- ii. the gas adsorbs into an immobile state
- iii. there is a finite number of adsorption sites that can each be filled by no more than one adsorbate molecule
- iv. all adsorption sites are energetically identical
- v. adsorbate molecules do not interact.

Considering these simplifying assumptions, the Langmuir adsorption isotherm may be derived from kinetic theory, statistical mechanics, or from a phenomenological perspective, and takes the form:

$$\theta = \frac{K_L P}{1 + K_L P} \quad (1.17)$$

with  $\theta = \frac{n}{n_m}$  being the fractional occupancy of the binding sites ( $n_m$  are the moles of adsorptive in the monolayer) and  $K_L$  an equilibrium constant given by an Arrhenius-type equation. Unfortunately, the Langmuir five simplifying assumptions are almost never entirely satisfied and the Langmuir isotherm cannot be applied over broad ranges of conditions. In particular, the Langmuir model breaks down if multilayer adsorption occurs, meaning every time that a surface contains macropores, mesopores, or even the larger micropores.

In 1938 Stephen Brunauer, Paul Emmett and Edward Teller extended the Langmuir model in order to take into consideration the multilayer adsorption.<sup>123</sup> They realized that in multilayer adsorption molecules do not successively fill one complete monolayer after another. Rather, fragments of multilayer stacks of varying sizes cover the adsorbent surface. Each layer is in dynamic equilibrium with the layers above and below it, much in the same way that the Langmuir model assumes a dynamic equilibrium between the adsorbed monolayer and the gas phase above it. Their theory is also based on a certain number of assumptions, which are:

- i. infinite layers may be adsorbed on a surface
- ii. there is no interaction among layers
- iii. each layer follows the Langmuir model.

The results of the Brunauer, Emmett, Teller, or BET, model provide the BET equation:

$$\frac{1}{n \left[ \left( \frac{P_0}{P} \right) - 1 \right]} = \frac{C - 1}{n_m C} \left( \frac{P}{P_0} \right) + \frac{1}{n_m C} \quad (1.18)$$

where  $n$  is the specific amount of gas adsorbed at the pressure  $\frac{P}{P_0}$ ,  $P$  and  $P_0$  are the equilibrium and saturation pressure,  $n_m$  is the specific monolayer capacity, and  $C$  is the BET constant

$$C = e^{\left( \frac{E_1 - E_L}{RT} \right)} \quad (1.19)$$

with  $E_1$  and  $E_L$  being respectively the enthalpy of adsorption for the first and the following layers.  $E_L$  is assumed to equal the enthalpy of liquefaction of the adsorbate.<sup>124</sup>

BET theory has proven particularly useful at measuring the specific surface areas of a number of materials. For high quality surface area determinations, nitrogen, argon, carbon dioxide, and krypton have been used. In particular, a plot of  $1/n \left[ \left( \frac{P_0}{P} \right) - 1 \right]$  versus  $P/P_0$  should yield a straight line in the relative pressure range of  $0.05 < P/P_0 < 0.3$ . Using linear regression, the slope and the intercept of this line are determined, from which the parameters  $n_{max}$  and  $C$  are calculated. The surface area may then be determined via  $n_{max}$ , using the established cross-sectional area of the probe molecule.

BET method can be applied to many Type II and Type IV isotherms, but extreme caution is needed in the presence of micropores (with Type I isotherms and combinations of Types I and II or Types I and IV). However, it might be impossible to separate the processes of monolayer-multilayer adsorption and micropore filling. With microporous adsorbents, the linear range of the BET plot might be very difficult to locate. In all cases, the first signal to validate the pertinence of the BET model is considered the BET constant ( $C$ ), which should always be positive. Moreover, the  $C$  value also gives a useful indication of the shape of the isotherm in the BET range. For example, if the value of  $C$  is at least  $\sim 80$  the knee of the isotherm is sharp and the point B (see Figure 1.5) is fairly well defined. It was this characteristic point that was first identified by Brunauer and Emmett as the stage of monolayer completion and the beginning of multilayer adsorption. If  $C$  is low ( $< \sim 50$ ) point B cannot be identified as a single point on the isotherm, there is an appreciable overlap of monolayer and multilayer adsorption and the precise interpretation of  $n_m$  is questionable. When  $C$  is very low ( $< 2$ ), the isotherm is either Type III or Type V and the application of the BET method is not appropriate. A high value of  $C$  ( $> \sim 150$ ) is generally associated with either adsorption on high-energy surface sites or filling of narrow micropores.<sup>125</sup>

Adsorption methods are universally employed for the determination of specific surface area, with the Brunauer–Emmett–Teller being the most widely adopted model for the surface area analysis. Nevertheless, the measurement of SSA cannot be unrelated by some specific features of the measurement system, such as the nature of the adsorptive used, the analysis temperature and the model adopted for the evaluation of the surface area, therefore these factors should always be expressed together with the reported result.

### **Pore size distribution evaluation**

For many years, nitrogen adsorption at 77 K has been generally accepted as the standard method for both micropore and mesopore size analysis but, for several reasons, it is now becoming evident that nitrogen is not an entirely satisfactory adsorptive for the assessment of the micropore size distribution. It is well known that the quadrupolar nature of the nitrogen molecule is largely responsible for the specific interaction with a variety of surface functional groups and exposed ions. This not only affects the orientation of the adsorbed nitrogen molecule on the adsorbent surface, but it also strongly affects the micropore filling pressure. For example, for many zeolites and MOFs the initial stage of physisorption is shifted to extremely low relative pressures ( $\sim 10^{-7}$ ). The rate of diffusion is slow in this ultra-low pressure range, which makes it difficult to measure equilibrated adsorption isotherms. Additional problems are associated with pre-adsorbed  $N_2$  molecules, which may block the entrance of narrow micropores, and with the instauration of specific interactions with surface functional groups so that the pore filling pressure is not clearly correlated with the pore size and structure. It follows that, in order to measure an adsorption isotherm accurately, careful

considerations should be given to the choice of the adsorptive and the operational temperature. In contrast to nitrogen, argon does not exhibit specific interactions with surface functional groups, however, the interpretation of argon isotherms at liquid nitrogen temperature is not straightforward. At 87 K this problem is avoided, since argon fills narrow micropores at significantly higher relative pressures in comparison with nitrogen at 77 K.<sup>126,127,128</sup> This leads to accelerated equilibration and permits the measurement of high resolution adsorption isotherms. Nevertheless, because of kinetic restrictions at cryogenic temperatures (87 K, 77 K), both Ar and N<sub>2</sub> adsorption are of limited value for the characterization of very narrow micropores. One way of addressing this problem is to use CO<sub>2</sub> (kinetic dimension 0.33 nm) as adsorptive at 273 K. At 273 K the saturation vapour pressure of CO<sub>2</sub> is very high (~ 3.5 MPa), hence the pressures required for micropore size analysis are in the moderate range (~ 0.1-100 kPa). Because of these relatively high temperatures and pressures, diffusion is much faster and pores as small as 0.4 nm can be accessed. On the other hand, the easily measurable maximum relative pressure for measurements with CO<sub>2</sub> at 273 K is  $p/p^0 \sim 3 \times 10^{-2}$  (corresponding to ambient pressure) and hence only pores < 1 nm can be explored in this way. Moreover, CO<sub>2</sub> should not be recommended for the pore size analysis of microporous solids with polar surface groups (e.g., oxides, zeolites, MOFs) since the quadrupole moment of CO<sub>2</sub> is even larger than that of N<sub>2</sub>, and this would make it difficult to correlate the CO<sub>2</sub> pore filling pressure with the size of the pores.

Once chosen the adsorptive gas, porosity information can be acquired from the analysis of the adsorption isotherm. If the physisorption isotherm is of Type I, with a virtually horizontal plateau, the limiting uptake may be taken as a simple measure of the micropore capacity, with respect to the adsorption of the particular gas at the operational temperature. To convert the adsorptive uptake into the micropore volume, it is usually assumed that the pores are filled with the condensed adsorptive in the normal liquid state. This assumption is known as the Gurvich rule. However, in practice, the plateau of the adsorption isotherm is rarely horizontal, since most microporous adsorbents have appreciable external surface areas and many have also pores in the mesopores range. It follows that the Gurvich rule cannot always be applied in a straightforward way to determine the micropore volume.

A number of different methods have been proposed for the analysis of physisorption isotherms given by microporous solids. They can be divided into the older macroscopic procedures and those based on statistical mechanics. One macroscopic approach involves the empirical comparison of an isotherm with an appropriate standard obtained on a non-porous reference material of similar chemical composition. In the *t-method* it is necessary to make use of a standard multilayer thickness curve, but this is dependent on the application of the BET method, which may not be strictly suitable. In order to overcome this problem the use of the  *$\alpha_s$ -plot* method is preferred because it does not require the evaluation of the monolayer capacity and it is also more adaptable than the *t-plot*. In this method the standard isotherm is plotted in a reduced form  $(n/n_x)_s$  versus the relative pressure  $p/p^0$ ,

where the normalising factor  $n_x$  is taken as the amount adsorbed at a preselected relative pressure (generally  $p/p^0 = 0.4$ ). In order to construct the  $\alpha_s$ -plot for a given adsorbent, the amount adsorbed  $n$  is plotted as a function of the reduced standard isotherm,  $\alpha_s = (n/n_x)_s$ . The micropore capacity is obtained by back extrapolation of a linear section of the  $\alpha_s$  plot. A refinement of the  $\alpha_s$  analysis makes use of high-resolution standard isotherm data at very low relative pressures. Another popular method for evaluation of the micropore volume is based on Dubinin's pore-volume filling theory. In accordance with the Dubinin–Radushkevich (DR) equation, a plot of  $\log n$  versus  $\log^2(p^0/p)$  is linear, provided that the micropore size has a uniform Gaussian distribution, and its extrapolation to the ordinate will give the micropore capacity. Although linear DR plots are reported for the physisorption of various gases and vapours by microporous carbons, there are numerous examples of the linear region being apparently absent or restricted to a limited range of low relative pressures. The applicability of the DR method is then questionable.<sup>129,127</sup>

It must be kept in mind that these classical methods do not allow for the effect of micropore size and shape on molecular packing so that the adsorbate cannot always have bulk-liquid like properties. This problem is addressed, instead, in methods based on *molecular simulation* (Monte Carlo simulations - MC) and *density functional theory* (DFT). An empirical way of studying microporosity is by the application of a number of molecular probes of progressively increasing molecular diameter. The method is based on the measurement of both adsorption rates and capacities. A sharp adsorption cut-off might be expected to correspond to a given micropore size, but this does not take into account of the complexity of most microporous materials. Although the results are often quite difficult to interpret, generally it is possible to obtain useful information about the effective range of window and/or pore entrance size. Various semi-empirical methods include those proposed by Horvath and Kawazoe (the HK method), Saito and Foley, and Cheng and Yang for the evaluation of the pore size distribution of slit, cylindrical and spherical pores, respectively.<sup>127,128,129</sup> Although these semi-empirical methods tend to underestimate the pore size, they may be useful for the comparison of microporous materials. Microscopic treatments such as density functional theory (DFT) and molecular simulation, which can describe the configuration of the adsorbed phase at the molecular level, are considered to provide a more reliable approach to pore size analysis over the complete nanopores range.<sup>128,130</sup> Therefore, DFT and MC have been developed into powerful methods for the description of the adsorption and phase behaviour of fluids confined in well-defined pore structures.<sup>131,130</sup> These procedures are based on the fundamental principles of statistical mechanics as applied to the molecular behaviour of confined fluids. They describe the distribution of adsorbed molecules in pores on a molecular level thus providing detailed information about the local fluid structure near the adsorbent surface. The fluid-solid interaction potential is dependent on the pore shape model. Different pore shape models (e.g., slit, cylinder, spherical geometries and hybrid shapes) have been developed for various material classes such as carbons, silicas, zeolites. Non-local-density functional theory (NLDF) based methods for pore size/volume analysis of nanoporous

materials are now available for many adsorption systems.<sup>127,128,130</sup> They are included in commercial software and are also featured in international standards (such as ISO 15901-3). These methods allow one to calculate for a particular adsorptive/adsorbent pair a series of theoretical isotherms in pores of different widths for a given pore shape. The series of theoretical isotherms is called the *kernel*, which can be regarded as a theoretical reference for a given class of adsorbent/adsorptive system. The calculation of the pore size distribution function is based on a solution of the general adsorption isotherm equation, which correlates the experimental adsorption isotherm with the kernel of the theoretical adsorption or desorption isotherms. Several approaches have been proposed to account for the heterogeneity of most adsorbents, which if not properly taken into account can lead to appreciable inaccuracy in the pore size analysis. Such methods include the development of complex 3D structural models of disordered porous solids by advanced molecular simulation techniques. The drawbacks of the conventional NLDFT model, which assumes a smooth and homogenous adsorbent surface, have been addressed by the introduction of two-dimensional DFT approaches.<sup>132</sup> Quenched solid density functional theory (QSDFT) is another approach to quantitatively allow for the effects of surface heterogeneity in a practical way.<sup>128,130</sup> It has been demonstrated that taking into account surface heterogeneity significantly improves the reliability of the pore size analysis of heterogeneous nanoporous materials. Finally, it must be stressed that the application of advanced methods based on DFT and MC can lead to reasonably accurate evaluation of the pore size distribution only if a given nanoporous system is compatible with the chosen DFT/MC kernel. If the chosen kernel is not consistent with the experimental adsorptive/adsorbent system, the derived pore size distribution may be significantly in error.

### 1.2.3 Adsorption from solution

A distinctive feature of adsorption from solution is that it always involves a competition between the solvent and the solute, which has to be taken into account in any complete analysis of the experimental data. In the case of adsorption from solution, the *apparent adsorption* of a solute at the liquid/solid interface is usually evaluated by measuring the decrease in its concentration when brought into contact with the adsorbent. The adsorption isotherm is then plotted as the apparent adsorption of the solute against the equilibrium concentration. At low concentrations, these adsorption isotherms mainly fall into two main types among those listed by Giles and Smith (1974): the Type L is concave to the concentration axis (analogous to Type I of the IUPAC classification) and the Type S is first convex and then concave to the concentration axis (analogous to Types III or V). A Type L isotherm having a long well-defined plateau is generally associated with monolayer adsorption of the solute and minimal competition from the solvent. A Type S isotherm is explained by a different balance between the adsorbate-adsorbent and adsorbate-adsorbate interactions: the latter are thought to be responsible for a *cooperative* adsorption mechanism, which produces an upward swing over the first part of the adsorption isotherm.<sup>126</sup>

The adsorption isotherms may be fitted with the Langmuir or Freundlich equations, depending on the modality of adsorption. The Langmuir model assumes monolayer coverage; the equation (1.17), for a solid-liquid system, can be expressed as

$$\frac{q_e}{q_m} = \frac{K_L C_e}{1 + K_L C_e} \quad (1.20)$$

where  $q_e$  is the equilibrium adsorption capacity,  $q_m$  is the maximum adsorption capacity (monolayer coverage),  $C_e$  is the equilibrium concentration of adsorptive and  $K_L$  is a constant related to the adsorption energy.<sup>133</sup> Linearization of the (1.20) gives:

$$\frac{C_e}{q_e} = \frac{C_e}{q_m} + \frac{1}{q_m K_L} \quad (1.21)$$

from the data fitting of the experimental  $q_e$  and  $C_e$ ,  $q_m$  and  $K_L$  can be derived.

The Freundlich equation is derived for multilayer adsorption, and in the case of adsorption from solution the (1.13) becomes

$$q_e = K_F C_e^{1/\eta} \quad (1.22)$$

with  $K_F$  and  $\eta$  being, respectively, indicative of the adsorption capacity and intensity. The parameter  $\eta$  is usually greater than unity. As this value becomes larger, the adsorption isotherm becomes more non-linear as its behaviour deviates further away.<sup>134</sup> Plotting  $\ln q_e$  versus  $\ln C_e$  would give

$$\ln q_e = \frac{1}{\eta} \ln C_e + \ln K_F \quad (1.23)$$

from which  $K_F$  and  $\eta$  can be easily derived.

### **Specific surface area analysis through adsorption from solution**

The specific surface area of some porous materials may be measured, in some specific cases, by means of adsorption from solution.<sup>135</sup> This technique is very important when the water solution manages to penetrate porous regions that the gases cannot, due to the swelling of the adsorbent in water.

Methylene blue (MB) has been used for decades in solution to evaluate the SSA of clay minerals. MB chemical formula is  $C_{16}H_{18}ClN_3S$  (see Figure 1.7), with a corresponding molecular weight of 319.87 g/mol. In aqueous solution it is a cationic dye ( $C_{16}H_{18}N_3S^+$ ) which absorbs to negatively charged clay surfaces.<sup>136,137</sup> Hence, the specific surface area of the particles can be determined by the amount of absorbed methylene blue.

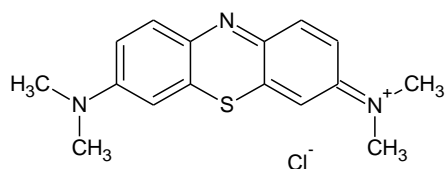


**Figure 1.7** Molecular structure of methylene blue

The methylene blue molecule has a rectangular shape with dimensions of approximately  $17 \text{ \AA} \times 7.6 \text{ \AA} \times 3.25 \text{ \AA}$ . This molecule may attach to the mineral surface in various orientations, so that the area covered by one MB molecule may vary:

- if the molecule lies on its largest face on the surface under study, the covered area is about  $130 \text{ \AA}^2$  per molecule;<sup>136,137,138</sup>
- if the molecule is tilted ( $65\text{-}70^\circ$ ) with respect to the surface under study, the covered area is about  $66 \text{ \AA}^2$  per molecule;<sup>139</sup>
- if the longest axis is oriented perpendicular to the surface, the covered area is about  $24.7 \text{ \AA}^2$  per molecule.<sup>140</sup>

The uncertainty in the assumption of the covered area can strongly affect the estimation of the specific surface area. The most common assumption is that the molecule lies flat on the mineral surface on its largest face; in this case, the area covered by one MB molecule is about  $130 \text{ \AA}^2$ . The methylene blue adsorption involves high bonding energy (ionic Coulombian attraction - chemisorption) and it is generally limited to a monolayer.

MB technique was confronted with  $\text{N}_2$  adsorption to ascertain the SSA of diverse clays,<sup>136,137,138,141</sup> and MB method rendered higher values of SSA with respect to  $\text{N}_2$  adsorption in swelling clays, as interlayer surfaces can be reached by exchangeable ions after hydration ( $3 < \text{SSA}_{\text{MB}}/\text{SSA}_{\text{N}_2} < 22$ ). However, for non-swelling clay minerals, there was no significant difference in specific surface area ( $<10\%$ ) determined by either dry or wet measurements.<sup>141</sup>

Assessment of surface area through adsorption from solution is also widely employed with graphene oxide (GO) samples. GO is the oxidized form of graphite, obtained using strong oxidizing agents, which install oxygenated functionalities onto the graphene layers. This process expands the layer separation and makes the material hydrophilic. Therefore, while graphite is a multilayer system, graphene oxide in water consists of a stable suspension of few layers and monolayers, the relative amount of the two depending on the extent of oxidation. If the solvent is removed, inevitable aggregation and stacking among graphene oxide layers will significantly reduce the exfoliation, therefore the surface area of the dry material is expected to be lower than the one measured in suspension.<sup>142</sup>

Several studies reported on the assessment of GO specific surface area through methylene blue adsorption from solution, and comparisons with the values given by gas adsorption measurements confirmed the expected discrepancy.<sup>143,144,145,146,147,148</sup> For example, experiments conducted by McAllister et al. on GO prepared by oxidation of graphite flakes through Staudenmaier method reported surface area of 1850 m<sup>2</sup>/g by MB adsorption and BET SSA from 600 to 700 m<sup>2</sup>/g, with BET results being subjected to the state of agglomeration of the powder.<sup>143</sup>

### **1.3 Aim of the work**

The aim of this thesis is to explore the microporous structure and the adsorption properties of innovative hyper-crosslinked polymers and nanocomposites, as well as their possible applications for water remediation and gas sorption and separation. Furthermore, a section of the work will be focused on the effect of the oxidation degree on the self-assembly properties and the specific surface area of graphene oxide. Within this work, the scientific interest on this subject derives from the need of obtaining an insight on the processability and the properties of this high surface area nanostructured material for possible applications as functional filler in HCL based nanocomposites.

In particular, chapter two will be focused on the study of the effects of inorganic porous nanofillers (multi-walled carbon nanotubes, MWCNTs) on the structure and the adsorption properties of styrene/vinylbenzyl chloride/divinylbenzene hyper-crosslinked polymers. A suitable surface modification strategy of the MWCNTs, by surface grafting of poly(vinylbenzyl chloride) (PVBC), is set up in order to promote the nanotube embedding within the gel-type precursor and their participation to the hyper-crosslinking step. The effects of the addition of MWCNTs on the structure, morphology and adsorption properties of the resin prepared by suspension polymerization followed by Friedel-Crafts hyper-crosslinking will be investigated.

In the following part of the thesis, described in chapter three, a new synthetic approach for the realization of HCL polymers and nanocomposites will be explored, based on the bulk prepolymerization of a precursor polymer followed by a traditional Friedel-Crafts alkylation step. The HCL polymers obtained by bulk prepolymerization will be fully characterized and compared to the suspension prepolymerized HCL polymers, in order to evaluate the effectiveness of the proposed approach. Moreover, through the new bulk prepolymerization synthetic route, HCL nanocomposites containing unmodified graphene nanoplatelets (GNP) or surface modified graphene oxide (GO) will be realized, with the objective of exploiting the high specific surface area of GO and to evaluate how this material can affect the properties of the resin. The structure, morphology and adsorption properties of the obtained microporous nanocomposites will be explored through spectroscopic and morphologic techniques and adsorption tests. Furthermore, in order to evaluate their applicability in engineered systems, these HCL resins and nanocomposites will be tested as functional fillers in

polysulfone membranes, potentially useful for water remediation, evaluating their effectiveness by phenol uptake from aqueous solution.

Chapter four will cover another possible application of the HCL polymers as functional filler for water purification. This work was developed in cooperation with the research group of Prof. Giovanni Filippone in DICMAPI, Federico II. New composite hydrogels, based on a chitosan matrix containing HCL particles, will be prepared with the objective of realizing new materials for broad-spectrum dye adsorption from aqueous solution. The composite morphology, mechanical and adsorption properties toward different dyes will be investigated and compared to those of the plain chitosan hydrogel.

The last part of this thesis, chapter five, will be focused on the effect of the oxidation degree on the self-assembly and the surface area of graphene oxide. This study was developed in collaboration with a doctoral colleague, Giuseppe Cesare Lama. GO samples will be prepared at different oxidation degrees through a Hummers modified procedure. The obtained GO samples will be characterized by elemental, spectroscopic, thermogravimetric, and calorimetric analysis. Moreover, morphological analysis and BET SSA analysis through nitrogen adsorption on cast and freeze-dried GO samples, combined to methylene blue adsorption analysis on GO water suspensions, will be performed to investigate the effect of the oxidation degree on the processability and the adsorption properties of graphene oxide.

## 1.4 References

- <sup>1</sup> P. Bernardo, E. Drioli and G. Golemme, *Ind. Eng. Chem. Res.*, 2009, **48**, 4638.
- <sup>2</sup> R. Dawson, A. I. Cooper and D. J. Adams, *Prog. Polym. Sci.*, 2012, **37**, 530
- <sup>3</sup> J. Weickert, R. B. Dunbar, H. C. Hesse, W. Wiedemann and L. Schmidt-Mende, *L. Adv. Mater.*, 2011, **23**, 1810
- <sup>4</sup> Jared B. DeCoste and Gregory W. Peterson *Chem. Rev.*, 2014, **114**, 5695
- <sup>5</sup> W. Lei, D. Portehault, D. Liu, S. Qin and Y. Chen, *Nature Communications*, 2013, **4**, 1777
- <sup>6</sup> Y. Han, Z. Xu, and C. Ga, *Adv. Funct. Mater.*, 2013, **23**, 3693
- <sup>7</sup> S. Merino, C. Martín, K. Kostarelos, M. Prato, and E. Vázquez, *ACS Nano*, 2015, **9**, 4686
- <sup>8</sup> C. Perego and R. Millini, *Chem. Soc. Rev.*, 2013, **42**, 3956
- <sup>9</sup> J. Weitkamp, *Solid State Ionics*, 2000, **1**, 175
- <sup>10</sup> Z. Li, H. Li, H. Xia, X. Ding, X. Luo, X. Liu and Y. Mu, *Chem. Eur.J.*, 2015, **21**,17355
- <sup>11</sup> Edward J. W. Crossland, Nakita Noel, Varun Sivaram, Tomas Leijtens,, Jack A. Alexander-Webber & Henry J. Snaith *Nature*, 2013, **495**, 215
- <sup>12</sup> Jianfeng Liu, Xinyan Xiao, Yinlong Shi and Caixia Wan, *Applied Surface Science*, 2014, **297**, 33
- <sup>13</sup> D. H. Everett, *Pure Appl. Chem.*, 1972, **31**, 577
- <sup>14</sup> R. Dawson, A. Laybourn, R. Clowes, Y. Z. Khimyak, D. J. Adams and A. I. Cooper, *Macromolecules*, 2009, **42**, 8809
- <sup>15</sup> J.-X. Jiang, C. Wang, A. Laybourn, T. Hasell, R. Clowes, Y. Z. Khimyak, J. Xiao, S. J. Higgins, D. J. Adams and A. I. Cooper, *Angew. Chem. Int. Ed.*, 2011, **50**, 1072
- <sup>16</sup> J. B. DeCoste and G. W. Peterson, *Chem. Rev.*, 2014, **114**, 5695
- <sup>17</sup> Michael Mastalerz, *Chem. Eur. J.*, 2012, **18**, 10082
- <sup>18</sup> J. L.C. Rowsell and O. M. Yaghi, *Microporous and Mesoporous Materials*, 2004, **73**, 3
- <sup>19</sup> O. K. Farha, I. Eryazici, N. C. Jeong, B. G. Hauser, C. E. Wilmer, A. A. Sarjeant, R. Q. Snurr, S. T. Nguyen, A. Ö. Yazaydın, J. T. Hupp, *J. Am. Chem. Soc.*, 2012, **134**, 15016
- <sup>20</sup> H.K. Chae, D.Y. Siberio-Pérez, J. Kim, Y. Go, M. Eddaoudi, A.J. Matzger, M. O'Keeffe and O.M. Yaghi, *Nature*, 2004, **427**, 523
- <sup>21</sup> H. Li, M. Eddaoudi, T.L. Groy and O.M. Yaghi, *J. Am. Chem. Soc.*, 1998, **120**, 8571
- <sup>22</sup> W. Mori, F. Inoue, K. Yoshida, H. Nakayama, S. Takamizawa and M. Kishita, *Chem. Lett.*, 1997, 1219
- <sup>23</sup> T. Ohmura, W. Mori, M. Hasegawa, T. Takei and A. Yoshizawa, *Chem. Lett.*, 2003, **32**, 34
- <sup>24</sup> T.M. Reineke, M. Eddaoudi, M. Fehr, D. Kelley and O.M. Yaghi, *J. Am. Chem. Soc.*, 1999, **121**, 1651
- <sup>25</sup> G.J. Halder, C.J. Kepert, B. Moubaraki, K.S. Murray and J.D. Cashion, *Science*, 2002, **298**, 1762
- <sup>26</sup> J.S. Seo, D. Whang, H. Lee, S.I. Jun, J. Oh, Y.J. Jeon and K. Kim, *Nature*, 2000, **404**, 982

- <sup>27</sup> A. P. Côté, A. I. Benin, N. W. Ockwig, M. O’Keeffe, A. J. Matzger, O. M. Yaghi, *Science*, 2005, **310**
- <sup>28</sup> S. J. Rowan, S. J. Cantrill, G. R. L. Cousins, J. K. M. Sanders and J. F. Stoddart, *Angew. Chem. Int. Ed.*, 2002, **41**, 898
- <sup>29</sup> S. B. Kalidindi, K. Yusenko and R. A. Fischer, *Chem. Commun.*, 2011, **47**, 8506
- <sup>30</sup> S. Y. Ding, J. Gao, Q. Wang, Y. Zhang, W. G. Song, C. Y. Su and W. Wang, *J. Am. Chem. Soc.*, 2011, **133**, 19816
- <sup>31</sup> X. S. Ding, J. Guo, X. Feng, Y. Honsho, J. D. Guo, S. Seki, P. Maitarad, A. Saeki, S. Nagase and D. Jiang, *Angew. Chem., Int. Ed.*, 2011, **50**, 1289
- <sup>32</sup> X. Ding, L. Chen, Y. Honsho, X. Feng, O. Saengsawang, J. Guo, A. Saeki, S. Seki, S. Irle, S. Nagase, V. Parasuk and D. Jiang, *J. Am. Chem. Soc.*, 2011, **133**, 14510
- <sup>33</sup> S. Wan, J. Guo, J. Kim, H. Ihee and D. Jiang, *Angew. Chem., Int. Ed.*, 2008, **47**, 8826
- <sup>34</sup> H. Furukawa and O. M. Yaghi, *J. Am. Chem. Soc.*, 2009, **131**, 8875
- <sup>35</sup> J. L. Mendoza-Cortè, T. A. Pascal and W. A. Goddard, *J. Phys. Chem. A*, 2011, **115**, 13852
- <sup>36</sup> J. Lan, D. Cao and W. Wang, *Langmuir*, 2010, **26**, 220
- <sup>37</sup> T. A. Skotheim, J. R. Reynolds, *Conjugated Polymers - Theory, Synthesis, Properties, and Characterization*, CRC Press, Boca Raton, FL, 2007.
- <sup>38</sup> K. Müllen, U. Scherf, *Organic, Light-Emitting Devices*, Wiley-VCH, Weinheim, 2006
- <sup>39</sup> Z. H. Peng, Y. C. Pan, B. B. Xu, J. H. Zhang, *J. Am. Chem. Soc.*, 2000, **122**, 6619
- <sup>40</sup> D. L. Trumbo, C. S. Marvel, *J. Polym. Sci. Part A*, 1986, **24**, 2311
- <sup>41</sup> C. Weder, *Chem. Commun.* 2005, 5378
- <sup>42</sup> J. X. Jiang, F. Su, A. Trewin, C. D. Wood, N. L. Campbell, H. Niu, C. Dickinson, A. Y. Ganin, M. J. Rosseinsky, Y. Z. Khimyak, A. I. Cooper, *Angew. Chem. Int. Ed.*, 2007, **46**, 8574.
- <sup>43</sup> J. X. Jiang, F. Su, A. Trewin, C. D. Wood, H. Niu, J. T. A. Jones, Y. Z. Khimyak, A. I. Cooper, *J. Am. Chem. Soc.*, 2008, **130**, 7710.
- <sup>44</sup> N. B. McKeown, S. Makhseed and P. M. Budd, *Chem. Commun.*, 2002, 2780
- <sup>45</sup> D. C. Sherrington, *Chem. Commun.*, 1998, 227
- <sup>46</sup> V. A. Davankov, V. Rogozhin and M. P. Tsyurupa, US Pat, 3729457, 1969
- <sup>47</sup> P. Veverka and K. Jerábek, *React. Funct. Polym.*, 1999, 41, 21
- <sup>48</sup> J.-H. Ahn, J.-E. Jang, C.-G. Oh, S.-K. Ihm, J. Cortés and D. C. Sherrington, *Macromolecules*, 2006, **39**, 627
- <sup>49</sup> N. Fontanals, J. Cortés, M. Galià, P. A. G. Cormack, R. M. Marcé, F. Borrull and D. C. Sherrington, *J. Polym. Sci., Part A: Polym. Chem.*, 2005, **43**, 1718
- <sup>50</sup> C. D. Wood, B. Tan, A. Trewin, H. Niu, D. Bradshaw, M. J. Rosseinsky, Y. Z. Khimyak, N. L. Campbell, R. Kirk, E. Stockel and A. I. Cooper, *Chem. Mater.*, 2007, **19**, 2034
- <sup>51</sup> J. Germain, J. M. J. Fréchet and F. Svec, *J. Mater. Chem.*, 2007, **17**, 4989
- <sup>52</sup> J. Germain, J. M. J. Fréchet and F. Svec, *Chem. Commun.*, 2009, 1526

- <sup>53</sup> W. Chaikittisilp, M. Kubo, T. Moteki, A. Sugawara-Narutaki, A. Shimojima and T. Okubo, *J. Am. Chem. Soc.*, 2011, **133**, 13832
- <sup>54</sup> V. A. Davankov and M. P. Tsyurupa, *React. Polym.*, 1990, **13**, 27
- <sup>55</sup> F. S. Macintyre, D. C. Sherrington and L. Tetley, *Macromolecules*, 2006, **39**, 5381
- <sup>56</sup> N. Fontanals, P. Manesiotes, D. C. Sherrington and P. A. G. Cormack, *Adv. Mater.*, 2008, **20**, 1298
- <sup>57</sup> J. Urban, F. Svec and J. M. J. Fréchet, *Anal. Chem.*, 2010, **82**, 1621
- <sup>58</sup> B. Li, R. Gong, W. Wang, X. Huang, W. Zhang, H. Li, C. Hu and B. Tan, *Macromolecules*, 2011, **44**, 2410
- <sup>59</sup> J. Urban and V. Škeříková, *J. Sep. Sci.*, 2014, **37**, 3082
- <sup>60</sup> F. Liu, J. Chen, A. Li, Z. Fei, J. Ge and Q. Zhang, *Adsorpt. Sci. Technol.*, 2004, **22**, 13
- <sup>61</sup> D. P. A. G. Cormack, A. Davies and N. Fontanals, *React. Funct. Polym.*, 2012, **72**, 939
- <sup>62</sup> S. Bhunia, B. Banerjee and A. Bhaumik, *Chem. Commun.*, 2015, **51**, 5020
- <sup>63</sup> M. E. Davis, *Nature*, 2002, **417**, 813
- <sup>64</sup> R. Szostak, *Molecular Sieves – Principles of Synthesis and Identification.*, 2nd Ed. Blackie Academic and Professional, London, 1998
- <sup>65</sup> H. H. Funke, M. G. Kovalchick, J. L. Falconer and R. D. Noble, *Ind. Eng. Chem. Res.*, 1996, **35**, 1575
- <sup>66</sup> L. C. Oliveira, D. I. Petkosicz, A. Smaniotto and S. B. Pergher, *Water Res.*, 2004, **38**, 3699
- <sup>67</sup> H. Zheng, F. Gao and V. Valtchev, *J. Mater. Chem. A*, 2016, **4**, 16756
- <sup>68</sup> K. V. Agrawal, B. Topuz, Z. Jiang, K. Nguenkam, B. Elyassi, M. Navarro, L. F. Francis and M. Tsapatsis, *AIChE J.*, 2013, **59**, 3458
- <sup>69</sup> K. V. Agrawal, B. Topuz, T. C. T. Pham, T. H. Nguyen, N. Sauer, N. Rangnekar, H. Zhang, K. Narasimharao, S. Basahel, L. F. Francis, C. W. Macosko, S. Al-Thabaiti, M. Tsapatsis and K. B. Yoon, *Adv. Mater.*, 2015, **27**, 3243
- <sup>70</sup> A. W. Harding, N. J. Foley, P. R. Norman, D. C. Francis and K. M. Thomas, *Langmuir*, 1998, **14**, 3858
- <sup>71</sup> M. Molina-Sabio, F. Rodriguez-Reinoso, F. Caturla and M. J. Selles, *Carbon*, 1995, **33**, 1105
- <sup>72</sup> S. Sircar, T. C. Golden and M. B. Pao, *Carbon*, 1996, **34**, 1
- <sup>73</sup> D. D. L. Chung, *J Mater Sci*, 2002, **37**, 1475
- <sup>74</sup> H. W. Kroto, *Nature*, 1985, **318**, 162
- <sup>75</sup> S. Iijima, *Nature*, 1991, **354**, 56
- <sup>76</sup> K. Novoselov and A. Geim, *Science*, 2004, **306**, 666
- <sup>77</sup> A. Hirsch, and O. Vostrowsky, *Top. Curr. Chem.*, 2005, **245**, 193
- <sup>78</sup> A. K. Geim and K. S. Novoselov, *Nature Materials*, 2007, **6**, 183
- <sup>79</sup> A. C. Neto, F. Guinea, N. M. Peres, K. S. Novoselov and A. K. Geim, 2009, **81**, 109
- <sup>80</sup> a) G. Gundiah, A. Govindaraj, N. Rajalakshmi, K.S. Dhathathreyan and C.N.R. Rao, *J Mater Chem*, 2003, **13**, 209; b) Takagi H, Hatori H, Soneda Y, Yoshizawa N and Yamada Y, *Mater Sci Eng B*, 2004, **108**, 143; c) E. Poirier, R. Chahine, P. Benard, D. Cossement, L. Lafi, E. Melancon, T.K.

- Bose, S. Désilets, *Appl Phys A*, 2004, **78**, 961; d) R. Bacs, C. Laurent, R. Morishima, H. Suzuki and M. Le Lay, *J Phys Chem B*, 2004, **108**, 12718
- <sup>81</sup> M. S. Rahaman, C. D. Vecitis and M. Elimelech, *Environ. Sci. Technol.*, 2012, **46**, 1556
- <sup>82</sup> J. K. Holt et al., *Science*, 2006, **312**, 1034
- <sup>83</sup> B. Corry, *J. Phys. Chem. B*, 2008, **112**, 1427
- <sup>84</sup> A.K. Geim, *Science*, 2009, **324**, 1530; b) Y.W. Zhu, S. Murali, W. W. Cai, X.S. Li, J. W. Suk and J. R. Potts, *Adv Mater*, 2010, **22**, 3906
- <sup>85</sup> M. D. Stoller, S. Park, Y. Zhu, J. Anand and R. S. Ruoff, *Nano Lett.*, 2008, **8**, 3498
- <sup>86</sup> a) Z. S. Wu, S. B. Yang, Y. Sun, K. Parvez, X. L. Feng and K. Mullen, *J Am Chem Soc*, 2012, **134**, 9082; b) H. Sun, Z. Xu and C. Gao, *Adv Mater*, 2013, **25**, 2554
- <sup>87</sup> a) Y. Zhao, C. G. Hu, Y. Hu, H. H. Cheng, G. Q. Shi and L. T. Qu, *Angew Chem Int Ed*, 2012, **51**, 11371; b) S. A. Al-Muhtaseb and J. A. Ritter, *Adv Mater*, 2003, **15**, 101
- <sup>88</sup> a) H. Hu, Z. B. Zhao, W.B. Wan, Y. Gogotsi and J.S. Qiu, *Adv Mater*, 2013, **25**, 2219; b) X. Z. Wu, J. Zhou, W. Xing, G. Q. Wang, H. Y. Cui and S. P. Zhuo, *J Mater Chem*, 2012, **22**, 23186
- <sup>89</sup> Y. Qian, I. M. Ismail and A. Stein, *Carbon*, 2014, **68**, 221
- <sup>90</sup> D. Yu, K. Goh, H. Wang, L. Wei, W. Jiang, Q. Zhang, L. Dai and Yuan Chen, *Nature Nanotechnology*, 2014, **9**, 555
- <sup>91</sup> A.W. Adamson, *Physical Chemistry of Surfaces*, Wiley, New York, 1990
- <sup>92</sup> J. Lyklema, *Fundamentals of Interface and Colloid Science, vol. 1*, Academic Press, London, 1991
- <sup>93</sup> B.L. Karger, L.R. Snyder and C. Horvath, *An Introduction to Separation Science*, Wiley, New York, 1973
- <sup>94</sup> a) C.J. King, *Separation Processes*, McGraw-Hill, New York, 1980; b) T. E. Whyte, C. M. Yon, E. H. Wagener, *Industrial Gas Separations*, ACS Symp. Ser. 1983; c) R.T. Yang, *Gas Separation by Adsorption Processes*, Imperial College Press, London, 1997
- <sup>95</sup> R.H. Ottawil, C.H. Rochester and A.L. Smith, *Adsorption from Solution*, Academic Press, London, 1983
- <sup>96</sup> G.D. Parfitt and C.H. Rochester, *Adsorption from Solution at the Solid-Liquid Interface*, Academic Press, London, 1983
- <sup>97</sup> M. Vallet-Regí, F. Balas and D. Arcos, *Angewandte Chemie International Edition*, 2007, **46**, 7548
- <sup>98</sup> B. C. Lippens and J. H. De Boer, *Journal of Catalysis*, 1965, **4**, 319
- <sup>99</sup> J. L. C. Rowsell and O. M. Yaghi, *Microporous and Mesoporous Materials*, 2004, **73**, 3
- <sup>100</sup> J. Rouquerol, F. Rodriguez-Reinoso, K.S.W. Sing and K.K. Unger, *Characterization of Porous Solids III*. Elsevier, Amsterdam, 1994
- <sup>101</sup> V.R. Deitz, *Bibliography of Solid Adsorbents*. National Bureau of Standards, Washington, DC, 1944
- <sup>102</sup> S.D. Forrester and C.H. Giles, *Chem. Ind.*, 1971, 831
- <sup>103</sup> N.T. De Saussure, *Gilbert's Annalen der Physik*. 1814, **47**, 113
- <sup>104</sup> E. Mitscherlich, *Annales Chim. Phys.*, 1843, **7**, 15

- <sup>105</sup> a) P. Chappuis, *Wied. Ann.*, 1879, **8**, 1; b) H. Kayser, *Wied Ann. Phys.*, 1881, **12**, 526; c) H. Kayser, *Wied Ann. Phys.* 1881, **14**, 450
- <sup>106</sup> H. Freundlich, *Z. Phys. Chem.*, 1907, **57**, 385
- <sup>107</sup> A. Zsigmondy, *Z. Anorg. Chem.*, 1911, **71**, 356
- <sup>108</sup> M. Polanyi, *Verb. Deutsch Phys. Ges.*, 1914, **16**, 1012
- <sup>109</sup> a) I. Langmuir, *J. Am. Chem. Soc.*, 1916, **38**, 2221; b) I. Langmuir, *J. Am. Chem. Soc.*, 1917, **39**, 1848; c) I. Langmuir, *J. Am. Chem. Soc.*, 1918, **40**, 1361
- <sup>110</sup> S. Brunauer, P.H. Emmett, E. Teller, *J. Am. Chem. Soc.*, 1938, **60**, 309
- <sup>111</sup> M. Thommes, K. Kaneko, A. V. Neimark, J. P. Olivier, F. Rodriguez-Reinoso, J. Rouquerol and K. S.W., *Sing Pure Appl. Chem.* 2015, **87**, 1051
- <sup>112</sup> P. W. Atkins, *Atkins Physical Chemistry, 7th Ed*; Oxford University Press, Oxford, 2002
- <sup>113</sup> B. M. W. Trapnell, *Chemisorption*, Butterworths, London, 1955
- <sup>114</sup> H. Igarashi, H. Uchida, M. Suzuki, Y. Sasaki and M. Watanabe, *App. Cat. A:Gen.*, 1997, **159**
- <sup>115</sup> J. E. Lennard-Jones, *Trans. Faraday Soc.*, 1932, **28**, 333
- <sup>116</sup> D. H. Everett and J. C. Prowl, *J. Chem. Soc. Farad. Trans.*, 1976, **72**, 619
- <sup>117</sup> S. J. Gregg and K. S. W. Sing, *Adsorption, Surface Area and Porosity*, Academic Press, 1982
- <sup>118</sup> A. Dąbrowski, *Advances in Colloid and Interface Science*, 2001, **93**, 135
- <sup>119</sup> S. Brunauer, *The Adsorption of Gases and Vapours*. Oxford University Press, Oxford, 1945
- <sup>120</sup> Brunauer, S., Deming, L.S., Deming, W.S., Teller, E., 1940. *J. Am. Chem. Soc.* 62, 1723.
- <sup>121</sup> D.W. Siderius, Gelb, L.D., *J. Chem. Phys.*, 2011, **135**, 1
- <sup>122</sup> Langmuir, I. *J. Am. Chem. Soc.* 1918, **40**, 1361
- <sup>123</sup> S. Brunauer, P. H. Emmett and E. Teller, *J. Am. Chem. Soc.* 1938, **60**, 309
- <sup>124</sup> a) S. J. Gregg and J. T. Jacobs, *Faraday Soc.* 1948, **44**, 574; b) A. Legras, A. Kondor, M. T. Heitzmann and R. W. Truss, *J. Chromatogr. A.* 2015, **273**, 1425
- <sup>125</sup> J. Rouquerol, P. Llewellyn and F. Rouquerol, *Stud. Surf. Sci. Catal.*, 2007, **49**, 160
- <sup>126</sup> J. Rouquerol, F. Rouquerol, K. S. W. Sing, P. Llewellyn and G. Maurin, *Adsorption by Powders and Porous Solids: Principles, Methodology and Applications*, Academic Press, 2014
- <sup>127</sup> S. Lowell, J. Shields, M. A. Thomas and M. Thommes, *Characterization of Porous Solids and Powders: Surface Area, Porosity and Density*, Springer, 2004
- <sup>128</sup> M. Thommes and K. A. Cychosz. *Adsorption*, 2014, **20**, 233
- <sup>129</sup> E. R. Cohen, T. Cvitas, J. G. Frey, B. Holmström, K. Kuchitsu, R. Marquardt, I. Mills, F. Pavese, M. Quack, J. Stohner, H. L. Strauss, M. Takami and A. J. Thor, *Quantities, Units and Symbols in Physical Chemistry, 3rd ed.*, RSC Publishing, Cambridge, UK, 2007
- <sup>130</sup> J. Landers, G. Y. Gor and A. V. Neimark, *Colloid. Surfaces A: Physicochem. Eng. Aspects*, 2013, **3**, 437
- <sup>131</sup> P. A Monson, *Microporous Mesoporous Mater.*, 2012, **47**, 160
- <sup>132</sup> J. Jagiello and J. P. Olivier, *J. Phys. Chem. C*, 2009, **113**, 19382
- <sup>133</sup> I. Langmuir, *J. Am. Chem. Soc.*, 1916, **38**, 2221

- <sup>134</sup> H.M.F. Freundlich, Z. Uber, *Phys. Chem.*, 1906, **57(A)**, 385
- <sup>135</sup> P. V. Sivapullaiah, B. Guru Prasad and M. M. Allam, *Geotechnical Testing Journal*, 2008, **6**, 503
- <sup>136</sup> P.T. Hang and G.W. Brindley, *Clays and Clay Minerals*, 1970, **18**, 203
- <sup>137</sup> G. Chen, J. Pan, B. Han and H. Yan, *Journal of Dispersion Science and Technology*, 1999, **4**, 1179
- <sup>138</sup> R. Aringhieri, G. Pardini, M. Gispert and A. Solé, *Agrochimica*, 1992, **36**, 224
- <sup>139</sup> G. Hähner, A. Marti, N.D. Spencer, and W.R. Caseri, *Journal of Chemical Physics*, 1996, **104**, 7749
- <sup>140</sup> M. Borkovec, Q. Wu, G. Degovics, P. Lagner and H. Sticher, *Colloids and Surfaces A: Physicochemical and Engineering Aspects*, 1993, **73**, 65
- <sup>141</sup> J.C. Santamarina, K.A. Klein, Y.H. Wang, and E. Prencke, *Can. Geotech. J.*, 2002, **39**, 233
- <sup>142</sup> P. Montes-Navajas, N. G. Asenjo, R. Santamaría, R. Menéndez, A. Corma and H. García, *Langmuir*, 2013, **29**, 13443
- <sup>143</sup> M. J. McAllister, J.-L. Li, D. H. Adamson, H. C. Schniepp, A.A. Abdala, J. Liu, M. Herrera-Alonso, D. L. Milius, R. Car, R. K. Prud'homme and I. A. Aksay, *Chem. Mater.*, 2007, **19**, 4396
- <sup>144</sup> T. Liu, Y. Li, Q. Du, J. Sun, Y. Jiao, G. Yang, Z. Wang, Y. Xia, W. Zhang, K. Wang, H. Zhu and D. Wu, *Colloids and Surfaces B: Biointerfaces*, 2012, **90**, 197
- <sup>145</sup> L. Chen, J. Yang, X. Zeng, L. Zhang and W. Yuan, *Mater. Express*, 2013, **4**, 281
- <sup>146</sup> W. Zhang, C. Zhou, W. Zhou, A. Lei, Q. Zhang, Q. Wan and B. Zou, *Environ Contam Toxicol*, 2011, **87**, 86
- <sup>147</sup> S.-T. Yang, S. Chen, Y. Chang, A. Cao, Y. Liu, H. Wang, *Journal of Colloid and Interface Science*, 2011, **1**, 24
- <sup>148</sup> W. Peng, H. Li, Y. Liu, S. Son, *Journal of Molecular Liquids*, 2016, **221**, 82

## Chapter 2

# Synthesis and adsorption study of hyper-crosslinked styrene-based nanocomposites containing multi-walled carbon nanotubes

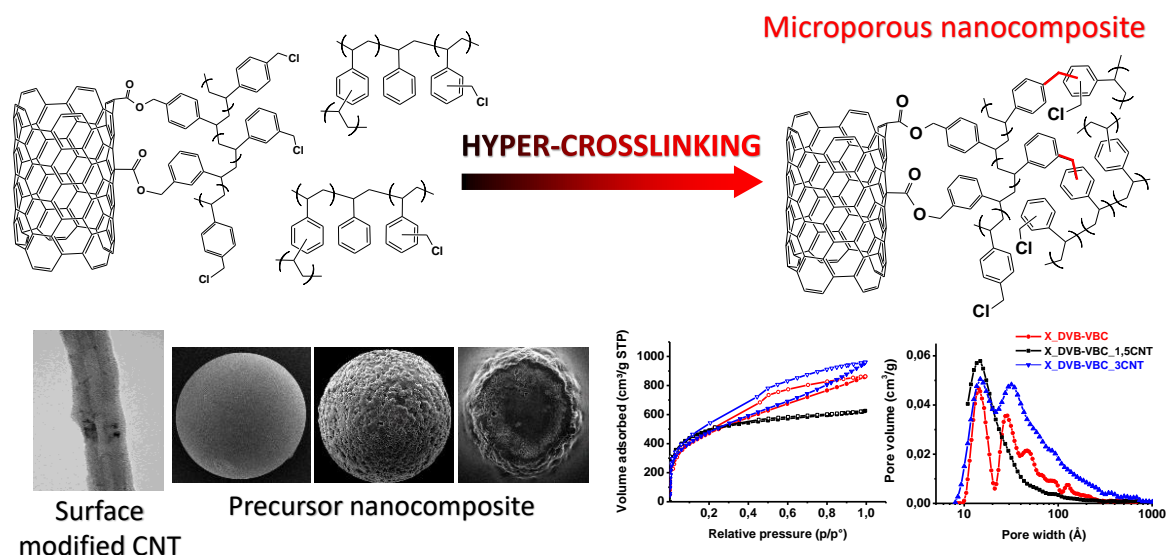
### Authors and affiliations

Rachele Castaldo,<sup>a,b</sup> Roberto Avolio,<sup>a</sup> Mariacristina Cocca,<sup>a</sup> Gennaro Gentile,<sup>a\*</sup> Maria Emanuela Errico,<sup>a</sup> Maurizio Avella,<sup>a</sup> Cosimo Carfagna<sup>a</sup> and Veronica Ambrogi<sup>a,b</sup>

<sup>a</sup> Institute for Polymers, Composites and Biomaterials, National Research Council of Italy, Via Campi Flegrei 34, 80078 Pozzuoli, Italy.

<sup>b</sup> Department of Chemical, Materials and Production Engineering, University of Naples, Piazzale Tecchio 80, 80125 Napoli, Italy.

## Abstract



New nanocomposite microporous materials obtained by adding functionalized multi-walled carbon nanotubes (MWCNT) to styrene/vinylbenzyl chloride/divinylbenzene hyper-crosslinked resins were prepared and characterized. In order to promote the embedding of the MWCNT within the gel-type precursor, a proper surface modification strategy was set up, based on the grafting of a poly(vinylbenzyl chloride) (PVBC) resin, able to participate to the hyper-crosslinking step, onto the nanotube surface. Characterization of the nanocomposites by FTIR spectroscopy and electron microscopy enabled the assessment of the effect of the nanotubes on the structure and the morphology of the resin. Moreover, gas sorption measurements indicated that by addition of nanotubes it is possible to modulate the pore size distribution, the uptake of CO<sub>2</sub> and H<sub>2</sub> and the CO<sub>2</sub>/N<sub>2</sub> selectivity. Finally, modified MWCNT are also able to improve the adsorption capacity of phenol from water solutions, suggesting the possible application of the new microporous nanocomposites for water remediation.

## Introduction

Porous materials characterized by high specific surface area (SSA) have attracted high scientific interest in recent years. High specific surface area and porosity, in fact, are the fundamental concepts for physical adsorption phenomena. Materials with physical adsorption properties are particularly interesting for their high sorption capacity and their low regeneration energy consumption. Adsorbent materials like activated carbons,<sup>1</sup> zeolites,<sup>2</sup> metal-organic frameworks,<sup>3,4</sup> covalent organic frameworks,<sup>5,6</sup> polymers of intrinsic microporosity,<sup>7</sup> hyper-crosslinked polymers<sup>8</sup> and carbon nanotubes<sup>9</sup> find application in gas separation<sup>10-12</sup> and storage,<sup>13,14</sup> catalysis,<sup>15</sup> and air<sup>16</sup> and water purification processes.<sup>17-19</sup> According to the IUPAC notation, porous materials are defined as microporous when containing pores with characteristic diameter up to 2 nm, mesoporous when having characteristic pores diameter comprised between 2 and 50 nm, or macroporous when being characterized by pores diameter over 50 nm.

Among microporous materials, hyper-crosslinked (HCL) resins stand out for their low density and high chemical and thermal stability<sup>20</sup> and for the possibility of tailoring their structure, porosity, and functionality.<sup>21-23</sup>

The most studied HCL resins are Davankov-type resins, which are prepared by post-crosslinking of polystyrenes.<sup>24-28</sup> One of the synthetic routes to produce them consists in the post crosslinking of linear or lightly crosslinked “gel-type” precursor resins based on styrene (ST), divinylbenzene (DVB) and vinylbenzyl chloride (VBC). The precursor resin is usually prepared by suspension polymerization, then through post crosslinking various structural bridges between neighbouring phenyl groups are obtained. The hyper-crosslinking process leads to a highly porous three-dimensional network, which displays high specific surface area and excellent sorption properties.

In particular, this class of micro/mesoporous materials is characterized by high crosslinking degree, small average pore diameter (lower than 3 nm), high BET surface area (up to about 1800 m<sup>2</sup>/g), and large pore volume (up to 0.8 cm<sup>3</sup>/g).<sup>28</sup>

A recent review of Fontanals et al.<sup>26</sup> well summarizes the structural and adsorption properties of HCL polystyrene resins. In particular, several studies have been focused on the effect of the compositions of DVB, ST and VBC on the final properties of the hyper-crosslinked product.<sup>29</sup> In fact, the degree of crosslinking in the gel-type precursor can be modulated by varying the DVB content, whereas changing the molar ratio between ST and VBC, and thus the relative amount of chloromethyl groups in the gel-type precursor, significantly affects the extent of the hyper-crosslinking. Within this class

of materials, the highest specific surface is reported for the system obtained by using 2 mol% of DVB and 98 mol% of VBC.<sup>30</sup>

Moreover, in the last years, several modification strategies have been proposed to improve the overall adsorption properties of HCL resins, to find alternative monomer compositions, including the use of bioderived monomers/macromers, or to add specific functionalities to the final materials with the objective of imparting selectivity towards the absorption of selected gases or low molecular weight substances. Jia et al.<sup>31</sup> have recently evaluated the effect of the solvent used during the hyper-crosslinking step on the surface properties and the adsorption properties of ST/VBC/DVB resins, showing that, also based on environmental and economic considerations, 1,2-dichloroethane is better option with respect to nitrobenzene. Li et al.<sup>32</sup> have synthesized a carbonyl modified VBC-based resin, characterized by improved adsorption properties toward an aromatic substance containing hydroxyl groups, i.e. glabridin, an isoflavonoid, from water solutions. Following the studies of Zeng et al.<sup>33-35</sup> that synthesized a series of polar-modified post-crosslinked polystyrene, Ling et al.<sup>36</sup> have recently developed a highly polar HCL resins based on DVB and glycidylmethacrylate, characterized by improved adsorption of salicylic acid from water.

As concerning the use of bioderived raw materials, Meng and Weber<sup>37</sup> have recently realized a novel microporous polymer by hyper-crosslinking of organosolv lignin that, after pyrolysis, shows good carbon dioxide adsorption and excellent CO<sub>2</sub>/N<sub>2</sub> selectivity.

Other methods for the modification of sorption properties of HCL resins are based on the embedding of micro/nanoparticles within the polymer network. Wang W. et al.<sup>38</sup> synthesized a magnetic DVB-based HCL resin filled with needle-like  $\gamma$ -Fe<sub>2</sub>O<sub>3</sub> particles, showing that the realized composite resin is suitable for rapid and efficient removal of organic pollutants from drinking water.

In this context, carbon nanomaterials, due to their intrinsic adsorption properties,<sup>39-42</sup> are very interesting candidates to modulate the properties of HCL resins. In particular, carbon nanotubes (CNT) are effective in CO<sub>2</sub> adsorption<sup>43</sup> and in removing organic and inorganic pollutants from air<sup>44,45</sup> or from water.<sup>46,47</sup> The high adsorption capacity of CNT is mainly attributed to their porous structure. Furthermore, CNT surface can be modified by chemical modification or thermal treatments, introducing functional groups that can enhance the selective adsorption toward specific substances.<sup>48</sup>

On this basis, in this work properly modified multi-walled carbon nanotubes (MWCNT) were for the first time incorporated into a ST/VBC/DVB HCL resin. The interaction of the fillers with the hosting matrix and their effect on the structure of the resin, the morphology, the specific surface area and porosity have been investigated. Furthermore, adsorption of phenol from water solution has been evaluated as a function of the composition of the resin and the amount of nanotubes.

## Experimental section

### Materials

CVD-grown MWCNT functionalized with  $-COOH$  groups (MWCNT-COOH, purity  $>95\%$ , functionality  $0.7$  wt%, diameter range  $20-50$  nm) were purchased from Cheap Tubes Inc. (Brattleboro, VT, USA).

Polyvinyl alcohol (PVA, Mowiol® 18-88, Mw  $\sim 130000$ ,  $86.7-88.7$  mol% hydrolysis), NaCl ( $>99\%$ , anhydrous), NaOH ( $\geq 97.0\%$ , pellets), tetraoctylammonium bromide (TOAB,  $>98\%$ ), Styrene (ST,  $>99.9\%$ ), 2,2'-azobis(2-methylpropionitrile) (AIBN,  $>98\%$ ), vinylbenzyl chloride (VBC,  $\geq 95.0\%$ , mixture of isomers,  $\sim 70\%$  meta +  $\sim 30\%$  para), p-divinylbenzene (DVB,  $85\%$ , meta isomer,  $\sim 10$  wt%),  $FeCl_3$  ( $\geq 97\%$ ), phenol ( $>99.5\%$ ) and all solvents were purchased by Sigma Aldrich (Milan, Italy) and used without further purification.

### Multi-walled carbon nanotubes surface modification

Carboxyl groups modified multi-walled carbon nanotubes (MWCNT-COOH) were functionalized by grafting their external surfaces with poly(vinylbenzyl chloride) (PVBC).<sup>49</sup>

PVBC was obtained by solution polymerization using the following procedure. VBC ( $5$  mL) was poured in a round-bottom flask filled with toluene ( $10$  mL). AIBN ( $0.054$  g) was added, the solution was heated to  $60$  °C and the reaction was carried out under reflux and under nitrogen for  $14$  hours. PVBC was precipitated in ethanol and dried under vacuum overnight.

MWCNT-COOH ( $600$  mg) were poured into  $350$  mL of a NaOH aqueous solution ( $0.005$  M) and stirred for  $15$  minutes. Then  $1$  g of TOAB was added and the mixture was heated to  $60$ °C. PVBC ( $300$  mg), pre-dissolved in  $250$  mL of toluene, was added to the mixture. The reaction was carried for  $7$  hours under vigorous stirring, after that the mixture was poured in a separatory funnel and the toluene phase was recovered and filtered. Modified MWCNT (MWCNT-PVBC) were purified from unreacted reagents by  $3$  washing cycles with chloroform and tetrahydrofuran, then they were dried in oven at  $50$ °C for  $24$  hours.

### Synthesis of the precursor gel-type resin by suspension polymerization

Poly(divinylbenzene-co-styrene-co-vinylbenzyl chloride) beads were obtained by suspension polymerization, using the following procedure.<sup>25</sup> A PVA ( $7.5$  g/L) and NaCl ( $33$  g/L) water solution ( $350$  mL) was poured into a suspension polymerization reactor fitted with a water condenser and a mechanical stirrer. The organic phase, composed of DVB, ST, VBC in two different molar

compositions, 2:0:98 and 2:49:49, and 0.5 phr of AIBN, was mixed and maintained for 30 min under nitrogen; then it was poured drop by drop in the aqueous phase (in a ratio of 20:1 wt/wt of aqueous phase:organic phase) under stirring at 425 rpm. The reaction was carried out under nitrogen at 80 °C for 6 h. The obtained beads were recovered on a 75 µm sieve and washed with 5 washing cycles of water and methanol. Then, the beads were further purified by Soxhlet extraction with acetone to eliminate remaining impurities. Finally, they were washed with methanol and diethyl ether on a paper filter and dried in a vacuum oven at 40 °C for at least 24 h.

Beads containing MWCNT-PVBC were prepared using a similar procedure. In this case, before reaction, the right amount of modified nanotubes (1.5 and 3.0 phr) was dispersed within the organic phase by sonication for 50 minutes, with a 500 W tip sonicator at the 25% power, with a 10s/50s ON/OFF cycle, under nitrogen. The initiator (AIBN), 0.5 phr, was then added and the whole mixture was poured drop by drop into the aqueous solution of PVA and NaCl. The obtained nanocomposite beads were washed and dried following the procedure used for the neat polymer beads.

### **Hyper-crosslinking of the gel-type resin**

The hyper-crosslinking reaction was performed using the following procedure.<sup>30</sup> The precursor resin was swollen in 1,2-dichloroethane (DCE), under nitrogen, for 2 h. Then the mixture was cooled to ~4 °C in an ice bath, and the Friedel-Crafts catalyst, FeCl<sub>3</sub>, was added. After allowing 2 h to achieve a uniform dispersion of FeCl<sub>3</sub> throughout the precursor beads, the temperature was raised to 80 °C and kept for 18 h. The hyper-crosslinked beads were then washed with methanol and dried in a vacuum oven for a day at 40 °C.

### **MWCNT-PVBC characterization**

The extent of the functionalization of the multi-walled carbon nanotubes by grafting of PVBC was evaluated by means of Fourier transform infrared spectroscopy (FTIR) analysis, energy dispersive X-ray analysis (EDX), thermogravimetric analysis (TGA) and transmission electron microscopy (TEM).

FTIR spectra were recorded on the neat PVBC resin, on pristine MWCNT-COOH, and on MWCNT-PVBC with a Perkin Elmer Spectrum One FTIR spectrometer. Spectra were collected using a resolution of 4 cm<sup>-1</sup> and 32 scan collections.

EDX analysis was performed on a FEI Quanta 200 FEG SEM equipped with an Oxford Inca Energy System 250 and an Inca-X-act LN<sub>2</sub>-free analytical silicon drift detector. A thin layer of pristine MWCNT-COOH and MWCNT-PVCB was deposited onto aluminium SEM stubs. The analysis was performed at 30 kV acceleration voltage. Average results and standard deviation values are based on three consecutive measurements on different areas of each sample.

TGA was performed on pristine and modified MWCNT with a Perkin Elmer Pyris Diamond TG/DTA analyzer, using nitrogen as purge gas (50 mL/min), heating about 3 mg of each sample from 100 to 900°C at 2°C/min.

Bright field TEM analysis of MWCNT-COOH and MWCNT-PVBC was performed on a FEI Tecnai G12 Spirit Twin (LaB<sub>6</sub> source) at 120 kV acceleration voltage. TEM images were collected on a FEI Eagle 4k CCD camera. Before the analysis, pristine MWCNT-COOH were dispersed in water and MWCNT-PVBC in toluene by sonication (2 min) with a 500 W tip sonicator set at 25% power. Carbon nanotubes were then collected by immersing holey carbon coated copper grids in the dispersion.

Furthermore, in order to prove the ability of the grafted PVBC phase to undergo the Friedel-Crafts reaction, MWCNT-PVBC were subjected to hyper-crosslinking following the procedure already described for gel-type resins and obtaining the sample coded X\_MWCNT-PVBC. This sample was characterized by FTIR spectroscopy, EDX and TGA, as above detailed.

Moreover, SSA was determined on pristine MWCNT-COOH, MWCNT-PVBC and MWCNT-PVBC through N<sub>2</sub> adsorption analysis performed at liquid nitrogen temperature using a Micromeritics ASAP 2020 analyzer. Prior to the analysis all the samples were degassed at 120°C under vacuum ( $P < 10^{-5}$  mbar). SSA was determined from the linear part of the Brunauer-Emmett-Teller (BET) equation.

### **Precursor beads characterization**

Precursor beads were characterized by FTIR and morphological analysis. ATR-FTIR spectra were recorded on the neat precursor and nanocomposite beads with the above described FTIR apparatus, equipped with a universal ATR sampling accessory, using a resolution of 4 cm<sup>-1</sup> and 32 scan collections.

Scanning electron microscopy (SEM) of the beads was performed by means of a FEI Quanta 200 FEG SEM in high vacuum mode. Before SEM observations, samples were mounted onto SEM stubs by means of carbon adhesive disks and sputter coated with a 15 nm thick Au-Pd layer. External surfaces as well as beads cross-sections were observed for all the samples at 10-30 kV acceleration voltage using a secondary electron detector.

### **HCL resins and nanocomposites characterization**

To confirm the extent of the hyper-crosslinking reaction, ATR-FTIR and EDX analysis were performed on the HCL samples using the above described equipment and experimental conditions.

Gas adsorption volumetric measures were performed on the HCL samples using a Micromeritics ASAP 2020 analyzer. All the adsorption measurements were performed using high purity gases (> 99.999 %). Prior to the analysis all the samples were degassed at 120°C under vacuum ( $P < 10^{-5}$  mbar) in the degas port of the analyzer. In particular, N<sub>2</sub> adsorption analysis was performed at liquid nitrogen temperature to evaluate the SSA and the pore size distribution of the samples. SSA was determined from the linear part of the Brunauer-Emmett-Teller (BET) equation. Non-local density functional theory (NLDFT) was applied to nitrogen adsorption isotherm curves to evaluate the pore size distribution of the materials.<sup>50</sup> N<sub>2</sub> and CO<sub>2</sub> adsorption analysis were performed at 298 K up to 1 bar, and the equilibrium selectivity of the materials towards CO<sub>2</sub> with respect to N<sub>2</sub> was evaluated as the ratio of the absolute adsorption values. H<sub>2</sub> uptake capacity was evaluated at 77 K up to 1 bar.

Equilibrium phenol adsorption in water was performed at 25 °C in the range of phenol concentrations 200-1500 mg/L. About 10 mg of HCL resins or nanocomposites were introduced into vials containing 10 mL of phenol solution at different concentrations. The vials were kept at 25°C until equilibrium was reached (at least 48 h). Therefore, the solution was removed from the vial and the final phenol concentration was measured using a Jasco V570 UV spectrophotometer. A calibration curve was built to determine the phenol concentration in water from the absorbance of the peak centred at 270 nm.

## Results and discussion

The synthetic approach used for the realization of HCL polystyrene based resins and nanocomposites consists of a 2-step procedure. First, a gel-type precursor resin is synthesized by free radical polymerization and then the corresponding HCL resin is obtained by Friedel-Crafts alkylation. The reaction scheme for this synthesis starting from DVB, ST and VBC is reported in Figure 2.1.

Preliminary attempts to realize beads containing commercial MWCNT induced the obtainment of materials with macroscopic phase separation/aggregation of the nanotubes (see Figure S2.1 in Supplementary Information). Therefore, it was necessary to design a suitable surface modification methodology of the nanotubes to promote their dispersion in the organic phase, and thus their quantitative inclusion within the precursor resin.

In order to obtain this result, a CNT modification strategy was adopted, aimed at grafting a poly(vinylbenzyl chloride) (PVBC) resin onto the surface of the nanotubes.<sup>49</sup> PVBC was also selected for the surface modification of MWCNT because the resulting MWCNT-PVBC, through their surface chloromethyl groups, could be able to react with the precursor resin during the hyper-crosslinking step.

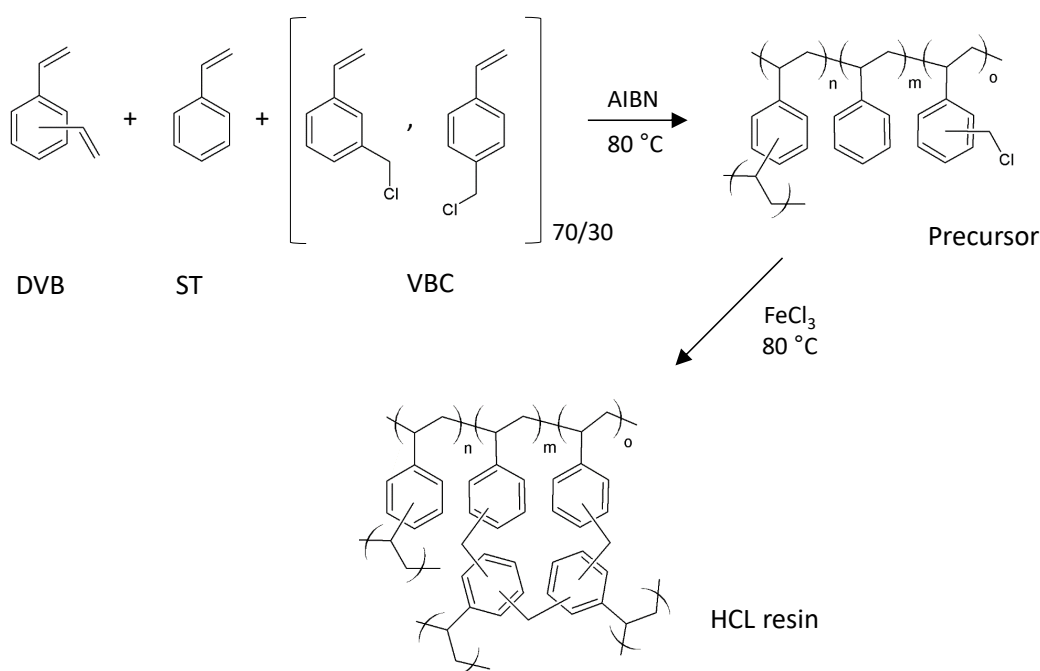


**Figure 2.1** Reaction scheme for the two-step synthesis of HCL resins based on divinylbenzene (DVB), styrene (ST) and vinylbenzyl chloride (VBC)

### Multi-walled carbon nanotubes surface modification

In order to prepare MWCNT-PVBC, commercial carboxyl functionalized carbon nanotubes, MWCNT-COOH, were dispersed in a NaOH solution. The reaction between the obtained carboxylate salts, MWCNT-COO<sup>-</sup>, in the aqueous phase, and PVBC, dissolved in toluene, occurred through nucleophilic substitution of MWCNT-COO<sup>-</sup> to replace the chloride leaving group of PVBC and it was promoted by the phase transfer catalyst TOAB (Figure 2.2a).

FTIR spectra of MWCNT-PVBC (Figure 2.2b) revealed the presence of a sharp absorption band centered at about 1265 cm<sup>-1</sup> (CH<sub>2</sub> wagging of the chloromethyl group),<sup>51</sup> of two convoluted absorption bands centered at 1420 and 1450 cm<sup>-1</sup> (scissoring of CH<sub>2</sub>), similarly to those observed for neat PVBC. Moreover, MWCNT-PVBC also showed the presence of complex absorption bands in the regions 2800-3000 (alkyl CH stretching) and 3000-3200 cm<sup>-1</sup> (aromatic CH stretching).

The quantitative evaluation of grafted PVBC was obtained by TGA. As it can be observed in Figure 2.2c, under nitrogen flow neat PVBC degrades through a two-step degradation process, with a 60% weight loss between 200°C and 550°C. In the same temperature range, MWCNT-COOH do not show an appreciable weight loss, their degradation starting slightly above 550°C. On the contrary, MWCNT-PVBC undergo to a degradation starting at about 250°C, with a weight loss of 5.3% between 250 and 500°C, attributed to the degradation of the grafted PVBC. Assuming that the presence of nanotubes do not influence the degradation process of PVBC, a 5.3% weight loss in the considered temperature range corresponds to an amount of grafted PVBC of 8.8 wt%.

A further confirmation of the occurrence of the grafting reaction was obtained by TEM analysis. Bright field TEM images of purified MWCNT-PVBC, reported in Figure 2.2d, show the presence of a homogeneous layer, about 2-3 nm thick, on the nanotube surface, indicating the occurrence of the grafting reaction. To be noted is that, considering a density of  $1.088 \text{ g cm}^{-3}$  for PVBC, an average radius and density of 25 nm and  $2.1 \text{ g cm}^{-3}$  for MWCNT and simplifying the morphology of the nanotubes to a perfectly cylindrical shape,<sup>52</sup> a thickness of 2.0 nm corresponds to a PVBC content of 7.9 wt%, in agreement with the estimation obtained by TGA.

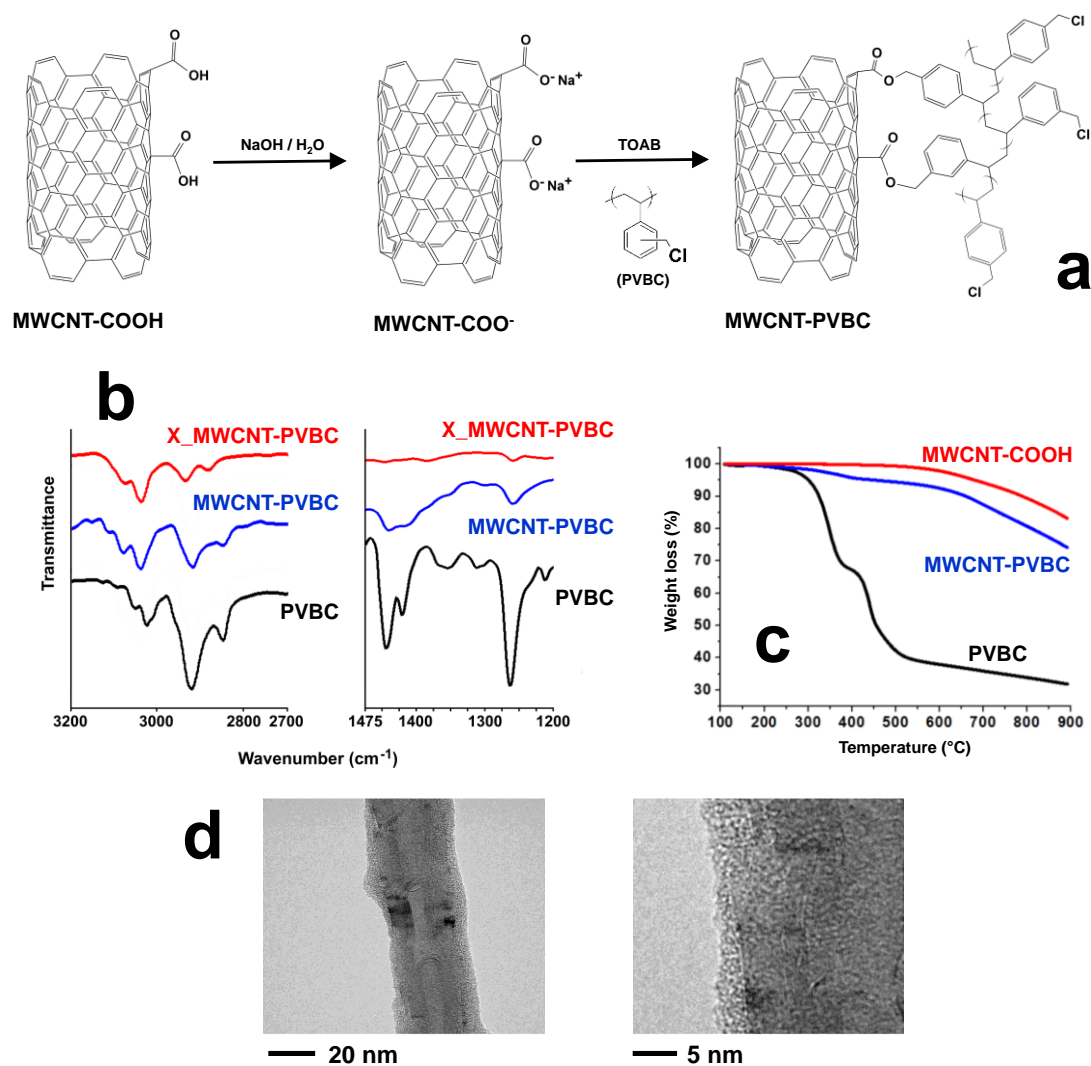


**Figure 2.2** Results of the characterization of surface modified carbon nanotubes (MWCNT-PVBC): a) scheme of the surface modification reaction; b) ATR-FTIR spectra of MWCNT-PVBC, PVBC and X\_MWCNT\_PVBC in the spectral range 3200-2700 and 1475-1200 cm<sup>-1</sup>; c) TGA traces under nitrogen flow of MWCNT-PVBC, MWCNT-COOH and PVBC; d) bright field TEM images of MWCNT-PVBC.

EDX analysis was used to evaluate the amount of unreacted chloromethyl groups in MWCNT-PVBC. The resulting chlorine/carbon weight ratio in the modified carbon nanotubes resulted  $1.78 \pm 0.38$  %. On the basis of stoichiometric considerations, a mixture of plain MWCNT and 8.8 wt% of PVBC would result in a chlorine/carbon weight ratio of 2.12 %. Therefore, it can be deduced that only about 16 % of the chlorine atoms of PVBC are replaced during the grafting reaction and then a large amount of residual chloromethyl groups of MWCNT-PVBC are still available for further reactions.

As detailed in the experimental, in order to confirm that the PVBC phase grafted onto modified carbon nanotubes is able to participate to the HCL reaction when nanotubes are embedded into the precursor resin, hyper-crosslinking of the modified nanotubes was performed using the procedure reported for the resin and nanocomposite beads. FTIR analysis of the obtained X\_MWCNT-PVBC sample confirmed the occurrence of the hyper-crosslinking reaction. In fact, as shown in Fig 2b, a significant decrease of the intensity of the absorption band centered at  $1265 \text{ cm}^{-1}$  was recorded for X\_MWCNT-PVBC in comparison to the MWCNT-PVBC sample, proving that the chloromethyl groups of the grafted PVBC can undergo the Friedel-Crafts reaction. EDX analysis further confirmed this result, as the residual chlorine/carbon weight ratio decreased from  $1.78 \pm 0.38$  of MWCNT-PVBC to  $0.68 \pm 0.22$  of X\_MWCNT-PVBC. Although FTIR and EDX indicated that the extent of the hyper-crosslinking was not complete, it was expected that a highly microporous layer could be obtained on the surface of the modified nanotubes, due to the presence of a partially HCL phase, thus inducing a significant increase of the SSA of the X\_MWCNT-PVBC with respect to the unmodified MWCNT-COOH and to the non-hyper-crosslinked MWCNT-PVBC. BET analysis confirmed the increase of SSA from  $113.7 \pm 0.7 \text{ m}^2/\text{g}$  and  $108.5 \pm 0.6 \text{ m}^2/\text{g}$  for MWCNT-COOH and MWCNT-PVBC, respectively, to  $140.8 \pm 0.3 \text{ m}^2/\text{g}$  for X\_MWCNT-PVBC. As the increase of SSA can be only due to the hyper-crosslinking of the grafted PVBC, based on geometric considerations it is possible to estimate the SSA of the grafted and hyper-crosslinked polymer phase. Therefore, hypothesizing a perfect cylindrical geometry of the nanotubes, a nanotube radius of 25 nm, a constant thickness of the grafted PVBC layer of 2.0 nm, and assuming density values of  $2.1 \text{ g/cm}^3$  for the nanotubes and  $1.34 \text{ g/cm}^3$  for the HCL PVBC phase,<sup>8</sup> the recorded increase corresponds to the formation of a HCL PVBC layer with SSA of about  $400 \text{ m}^2/\text{g}$ . This value is very low in comparison to SSA obtained for VBC based HCL Davankov type resins (up to  $1800 \text{ m}^2/\text{g}$ ), but, in agreement with FTIR and EDX results, can be easily explained considering the low mobility of the grafted PVBC phase that, in the case under consideration, is constrained on the nanotube surface, thus precluding the possibility of achieving a high extent of hyper-crosslinking.

## Synthesis of the gel-type precursors by suspension polymerization

The synthesis of gel-type precursor beads was performed by radical suspension polymerization starting from two different mixtures of monomers, DVB:VBC=2:98 molar ratio and DVB:ST:VBC=2:49:49 molar ratio, coded as DVB-VBC and DVB-ST-VBC, respectively. Nanocomposite beads were realized using the same monomer compositions and adding 1.5 and 3.0 phr of MWCNT-PVBC, thus obtaining the samples coded as DVB-VBC\_1.5CNT, DVB-VBC\_3CNT, DVB-ST-VBC\_1.5CNT and DVB-ST-VBC\_3CNT. In all cases, lightly crosslinked beads were produced, where the low amount of crosslinks is due to the bifunctional DVB monomer.

In Figure 2.3 ATR-FTIR spectra of gel type precursors and hyper-crosslinked resins and nanocomposites are reported. These latter will be discussed in the next section. As concerning the gel type precursors, DVB-VBC and DVB-ST-VBC spectra show the absence of residual double bonds and the presence at  $1265\text{ cm}^{-1}$  of the absorption band diagnostic for the chloromethyl groups of the VBC unit. Of course, the ATR-FTIR spectrum of DVB-ST-VBC is characterized by a lower intensity of the chloromethyl absorption band due to the lower relative amount of VBC.

FTIR spectra of the corresponding gel-type nanocomposites containing 1.5 and 3.0 phr of MWCNT-PVBC, not reported in Figure 2.3, did not show significant differences with respect to the unfilled resins, thus indicating that MWCNT-PVBC do not negatively affect the synthesis of the gel type precursors.

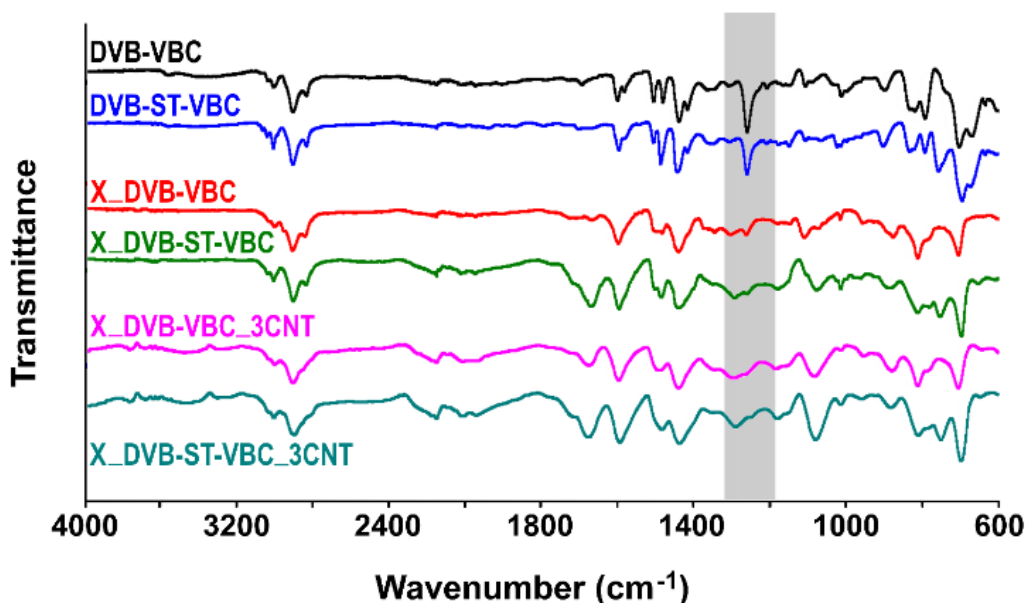


**Figure 2.3** ATR-FTIR spectra of the gel-type precursor resins (DVB-VBC and DVB-ST-VBC), the corresponding hyper-crosslinked resins (X\_DVB-VBC and X\_DVB-ST-VBC) and nanocomposites containing 3 phr of MWCNT-PVBC (X\_DVB-VBC\_3CNT and X\_DVB-ST-VBC\_3CNT)

SEM images of the gel-type resins and nanocomposite beads are reported in Figure 2.4 and 1.5. As it can be observed, all the beads have a spherical shape, their diameter ranging between 100 and 400  $\mu\text{m}$ , irrespectively of the presence of nanotubes. As concerning the external morphology, neat DVB-VBC and DVB-ST-VBC beads (Figure 2.4a and e) show a smooth surface, while an increased roughness was recorded for both compositions increasing the relative amount of MWCNT-PVBC. This roughness is attributed to the presence of appreciable amounts of nanotubes on the beads surface, as shown by high magnification SEM images in Figure 2.4d (DVB-VBC\_3CNT) and 4h (DVB-ST-VBC\_3CNT).

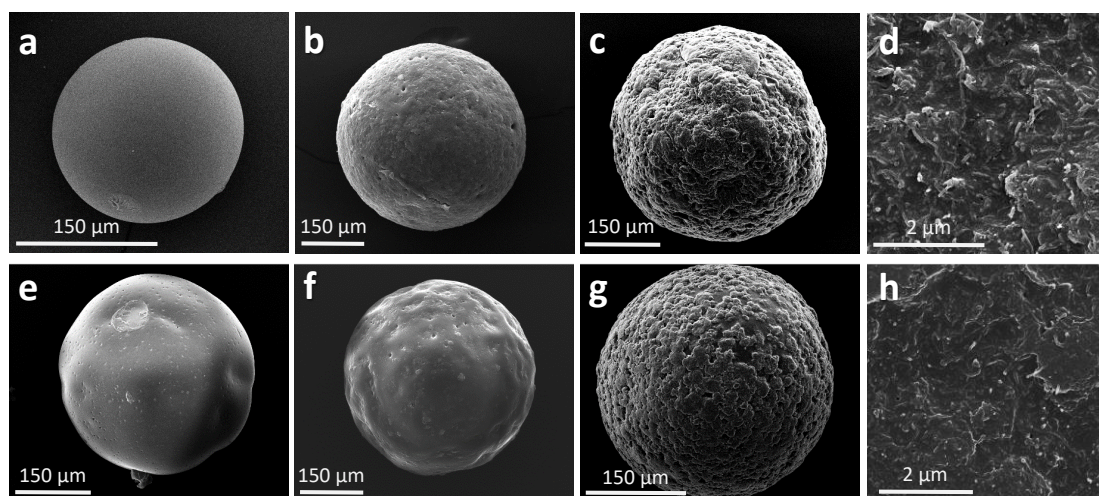


**Figure 2.4** SEM micrographs of the precursor beads: DVB-VBC (a), DVB-VBC\_1.5CNT (b), DVB-VBC\_3CNT (c,d), DVB-ST-VBC (e), DVB-ST-VBC\_1.5CNT (f), DVB-ST-VBC\_3CNT (g,h)

In order to evaluate the distribution within the whole volume of the beads, SEM analysis was also performed on the beads sections (see Figure 2.5). In stark contrast with the smooth and plain section of the neat beads observed for both compositions (see Figure S2.2 in Supplementary Information), all the samples containing MWCNT-PVBC show a complex structure, almost irrespectively of the nanotube content.

In particular, as shown in Figure 2.5 for the samples containing 3phr of MWCNT-PVBC, just under the external corrugated layer of the beads, a macroporous layer with cylindrical pores of 300-400 nm diameter is evidenced, containing MWCNT-PVBC (Figure 2.5d and h). Finally, a dense core containing a lower amount of MWCNT-PVBC with respect to the external layer is shown in Figure 2.5c and g.

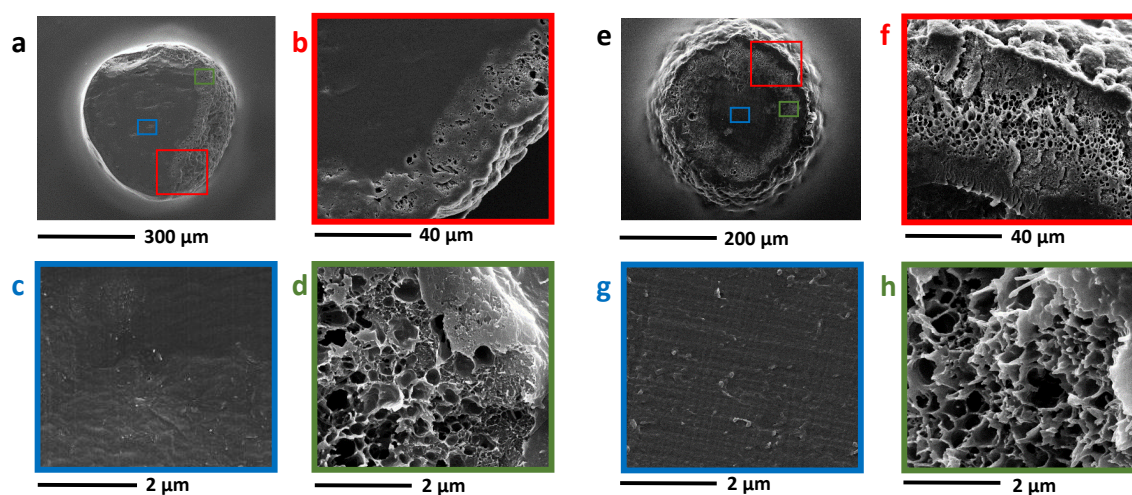


**Figure 2.5** SEM micrographs of sections of the precursor beads: DVB-VBC\_3CNT (a-d), DVB-ST-VBC\_3CNT (e-h)

The obtained results confirm the uneven distribution of MWCNT, which is an interesting phenomenon already observed in different systems, such as immiscible polymer blends<sup>53</sup> and water/paraffin emulsions. In the latter case, wax microparticles in which carbon nanotubes are selectively located at the particles surfaces have been obtained by cooling of water/paraffin wax Pickering emulsions.<sup>54</sup> The partially selective localization of the MWCNT at the surface of the gel-type precursor beads is expected to affect the adsorption properties of the HCL nanocomposites.

### HCL resins and nanocomposites characterization

For the investigated class of materials, the hyper-crosslinking of the precursor beads was performed in a solvent-swollen state by using DCE,<sup>31</sup> through the reaction of the chloromethyl groups of the VBC monomer, inducing the formation of methylene bridges between neighbouring aromatic rings of the resin. Hyper-crosslinking preserves the porosity even when the swelling solvent is removed and thus provides high specific surface area to the materials.<sup>55</sup> As already stated, for the systems containing MWCNT-PVBC, modified nanotubes are able to participate to the hyper-crosslinking reaction with the precursor resin through the chloromethyl groups of the grafted PVBC resin. This can induce the formation of a highly interconnected network of resin and nanotubes, which, in combination with the particular morphology and structure of the precursor beads containing modified nanotubes, supported the hypothesis that the addition of MWCNT-PVBC can affect the porosity and the adsorption properties of the HCL resin.

### *- ATR-FTIR and EDX analysis*

The extent of the hyper-crosslinking reaction in the investigated systems was verified by means of ATR-FTIR analysis. As shown in Figure 2.3 for the resins X\_DVB-VBC and X\_DVB-ST-VBC, the almost complete disappearance of the sharp absorption band centered at  $1265\text{ cm}^{-1}$  (evidenced with the grey rectangle in Figure 2.3), characteristic of the  $\text{CH}_2\text{Cl}$  group, confirmed the occurrence of the hyper-crosslinking. A similar behaviour was also observed for all the samples containing MWCNT-PVBC, as shown in Figure 2.3 for nanocomposites X\_DVB-VBC\_3CNT and X\_DVB-ST-VBC\_3CNT. EDX analysis performed on the HCL samples confirmed the occurred reaction, revealing for all the investigated systems a residual chlorine content close to 1.5-2.0 wt%, with no significant differences amongst the samples. In agreement with FTIR results, this value, compared to the original chlorine contents of about 13 and 22 wt% of the DVB-ST-VBC and DVB-VBC based resin and nanocomposite precursors, respectively, indicates the large extent of the hyper-crosslinking.

Moreover, in Figure 2.3 are also evident, for the HCL resins and for the nanocomposites containing 3 phr of surface modified CNT, complex absorption bands in the wavenumber range  $1650\text{-}1780\text{ cm}^{-1}$ . These bands are much more intense in the case of systems obtained by the DVB-ST-VBC precursors.

In previous studies,<sup>56</sup> for HCL reactions carried out in nitrobenzene, these absorption bands have been attributed to the oxidation of chloromethyl groups to carbonyl ones promoted by the solvent and further oxidation of the carbonyls to carboxyl groups promoted by oxygen. In our case, we used DCE as a swelling medium for the HCL reaction, and therefore the presence of large amounts of carboxyl groups was unexpected. A detailed explanation of the presence of absorption bands in the range  $1600\text{-}1740\text{ cm}^{-1}$  for HCL Davankov-type resins was reported by Tsyurupa et al.,<sup>57</sup> that denied the presence of  $\text{C}=\text{O}$  functionalities in the HCL polystyrenes, attributing these bands to hindered vibrations of carbon-carbon bonds and valence angles in aromatic rings. In our case, the hypothesis denying the dependence of these bands on  $\text{C}=\text{O}$  groups is confirmed by EDX results on the HCL systems that have evidenced comparable oxygen contents,  $3.72 \pm 0.13\text{ mol}\%$  and  $3.55 \pm 0.23\text{ mol}\%$ , for X\_DVB-VBC and for X\_DVB-ST-VBC, respectively, with no significant differences recorded for the corresponding nanocomposites. Although this subject is outside the scope of this work, further investigations would be needed to explain why the intensity of these absorption bands is higher for the systems with the lower VBC content with respect to the DVB-VBC systems.

*- Specific surface area and pore size distribution*

Results of the BET SSA and DFT analysis of the HCL resins and nanocomposites are reported in Table 2.1. As it can be observed by the nitrogen adsorption/desorption isotherms at 77 K in Figure 2.6, all the materials present a type II isotherm, with hysteresis in desorption attributed to the solubility of nitrogen in the HCL polymer.<sup>58</sup>

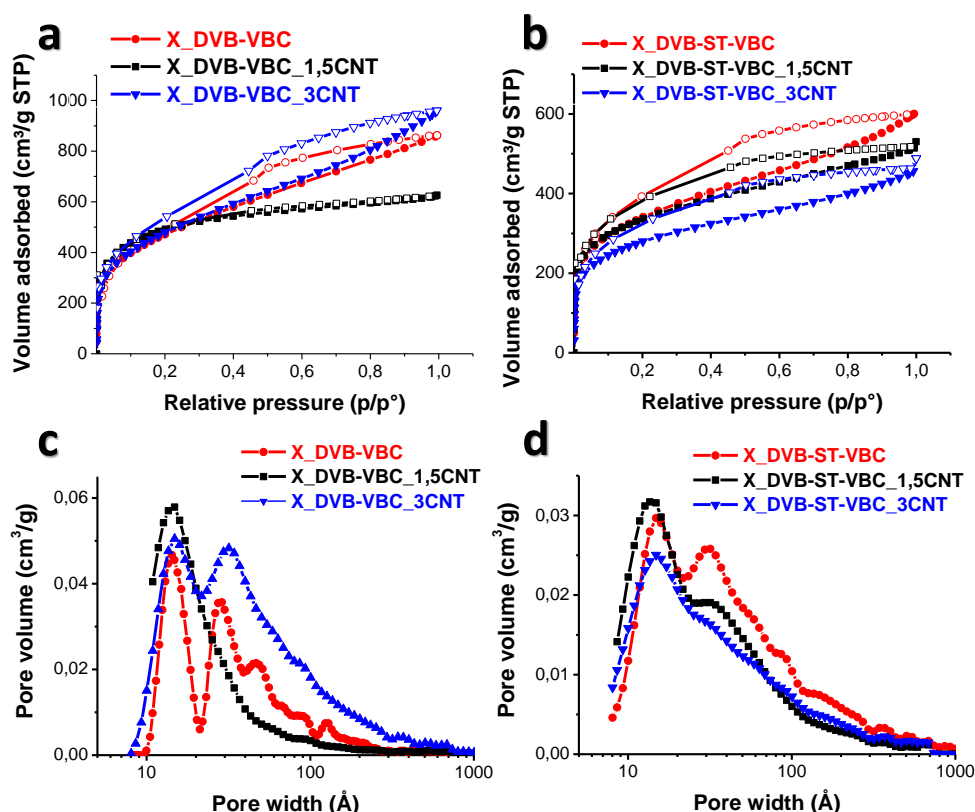


**Figure 2.6** Nitrogen adsorption (filled symbols) and desorption (empty symbols) isotherms at 77K (a,b) and DFT pore size distribution (c,d) of the HCL resins and nanocomposites.

**Table 2.1** Results of SSA and pore size distribution analysis, CO<sub>2</sub> and H<sub>2</sub> uptake, CO<sub>2</sub>/N<sub>2</sub> selectivity

sample	BET SSA (m <sup>2</sup> /g)	microporosity fraction (%)	micropores volume (cm <sup>3</sup> /g)	total pore volume (cm <sup>3</sup> /g)	CO <sub>2</sub> uptake (wt%) <sup>a</sup>	CO <sub>2</sub> /N <sub>2</sub> selectivity <sup>b</sup>	H <sub>2</sub> uptake (wt. %) <sup>c</sup>
X_DVB-VBC	1715 ± 4	32	0.39	1.21	2.99	10.5	1.11
X_DVB-VBC_1,5CNT	1743 ± 18	64	0.54	0.84	3.55	11.0	1.39
X_DVB-VBC_3CNT	1750 ± 4	28	0.38	1.36	3.46	13.6	1.35
X_DVB-ST-VBC	1219 ± 6	37	0.31	0.83	3.26	14.8	1.08
X_DVB-ST-VBC_1,5CNT	1189 ± 9	47	0.34	0.72	3.46	20.9	1.04
X_DVB-ST-VBC_3CNT	1069 ± 7	38	0.28	0.74	2.61	19.8	1.09

<sup>a</sup> measured at 298 K and 750 mmHg; <sup>b</sup> calculated at 298 K and 100 mmHg; <sup>c</sup> measured at 77K and 750 mmHg

The obtained HCL materials show two different ranges of specific surface area. The set of HCL resins and nanocomposites obtained by the DVB-VBC systems have SSA values of 1700-1750 m<sup>2</sup>/g, whereas the samples prepared from the DVB-ST-VBC show SSA values of 1000-1200 m<sup>2</sup>/g. This difference was already reported,<sup>8,29,30</sup> and it is explained considering the high amount of chloromethyl groups in the DVB-VBC class of materials, and thus their higher potentiality to induce the formation of methylene bridges between adjacent aromatic rings with respect to the DVB-ST-VBC systems.

By addition of MWCNT-PVBC, only a slight increase of the SSA was obtained for the DVB-VBC system, while for the DVB-ST-VBC resins the SSA was not significantly influenced by addition of 1.5 phr of MWCNT-PVBC and decreased from 1219 to 1069 m<sup>2</sup>/g at 3.0 phr nanotubes loading.

Instead, the presence of modified nanotubes significantly influences the porosity of the resins. Applying the NLDFT to the nitrogen absorption isotherm curves and assuming a slit pore geometry, all systems are characterized by micro- and mesoporosity, with pore diameters basically up to 10 nm. For both the investigated monomer compositions, HCL nanocomposites containing 1.5 phr of MWCNT-PVBC showed a reduction of the total pore volume and an appreciable increase of the microporosity fraction, as reported in Table 2.1. In particular, X\_DVB-VBC\_1.5CNT resulted in the highest microporosity fraction (0.64), which is also noticeable from the shape of the nitrogen absorption isotherm. In fact, for this sample the nitrogen adsorption mainly occurs at relative pressure  $p/p_0 < 0.3$ , and in this region the gas adsorption is ascribed to the smallest pores. With increasing the pressure, the sample was not able to adsorb a further significant volume of nitrogen, confirming the presence of a reduced number of mesopores. X\_DVB-VBC\_1.5CNT also exhibited the smallest hysteresis loop, and this phenomenon is in agreement with the thermodynamic theory stating that the hysteresis area decreases with the decreasing of the pore size.<sup>59,60</sup>

By increasing the nanofiller loading to 3.0 phr a reduction of the microporosity with respect to the systems containing 1.5 phr of MWCNT-PVBC was recorded. This effect can be ascribed to the preferential localization of the nanotubes on the beads surface during the polymerization of the precursor, as shown by morphological analysis. This phenomenon induces the formation of nanotube clusters, whose dimension increases with increasing the overall nanotube amount. Agglomeration of nanotubes can inhibit the extensive hyper-crosslinking between the PVBC resin grafted on the nanotube and the bulk resin, thus leading to an increase of the mesoporosity fraction.

#### **- *CO<sub>2</sub> uptake and CO<sub>2</sub>/N<sub>2</sub> selectivity***

Physisorption is considered a promising technology for CO<sub>2</sub> capture, offering possible energy savings compared to other more established absorption technologies. In this view microporous hyper-

crosslinked resins are interesting candidates for CO<sub>2</sub> capture and research efforts aim at improving the selectivity of CO<sub>2</sub> sorption with respect to N<sub>2</sub>.<sup>61</sup>

Results obtained on the investigated systems from CO<sub>2</sub> and N<sub>2</sub> adsorption test at 298 K and CO<sub>2</sub>/N<sub>2</sub> absorption selectivity at low pressure are reported in Table 2.1. CO<sub>2</sub> absorption values recorded for the HCL resins and nanocomposites are in agreement with the literature values for microporous polymers, confirming that there is not a direct correlation between SSA and CO<sub>2</sub> adsorption. In fact, as evidenced in Table 2.1, despite to the large differences observed in the SSA, comparable CO<sub>2</sub> uptake values at 750 mmHg were obtained for the DVB-VBC and for the DVB-ST-VBC resins and nanocomposites. Moreover, the highest CO<sub>2</sub> adsorption values were obtained, for both the systems at 1.5 phr MWCNT-PVBC loading, i.e. the samples showing the highest microporosity fractions.

Moreover, either the monomer composition, either the presence of modified nanotubes significantly affected the CO<sub>2</sub>/N<sub>2</sub> selectivity. In particular, the X\_DVB-ST-VBC resin showed higher selectivity in comparison to the X\_DVB-VBC resin. This effect can be ascribed to the preferential interaction between CO<sub>2</sub> and the  $\pi$ -electron density of aromatic rings. Styrene resins have been already reported as selective systems toward CO<sub>2</sub> capture, even if their CO<sub>2</sub> adsorption capacity is quite low.<sup>60</sup>

Furthermore, as concerning HCL nanocomposites, for both systems a noteworthy improvement of the selectivity was obtained in presence of nanotubes, with selectivity values up to about 20 obtained for the X\_DVB-ST-VBC\_1.5CNT and X\_DVB-ST-VBC\_3CNT nanocomposite systems. Therefore, carbon nanotubes with their extended  $\pi$ -conjugation are able to further improve the CO<sub>2</sub> adsorption with respect to N<sub>2</sub>.

All these results confirms a necessary trade-off between absolute adsorption and selectivity often registered in the literature. In fact, simultaneous improvements in selectivity and absolute adsorption had been only generally obtained by introducing moieties able to enhance CO<sub>2</sub> binding affinities, like amines.<sup>5,21,60,61</sup> Nevertheless, there are many cases in which the increase of the selectivity occurs with a decrease of the overall CO<sub>2</sub> uptake. For instance, Dawson et al.<sup>62</sup> synthesized microporous copolymers starting from aniline and benzene. With increasing the content of aniline CO<sub>2</sub>/N<sub>2</sub> selectivity increases from 15.9 to 49.2 but CO<sub>2</sub> uptake decreases from 1.61 mmol/g to 0.35 mmol/g. In our systems, the best compromise was found for the nanocomposite system X\_DVB-ST-VBC\_1.5CNT, for which the recorded CO<sub>2</sub> uptake was found 0.80 mmol/g and the corresponding CO<sub>2</sub>/N<sub>2</sub> selectivity was 20.9.

Nevertheless, for our systems there is still room for further functionalization of the MWCNT or the resin itself to promote even more selective CO<sub>2</sub>/N<sub>2</sub> adsorption, but the obtained results indicate that the loading of nanotubes to low VBC content Davankov-type resins is a promising basis to realize highly selective systems.

### **- H<sub>2</sub> adsorption**

As widely stated, the spread of hydrogen for fuel applications is still limited by the lack of a cost-effective, efficient and safe method to store the gas. Research are currently in course to enhance H<sub>2</sub> absorption properties of organic materials.<sup>63</sup> The isosteric heat of H<sub>2</sub> adsorption for most carbonaceous materials is too low to enable significant adsorption phenomena at room temperature and H<sub>2</sub> adsorption is usually investigated at 77 K.<sup>64</sup> In this view, hydrogen adsorption analysis were performed at 77K and up to 750 mmHg on the realized systems, in order to evaluate the effect of the monomer composition and the nanotube addition on the H<sub>2</sub> uptake of the resins. Results are reported in Table 2.1 and show adsorption values comparable to those reported in the literature.<sup>65-70</sup> As already observed for room temperature CO<sub>2</sub> uptake, H<sub>2</sub> uptake at 77 K is not directly correlated to the SSA, as at 750 mmHg the X\_DVB-VBC and the X\_DVB-ST-VBC resins show comparable values of hydrogen adsorption. As concerning the effect of the nanotubes, MWCNT-PVBC inclusion was not able to induce significant changes in the hydrogen adsorption capacity of the X\_DVB-ST-VBC resin, while it promoted an increased uptake for the X\_DVB-VBC resin. By adding 1.5 or 3.0 phr of MWCNT-PVBC, the hyper-crosslinked DVB-VBC resin capacity increased by 25 or 21 %, respectively. Both these HCL nanocomposites show higher SSA and room temperature CO<sub>2</sub> uptake with respect to the neat X\_DVB-VBC resin, evidencing that the addition of nanotubes is able to improve the overall adsorption properties of the system.

### **- Phenol extraction**

Phenol extraction by using hyper-crosslinked resins is a promising approach for water purification.<sup>58,71,72</sup> The phenol adsorption capacity of these systems are affected by several factors including SSA, pore structure, and affinity between adsorbate and adsorbent.<sup>73</sup>

Phenol adsorption capacity of HCL resins and nanocomposites was evaluated by phenol extraction tests from water solutions. Figure 2.7 shows the equilibrium phenol adsorption curves of the investigated materials. Adsorption equilibrium curves were fitted with the Freundlich equation

$$Q = K_F C^{1/n} \quad (1.1)$$

where Q (mmol/kg) is the amount of adsorbate extracted for unit mass of adsorbent, C (mmol/L) is the adsorbate concentration at equilibrium, K<sub>F</sub> (mmol<sup>n-1</sup> L<sup>n</sup>/kg) is the Freundlich coefficient indicating the adsorption capacity and n is a parameter used as an indicator of the intensity of the adsorption. Higher the maximum capacity, higher the Freundlich coefficient. Lower the n value, more favourable is the adsorption.<sup>17</sup> The calculated Freundlich parameters K<sub>F</sub> and n are reported in Table 2.2.

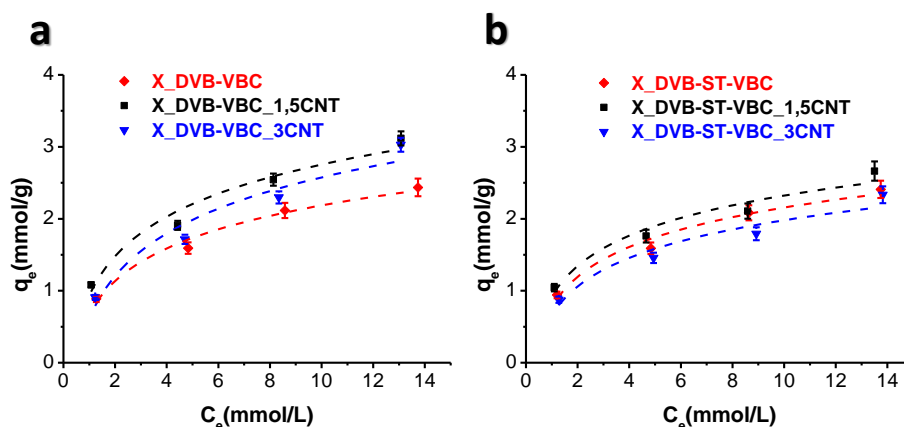


**Figure 2.7** Phenol adsorption isotherms measured at 298 K: a) X\_DVB-VBC systems; b) X\_DVB-ST-VBC systems

**Table 2.2** Freundlich parameters ( $K_F$  and  $n$ ) calculated from the fitting of the phenol adsorption curves and corresponding correlation coefficients  $R^2$

Sample	$K_F$	$n$	$R^2$
X_DVB-VBC	0.80	2.31	0.99
X_DVB-VBC_1.5CNT	1.04	2.36	0.97
X_DVB-VBC_3CNT	0.81	1.99	0.95
X_DVB-ST-VBC	0.87	2.56	0.98
X_DVB-ST-VBC_1.5CNT	1.00	2.75	0.96
X_DVB-ST-VBC_3CNT	0.78	2.51	0.94

DVB-VBC resins and nanocomposites showed slightly higher adsorption capacity than the DVB-ST-VBC systems. In particular, X\_DVB-VBC reaches values of adsorption comparable to those found in literature for similar resins.<sup>17</sup> By addition of 1.5 phr of MWCNT-PVBC an appreciable increase in phenol uptake was registered for both the compositions, with a corresponding increase of the  $K_F$  coefficient. At higher CNT loading, a decrease of the phenol adsorption capacity of the systems was recorded. It is noteworthy that X\_DVB-ST-VBC\_1.5CNT reaches values of adsorption higher than X\_DVB-VBC, even if X\_DVB-ST-VBC\_1.5CNT has significantly smaller specific surface area. As there is not a direct correlation between the SSA and the phenol uptake, the improved adsorption capacity of the systems containing 1.5 phr of nanotubes can be mainly ascribed to their higher microporosity, obtained as a consequence of the effective nanotube addition.

## Conclusions

In this work properly modified multi-walled carbon nanotubes (MWCNT) were for the first time incorporated into a styrene/vinylbenzyl chloride/divinylbenzene hyper-crosslinked resin obtained by post-crosslinking of a lightly crosslinked type precursor. In order to promote the embedding of the nanotubes within the gel-type precursor, a proper surface modification strategy was set up, based on the grafting of a poly(vinylbenzyl chloride) (PVBC) resin onto the surface of the nanotubes, able to react with the resin, through the chloromethyl groups, during the hyper-crosslinking step.

FTIR spectroscopy evidenced that modified carbon nanotubes do not negatively affect neither the suspension polymerization of the lightly crosslinked resin, neither the hyper-crosslinking step. By addition of modified carbon nanotubes, a complex morphology of the precursor nanocomposite beads was revealed by SEM analysis.

Carbon nanotubes slightly affected the SSA of the final resins, with moderate changes recorded as a function of the nanofiller loading and the composition of the resin. Nevertheless, for both the investigated compositions, at low nanofiller loadings a significant increase of the microporosity fraction was observed, up to 64% for the sample X\_DVB-VBC\_1.5CNT, that also showed improved CO<sub>2</sub> uptake (up to 3.55 wt%) and H<sub>2</sub> uptake (up to 1.39 wt%). Interestingly, also for the system X\_DVB-ST-VBC, containing the styrene co-monomer and showing lower SSA, at 1.5 wt% CNT loading, an increase of the CO<sub>2</sub> uptake was recorded, reaching values comparable to those obtained for the X\_DVB-VBC systems.

Moreover, despite the absence of proper functionalization strategies aimed at inserting moieties with high affinity towards CO<sub>2</sub>, the addition of nanotubes also promoted an increase of the CO<sub>2</sub>/N<sub>2</sub> selectivity, thus indicating that the embedding in Davankov-type resins of carbon nanotubes, characterized by their extended  $\pi$ -conjugation, is a promising approach to realize highly selective systems towards CO<sub>2</sub> absorption.

Finally, preliminary tests of phenol adsorption from water solutions were carried out to evaluate possible applications of the investigated systems for water remediation. Also in this case, the addition of carbon nanotubes to the resins was able to improve the overall adsorption capacity of phenol, in particular for the DVB-VBC system.

All these results confirm that the addition of the properly surface modified carbon based nanofillers, able to interact with the hosting resin during the synthesis of the precursor and to participate to the hyper-crosslinking reaction, is a promising approach to modulate and improve either the gas sorption properties either the removal ability of organic contaminants from water of styrene/vinylbenzyl chloride/divinylbenzene microporous polymers.

## Supplementary information



**Figure S2.1.** Inhomogeneous product obtained by the suspension polymerization of 2 mol% DVB, 98 mol% VBC and 3 phr of unmodified MWCNT.

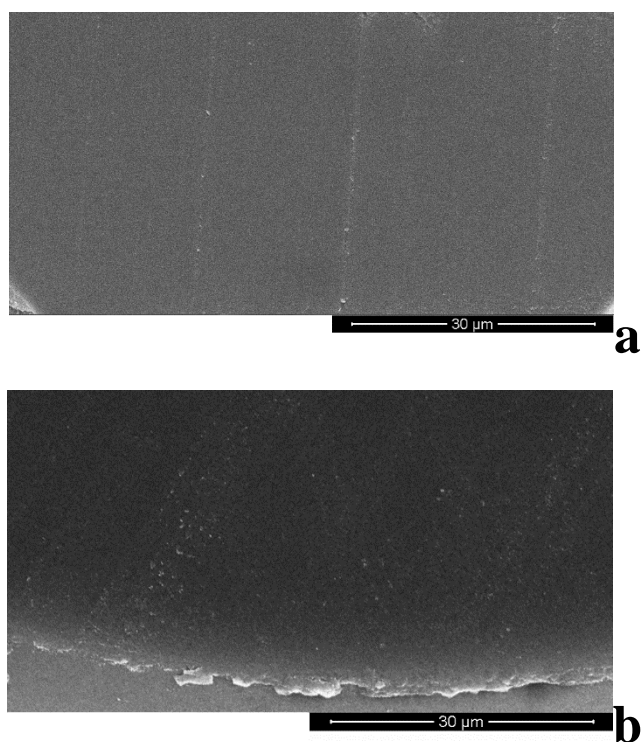


**Figure S2.2.** SEM micrographs of the cross-sections of: a) DVB-VBC precursor beads; b) DVB-ST-VBC precursor beads.

## References

- <sup>1</sup> Dąbrowski, P. Podkościelny, Z. Hubicki and M. Barczak, *Chemosphere*, 2005, **58**, 1049.
- <sup>2</sup> J. Weitkamp, *Solid state ionics*, 2000, **131**, 175
- <sup>3</sup> J.L.C. Rowsell and O.M. Yaghi, *Microporous and Mesoporous Materials*, 2004, **73**, 3.
- <sup>4</sup> H. Furukawa, N. Ko, Y.B. Go, N. Aratani, S.B. Choi, E. Choi, A.Ö. Yazaydin, R.Q. Snurr, M. O’Keeffe, J. Kim and O.M. Yaghi, *Science*, 2010, **329**, 424.
- <sup>5</sup> H.A. Patel, S.H. Je, J. Park, D.P. Chen, Y. Jung, C.T. Yavuz and A. Coskun, *Nat. Commun.*, 2013, **4**, 1357.
- <sup>6</sup> S.-Y. Ding, J. Gao, O. Wang, Y. Zhang, W.-G. Song, C.-Y. Su, W. Wang, *J. Am. Chem. Soc.*, 2011, **133**, 19816.
- <sup>7</sup> N. B. McKeown and P. M. Budd, *Chem. Soc. Rev.*, 2006, **35**, 675.
- <sup>8</sup> J. Lee, C. D. Wood, D. Bradshaw, M. J. Rosseinsky, A. I. Cooper, *Chem. Commun.*, 2006, **25**, 2670.
- <sup>9</sup> D.Lin and B. Xing, *Environ. Sci.*, 2008, **42**, 7254.
- <sup>10</sup> P. Bernardo, E. Drioli and G. Golemme, *Ind. Eng. Chem. Res.*, 2009, **48**, 4638.
- <sup>11</sup> H. Yang, Z. Xu, M. Fan, R. Gupta, R.B. Slimane, A.E. Bland and I. Wright, *Journal of Environmental Sciences*, 2008, **20**, 14
- <sup>12</sup> R.T. Yang, *Gas Separation by Adsorption Processes*, Butterworth Publishers, Stoneham, 2013.
- <sup>13</sup> R. Dawson, A.I. Cooper and D.J. Adams, *Progress in Polymer Science*, 2012, **37**, 530.
- <sup>14</sup> R.E. Morris and P.S. Wheatley, *Angew. Chem. Int. Ed.*, 2008, **47**, 4966.
- <sup>15</sup> A. Corma, *Chem. Rev.*, 1997, **97**, 2373
- <sup>16</sup> C.F. Martín, E. Stöckel, R. Clowes, D.J. Adams, A.I. Cooper, J.J. Pis, F. Rubiera and C. Pevida, *J. Mater. Chem.*, 2011, **21**, 5475
- <sup>17</sup> A. Li, Q. Zhang, G. Zhang, J. Chen, Z. Fei and F.L. Li, *Chemosphere*, 2002, **47**, 981.
- <sup>18</sup> K. Yang, W. Wu, Q. Jing and L. Zhu, *Environ. Sci. Technol.*, 2008, **42**, 7931.
- <sup>19</sup> X.Wang, P.D. Patil, C. He, J. Huang and Y.-N. Liu, *J. Appl. Polym. Sci.*, 2015, **132**, 41597.
- <sup>20</sup> R.T. Woodward, L.A. Stevens, R. Dawson, M. Vijayaraghavan, T. Hasell, I.P. Silverwood, A.V. Ewing, T. Ratvijitvech, J.D. Exley, S.Y. Chong, F. Blanc, D.J. Adams, S.G. Kazarian, C.E. Snape, T.C. Drage and A.I. Cooper, *J. Am. Chem. Soc.*, 2014, **136**, 9028.
- <sup>21</sup> R. Dawson, A.I. Cooper and D.J. Adams, *Polym. Int.*, 2013, **62**, 345.
- <sup>22</sup> R. Dawson, L.A. Stevens, T.C. Drage, C.E. Snape, M.W. Smith, D.J. Adams and A.I. Cooper, *J. Am. Chem. Soc.*, 2012, **134**, 10741.
- <sup>23</sup> J. Germain, F. Svec and J.M.J. Fréchet, *Chem. Mater.*, 2008, **20**, 7069.
- <sup>24</sup> R. Dawson, E. Stöckel, J.R. Holst, D.J. Adams and A.I. Cooper, *Energy Environ. Sci.*, 2011, **4**, 4239..

- <sup>25</sup> N. Fontanals, J. Cortés, M. Galià, R.M. Marcé, P.A.G. Cormack, F. Borrull and D.C. Sherrington, *J. Polym. Sci. Part A Polym. Chem.*, 2005, **43**, 1718.
- <sup>26</sup> N. Fontanals, R.M. Marcé, F. Borrull and P.A.G. Cormack, *Polym. Chem.*, 2015, **6**, 7231.
- <sup>27</sup> S. Shen, X. Zhang and L. Fan, *Mater. Lett.*, 2008, **62**, 2392
- <sup>28</sup> M.P. Tsyurupa and V.A. Davankov, *Reactive & Functional Polymers*, 2006, **66**, 768.
- <sup>29</sup> Q.-Q. Liu, L. Wang, A.-G. Xiao, H.-J. Yu and Q.-H. Tan, *Eur. Polym. J.*, 2008, **44**, 2516.
- <sup>30</sup> J.-H. Ahn, J.-E. Jang, C.-G. Oh, S.-K. Ihm, J. Cortez and D.C. Sherrington, *Macromolecules*, 2006, **39**, 627.
- <sup>31</sup> L. Jia, X. Song, J. Wu and C. Long, *J. Phys. Chem.C*, 2015, **119**, 21404.
- <sup>32</sup> X. Li, Y. Liu, D. Di, G. Wang and Y. Liu, *Colloids and Surfaces A: Physicochem. Eng. Aspects*, 2016, **500**, 1.
- <sup>33</sup> X. Zeng, H. Chen, Y. Zheng, W. Tao, Y. Fan, L. Huang and L. Mei, *J. Colloid Interface Sci.*, 2012, **385**, 166
- <sup>34</sup> X. Zeng, T. Yu, P. Wang, R. Yuan, Q. Wen, Y. Fan, C. Wang and R. Shi, *J. Hazard. Mater.*, 2010, **177**, 773.
- <sup>35</sup> X. Zeng, Y. Fan, G. Wu, C. Wang and R. Shi, *J. Hazard. Mater.*, 2009, **169**, 1022.
- <sup>36</sup> X. Ling, H. Li, H. Zha, C. He and J. Huang, *Chemical Engineering Journal*, 2016, **286**, 400.
- <sup>37</sup> Q.B. Meng and J. Weber, *ChemSusChem*, 2014, **7**, 3312.
- <sup>38</sup> W. Wang, Y. Ma, Q. Zhou, C. Shuang, M. Zhang and A. Li, *Front. Environ. Sci. Eng.*, 2015, **9**, 96.
- <sup>39</sup> M.J. Allen, V.C. Tung and R.B. Kaner, *Chem. Rev.*, 2010, **110**, 132.
- <sup>40</sup> F.L. Darkrim, P. Malbrunot and G.P. Tartaglia, *International Journal of Hydrogen Energy*, 2002, **27**, 193.
- <sup>41</sup> X. Ren, C. Chen, M. Nagatsu and X. Wang, *Chemical Engineering Journal*, 2011, **170**, 395.
- <sup>42</sup> J. Zhao, A. Buldum, J. Han and J.P. Lu, *Nanotechnology*, 2002, **13**, 195.
- <sup>43</sup> C.-H. Yu, C.-H. Huang and C.-S. Tan, *Aerosol Air Qual. Res.*, 2012, **12**, 745.
- <sup>44</sup> S. Agnihotri, M.J. Rood and M. Rostam-Abadi, *Carbon*, 2005, **43**, 2379.
- <sup>45</sup> R.Q. Long and R.T. Yang, *J Am Chem. Soc.*, 2001, **123**, 2058
- <sup>46</sup> Y.H. Li, S. Wang, Z. Luan, J. Ding, C. Xu and D. Wu, *Carbon*, 2003, **41**, 1057.
- <sup>47</sup> F. Su and C. Lu, *J. Environ Sci Health Part A: Toxic/Hazard Subst Environ Eng*, 2007, **42**, 1543.
- <sup>48</sup> F. Su, C. Lu, W. Cnen, H. Bai and J.F. Hwang, *Science of the Total Environment*, 2009, **407**, 3017.
- <sup>49</sup> X. Chen, M. Zhou, Q. Hou, X. Tu and X. Wu, *Macromolecular Chemistry and Physics*, 2013, **214**, 1829.
- <sup>50</sup> J. Landers, G.Y. Gor and A.V. Neimark, *Colloids and Surfaces A: Physicochem. Eng. Aspects*, 2013, **437**, 3.

- <sup>51</sup> P.B. Nagabalasubramanian, S. Periandy and S. Mohan, *Spectrochimica Acta Part A*, 2010, **77**, 150
- <sup>52</sup> V. Ambrogi, G. Gentile, C. Ducati, M.C. Oliva and C. Carfagna, *Polymer*, 2012, **53**, 291.
- <sup>53</sup> G. Nasti, G. Gentile, P. Cerruti, C. Carfagna, V. Ambrogi, *Polymer*, 2016, **99**, 193.
- <sup>54</sup> N.M. Briggs, J.S. Weston, B. Li, D. Venkataramani, C.P. Aichele, J.H. Harwell, S.P. Crossley, *Langmuir* 2015, **31**, 13077.
- <sup>55</sup> M.P. Tsyurupa and V.A. Davankov, *Reactive & Functional Polymers*, 2002, **53**, 193.
- <sup>56</sup> G. Meng, A. Li, W. Yang, F. Liu, X. Yang and Q. Zhang, *European Polymer Journal*, 2007, **43**, 2732.
- <sup>57</sup> M.P. Tsyurupa, Z.K. Blinnikova, Y.A. Davidovich, S.E. Lyubimov, A.V. Naumkin and V.A. Davankov, *Reactive & Functional Polymers*, 2012, **72**, 973.
- <sup>58</sup> V.V. Azanova and J. Hradil, *React. Funct. Polym.*, 1999, **41**, 163.
- <sup>59</sup> P.I. Ravikovitch, S.C.Ó. Domhnaill, A.V. Neimark, F. Schüth and K.K. Unger, *Langmuir*, 1995, **11**, 4765.
- <sup>60</sup> R. Evans, U.M.B. Marconi and P. Tarazona, *J. Chem. Soc., Faraday Trans. 2*, 1986, **82**, 1763.
- <sup>61</sup> J. Wang, J.G.W. Yang, G. Yi and Y. Zhang, *Chem. Commun.*, 2015, **51**, 15708.
- <sup>62</sup> R. Dawson, T. Ratvijitvech, M. Corker, A. Laybourn, Y.Z. Khimyak, A.I. Cooper and D.J. Adams, *Polym. Chem.*, 2012, **3**, 2034.
- <sup>63</sup> L. Pan, Q. Chen, J.-H. Zhu, J.-C. Yu, Y.-J. He and B.-H. Han, *Polym. Chem.*, 2015, **6**, 2478.
- <sup>64</sup> C.D. Wood, B. Tan, A. Trewin, H. Niu, D. Bradshaw, M.J. Rosseinsky, Y.Z. Khimyak, N.L. Campbell, R. Kirk, E. Stöckel and A.I. Cooper, *Chem. Mater.*, 2007, **19**, 2034.
- <sup>65</sup> J. Germain, J. Hradil, J.M.J. Fréchet and F. Svec, *Chem. Mater.*, 2006, **18**, 4430.
- <sup>66</sup> B. Li, R. Gong, W. Wang, X. Huang, W. Zhang, H. Li, C. Hu and B. Tan, *Macromolecules*, 2011, **44**, 2410.
- <sup>67</sup> K. M. Thomas, *Catal. Today*, 2007, **120**, 389.
- <sup>68</sup> H. Furukawa and O.M. Yaghi, *J. Am. Chem. Soc.*, 2009, **131**, 8875.
- <sup>69</sup> B. Panella, M. Hirscher and S. Roth, *Carbon*, 2005, **43**, 2209
- <sup>70</sup> E. Poirier, R. Chahine and T.K. Bose, *International Journal of Hydrogen Energy*, 2001, **26**, 831.
- <sup>71</sup> J. Huang, X. Jin and S. Deng, *Chem. Eng. J.*, 2012, **192**, 192
- <sup>72</sup> X. Zhang, A. Li, Z. Jiang and Q. Zhang, *J. Hazard. Mater.*, 2006, **137**, 1115.
- <sup>73</sup> K. Yang and B. Xing, *Chem. Rev.*, 2010, **110**, 5989.

# Chapter 3

## **A new synthetic approach towards hyper-crosslinked styrene-based polymers and nanocomposites**

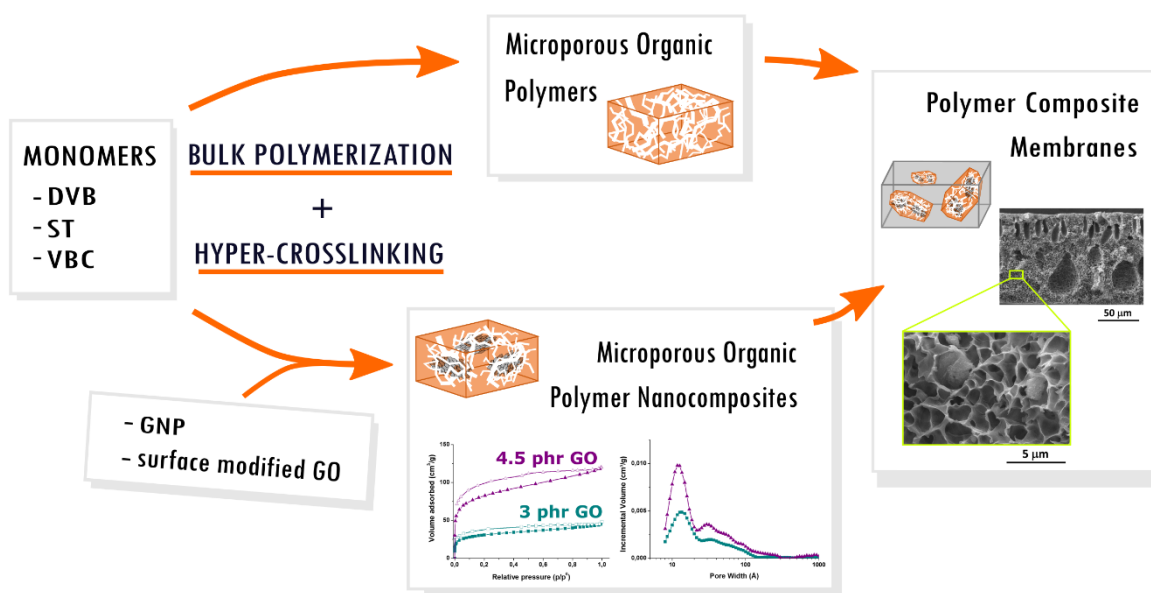
### **Authors and affiliations**

Rachele Castaldo,<sup>a,b</sup> Roberto Avolio,<sup>a</sup> Mariacristina Cocca,<sup>a</sup> Gennaro Gentile,<sup>a\*</sup> Maria Emanuela Errico,<sup>a</sup> Maurizio Avella,<sup>a</sup> Cosimo Carfagna<sup>a</sup> and Veronica Ambrogi<sup>a,b</sup>

<sup>a</sup> Institute for Polymers, Composites and Biomaterials, National Research Council of Italy, Via Campi Flegrei 34, 80078 Pozzuoli, Italy.

<sup>b</sup> Department of Chemical, Materials and Production Engineering, University of Naples, Piazzale Tecchio 80, 80125 Napoli, Italy.

## Abstract



In this work we describe a new synthetic approach for the realization of hyper-crosslinked (HCL) styrene resins, based on the bulk prepolymerization of a gel type precursor followed by a traditional Friedel-Crafts alkylation step. The obtained HCL materials show comparable properties with respect to the corresponding resins obtained by typical suspension prepolymerization. The versatility of the proposed process is demonstrated through the realization of two innovative classes of advanced materials, i.e. HCL microporous organic polymer nanocomposites (MOPNs) and polymer membranes containing HCL fillers, which can both represent very promising strategies towards wide and successful application of Davankov-type materials for gas separation and storage and for water remediation.

## Introduction

Microporous organic polymers (MOPs) are an interesting class of materials because of their potential applications for adsorption of organic substances,<sup>1</sup> heterogeneous catalysis,<sup>2</sup> and gas separation and storage.<sup>3</sup>

Amongst MOPs, hyper-crosslinked (HCL) resins have been and are constantly under investigation for their low density and their high chemical and thermal stability.<sup>4</sup> Moreover, several research efforts have been carried out to tailor their structure, porosity and functionality in order to improve their overall adsorption properties and their selectivity towards specific substances.<sup>5,6,7</sup>

Widely investigated HCL resins are the so-called Davankov-type resins, obtained by post-crosslinking of polystyrenes.<sup>8,9</sup> They are synthesized by post crosslinking of linear or lightly crosslinked gel-type precursor resins based on divinylbenzene (DVB) and vinylbenzyl chloride (VBC), where the precursor is prepared by suspension polymerization. This leads to polymer beads with different size, ranging from the micro to the nanoscale. By optimization of the VBC/DVB ratio, after hyper-crosslinking of micrometric precursor beads, materials with specific surface (SSA) values close to 2000 m<sup>2</sup>/g are obtained,<sup>10</sup> while starting from nanometric beads, with average diameter lower than 500 nm, SSA values of 1300-1500 m<sup>2</sup>/g can be reached,<sup>11,12</sup> with yields ranging between 70 to 90 mass%. To be noted is that these values also correspond to the final yields after HCL, as the Friedel-Crafts alkylation is characterized in all cases by a practically quantitative recovery of the product.

Other interesting strategies have been proposed in the last years for the realization of high SSA polymers with tailored porosity. To be mentioned, there are those reported by Li et al.,<sup>13</sup> that have synthesized tetraphenyladamantane-based porous poly(Schiff base)s with BET surface area close to 1000 m<sup>2</sup>/g and by Shen et al.,<sup>14</sup> that have synthesized polycyanurate networks with BET surface areas up to about 720 m<sup>2</sup>/g.

Nevertheless, the key-factors limiting the application of these porous resin is considered their complex synthetic procedure, as the successful preparation of MOPs requires the use of expensive and non-environmental friendly substances, such as catalysts and halogen-containing monomers, and extensive laboratory work.<sup>15,16</sup>

Recently, a new synthetic approach has been proposed for the realization of HCL MOPs, based on the alternating radical copolymerization of bismaleimides and DVB.<sup>17</sup> These MOPs are prepared by one-step solution polymerization, thus overcoming the two-step procedure used for the synthesis of HCL Davankov-type resins. Materials with a maximum SSA of about 840 m<sup>2</sup>/g are obtained with interesting gas capture capacity. With an alternative synthetic strategy, aimed at finding alternative

inexpensive and sustainable monomers for the realization of MOPs, Gao et al. realized high SSA HCL materials by Friedel-Crafts reaction starting from coal tar.<sup>18</sup>

Starting from the needs for new efficient synthetic approaches for the realization of MOPs with high SSA, in this work we report the synthesis of new HCL styrene based resins obtained by a modified Davankov method. In particular, instead of the suspension or solution polymerization, the gel type precursor was for the first time realized by bulk polymerization, followed by a traditional Friedel-Crafts alkylation step.

Both the lightly crosslinked prepolymers and the HCL resins were fully characterized in comparison to the corresponding materials prepared by traditional suspension polymerization followed by the hyper-crosslinking step. Furthermore, the effect of the composition of the mass-prepolymerized HCL resin was also investigated through the synthesis of materials with a reduced content of the halogenated monomer vinylbenzyl chloride.

Finally, the versatility of the proposed process was demonstrated through the realization of two innovative classes of advanced materials, i.e. HCL microporous organic polymer nanocomposites (MOPNs) and polymer mixed matrix membranes containing HCL fillers, which can both represent very interesting strategies towards a wide and successful application of MOPs for gas separation and storage and for water remediation.

## **Experimental section**

### **Materials**

Styrene (ST, > 99.9 %), vinylbenzyl chloride (VBC,  $\geq 95.0$  %, mixture of isomers,  $\sim 70$  % meta +  $\sim 30$  % para), p-divinylbenzene (DVB, 85%, meta isomer,  $\sim 10$  wt%), 2,2'-azobis(2-methylpropionitrile (AIBN, > 98%), NaOH ( $\geq 97.0$  %, pellets), tetraoctylammonium bromide (TOAB, > 98 %), FeCl<sub>3</sub> ( $\geq 97$  %), phenol (> 99.5 %), graphene oxide (GO) as a dispersion in water (4 mg/mL), polysulfone (PSF, poly[oxy-1,4-phenylenesulfonyl-1,4-phenyleneoxy-1,4-phenylene(1-methylethylidene)-1,4-phenylene], average Mw  $\sim 35,000$ , average Mn  $\sim 16,000$ , pellets), and all solvents were purchased by Sigma Aldrich (Milan, Italy) and used without further purification.

Graphene nanoplatelets (GNP) grade C, average lateral dimensions 1-2  $\mu\text{m}$  according to the datasheet provided by the supplier, were purchased from XG Science (Lansing, MI, USA).

### **Synthesis of the precursor resins**

Poly(divinylbenzene-co-styrene-co-vinylbenzyl chloride) precursor resins and nanocomposites were obtained by bulk polymerization. For neat resins, DVB, ST and VBC were mixed in two compositions, 2:0:98 and 2:49:49 DVB:ST:VBC molar ratio. After mixing the monomers, 0.5 phr of AIBN were added and the mixture was kept at 80°C in a flask for 30 minutes under nitrogen. Therefore, the mixture was poured in a glass bottle and cured in oven for 24 h at 80°C, then purified by multiple washings with methanol, acetone and diethyl ether, and then dried in vacuum oven at 40 °C for 24 h. The obtained samples were coded b\_DVB-VBC and b\_DVB-ST-VBC, respectively. Precursors with the same monomer ratio were also prepared by suspension polymerization, as described in a previous work<sup>19</sup> (Chapter 2 of this thesis), and here coded as DVB-VBC and DVB-ST-VBC.

### **Synthesis of the precursor nanocomposites**

Precursor nanocomposites were obtained by mixing DVB, ST and VBC in the monomer ratios used for the plain resins, with 3.0 phr of carbon nanofillers (GNP and modified GO). For GNP, the nanofiller was used as received, whereas for GO, in water dispersion, a preliminary surface functionalization was performed. In particular, GO was surface modified by grafting poly(vinylbenzyl chloride) (PVBC). The GO solution was diluted in a 0.005 M NaOH aqueous solution to obtain a dispersion of 600 mg of GO in 350 mL of NaOH solution. Then 1 g of TOAB was added and the mixture was heated to 60 °C. PVBC (300 mg), pre-dissolved in 250 mL of toluene, was added to the mixture. The reaction was carried for 7 hours under vigorous stirring; after that, the mixture was poured in a separatory funnel and the toluene phase was recovered and filtered. Modified GO (GO-PVBC) was purified from unreacted reagents by 3 washing cycles with chloroform and tetrahydrofuran, and then it was dried in oven at 50°C for 24 hours.

To promote the effective nanofiller dispersion in the polymer matrix, the monomer mixtures containing GNP or GO-PVBC were sonicated for 50 minutes with a 500 W tip sonicator at 25% power, with a 10s/50s ON/OFF cycle. Then, AIBN was added and the system was stirred at 80° C under nitrogen. This phase was prolonged until the mixture viscosity increased enough to hinder the nanofiller re-aggregation, in each case from 30 to 45 minutes, and then the polymerization was completed in oven for 24 h in a closed bottle, following the procedure already adopted for the plain resins. The precursor nanocomposites were purified by multiple washings with methanol, acetone and diethyl ether, and then dried in vacuum oven at 40 °C for 24 h.

Furthermore, another series of nanocomposite samples based on the monomers ratio 2:98 DVB:ST and containing 3.0 and 4.5 phr of GO-PVBC were prepared with the same methodology.

The obtained precursor nanocomposites are codified as reported in Table 3.1, together with the plain resins prepared in this work.

**Table 3.1** Codes and compositions of the precursor resins and nanocomposites prepared

sample	precursor polymerization	DVB	ST	VBC	GNP	GO
		(mol %)			content (phr)	
DVB-VBC	suspension	2	0	98	-	-
DVB-ST-VBC	suspension	2	49	49	-	-
b_DVB-VBC	bulk	2	0	98	-	-
b_DVB-ST-VBC	bulk	2	49	49	-	-
b_DVB-VBC_3GNP	bulk	2	0	98	3.0	-
b_DVB-ST-VBC_3GNP	bulk	2	49	49	3.0	-
b_DVB-VBC_3GO	bulk	2	0	98	-	3.0
b_DVB-ST-VBC_3GO	bulk	2	49	49	-	3.0
b_DVB-ST_3GO	bulk	2	98	0	-	3.0
b_DVB-ST_4.5GO	bulk	2	98	0	-	4.5

### Hyper-crosslinking of the gel-type resins and nanocomposites

The gel-type precursor polymers and nanocomposites were hyper-crosslinked using the following procedure.<sup>20</sup> Precursors were swollen in 1,2-dichloroethane (DCE), under nitrogen, for 2 h. Then the mixtures were cooled to ~4 °C in an ice/NaCl bath, and the Friedel-Crafts catalyst, FeCl<sub>3</sub>, was added. Therefore, the system was heated to 80 °C and kept at this temperature for 18 h. The hyper-crosslinked resins and nanocomposites were then washed with methanol and dried in a vacuum oven at 40 °C for at least 24 h. Samples were coded as the corresponding precursor resins and nanocomposites, reported in Table 3.1, adding the prefix X\_.

### Polysulfone composite membranes preparation

The hyper-crosslinked resin X\_b\_DVB-VBC and the hyper-crosslinked nanocomposite X\_b\_DVB-ST\_4.5GO were milled in a planetary ball-milling system Retsch PM100, using a 125 mL steel milling cup and 10 mm diameter steel milling spheres in a spheres/resin weight ratio 7:1, at 600 rpm for 8 hours. The obtained materials, respectively coded X\_b\_DVB-VBC\_BM and X\_b\_DVB-ST\_4.5GO\_BM, were embedded in porous polysulfone (PSF) membranes at 20 wt% loading.

PSF membranes were prepared dissolving the polymer in DMF (20 wt% concentration) under stirring at room temperature overnight. After 24 h for the complete removal of air bubbles from the solution, the solution was cast (about 400 μm thickness) on a glass substrate using a hand-casting knife. The obtained liquid film was immediately immersed, together with the glass support, in a water coagulation bath at 25 °C and kept in water for 24 h for the complete removal of the solvent. The PSF membrane was then dried in oven at 60 °C overnight.

Porous PSF membranes containing 20 wt% of X\_b\_DVB-VBC\_BM (PSF\_20X) and X\_b\_DVB-ST\_4.5GO\_BM, (PSF\_20XGO) were prepared in the same way, after dispersing the milled resin in the PSF/DMF solution through stirring at room temperature for about 4 h.

### **Characterization of neat and modified carbon nanofillers**

GO-PVBCB was analyzed by means of Fourier transform infrared spectroscopy (FTIR) in attenuated total reflectance (ATR) mode to evaluate the extent of the surface modification. By comparison, ATR-FTIR spectra were recorded on PVBC and on dried GO. Spectra were recorded with a Perkin Elmer Spectrum One FTIR spectrometer equipped with an ATR module, using a resolution of  $4\text{ cm}^{-1}$  and 32 scan collections.

Energy Dispersive X-ray (EDX) analysis was performed using a FEI Quanta 200 FEG SEM equipped with an Oxford Inca Energy System 250 and an Inca-X-act LN2-free analytical silicon drift detector. A thin layer of GO and GO-PVBC was deposited onto aluminum SEM stubs. The analysis was performed at 30 kV acceleration voltage. Average results and standard deviation values are based on three consecutive measurements on different areas of each sample.

Bright field Transmission Electron Microscopy (TEM) analysis of GO and GO-PVBC was performed on a FEI Tecnai G12 Spirit Twin (LaB6 source) at 120 kV acceleration voltage. TEM images were collected on a FEI Eagle 4k CCD camera. Before the analysis, GO-PVBC was dispersed in toluene by sonication (2 min) with a 500 W tip sonicator set at 25% power. Water dispersed GO was used as obtained. The samples were then collected by immersing holey carbon coated copper grids in the dispersion.

### **Characterization of the precursor resins and nanocomposites**

The precursor resins b\_DVB-VBC and b\_DVB-ST-VBC and the corresponding nanocomposites containing 3.0 phr of GO-PVBC and GNP were characterized by FTIR analysis. In particular, ATR-FTIR spectra were recorded on the neat precursor resins and nanocomposites by means of the above described FTIR apparatus, equipped with a universal ATR sampling module, using a resolution of  $4\text{ cm}^{-1}$  and 32 scan collections.

Solid-state  $^{13}\text{C}$  cross-polarization (CP) NMR spectra were collected on precursor resins and nanocomposites using a Bruker Avance II 400 spectrometer operating at a static field of 9.4 T, equipped with a 4 mm magic angle spinning (MAS) probe, using a  $1\text{H}$   $\pi/2$  pulse width of  $3.6\ \mu\text{s}$ , a contact time of 2 ms and a repetition time of 5. Finely ground samples were packed into 4 mm zirconia rotors sealed with Kel-F caps and spun at a spinning speed ranging from 11 to 13 kHz. All spectra were referenced to external adamantane (CH signal at 38.48 ppm downfield of tetramethylsilane (TMS), set at 0.0 ppm).

The distribution of the carbon nanofillers in the nanocomposite precursors was explored by TEM analysis, with the above described apparatus. Before the analysis, ultrathin sections of the samples were prepared with a Leica UC7 ultramicrotome (nominal thickness 100 nm) and deposited on TEM copper grids. TEM observations were performed in bright field mode using an acceleration voltage of 120 kV.

### **Characterization of the HCL resins and nanocomposites**

ATR-FTIR and solid-state  $^{13}\text{C}$  CP/MAS NMR spectra were also collected on HCL resins and nanocomposites as detailed for the precursor resins. Furthermore, EDX analysis was performed to determine the Cl/C atomic ratio using the equipment and the experimental conditions already described for the characterization of neat and modified carbon nanofillers.

HCL nanocomposites were also characterized by bright field TEM analysis. Before the analysis, the samples were embedded in a polystyrene resins and ultrathin sections were obtained by room temperature ultramicrotomy.

Gas adsorption volumetric analysis was performed on the HCL resins and nanocomposites using a Micromeritics ASAP 2020 analyzer. SSA was determined by nitrogen adsorption measurements at 77 K from the linear part of the BET equation. Non-local density functional theory (NLDFT) was applied to the nitrogen adsorption isotherms to evaluate the pore size distribution of the materials.  $\text{N}_2$  and  $\text{CO}_2$  adsorption analysis were also performed at 298 K up to 1 bar.  $\text{H}_2$  uptake capacity was evaluated at 77 K up to 1 bar. Prior to the analysis all the samples were degassed at 120°C under vacuum ( $P < 10^{-5}$  mbar); all the adsorption measurements were performed using high purity gases ( $> 99.999\%$ ).

Phenol adsorption tests from water were performed on HCL resins and nanocomposites at 25 °C at the phenol concentration of 1500 mg/L. About 10 mg of HCL resins or nanocomposites were introduced into vials containing 10 mL of the phenol solution. The vials were kept at 25°C until equilibrium was reached (at least 48 h). Therefore, the solution was removed from the vial and the final phenol concentration was measured using a Jasco V570 UV spectrophotometer. A previously recorded calibration curve was used to determine the phenol concentration in water from the absorbance of the peak centred at 270 nm.

### **Characterization of the PSF membranes**

Plain and composite PSF membranes were characterized by SEM analysis. The sections of the membranes were observed after their cryogenic fracture. The HCL fillers used in the membranes were also observed by SEM analysis, before and after their size reduction by ball-milling.

Phenol adsorption tests were performed on PSF and composite membranes using the conditions already adopted for the HCL resins and nanocomposites, using about 200 mg of membrane for each measurement. By comparison, ball-milled resins X\_b\_DVB-VBC\_BM and X\_b\_DVB-ST\_4.5GO\_BM in powder form were characterized in the same way.

## **Results and discussion**

In this paper a new synthetic process for the realization of Davankov-type HCL resins is described, based on the bulk prepolymerization of a lightly cross-linked precursor followed by a Friedel-Crafts reaction. This process represents a significant innovation with respect to the traditional HCL styrene based resins, usually prepared by suspension prepolymerization followed by the HCL step.

The proposed approach showed several advantages. First, it allowed to significantly increasing the yields and reducing the amount of chemicals and by-products during the precursor synthesis. Moreover, the proposed process resulted very versatile, because it could be used “on demand” for the realization of different classes of advanced materials, as schematized in Figure 3.1.

On the one hand, it allowed to easily embedding, within the final HCL porous structure, different functional nanofillers, thus allowing the realization of a new class of advanced microporous organic polymer nanocomposites (MOPNs). On the other hand, through mechanical processes able to reduce and homogenise the size of the obtained HCL resins and nanocomposites, these microporous materials could be used as functional fillers in polymer membranes, able to enhance their adsorption properties.

With these objectives, the work here presented is organized in three sections. In the first one, new bulk prepolymerized resins are characterized in comparison to traditional suspension prepolymerized resins. In the second one, the design and the characterization of new MOPNs are described, showing the extended possibilities offered by this new class of nanocomposites. Finally, the developments obtained on the realization of polymer membranes containing HCL functional fillers are presented.

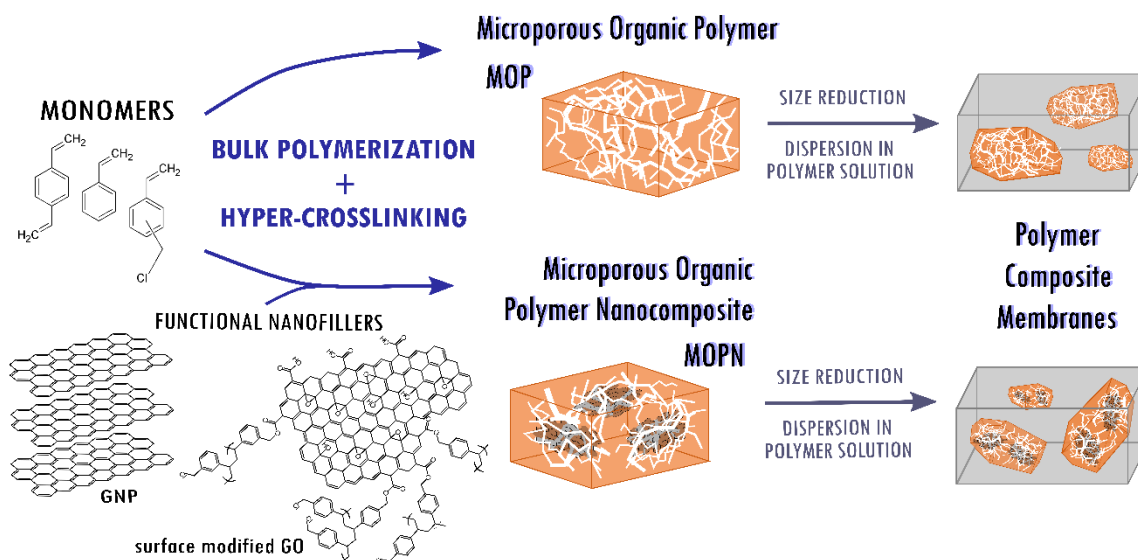


**Figure 3.1** Innovative systems based on microporous polymers and nanocomposites obtained through bulk prepolymerization followed by Friedel-Crafts hyper-crosslinking.

### Bulk prepolymerized precursors and HCL resins

b\_DVB-VBC and b\_DVB-ST-VBC precursor resins were prepared as detailed in the experimental. After purification, yields of reactions were for both systems > 99.0 wt%, this result representing a significant improvement with respect to yields obtained for the corresponding materials prepared by suspension prepolymerization (DVB-VBC: yield = 84.5 wt%; DVB-ST-VBC: yield = 87.1 wt%).

FTIR and  $^{13}\text{C}$  CP/MAS NMR analysis were performed on the gel type resins b\_DVB-VBC and b\_DVB-ST-VBC in comparison with the same materials prepared by suspension polymerization. FTIR analysis results of the divinylbenzene/vinylbenzyl chloride systems are reported in Figure 3.2, together with those of the HCL resins that will be discussed later in the text. The b\_DVB-VBC system did not show the presence of residual double bonds. Moreover, the typical absorption band of chloromethyl groups of the VBC unit were observed, centred at  $1265\text{ cm}^{-1}$ . The recorded spectrum was superposable with that collected on DVB-VBC, i.e. the corresponding material prepared by suspension polymerization, suggesting that the proposed bulk polymerization process did not affect the reaction mechanism and its extent. Similar results were observed for the divinylbenzene/styrene/vinylbenzyl chloride systems, with a complete overlapping of the ATR-FTIR spectra recorded for the sample prepared in bulk, b\_DVB-ST-VBC, with the similar material prepared by suspension polymerization.

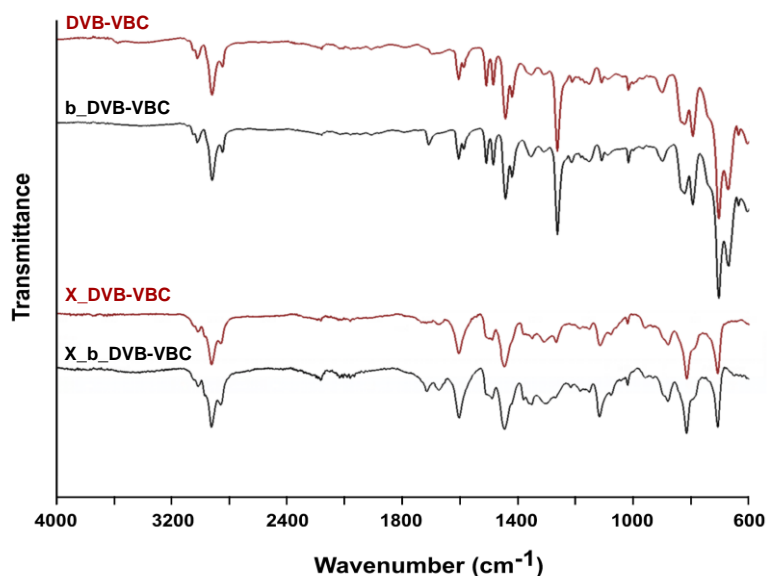


**Figure 3.2** ATR-FTIR spectra of the precursor resins DVB-VBC and b\_DVB-VBC, prepared respectively by suspension and bulk polymerization, and the corresponding hyper-crosslinked resins X\_DVB-VBC and X\_b\_DVB-VBC.

$^{13}\text{C}$  CP/MAS NMR analysis confirmed these results. Spectra of the precursor resins b\_DVB-VBC and DVB-VBC (Figure 3.3) showed the main signals of PVBC with no significant difference between the two different reaction methods. In the suspension-polymerized resin an additional peak at  $\approx 65\text{ppm}$  was observed, compatible with residual poly(vinyl alcohol) used as a surfactant during the reaction procedure that was not possible to remove through the repeated washing cycles due to its entrapping within the lightly cross-linked structure of the resin.

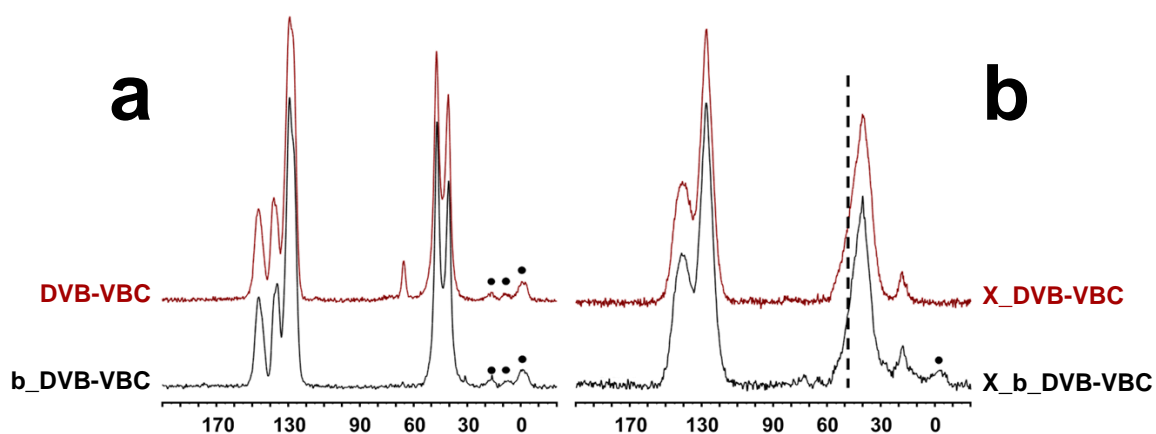


**Figure 3.3**  $^{13}\text{C}$  CP/MAS NMR spectra of the precursor resins DVB-VBC and b\_DVB-VBC (a) and the corresponding hyper-crosslinked resins (b). The position of the  $\text{CH}_2\text{Cl}$  resonance in (b) is indicated by a dashed line. Spinning sidebands in (a) and (b) are marked by dots.

The effect of the prepolymerization process on the final hyper-crosslinked materials was verified by means of ATR-FTIR, EDX and  $^{13}\text{C}$  CP/MAS NMR analysis. As showed in Figure 3.2 for the resins X\_b\_DVB-VBC and X\_DVB-VBC, the disappearance of the sharp absorption band centered at  $1265\text{ cm}^{-1}$  confirmed the occurrence of the hyper-crosslinking, with no significant differences with respect to the X\_DVB-VBC. A similar behaviour was also recorded for the divinylbenzene/styrene/vinylbenzyl chloride system, indicating that, for both compositions, the extent of hyper-crosslinking is not significantly affected by the nature of the prepolymerization step.

After hyper-crosslinking, bulk and suspension prepolymerized products also show very similar  $^{13}\text{C}$  CP/MAS NMR spectra, as shown in Figure 3.3b. The large conversion degree of the hyper-crosslinking reaction is confirmed by the nearly complete disappearance of the chloromethyl signal (47 ppm), though a more precise estimation is hindered by the complex shape of the broad aliphatic peak centered at 40 ppm.

EDX analysis allowed to obtain a quantitative evaluation of the residual amount of chlorine after hyper-crosslinking. For X\_b\_DVB-VBC, the final Cl/C ratio was found  $0.840 \pm 0.007\text{ mol}\%$ , whereas for X\_b\_DVB-ST-VBC it was found  $0.709 \pm 0.048\text{ mol}\%$ . Considering the initial Cl/C atomic ratio of the precursors, respectively 12.2 and 6.1 mol%, the yield of hyper-crosslinking was 93.1 % for the DVB/VBC system and 88.4 % for the DVB/ST/VBC system. This result is in agreement with that obtained on the suspension prepolymerized systems, for which a comparable lower yield of hyper-crosslinking was found for the material containing the styrene unit.

The microporous structure and the adsorption properties are major properties of the HCL resins.<sup>21,22</sup> On this basis, HCL resins prepared by bulk prepolymerization were also characterized by BET SSA and DFT analysis. Results are reported in Figure 3.4 and Table 3.2, together with those of the nanocomposites, that will be discussed later in the paper. As it can be observed in Figure 3.4, both HCL resins prepared from the bulk prepolymerized precursors, X\_b\_DVB-VBC and X\_b\_DVB-ST-VBC, showed a type II isotherm for nitrogen adsorption at 77 K, with a pronounced hysteresis during the desorption step due to the solubility of nitrogen in the material<sup>23</sup> and the presence of a mesoporous fraction.<sup>24</sup> Moreover, the HCL resins showed two different ranges of specific surface area. In particular, the BET surface area of the resin X\_DVB-VBC was  $1910\text{ m}^2/\text{g}$ , whereas that of the resin X\_DVB-ST-VBC was  $1055\text{ m}^2/\text{g}$ . The nitrogen adsorption behaviour and the BET surface area values were very similar to those observed for the HCL resins prepared through suspension prepolymerization followed by Friedel-Crafts hyper-crosslinking.<sup>19</sup> Additionally, it is to be noticed that for the system X\_b\_DVB-VBC the BET surface area and the total pore volume of the bulk prepolymerized HCL resin were even higher than those recorded for the suspension prepolymerized X\_DVB-VBC resin (BET SSA  $1715\text{ m}^2/\text{g}$ , total pore volume  $1.21\text{ cm}^3/\text{g}$ ). Also, room temperature  $\text{CO}_2$  uptake and liquid nitrogen temperature  $\text{H}_2$  uptake of the bulk prepolymerized resins were comparable or even higher than those previously reported for the corresponding suspension prepolymerized X\_DVB-VBC and X\_DVB-ST-VBC resins.

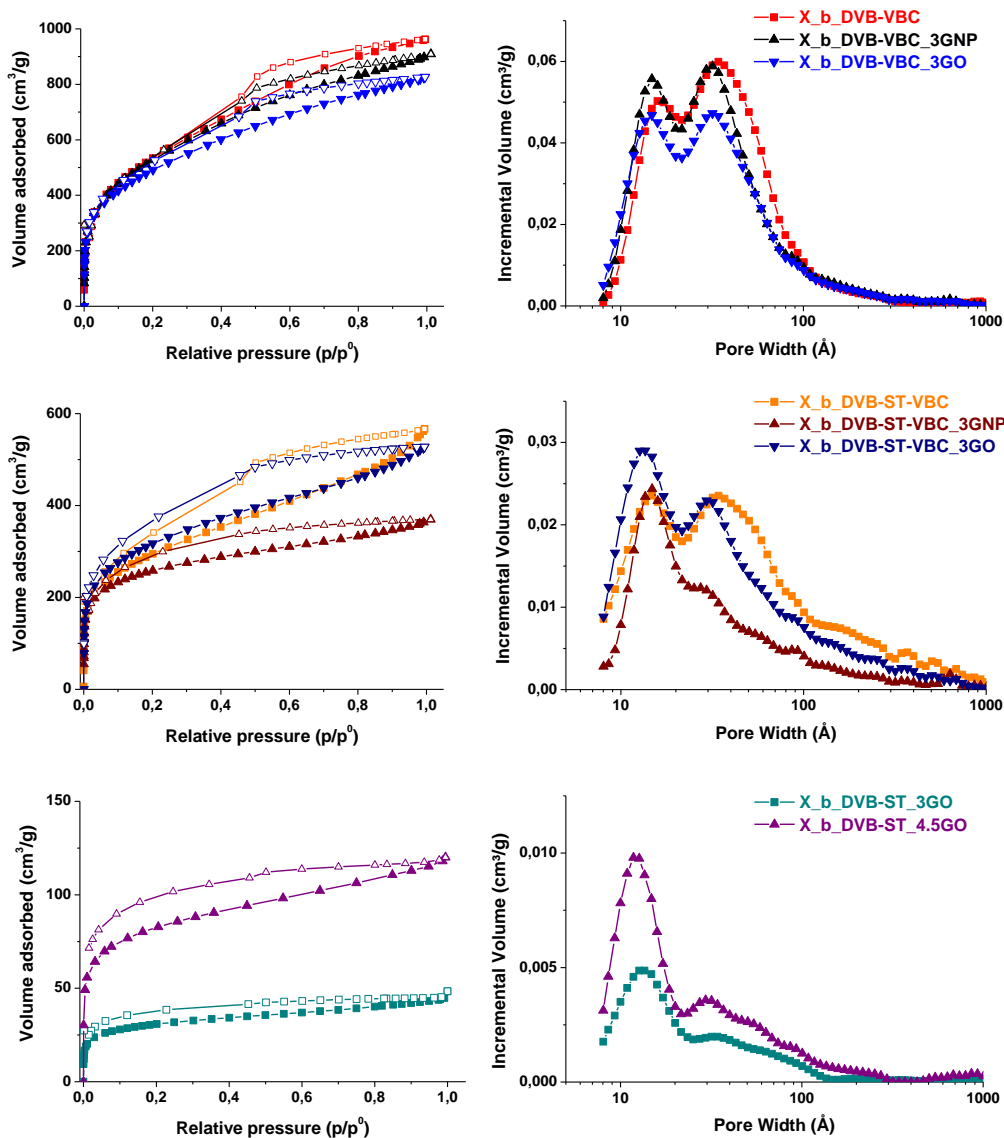


**Figure 3.4** Nitrogen adsorption (filled symbols) and desorption (empty symbols) isotherms at 77K (on the left) and DFT pore size distribution (on the right) of the HCL resins and nanocomposites prepared by bulk prepolymerization.

**Table 3.2** Results of SSA and pore size distribution analysis, CO<sub>2</sub> uptake, and H<sub>2</sub> uptake

sample	BET SSA (m <sup>2</sup> /g)	microporosity fraction (%)	total pore volume (cm <sup>3</sup> /g)	CO <sub>2</sub> uptake (wt%) <sup>a</sup>	H <sub>2</sub> uptake (wt. %) <sup>b</sup>
X_b_DVB-VBC	1910 ± 20	30	1.35	3.97	1.29
X_b_DVB-ST-VBC	1055 ± 10	33	0.79	2.62	0.75
X_b_DVB-VBC_3GNP	1880 ± 20	41	1.29	3.48	1.46
X_b_DVB-ST-VBC_3GNP	917 ± 8	56	0.49	2.63	0.98
X_b_DVB-VBC_3GO	1720 ± 20	37	1.13	4.03	1.33
X_b_DVB-ST-VBC_3GO	1132 ± 7	42	0.71	2.85	1.08
X_b_DVB-ST_3GO	170 ± 1	57	0.09	1.17	0.22
X_b_DVB-ST_4.5GO	295 ± 3	58	0.16	1.27	0.46

## **Microporous organic polymer nanocomposites (MOPNs)**

Combining porous resins and inorganic nanofillers, such as carbon based nanostructured materials, metal nanoparticles and metal oxide magnetic nanoparticles has been an intriguing research challenge in the last years. For instance, porous resins and carbon nanotubes<sup>25</sup> and HCL styrene based resins containing magnetic nanoparticles<sup>26</sup> were investigated for water remediation from antibacterial agents, while nanocomposites based on HCL styrene resins containing Pd nanoparticles were reported for applications in catalysis.<sup>27</sup> The investigated systems were prepared by impregnation of prepolymerized precursors or by complex procedures including a suspension prepolymerization step.

For the realization of porous nanocomposites, the effective dispersion of the nanofillers within the resin is not an easy task. Recently we demonstrated the uneven distribution of carbon nanotubes in HCL resins prepared by suspension polymerization, with selective localization of the nanofillers on the surface of precursor beads prepared by suspension prepolymerization<sup>19</sup> (Chapter 2 of this thesis). On the contrary, the here proposed bulk prepolymerization procedure allowed a facile embedding of carbon nanofillers within the precursor resin.

In particular, two different carbon nanofillers were selected for the realization of new MOPNs. In a first approach, plain graphite nanoplatelets (GNP) were dispersed in the monomers mixture by sonication and, after addition of the initiator, the precursor nano-composite was obtained by radical polymerization.

In a second approach, surface modified graphene oxide nanoplatelets were embedded in the precursor gel using the same procedure. In this case, a preliminary surface modification strategy was applied to GO, by grafting on the nanoplatelets surface a poly(vinylbenzyl chloride) (PVBC) layer. As already demonstrated for carbon nanotubes modified in the same way,<sup>19</sup> surface modified GO-PVBC is able to interact with the hosting resin during the synthesis of the precursor and to participate to the hyper-crosslinking reaction. Results of the characterization of the obtained GO-PVBC are reported in Figure S3.1 in Supplementary Information.

Applying this second approach, based on the embedding of a modified nanofiller coated with a polymer phase containing chloromethyl groups able to undergo Friedel-Crafts hyper-crosslinking, it was also possible to design and realize a new class of microporous nanocomposites. These nanocomposites were based on a styrene/divinylbenzene precursor, i.e. without the vinylbenzyl chloride monomer. In this new class of materials the micropores were generated during the hyper-crosslinking occurring at the interface between the modified nanoplatelets and the styrene based matrix, as schematized in Figure 3.5. To be noted, in this case, is the very low amount of halogenated monomer in the final composition. As the amount of the grafted PVBC phase onto GO was estimated by EDX about 9.63 wt% with respect to GO, in the nanocomposite precursor based on styrene/divinylbenzene containing 4.5 phr of GO-PVBC (b\_DVB-ST\_4.5GO) the final chlorine

amount was 0.10 wt%. This value is to be compared to the chlorine amounts of 22.8 wt% and 13.5 wt% in the b\_DVB-VBC and b\_DVB-ST-VBC, respectively.

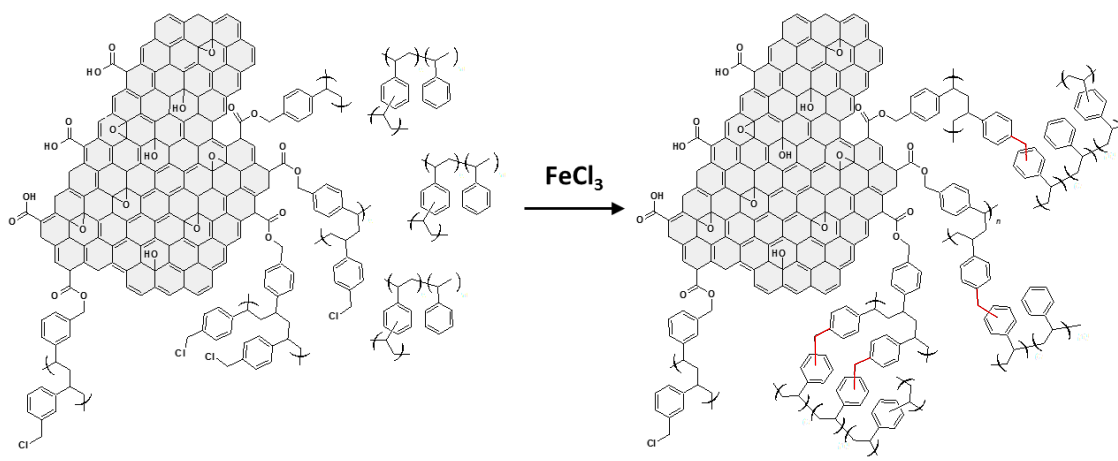


**Figure 3.5** Scheme of the hyper-crosslinking reaction at the interface between the chlorine-free precursor resin and the surface modified graphene oxide (GO-PVBC)

ATR-FTIR analysis carried out on the nanocomposite precursors (Figure 3.6a) indicated that the presence of the plain GNP and the modified GO do not affect the prepolymerization step. FTIR spectra of all the precursors did not show the presence of residual double bonds. Moreover, all the precursor nanocomposites containing the VBC monomer (b\_DVB-VBC\_3GNP, b\_DVB-ST-VBC\_3GNP, b\_DVB-VBC\_3GO and b\_DVB-ST-VBC\_3GO) showed the presence of the chloromethyl group at about  $1265\text{ cm}^{-1}$ , whose intensity was directly correlated to the relative amount of VBC, while this peak was not detectable in b\_DVB-ST\_3GO and b\_DVB-ST\_4.5GO.  $^{13}\text{C}$  CP/MAS NMR analysis confirmed that the presence of the nanofillers did not influence the final structure of the precursors in comparison to the neat resin, as showed in Figure S3.2 in Supplementary Information for nanocomposites precursors based on DVB/ST/VBC.

The effect of the presence of nanofillers GNP and GO-PVBC on the final hyper-crosslinked materials was also verified by means of ATR-FTIR. As showed in Figure 3.6b, for all the resins prepared from monomer mixtures containing the VBC monomer, the almost complete disappearance of the absorption band diagnostic for the chloromethyl group confirmed that the hyper-crosslinking was almost quantitative, comparable to that occurring on the neat resins.

As concerning the samples prepared by the styrene/divinylbenzene monomers, the sharp chloromethyl absorption, not present in the precursors, cannot be used to monitor the extent of the Friedel-Crafts hyper-crosslinking step. Nevertheless, a significant difference between FTIR spectra of hyper-crosslinked materials X\_b\_DVB-ST\_3GO and X\_b\_DVB-ST\_4.5GO and the corresponding precursors was the presence for the hyper-crosslinked nanocomposites of a new absorption band centred at about  $805\text{ cm}^{-1}$ . This band was attributed to the presence of disubstituted

aromatic groups, present only in small amount in the precursor due to the DVB monomer, thus confirming the occurrence of the hyper-crosslinking.

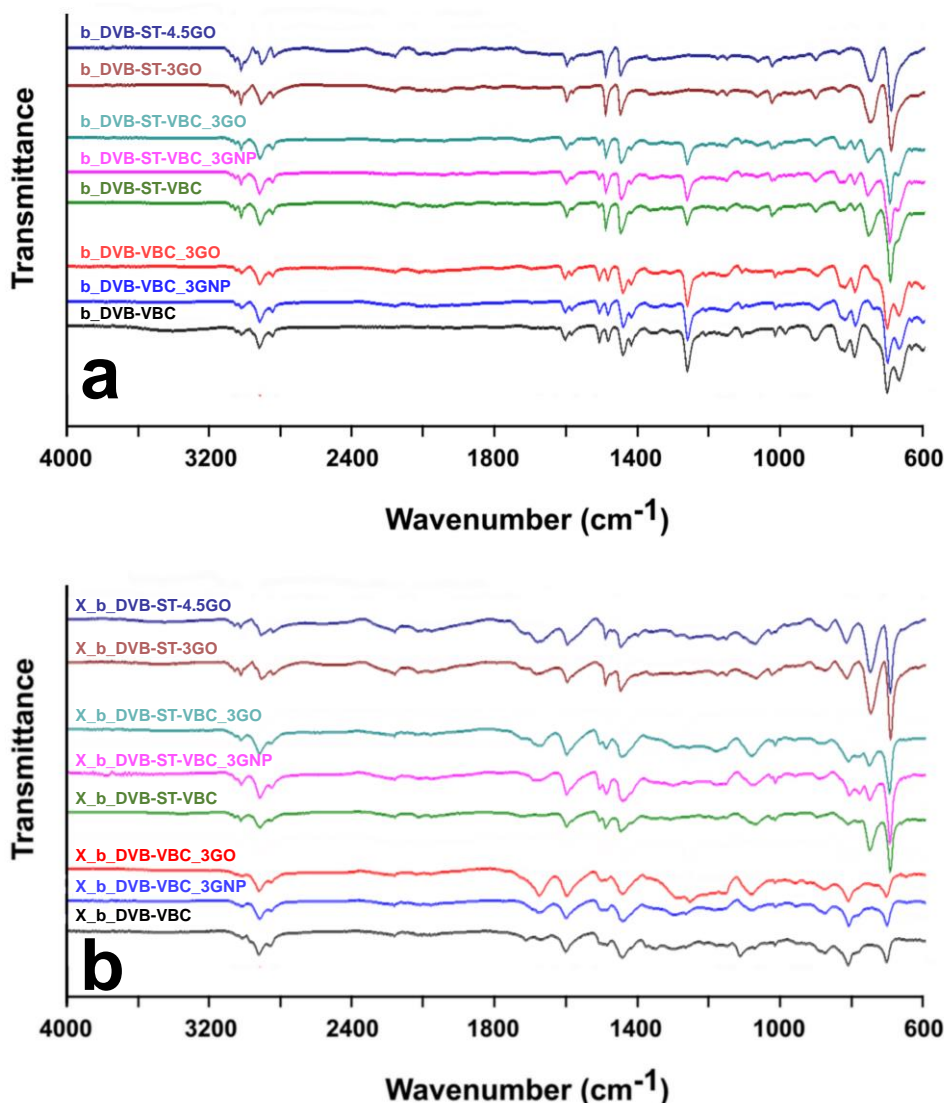


**Figure 3.6** ATR-FTIR spectra of the precursors resin and nanocomposites (a) and the corresponding hyper-crosslinked materials (b)

Moreover, it is also to be remarked the presence, in the spectra of the HCL nanocomposites, of a complex absorption band in the wavenumber range 1650-1780 cm<sup>-1</sup>. These band, often recorded in HCL resins, even those prepared by suspension prepolymerization,<sup>19</sup> has been well discussed by Tsyurupa et al.,<sup>28</sup> which attributed it to hindered vibrations of carbon-carbon bonds and valence angles in aromatic rings.

TEM and SEM analysis were used to evaluate the nanofillers dispersion within the precursor resins and the morphology of the HCL nanocomposites, as showed in Figure 3.7. As it can be observed, nanocomposite precursors containing GNP show a good distribution of the filler within the polymer matrix. GNP are mainly agglomerated in multilayers graphene stacks, with lateral dimensions

ranging between about 300 nm and few microns, corresponding to the original size of the commercial nanoplatelets used in this work. The distribution and the cluster size of GNP were very similar for both the investigated monomers ratios (DVB:VBC 2:98 and DVB:ST:VBC 2:49:49 by mole). Improved dispersion was obtained for the nanocomposites containing surface modified graphene oxide, due to the presence of the grafted PVBC phase on the GO surface, able to improve the matrix/filler compatibility. GO-PVBC was well distributed within all the three investigated polymer matrices, including, in this case, the chlorine-free matrix obtained from the monomers ratio DVB:ST 2:98 by mole. The presence and the good dispersion of the GO sheets in the HCL nanocomposite X\_b\_DVB-ST\_4.5GO is showed in SEM images reported in Figure 3.7. At higher magnifications (Figure 3.7h), the presence of aligned GO sheets was observed, well embedded within the HCL matrix, and pores with average size lower that 80 nm were also evidenced at the interface between modified GO nanoplatelets and the DVB-ST resin.

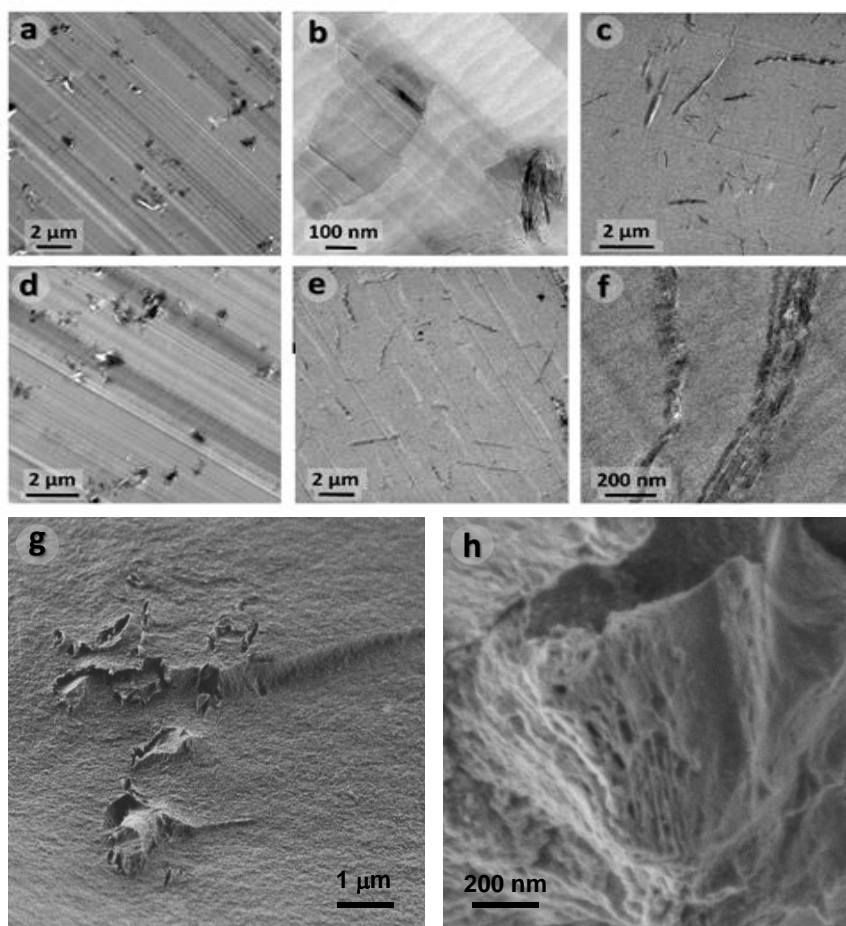


**Figure 3.7** Results of TEM and SEM analysis of precursor and HCL nanocomposites. TEM micrographs of the precursor nanocomposites: (a,b) b\_DVB-VBC\_3GNP; (c) b\_DVB-VBC\_3GO; (d) b\_DVB-ST-VBC\_3GNP; (e,f) b\_DVB-ST-VBC\_3GO; (g,h) SEM micrographs of X\_b\_DVB-ST\_4.5GO

Gas adsorption properties of HCL nanocomposites are reported in Table 3.2, together with those of the neat HCL matrices. For the system DVB/ST the comparison with the neat matrix was not possible, as the precursor resin b\_DVB-ST, that does not contain chloromethyl groups, cannot be hyper-crosslinked by Friedel-Crafts reaction. Considering the DVB/VBC system, by adding GNP the BET SSA remained almost unchanged with respect to the neat matrix, whereas an increase of the microporosity fraction and a corresponding increase of the H<sub>2</sub> absorption was recorded. A similar increase of the microporosity fraction was also obtained in presence of 3 phr of GO-PVBC nanofiller, but in this case the effect on the H<sub>2</sub> and CO<sub>2</sub> adsorption properties was negligible.

Worth of note, instead, was the change in the pore size distribution obtained for the DVB/ST/VBC system by addition of either GNP either GO-PVBC. As also clear from Figure 3.4 (right column, central panel), the pore size distribution curves of the nanocomposite samples tended toward a unimodal distribution, more accentuated for X\_b\_DVB-ST-VBC\_3GNP, for which also an evident change in the shape of the nitrogen isotherm was registered. Most part of the gas adsorption was accomplished at low pressure, and this result corresponded to an increase of the microporosity fraction up to 56%. The sample X\_b\_DVB-ST-VBC\_3GO, instead, showed lower microporosity than the one containing GNP, but higher total porosity and SSA. The microporous fraction played a key role in hydrogen adsorption,<sup>29</sup> resulting in a significant increase of the total amount of H<sub>2</sub> adsorbed. The improvements obtained for the HCL DVB/ST/VBC nanocomposites containing GNP and GO, with respect to the neat HCL resin were about 31 and 44 %, respectively.

Moreover, very interesting was the effect of the addition of GO-PVBC to the chlorine-free DVB/ST matrix. Increasing the nanofiller loading up to 4.5 wt%, a progressive increase of the BET SSA was recorded, up to 295 m<sup>2</sup>/g. Higher GO-PVBC loadings, instead, induced significant nanofiller agglomeration phenomena, responsible for a decrease of the adsorption properties of the HCL nanocomposites with respect to the X\_b\_DVB-ST\_4.5GO system. The high surface area values recorded for the systems X\_b\_DVB-ST\_3GO and X\_b\_DVB-ST\_4.5GO were the ultimate confirmation that the PVBC phase grafted on the GO surface was not only able to improve the dispersibility of the filler within the resin, but was also able to react with the styrene matrix. In fact, as already discussed and schematized in Figure 3.5, for this class of materials the hyper-crosslinking can only occur between the chloromethyl groups of the PVBC layer grafted onto the GO nanoplatelets and the embedding styrene polymer, generating a new kind of interfacial microporosity. Indeed, intra-hyper-crosslinking of the PVBC phase cannot be excluded. Nevertheless, this mechanism is not able to explain the high surface area values since the low amount of modified nanofiller would not be able to generate a significant microporosity within the nanocomposite. Besides, due to reduced mobility of the grafted PVBC phase, the extent of intra-PVBC-hyper-crosslinking can be considered very low with respect to the hyper-crosslinking occurring at the matrix/filler interphase.

As concerning the pore textural analysis, an almost unimodal pore size distribution was recorded for the HCL DVB/ST nanocomposites, with microporosity fraction of 57 - 58 % irrespectively on the nanofiller content. This result is consistent with those obtained on nanocomposite materials prepared using different monomer compositions. Gas adsorption properties were also very significant for the X\_b\_DVB-ST\_4.5GO sample, with total room temperature CO<sub>2</sub> uptake of 1.27 wt% and liquid nitrogen temperature H<sub>2</sub> uptake of 0.46 wt%. These results can be considered extraordinary if one compares the adsorption properties of these HCL materials with their very low chlorine content, close to 0.10 wt%.

Apart from gas adsorption, water remediation is one of the key applications foreseen for HCL resins,<sup>30,31,32</sup> and interesting research works are focused on the evaluation of these systems as adsorbent agents by analysis of their phenol adsorption capacity from water solutions.<sup>33,34</sup> Phenol adsorption of HCL resins is affected by different factors, such as their SSA, pore textural properties, and affinity between the resin and the adsorbate.<sup>35</sup> On this basis, the new MOPNs were also characterized by phenol adsorption tests from water solution in comparison with the corresponding plain HCL resins. Results are reported in Table 3.3, and they include tests performed using mixed matrix membranes that will be discussed in the next section.

As already reported for analogous systems prepared by suspension prepolymerization followed by Friedel-Crafts hyper-crosslinking,<sup>19</sup> higher amount of chloromethyl groups in the precursor resins induced higher phenol adsorption capacity. As concerning the effect of the nanofillers, for the DVB/VBC system no differences were recorded in the phenol uptake of nanocomposites containing GNP or GO-PVBC with respect to the corresponding HCL resin X\_b\_DVB-VBC. On the contrary, either GNP either GO-PVBC induced an improvement of the phenol uptake in the DVB-ST-VBC system. This effect can be correlated to the increased microporosity recorded for the HCL nanocomposites with respect to the X\_b\_DVB-ST-VBC resin and to the presence of the graphene nanofillers, characterized by a high affinity towards the adsorbate.<sup>36</sup>

Finally, the nanocomposite systems prepared starting from the DVB-ST monomer mixture showed very interesting phenol uptake, with a maximum equilibrium adsorption capacity  $q_e$  of 1.16 mmol/g for the X\_b\_DVB-ST\_4.5GO system, to be compared with a negligible  $q_e$  for the corresponding neat precursor resin. Evaluating the  $q_e$  value registered for the MOPN containing 4.5 phr of GO in comparison to its overall surface area and pore texture properties, the recorded outstanding equilibrium adsorption capacity cannot be explained only on the basis of the high microporosity fraction of the HCL nanocomposite, and the preferential affinity of the adsorbate with the graphene nanofiller must be also taken into account. This confirms that the use of functional nanofillers for the realization of new microporous organic polymer nanocomposites is a promising strategy for the realization of an advanced class of materials with tailored adsorption properties.

**Table 3.3** Results of phenol adsorption tests from water solutions performed on HCL resins and nanocomposites and on mixed matrix membranes

	<b>Sample</b>	<b>Phenol adsorption (<math>q_e</math>, mmol/g)</b>
Resins	X_b_DVB-VBC	$2.37 \pm 0.01$
	X_b_DVB-ST-VBC	$1.99 \pm 0.06$
MOPNs	X_b_DVB-VBC_3GNP	$2.39 \pm 0.03$
	X_b_DVB-ST-VBC_3GNP	$2.16 \pm 0.22$
	X_b_DVB-VBC_3GO	$2.38 \pm 0.09$
	X_b_DVB-ST-VBC_3GO	$2.14 \pm 0.23$
	X_b_DVB-ST_3GO	$0.62 \pm 0.11$
	X_b_DVB-ST_4.5GO	$1.16 \pm 0.07$
	Membranes	PSF
PSF_20X		$0.57 \pm 0.01$
PSF_20XGO		$0.42 \pm 0.01$

### Polysulfone membranes

The embedding of porous nanostructured fillers in a continuous polymer phase is a successful strategy for the realization of engineered systems with applications in the environmental and energy fields. Recently, this approach has been successfully exploited by the realization, for instance, of mixed matrix membranes (MMMs) for water purification (ultrafiltration, reverse osmosis, nanofiltration)<sup>37</sup> and for liquid-liquid and gas separations,<sup>38,39</sup> with improved performances in terms of efficiency and antifouling properties. MMMs are obtained by the dispersion and the embedding of a microporous phase in a continuous polymer phase, and their final performances derive from the synergistic combination of the properties of their constituting materials.<sup>40</sup> Different fillers have been effectively tested for the realization of MMMs, such as inorganic nanostructured materials,<sup>41</sup> organic, including bioderived, materials, and polymer based hybrid materials. Among organic filler-based membranes, cyclodextrin, polypyrrole, polyaniline, chitosan beads and semi-interpenetrating network polymeric nanoparticles have been tested as active agents in polymer membranes obtained by blending and phase inversion.<sup>42,43,44,45,46</sup> As concerning the polymer matrix, polysulfone (PSF) has been widely used due to its mechanical strength, thermo-stability, stability against chemicals and relative hydrophobicity.<sup>47,48,49</sup>

On these bases, the last part of this work was finalized to demonstrate the possibility of embedding microporous hyper-crosslinked resins and nanocomposites in a PSF membrane for possible water remediation applications.

Morphological analysis carried out on HCL resins and nanocomposites prepared by bulk prepolymerization followed by Friedel-Crafts hyper-crosslinking (see Figure 3.8) revealed that the final HCL materials have irregular particle shape with dimensions ranging from 5 to 200  $\mu\text{m}$ , the nanocomposite HCL particles showing a relatively slightly lower size. To be remarked is that this particle size was comparable to the particle size obtained by the hyper-crosslinking of gel-type precursor resins prepared by suspension polymerization (see Figure S3.3 in Supplementary Information). In fact, for these latter, the original spherical shape of gel-type particles is completely disrupted during the hyper-crosslinking step, giving rise to particles with irregular morphology and size.

In order to meet the requirements for their embedding in PSF membranes, a ball-milling treatment was performed on the X\_b\_DVB-VBC and X\_b\_DVB-ST\_4.5GO samples. The obtained materials, whose representative SEM micrographs are reported in Figure 3.8, showed particle size in the range from about 50 nm to about 10  $\mu\text{m}$ , compatible for the final application in PSF membranes with approximate thickness of 200  $\mu\text{m}$ .

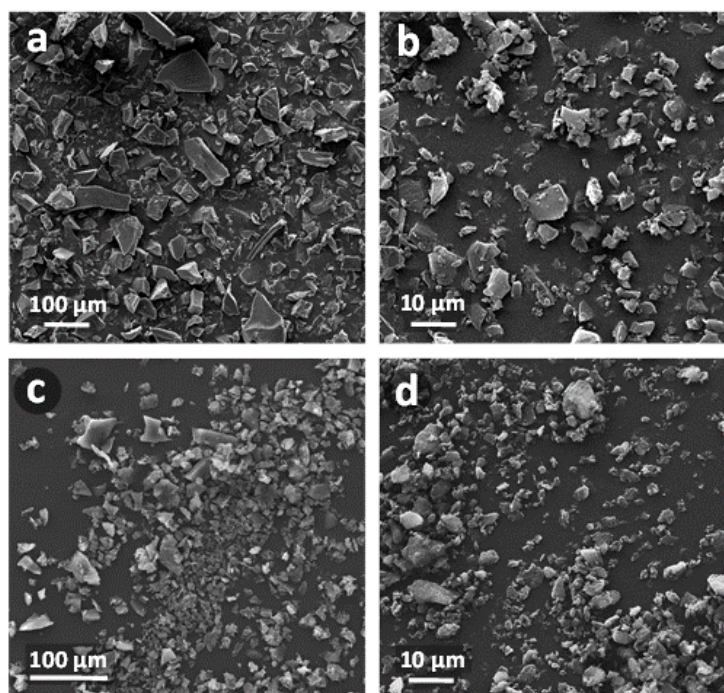


**Figure 3.8** SEM micrographs of: (a) X\_b\_DVB-VBC; (b) X\_b\_DVB-VBC\_BM; (c) X\_b\_DVB-ST\_4.5GO; (d) X\_b\_DVB-ST\_4.5GO\_BM

Analogously to plain HCL resins, ball-milled samples X\_b\_DVB-VBC\_BM and X\_b\_DVB-ST\_4.5GO\_BM were characterized by nitrogen adsorption tests and their pore size distribution was calculated applying the NLDFT. Results are reported in Figure S3.4 in Supplementary Information. After ball-milling, the HCL resins and nanocomposites still showed a type II isotherm, with a

pronounced hysteresis during the desorption step. For both samples, ball-milling induced a decrease of the BET surface area, with final BET SSA values of 1600 m<sup>2</sup>/g for X\_b\_DVB-VBC\_BM and 186 m<sup>2</sup>/g for X\_b\_DVB-ST\_4.5GO\_BM, to be compared to the BET SSA recorded for the corresponding plain HCL materials of 1910 m<sup>2</sup>/g and 295 m<sup>2</sup>/g, respectively. Moreover, a negligible effect of the ball-milling was found on the microporosity fraction and on the average pore size.

The BET SSA reduction was somehow expected as a possible drawback of the mechanical treatment. In fact, a decrease of the surface area after ball-milling was previously obtained on inorganic materials, such as  $\gamma$ -alumina,<sup>50</sup> explained in this case by the change of the crystal structure promoted by the treatment, and change of the crystal structure was already described also for organic materials.<sup>51</sup> Nevertheless, for HCL resins, the decrease of BET SSA associated with the ball-milling can be better explained considering that the size reduction may induce the exposure of part of the volume of the pores originally located in the inner part of bigger particles to the surface of the obtained smaller particles, thus destroying them. This phenomenon can reduce the overall porosity of the material. Nevertheless, the resulting BET SSA and overall adsorption properties of the ball-milled HCL resin X\_b\_DVB-VBC\_BM and HCL nanocomposite X\_b\_DVB-ST\_4.5GO\_BM are still high enough for possible applications as active fillers in PSF membranes.

The obtained membranes, containing 20 wt% of the HCL resin X\_b\_DVB-VBC\_BM and nanocomposite X\_b\_DVB-ST\_4.5GO\_BM, were prepared by phase inversion. Plain PSF membranes were prepared by comparison using the same method. SEM micrographs of their surfaces and cross sections are reported in Figure 3.9. All the membranes showed similar asymmetric morphology, with a more dense upper skin and a porous sublayer.<sup>52</sup> The upper level showed the presence of nanosized pores, with average dimensions ranging between 10-100 nm. The membrane sections were characterized by large drop-like pores distributed in a sponge-like structure consisting of smaller, interconnected pores with dimensions 0.5-4  $\mu$ m. This interconnected porosity reached the lower surfaces that showed the presence of larger pores, with homogeneous dimensions, significantly larger than the ones revealed on the upper surfaces. Minor differences between the structure of the plain PSF membranes and the membranes containing the HCL fillers can be attributed to changes of the diffusion rate of the solvent and the non-solvent, very small even at the very high loading level investigated.

As concerning the fillers in the PSF\_20X and PSF\_20X\_GO membranes, hyper-crosslinked particles are well embedded in the pores of the membranes, as it was shown in Figure 3.9(g,k), and some particles are also embedded within the external layers, as shown in Figure 3.9(h,l).

Phenol adsorption tests were finally carried out on the plain and composite membranes. Results are reported in Table 3.3. As shown, the plain PSF membrane showed a significant phenol uptake, with an equilibrium adsorption capacity  $q_e$  of 0.34 mmol/g. By addition of the HCL DVB/VBC particles, the phenol uptake reached  $q_e = 0.57$  mmol/g, with a relevant improvement of the 68 % with respect

to the plain PSF membrane. Also for the membrane containing the nanocomposite GO-based filler, PSF\_20X\_GO, an improvement of about 24 % was recorded, that is to be considered outstanding taking into account its very low chlorine content and the consequent lower BET SSA.

Even if flow test measurements will be needed to confirm the efficiency of these new composite membranes, the obtained results were very promising for their application as effective systems for organic pollutants rejection from water.

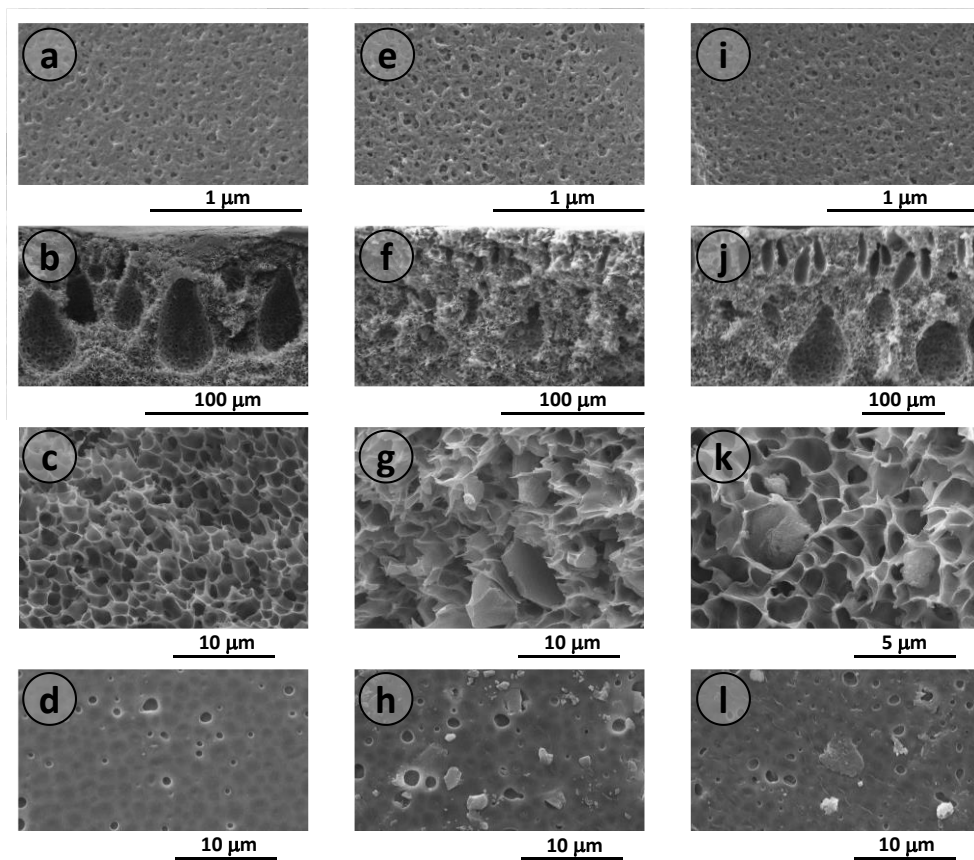


**Figure 3.9** SEM micrographs of: (a,b,c,d) PSF membrane; (e,f,g,h) PSF\_20X membrane; (i,j,k,l) PSF\_20XGO membrane. First line: upper surfaces; second and third lines: membranes cross-sections; fourth line: lower surfaces

## Conclusions

In this work, we reported the results obtained by using a new synthetic approach for the realization of hyper-crosslinked Davankov-type styrene based resin, based on the bulk polymerization of a gel-type precursor followed by a traditional Friedel-Crafts alkylation step. The new synthetic protocol was applied for the realization of high SSA divinylbenzene/vinylbenzyl chloride based resins and on divinylbenzene/styrene/vinylbenzyl chloride resins, these latter characterized by a relative lower content of the halogenated monomer vinylbenzyl chloride. The characterization of the realized materials showed that the proposed process did not influence the mechanism of the reaction, the structure of the intermediate gel-type resins and the structure and the adsorption properties of the final hyper-crosslinked materials.

Furthermore, new relevant application possibilities offered by this new synthetic protocol were demonstrated through the realization of two innovative classes of materials.

First, by applying the bulk prepolymerization method, new hyper-crosslinked microporous organic polymer nanocomposites (MOPNs) were prepared, in which GNP and surface modified GO nanofillers were effectively embedded in the polymer phase. Using surface modified GO, i.e. GO nanoplatelets grafted with a polymer phase able to participate to the hyper-crosslinking step through its chloromethyl groups, microporous nanocomposites based on a styrene/divinylbenzene precursor, i.e. without the chlorinated monomer, were also realized. Their microporosity was only generated during the hyper-crosslinking occurring at the interface between the modified GO nanoplatelets and the styrene based matrix. Despite to their reduced specific surface area with respect to traditional Davankov-type resins, these new MOPNs showed excellent gas adsorption properties and phenol uptake from water solutions.

Second, new polymer mixed matrix membranes based on polysulfone and containing hyper-crosslinked fillers were prepared, in which the microporous resin and nanocomposite particles were effectively embedded within the sponge-like structure of the membranes. Results obtained by phenol adsorption tests from water solutions demonstrated that the addition of the functional microporous fillers within the polysulfone phase was able to induce significant improvements of the equilibrium adsorption capacity, up to 67%.

Either the realization of new MOPNs either the embedding of the functional fillers in composite membranes, demonstrated, in our opinion, the versatility of the bulk prepolymerization synthesis. The obtained results can pave the way to a wider and more effective application of Davankov-type hyper-crosslinked resins for gas separation and storage and for water remediation.

## Supplementary information

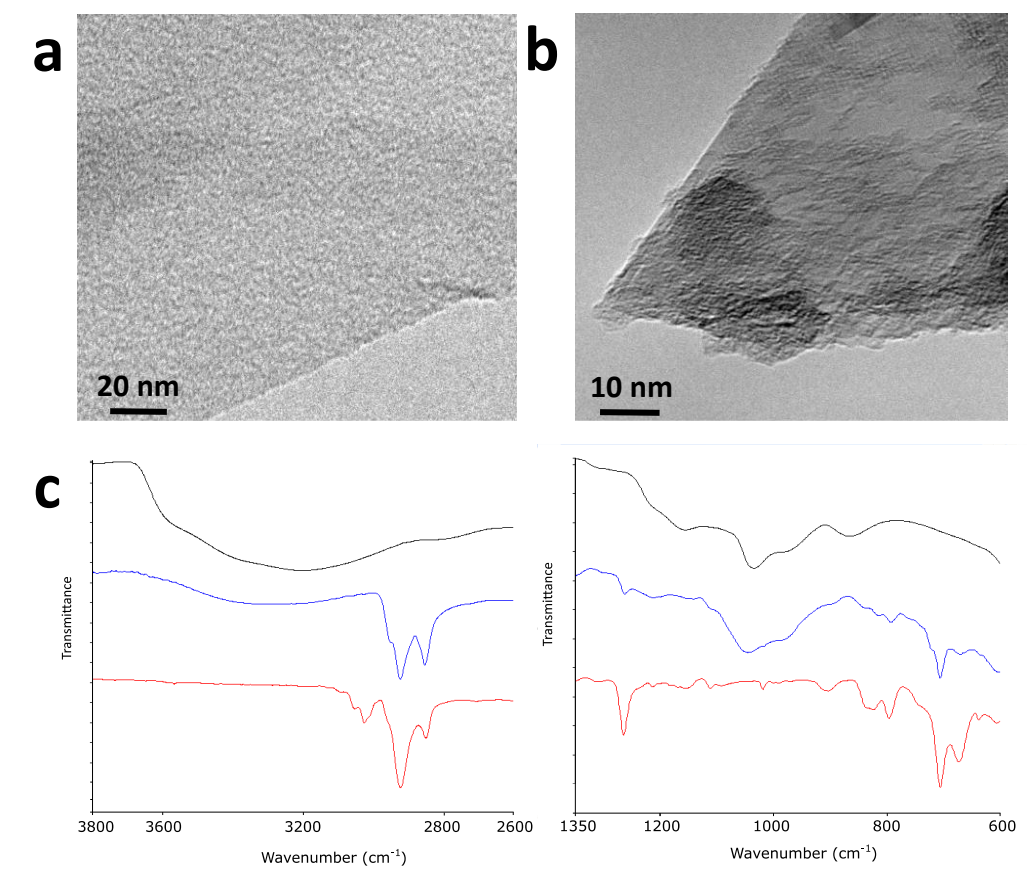


**Figure S3.1** a, b) TEM micrographs of GO, GO-PVBC; c) FTIR spectra of GO (black curve), GO-PVBC( blue curve) and PVBC (red curve)

EDX analysis was performed to estimate the amount of resin grafted to the graphene sheets.

Element	C	O	Cl
Weight %	66.11 ± 1.15	31.21 ± 0.77	2.68 ± 0.18

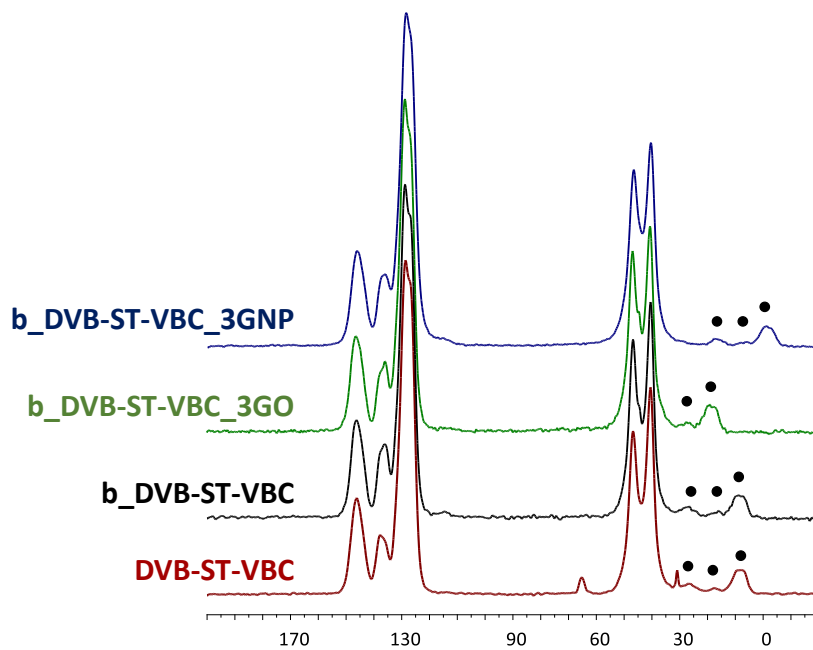


**Figure S3.2**  $^{13}\text{C}$  NMR spectra of the DVB/ST/VBC precursors (spinning sidebands are marked by a dot)

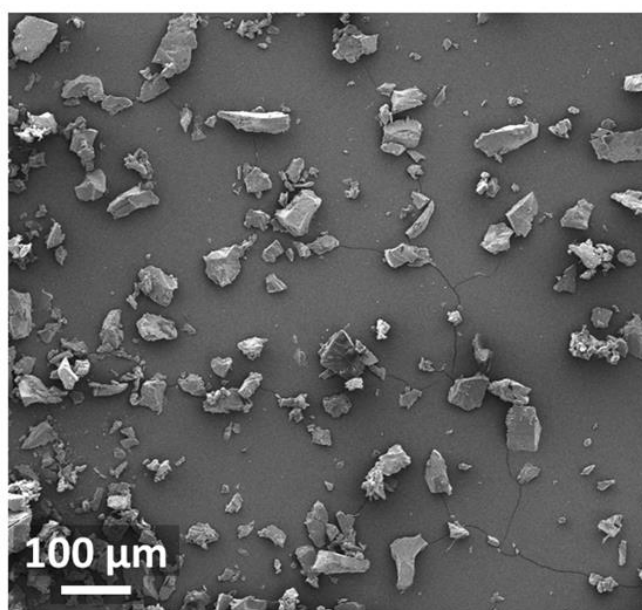


**Figure S3.3** SEM image of the X\_DVB-VBC resin as obtained by suspension prepolymerization followed by the hyper-crosslinking step

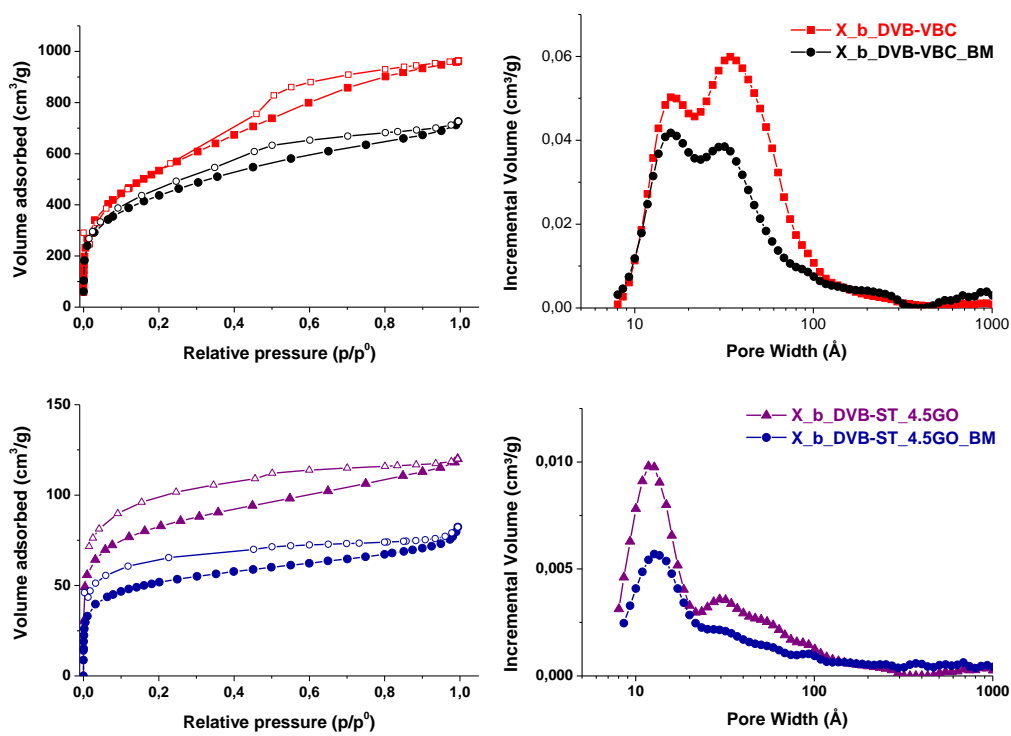


**Figure S3.4** Nitrogen adsorption (filled symbols) and desorption (empty symbols) isotherms at 77K (on the left) and DFT pore size distribution (on the right) of the plain and ball-milled HCL resins and nanocomposites

## References

- <sup>1</sup> A. Li, Q. Zhang, G. Zhang, J. Chen, Z. Fei and F. Liu, *Chemosphere*, 2002, **47**, 981.
- <sup>2</sup> N. B. McKeown and P. M. Budd, *Chem. Soc. Rev.*, 2006, **35**, 675.
- <sup>3</sup> A. K. Sekizkardes, J. T. Culp, T. Islamoglu, A. Marti, D. Hopkinson, C. Myers, H. M. El-Kaderi and H. B. Nulwala, *Chem. Commun.*, 2015, **51**, 13393.
- <sup>4</sup> R. T. Woodward, L. A. Stevens, R. Dawson, M. Vijayaraghavan, T. Hasell, I. P. Silverwood, A. V. Ewing, T. Ratvijitvech, J. D. Exley, S. Y. Chong, F. Blanc, D. J. Adams, S. G. Kazarian, C. E. Snape, T. C. Drage and A.I. Cooper, *J. Am. Chem. Soc.*, 2014, **136**, 9028.
- <sup>5</sup> R. Dawson, A. I. Cooper and D. J. Adams, *Polym. Int.*, 2013, **62**, 345.
- <sup>6</sup> R. Dawson, L. A. Stevens, T. C. Drage, C. E. Snape, M. W. Smith, D. J. Adams and A. I. Cooper, *J. Am. Chem. Soc.*, 2012, **134**, 10741.
- <sup>7</sup> J. Germain, F. Svec and J. M. J. Fréchet, *Chem. Mater.*, 2008, **20**, 7069.
- <sup>8</sup> M. P. Tsyurupa and V. A. Davankov, *React. Funct. Polym.*, 2006, **66**, 768
- <sup>9</sup> N. Fontanals, J. Cortés, M. Galià, R. M. Marcé, P. A. G. Cormack, F. Borrull and D. C. Sherrington, *J. Polym. Sci. Part A Polym. Chem.*, 2005, **43**, 1718.
- <sup>10</sup> N. Fontanals, R. M. Marcé, F. Borrull and P. A. G. Cormack, *Polym. Chem.*, 2015, **6**, 7231
- <sup>11</sup> F. S. Macintyre, D. C. Sherrington, L. Tetley, *Macromolecules*, 2006, **39**, 5381
- <sup>12</sup> B. Li, X. Huang, L. Liang and B. Tan, *J. Mater. Chem.*, 2010, **20**, 7444.
- <sup>13</sup> G. Li, B. Zhang, J. Yan and Z. Wang, *Chem. Commun.*, 2014, **50**, 1897.
- <sup>14</sup> C. Shen, J. Yan, G. Deng, B. Zhang and Z. Wang, *Polym. Chem.*, 2017, **8**, 1074.
- <sup>15</sup> Z. Guan, B. Li, G. Hai, X. Yang, T. Li and B. Tan, *RSC Adv.*, 2014, **4**, 36437.
- <sup>16</sup> B. Li, Z. Guan, W. Wang, X. Yang, J. Hu, B. Tan and T. Li, *Adv. Mater.*, 2012, **24**, 3390.
- <sup>17</sup> H. Gao, L. Ding, W. Li, G. Ma, H. Bai and L. Li, *ACS Macro Lett.*, 2016, **5**, 377–381
- <sup>18</sup> H. Gao, L. Ding, H. Bai and L. Li, *Chem. Sus. Chem.*, 2017, **3**, 618.
- <sup>19</sup> R. Castaldo, R. Avolio, M. Cocca, G. Gentile, M. E. Errico, M. Avella, C. Carfagna and V. Ambrogi, *RSC Adv.*, 2017, **7**, 6865.
- <sup>20</sup> J.-H. Ahn, J.-E. Jang, C.-G. Oh, S.-K. Ihm, J. Cortez and D.C. Sherrington, *Macromolecules*, 2006, **39**, 627.
- <sup>21</sup> J. Germain, J. Hradil, J. M. J. Frechet and F. Svec, *Chem. Mater.*, 2006, **18**, 4430.
- <sup>22</sup> S. Shen, X. Zhang and L. Fan, *Mater. Lett.*, 2008, **62**, 2392.
- <sup>23</sup> V. V. Azanova and J. Hradil, *React. Funct. Polym.*, 1999, **41**, 163.
- <sup>24</sup> M. Thommes, K. Kaneko, A. V. Neimark, J. P. Olivier, F. Rodriguez-Reinoso, J. Rouquerol and K. S. W. Sing, *Pure Appl. Chem.*, 2015, **87**, 1051
- <sup>25</sup> W. Yang, Y. Lu, F. Zheng, X. Xue, N. Li and D. Liu, *Chem. Eng. J.*, 2012, **179**, 112.

- <sup>26</sup> V. V. Tolmacheva, V. V. Apyari, B. N. Ibragimova, E. V. Kochuk, S. G. Dmitrienko and Yu. A. Zolotov, *J. Anal. Chem.*, 2015, **70**, 1313.
- <sup>27</sup> K. Jeřábek, M. Zecca, P. Centomo, F. Marchionda, L. Peruzzo, P. Canton, E. Negro, V. Di Noto and B. Corain, *Chem. Eur. J.*, 2013, **19**, 9381.
- <sup>28</sup> M. P. Tsyurupa, Z. K. Blinnikova, Y. A. Davidovich, S. E. Lyubimov, A. V. Naumkin and V. A. Davankov, *React. Funct. Polym.*, 2012, **72**, 973.
- <sup>29</sup> M. Armandi, B. Bonelli, C. Otero Arean and E. Garrone, *Micropor. Mesopor. Mater.*, 2008, **112**, 411.
- <sup>30</sup> Z. Xu, Q. Zhang and H. H. P. Fang, *Crit. Rev. Environ. Sci. Technol.*, 2003, **33**, 363.
- <sup>31</sup> B. Pan, B. Pan, W. Zhang, L. Lv, Q. Zhang and S. Zheng, *Chem. Eng. J.*, 2009, **151**, 19.
- <sup>32</sup> I. Y. İpek, N. Kabay, M. Yüksel, D. Yapıcı and Ü. Yüksel, *Desalination*, 2012, **306**, 24.
- <sup>33</sup> J. Huang, X. Jin and S. Deng, *Chem. Eng. J.*, 2012, **192**, 72.
- <sup>34</sup> X. Zhang, A. Li, Z. Jiang and Q. Zhang, *J. Hazard. Mater.*, 2006, **137**, 1115.
- <sup>35</sup> K. Yang and B. Xing, *Chem. Rev.*, 2010, **110**, 5989.
- <sup>36</sup> Y. Li, Q. Du, T. Liu, J. Sun, Y. Jiao, Y. Xia, L. Xia, Z. Wang, W. Zhang, K. Wang, H. Zhu and D. Wu., *Mater. Res. Bull.*, 2012, **47**, 1898.
- <sup>37</sup> N. Mehwish, A. Kausar and M. Siddiq, *Polym. Plast. Technol. Eng.*, 2014, **53**, 1290.
- <sup>38</sup> A. Khazaei, V. Mohebbi, R. M. Behbahani and S. A. Ahmad Ramazani, *Polym. Plast. Technol. Eng.*, 2017, in press, DOI: 10.1080.03602559.2016.1275682.
- <sup>39</sup> Z. Qiao, S. Zhao, J. Wang, S. Wang, Z. Wang and M. D. Guiver, *Angew. Chem. Int. Ed.*, 2016, **55**, 9321.
- <sup>40</sup> D. Qadir, H. Mukhtar and L. K. Keong, *Sep. Purif. Rev.*, 2017, **46**, 62.
- <sup>41</sup> P. S. Goh, B. C. Ng, W. J. Lau and A. F. Ismail, *Sep. Purif. Rev.*, 2015, **44**, 216.
- <sup>42</sup> F. V. Adams, E. N. Nxumalo, R. W. Krause, E. M. Hoek and B. B. Mamba, *J. Membrane Sci.*, 2012, **405**, 291.
- <sup>43</sup> F. V. Adams, E. N. Nxumalo, R. W. Krause, E. M. Hoek and B. B. Mamba, *Phys. Chem. Earth A/B/C*, 2014, **67**, 71.
- <sup>44</sup> Z. Fan, Z. Wang, N. Sun, J. Wang, and S. Wang, *J. Membr. Sci.*, 2008, **320**, 363.
- <sup>45</sup> K. K. Tetala and D. F. Stamatialis, *Sep. Purif. Tech.*, 2013, **104**, 214.
- <sup>46</sup> W. Zhao, J. Huang, B. Fang, S. Nie, N. Yi, B. Su, H. Li and C. Zhao, *J. Membr. Sci.*, 2011, **369**, 258.
- <sup>47</sup> B. M. Ganesh, A. M. Isloor and A. F. Ismail, *Desalination*, 2013, **313**, 199.
- <sup>48</sup> N. N. R. Ahmad, C. P. Leo, A. W. Mohammad and A. L. Ahmad, *Micropor. Mesopor. Mater.*, 2016, in press, DOI: 10.1016/j.micromeso.2016.10.001
- <sup>49</sup> M. Wang, L. G. Wu, J. X. Mo and C.-J. Gao, *J. Membr. Sci.*, 2006, **274**, 200.
- <sup>50</sup> S. R. Chauruka, A. Hassanpour, R. Brydson, K. J. Roberts, M. Ghadiri and H. Stitt, *Chem. Eng. Sci.*, 2015, **134**, 774.

- <sup>51</sup> R. Avolio, I. Bonadies, D. Capitani, M. E. Errico, G. Gentile and M. Avella, *Carbohydr. Polym.*, 2012, **87**, 265.
- <sup>52</sup> R. Rezaee, S. Nasser, A. H. Mahvi, R. Nabizadeh, S. A. Mousavi, A. Rashidi, A. Jafari, S. Nazmara, *J. Environ. Health Sci. Eng.*, 2015, **13**, 61.

# Chapter 4

## Chitosan hydrogels containing hyper-crosslinked resins as new broad-spectrum adsorbents for efficient water purification

### Authors and affiliations

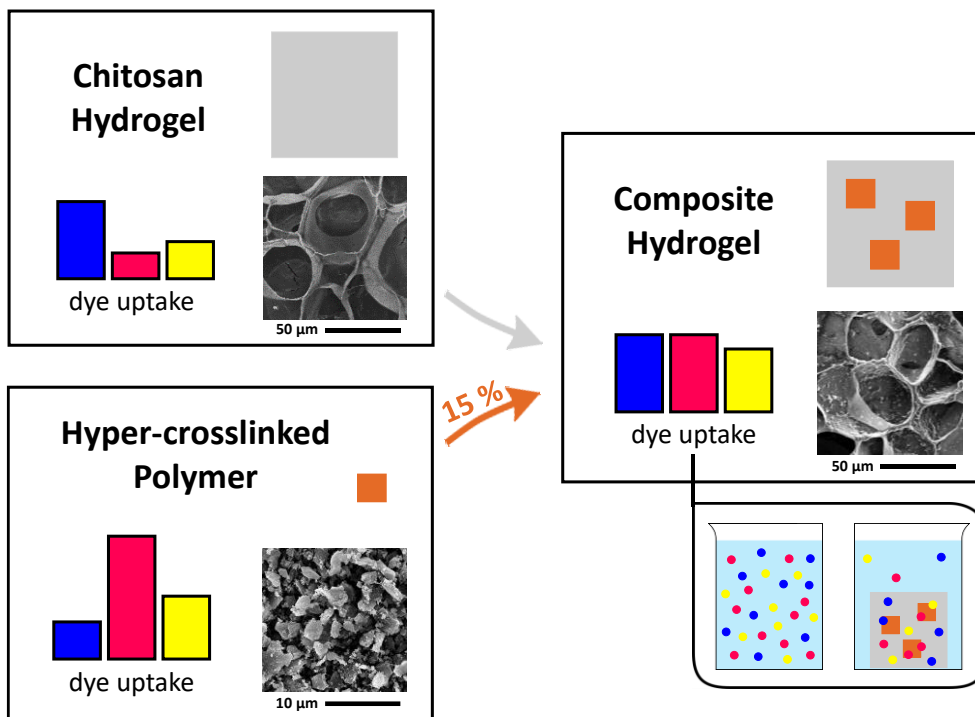
Rachele Castaldo,<sup>a,b</sup> Rosaria Altobelli,<sup>b</sup> Gennaro Gentile,<sup>a</sup> Lucia Gioiella,<sup>b</sup> Giovanni Filippone,<sup>b</sup> Martina Salzano De Luna,<sup>b,c</sup> Maurizio Avella<sup>a</sup> and Veronica Ambrogi<sup>a,b</sup>

<sup>a</sup> Institute for Polymers, Composites and Biomaterials, National Research Council of Italy, Via Campi Flegrei 34, 80078 Pozzuoli, Italy.

<sup>b</sup> Department of Chemical, Materials and Production Engineering, University of Naples, Piazzale Tecchio 80, 80125 Napoli, Italy.

<sup>c</sup> Institute for Polymers, Composites and Biomaterials, National Research Council of Italy, Piazzale E. Fermi 1, 80055, Portici, Italy.

## Abstract



We report here the preparation and the characterization of a new polymer composite based on a chitosan matrix containing hyper-crosslinked (HCL) polymer particles. A HCL resin based on divinylbenzene and vinylbenzyl chloride was prepared through bulk polymerization of a gel-type precursor polymer followed by Friedel-Crafts alkylation. Chitosan composite hydrogels containing 15 wt% of HCL polymers were prepared by solvent exchange technique. The composite hydrogel was based on two polymers very different and both widely studied for their adsorption properties. The resulting composite was characterized by a good dispersion of the filler and displayed comparable or even better mechanical properties than the plain chitosan hydrogel. Adsorption tests on the composite hydrogel towards various dyes demonstrated that efficient new composites for broad-spectrum water remediation can be prepared combining the chitosan and the HCL polymers adsorption properties.

## Introduction

Waste water treatment is a current significant environmental issue. In plastic, paper, textile and dye industries large amounts of water are used in the production systems, getting contaminated by various chemical products such as organic or inorganic molecules, metal contaminants and all kinds of dyes.<sup>1,2,3</sup>

Some classical remediation approaches are coagulation, flocculation, precipitation, electrocoagulation, electrofloatation, biodegradation, membrane separation and ion exchange.<sup>4</sup> New techniques consider the use of waste materials from industries, like activated carbon derived from solid wastes,<sup>5</sup> industrial by-products such as fly ash or active sludge (convenient for their local availability),<sup>6</sup> natural materials like clays,<sup>7</sup> zeolites<sup>8</sup> or siliceous materials,<sup>9</sup> biomass<sup>10</sup> or biosorbents based on chitin or chitosan.<sup>11</sup>

Biopolymers, in particular, which are particularly attractive because of their biocompatibility and biodegradability, offer the interesting possibility of tailoring their adsorption characteristics by selecting the preparation conditions and adjusting their selectivity through functionalization. Amongst biopolymers, chitosan is widely studied for the adsorption of organic substances or metal ions from water. Chitosan is a linear polysaccharide produced by the deacetylation of chitin, a natural occurring polymer found in the crustaceans shells. Several advantages are related to the use of chitosan or its derivatives in waste water purification:

- cost-efficiency, being chitosan the second more abundant polymer on earth, next to cellulose;
- versatility of the manufacture, since it is possible to produce, through green processes, films, membranes, sponges or hydrogels;
- high adsorption capacities,
- fast and reversible adsorption of dyes from concentrated or very diluted concentration of dyes.

Many studies focused on the chitosan mechanism adsorption, relying on his cationic nature. Chitosan amino groups can undergo protonation, and the protonated amines adsorb dyes of metal ions through chelation or electrostatic attraction.<sup>12</sup> In all cases, the form in which chitosan is presented has a significant influence on the physical adsorption capacity; gels, for example, are more suitable than flakes, powders or particles because of their intrinsic higher surface area.

To further enhance chitosan adsorption, strategies such as chemical modification<sup>13</sup> or preparation of composites<sup>12</sup> are usually pursued. In particular, many studies reported the preparation of chitosan-based composites for adsorption applications using different kinds of functional fillers, from natural

materials like silicates, aluminosilicates, activated clays, ceramic particles, magnetic minerals and cellulose,<sup>14</sup> to synthetic materials like graphene oxide<sup>15</sup> or polymers, as polyvinyl chloride beads,<sup>16</sup> polyvinyl alcohol<sup>17</sup> or polyurethane.<sup>18</sup>

Amongst the various polymers displaying high adsorption properties, outstanding performances characterize the hyper-crosslinked (HCL) resins, highly porous materials obtained by the extensive crosslinking of a linear or lightly crosslinked polymer.<sup>19</sup> HCL resins stand out for their high chemical and thermal stability<sup>20</sup> and for the possibility of tailoring their structure, porosity and functionalities.<sup>21,22,23</sup> Davankov and Tsyurupa first synthesized HCL resins based on polystyrene in 1969.<sup>24</sup> Linear or lightly crosslinked styrenic polymers have been widely explored ever since, modulating their possible monomeric compositions and varying their synthesis, aiming to modulate the porosity, the morphology and the specific surface area (SSA) of the resulting product.<sup>25,26</sup> In a typical synthetic procedure, Davankov-type HCL resins are prepared by a two-step reaction: the suspension polymerization of a linear or lightly crosslinked precursor polymer and the extensive crosslinking of the precursor polymer using a bishalide and a Friedel-Crafts catalyst. The hyper-crosslinking process leads to a highly porous three-dimensional network, which displays high specific surface area and excellent adsorption properties. In particular, starting from vinylbenzyl chloride (VBC) and 2 mol % of divinylbenzene (DVB), hyper-crosslinked polymers with a specific surface area of about 2000 m<sup>2</sup>/g are obtained.<sup>25</sup> Several kinds of HCL resins properly designed and functionalized for adsorption of different gases<sup>27,28</sup> and water contaminants<sup>29,30</sup> are reported in the literature. Liu et al., for example, successfully employed hyper-crosslinked polymeric nanoparticles in the solid-phase microextraction (SPME) technique, covering SPME fibers to adsorb aromatic pollutants.<sup>31</sup> In a previous work,<sup>32</sup> and in Chapter 3 of this thesis, the synthesis of HCL styrene resins through a new synthetic approach based on the bulk prepolymerization of the precursor polymer, followed by the typical Friedel-Crafts reaction is proposed. The as obtained polymers have comparable BET SSA, porosity and adsorption properties than those prepared by the traditional procedure involving the suspension polymerization of the precursor polymer.

Starting from the need of a new purification technology that could simultaneously face the uptake of different substances from water, this work focused on the preparation and the characterization of a new composite material based on a chitosan hydrogel matrix containing nano- and micrometric HCL particles. The aim is to combine the adsorption properties of the matrix and the filler in a new broad-spectrum adsorbent.

## Experimental section

### Materials

Vinylbenzyl chloride (VBC,  $\geq 95.0\%$ , mixture of isomers,  $\sim 70\%$  meta +  $\sim 30\%$  para), p-divinylbenzene (DVB, 85%, meta isomer,  $\sim 10$  wt%), 2,2'-azobis(2-methylpropionitrile) (AIBN,  $> 98\%$ ),  $\text{FeCl}_3$  ( $\geq 97\%$ ), Chitosan (medium molecular weight), Indigo Carmine, Rhodamine 6G and Sunset Yellow FCF were purchased by Sigma Aldrich (Milan, Italy) and used without further purification.

### Preparation of the hyper-crosslinked resins

A hyper-crosslinked resin based on vinylbenzyl chloride (VBC) and divinylbenzene (DVB) was prepared by a two-step procedure based on the radical bulk polymerization of the precursor resin and its hyper-crosslinking through Friedel-Crafts reaction.<sup>32</sup>

DVB and VBC in the molar ratio 2:98 were mixed with 0.5 phr of AIBN under nitrogen for 30 min, then the mixture was poured in a glass bottle and cured in oven at  $80\text{ }^\circ\text{C}$  for 24 h. The product was purified by multiple washings with methanol, acetone and diethyl ether, and then dried in a vacuum oven at  $40\text{ }^\circ\text{C}$  for 24 h.

The precursor poly(divinylbenzene-co-vinylbenzyl chloride), coded DVB-VBC, was swollen in 1,2-dichloroethane (DCE), under nitrogen, for 2 h. Then the mixtures were cooled to  $\sim 4\text{ }^\circ\text{C}$  in an ice/NaCl bath, and the Friedel-Crafts catalyst,  $\text{FeCl}_3$ , was added in a molar ratio 1:1 of  $\text{CH}_2\text{Cl}:\text{FeCl}_3$ . The system was heated to  $80\text{ }^\circ\text{C}$  and kept at this temperature for 18 h. Purification from unreacted reagents and side reaction products was performed as described for the precursor polymer.

The hyper-crosslinked resin (coded HR0) was milled in a planetary ball-milling system Retsch PM100, using a 125 mL steel milling cup and 10 mm diameter steel milling spheres in a spheres/resin weight ratio 40:1, at 600 rpm for 4 hours. This sample will be named HR in the following.

### Chitosan and composite hydrogel preparation

Chitosan was dissolved in a 98/2 v/v % mixture of bi-distilled water and acetic acid via magnetic stirring at room temperature for 72 h at chitosan concentration in the starting solution  $\Phi_{\text{CS}} = 3$  w/v%.

A simple hydrogel assembly was obtained by solvent exchange, that is a direct but controlled exposure to aqueous alkaline solutions.<sup>33,34</sup> In detail, 2 mL of chitosan solution were poured into glass test tubes, and then an aqueous solution of sodium hydroxide ( NaOH ) at concentration  $\Phi_{\text{NaOH}} = 6 \text{ w/v } \%$  was carefully poured on the top by using a needle, so as not to disturb the liquid/liquid interface and to ensure a regular diffusion through it. The formation of the physical network of chitosan chains proceeds over time from the liquid-liquid interface between the two solutions towards the bottom of the glass tube, following the diffusion of the alkaline species in the chitosan solution due to the concentration gradient. At the end of the process, the chitosan hydrogel was collected, cut into cylindrical-shaped specimens (diameter 10 mm, thickness 5 mm), extensively rinsed with bi-distilled water until neutralization, and stored in water until use. The volume ratio of the chitosan:NaOH solution was fixed to 1:1.

A composite chitosan hydrogel containing 15 wt % of HR was prepared following a similar procedure. First, during the chitosan dissolution the HR particles were dispersed in the chitosan phase, then gelation was promoted as described before.

Chitosan and composite samples were freeze-dried, in order to evaluate their morphology by scanning electron microscopy and gas adsorption tests. Lyophilization was performed using a freeze dryer Edwards Modulyo equipment. Prior to the freeze-drying, the hydrogels were frozen at  $-20^{\circ}\text{C}$  and kept at this temperature overnight. Then, freeze-drying was performed at  $-80^{\circ}\text{C}$  and  $5 \times 10^{-2}$  torr for 48h.

Hydrogel samples are coded CS and CS-15HR; freeze-dried samples will be referred as FD-CS and FD-CS-15HR.

## Hydrogels characterization

The mechanical behavior of the hydrogels in the swollen state was investigated by unconfined compression tests on cylindrical-shaped specimens fully immersed in bi-distilled water. The samples were squeezed at a controlled speed of  $2 \mu\text{m/s}$ , and the normal force  $F_N$  and the displacement of the plate,  $\Delta h$ , were recorded during time. The engineering stress ( $\sigma$ ) and strain ( $\epsilon$ ) were calculated as  $\sigma = F_N/A_0$  and  $\epsilon = \Delta(h/h_0)$ , where  $A_0$  and  $h_0$  are the initial cross section and the height of the sample. The compressive modulus,  $E_c$ , was then estimated for each system in the linear region of the stress-strain curve. Ten independent measurements were carried out for each sample.

The adsorption ability of the hydrogels was estimated through batch adsorption tests from mono-component solutions of three dyes, indigo carmine (IC), Rhodamine 6g (RH) and Sunset Yellow FCF (SY) (molecular structures reported in Figure 4.1). Stock solutions were prepared by dissolving 1.0 g/L of dye in bi-distilled water, and then solutions at different dye concentration (20-600 mg/L) were obtained by dilution. Therefore, 10 mg of chitosan or

composite hydrogel were added in glass flasks containing the dye solutions. The flasks were agitated at 150 rpm and  $T=25^{\circ}\text{C}$  using a thermostated agitator (SKI 4, Argo Lab). Equilibrium was assumed when the dye concentration in the solution proved to be stable over three consecutive measurements. The dye concentration was determined with a spectrophotometer at the characteristic maximum absorbance wavelength,  $\lambda_{\text{max}}$ , of each dye (611 nm for IC, 527 nm for RH, 482 nm for SY). All the experiments were carried out in replicate, and blanks were performed. The equilibrium adsorption capacity,  $q_e$ , was determined as:

$$q_e = V \cdot (C_0 - C_e) / m \quad (4.1)$$

where  $C_0$  is the initial dye concentration (mg/L),  $C_e$  is the equilibrium dye concentration in liquid phase (mg/L),  $m$  is the amount of dry chitosan or composite hydrogel (g), and  $V$  is the total volume of dye solution (L).<sup>4</sup>

The morphology of the freeze-dried hydrogels was analysed by means of scanning electron microscopy (SEM), using a FEI Quanta 200 FEG SEM in high vacuum mode. Before SEM observations, the chitosan and composite gels were cryo-fractured and sputter coated with a 15 nm thick Au–Pd layer. All samples were observed at 10 kV acceleration voltage using a secondary electron detector.

Gas adsorption analysis were performed on the chitosan and composite freeze-dried hydrogels. The measurements were performed using a Micromeritics ASAP 2020 analyzer, using high purity gases (>99.999%). Prior to the analysis, the hyper-crosslinked samples were degassed at  $70^{\circ}\text{C}$  under vacuum ( $P < 10^{-5}$  mbar). SSA was determined from the linear part of the Brunauer-Emmett-Teller (BET) equation. Non-local density functional theory (NLDFT) was applied to the  $\text{N}_2$  adsorption isotherm curves to evaluate the pore size distribution of the materials.

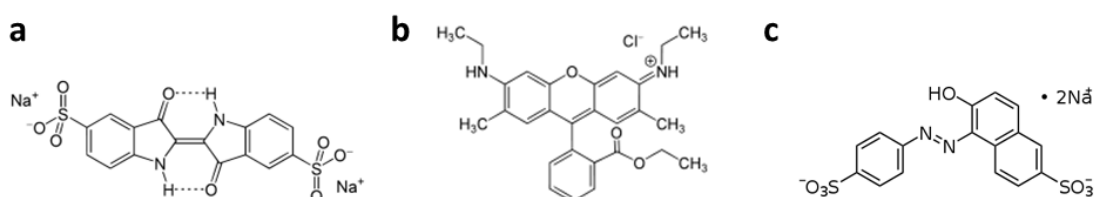


**Figure 4.1** Molecular structure of Indigo Carmine(a), Rhodamine 6G(b) and Sunset Yellow FCF(c)

## **Hyper-crosslinked resins characterization**

The precursor and the hyper-crosslinked resins were characterized by FTIR analysis. ATR-FTIR spectra were recorded with a Perkin Elmer Spectrum One FTIR spectrometer equipped with an ATR module, using a resolution of  $4\text{ cm}^{-1}$  and 32 scan collections.

Energy Dispersive X-ray (EDX) analysis was performed on the precursor and the hyper-crosslinked resins using a FEI Quanta 200 FEG SEM equipped with an Oxford Inca Energy System 250 and an Inca-X-act LN2-free analytical silicon drift detector. A thin layer of DVB-VBC and HR0 was deposited onto aluminum SEM stubs. The analysis was performed at 30 kV acceleration voltage. Average results and standard deviation values are based on three consecutive measurements on different areas of each sample.

The plain and ball-milled hyper-crosslinked resins were analysed by means of SEM analysis and volumetric gas adsorption in the same conditions described for the freeze-dried hydrogels.

Also, dye adsorption measurements were performed on the ball-milled resin in the same way reported for the hydrogels. About 10 mg of HR were used in each test.

## **Results and discussion**

In this work, new composite hydrogels were obtained by the combination of chitosan and hyper-crosslinked divinylbenzene/vinylbenzyl chloride polymer particles. Chitosan hydrogels were obtained through physical crosslinking induced by alkaline solution. The HCL particles were prepared by bulk polymerization followed by Friedel-Crafts reaction. These HCL resins are usually obtained by suspension or emulsion polymerization, followed by hyper-crosslinking. The bulk polymerization permits to significantly reduce the amount of solvent waste connected with the traditional suspension or emulsion procedure, at the same time letting to obtain materials with comparable SSA and adsorption properties similar to those prepared through the traditional procedures.<sup>32</sup>

### **Hyper-crosslinked polymer particles preparation**

Hyper-crosslinked polymers based on VBC and DVB were prepared by a Davankov modified procedure, based on the bulk prepolymerization of a lightly crosslinked poly(VBC-DVB) and the hyper-crosslinking through Friedel-Crafts reaction. DVB in the amount of the 2 mol% induces of a light degree of crosslinking in the precursor resin; during the hyper-crosslinking the chloromethyl

groups of the VBC create methylene bridges between neighbouring phenyl rings, introducing new crosslinks additional to those due to the DVB. The final material exhibits high crosslinked structure after solvent removal, displaying an expanded, rigid, three-dimensional network. A scheme of the reaction is presented in Figure 4.2. FTIR analysis on the precursor and the hyper-crosslinked polymers confirms the extent of the hyper-crosslinking reaction. The ATR-FTIR spectra, reported in Figure S4.1, show the significant disappearing of the characteristic absorption band of the chloromethyl groups of the VBC monomer after hyper-crosslinking ( $\text{CH}_2$  wagging of the chloromethyl group,  $1265\text{ cm}^{-1}$ ).<sup>35</sup> The residual amount of chlorine after hyper-crosslinking was also evaluated through EDX analysis. The Cl/C ratio in the HCL polymer was found  $0.840 \pm 0.007\text{ mol}\%$ ; considering that the initial Cl/C ratio of the precursor polymer is  $12.2\text{ mol}\%$ , the yield of hyper-crosslinking was  $93.1\%$ .

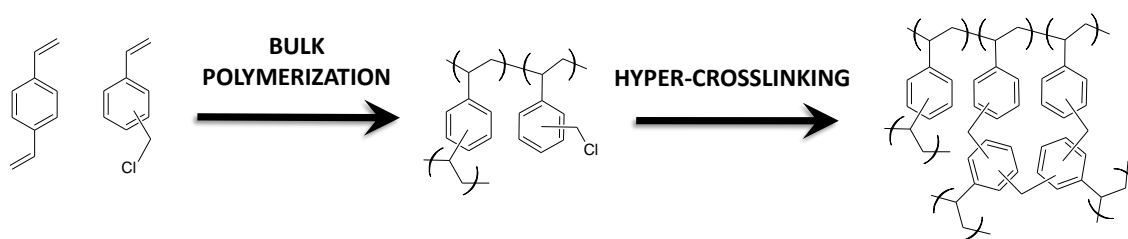


**Figure 4.2** Hyper-crosslinked polymers synthesis schematic

### Morphology of the hyper-crosslinked resins and the freeze-dried hydrogels

SEM micrographs of the ball-milled HCL resin and the fractured sections of the freeze-dried hydrogels are reported in Figure 4.3.

After ball-milling, the size of the HCL resin was in the range  $50\text{ nm} - 5\text{ }\mu\text{m}$ . As before milling the HR0 resin particles dimension ranged from  $5\text{ to }200\text{ }\mu\text{m}$  (See Figure S4.2), the ball milling was very effective to reduce the particle size for their embedding in the chitosan hydrogel.

SEM micrograph of the freeze-dried chitosan hydrogel is reported in Figure 4.2 (c), whereas in Figure 4.2 (d-f) micrographs of the chitosan sample containing HR particles are shown. As it can be observed, the porous structure of the plain chitosan hydrogel was preserved during the freeze-drying and pores with dimensions ranging from about  $1\text{ }\mu\text{m}$  to about  $20\text{ }\mu\text{m}$  were clearly visible. As concerning the composite FD-CS-15HR, micro/nanoparticles were well distributed within the pore walls and no agglomeration phenomena were observed. Furthermore, a good chitosan/HCL filler interfacial adhesion was evidenced, and HR particles were well embedded within the chitosan phase, despite to the different hydrophilic/hydrophobic nature of these components.

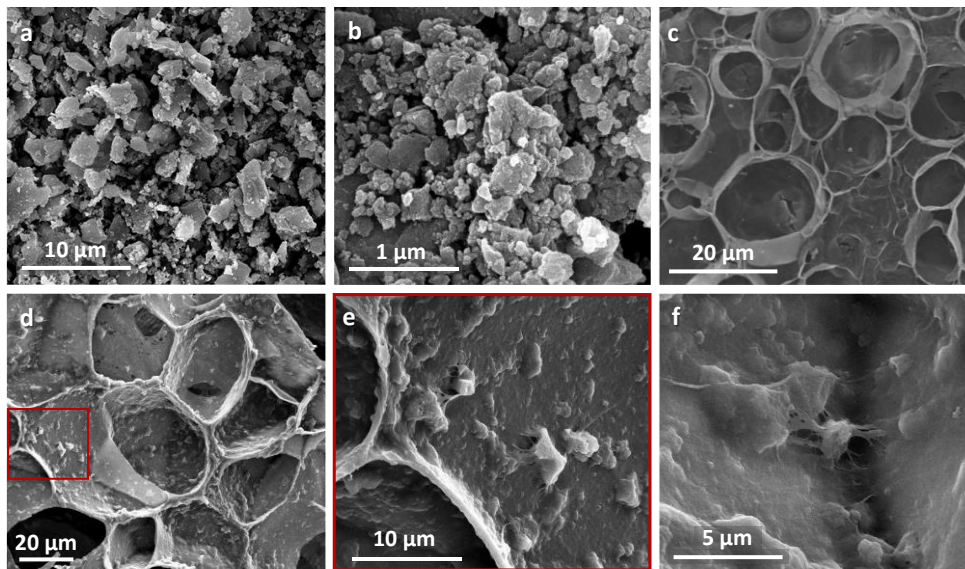


**Figure 4.3** SEM micrographs of: HR (a-b), FD-CS (c), FD-CS-15HR (d, e, f). In (e) is reported a magnification of the area identified with a rectangle in (d)

### Chitosan and composite hydrogels characterization

Compression tests were carried out on chitosan and composite hydrogels to evaluate the effect of the addition of the HCL particles on the mechanical properties of the gel. Results are shown in Figure 4.4. By adding 15 % of HR in the chitosan matrix, a significant 60 % increase in the compression elastic modulus was recorded. Worth of note is that this increase did not occur at the expense of the deformability of the sample, as the maximum strain reached by the plain chitosan hydrogel and the composite hydrogel before failure were comparable.

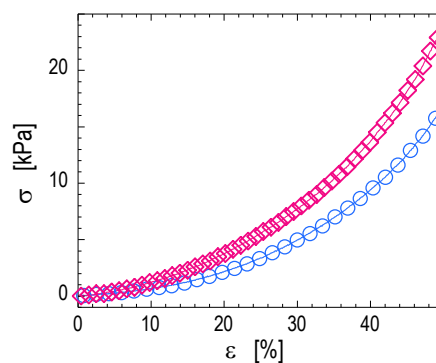


**Figure 4.4** Mechanical compression test results of CS (blu circles) and CS-15HR (pink diamonds)

## Freeze-dried hydrogels and hyper-crosslinked polymer particles gas adsorption

Nitrogen adsorption is a characteristic property for the materials displaying high micro- and mesoporosity, and the analysis of the adsorption isotherms permits to evaluate the porosity distribution of the materials. Nitrogen adsorption isotherms at 77 K were measured on the HR particles, the plain FD-CS hydrogel and the composite FD-CS-15HR hydrogel, and DFT pore size distribution were calculated. Results are reported in in Figure 4.5.

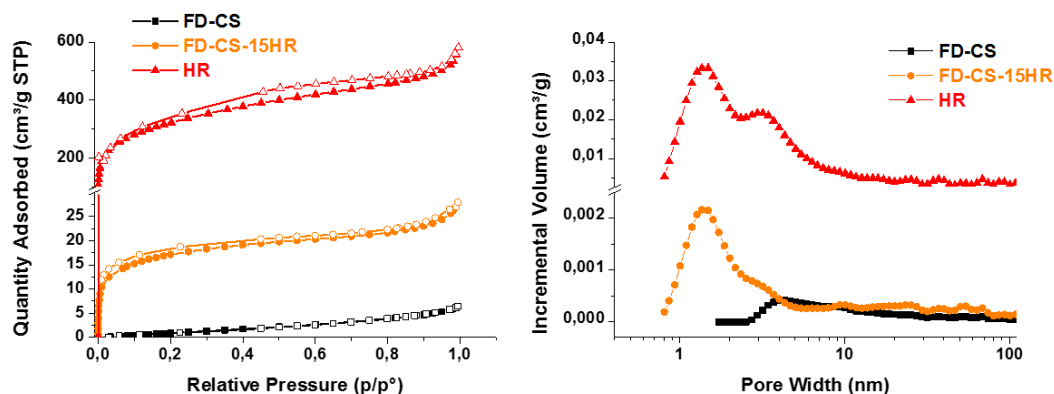


**Figure 4.5** Nitrogen adsorption (filled symbols) and desorption (empty symbols) isotherms at 77 K up to 1 bar (left) and DFT pore size distribution (right) of the freeze-dried hydrogels and the hyper-crosslinked resin

HR showed a type II isotherm, that is typical of materials characterized by simultaneous micro- and mesoporosity.<sup>36</sup> Major adsorption was displayed at very low relative pressure (before 0.01 p/p<sub>0</sub>), indicating the existence of significant microporosity and, at higher pressure, an inversion of the isotherm curvature was observed, characteristic of the multi-layer adsorption in mesopores. The recorded hysteresis of the HR curve was also indicative of the presence of mesopores. DFT pore size distribution clearly confirmed the presence of two major classes of pores, the first ones with average size lower than 2 nm, and the second ones with a size distribution centred at about 3 nm. HR displayed a BET SSA of  $1092 \pm 19$  m<sup>2</sup>/g, and was characterized by the 39% of microporosity fraction. The nitrogen adsorption isotherm and the DFT pore size distribution of the hyper-crosslinked resin before mechanical processing (HR0) is reported in Supplementary information, in Figure S4.3.

CS adsorbed very low amounts of nitrogen in the adopted conditions. The corresponding analysis of the pore size was not very significant, even if the presence of small amount of pores with average size lower than 100 nm was evidenced.

Gas adsorption measurement on the composite hydrogel revealed the characteristic porosity of HR, even if in lower amount with respect to the quantity of HR included in the composite (see Table S4.1

for the detailed results). While in the swollen state of the hydrogel most of the HR porosity can be considered available, the reduced porosity of the HCL resin in the freeze-dried composite hydrogel can be explained considering that during freeze-drying part of the pores of the HCP particles may be occluded by the chitosan matrix.

### Dye adsorption tests

The equilibrium adsorption isotherms of the new CS/HR composite, the plain CS hydrogel and the hyper-crosslinked resin towards Indigo Carmine (IC), Rhodamine 6G (RH) and Sunset Yellow FCF (SY) are showed in Figure 4.6. To examine the adsorbent-adsorbate interaction, Freundlich and Langmuir models are usually employed to fit the data. In Table 4.1 are reported the Freundlich and Langmuir characteristic parameters and the fit correlations coefficients for all the system tested. Freundlich model accounts for multilayer adsorption, and expresses the relation between the equilibrium adsorption ( $q_e$ ) and the equilibrium concentration ( $C_e$ ) through:

$$q_e = K_F C_e^{1/n} \quad (4.2)$$

where  $K_F$  and  $n$  are, respectively, indicative of the adsorption capacity and intensity.<sup>37,38</sup> On the other hand, Langmuir adsorption theory considers adsorption to be homogeneous, all the adsorption sites to be energetically equivalent, and the coverage to be in monolayer.<sup>39,40</sup> Langmuir equilibrium adsorption equation is:

$$\frac{q_e}{q_m} = \frac{K_L C_e}{1 + K_L C_e} \quad (4.3)$$

with  $q_m$  indicating the maximum adsorption capacity, corresponding to complete monolayer coverage, and  $K_L$  being a constant related to the adsorption energy.

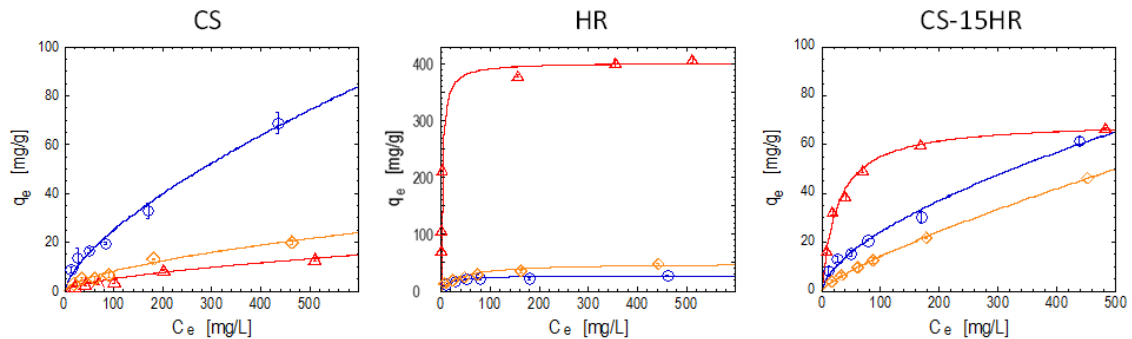


**Figure 4.6** CS, HR and CS-15HR equilibrium dye adsorption isotherms. IC, RH and SY uptake is represented, respectively, with blue circles, red triangles and yellow diamonds

Chitosan showed in all cases a Freundlich type isotherm, demonstrating much better affinity with IC than with RH and SY. In fact, within the investigated range of concentration of the dyes, chitosan maximum equilibrium uptake was about 69 mg/g for the IC, and about 13 and 20 mg/g for RH and SY, respectively. As concerning the hyper-crosslinked particles, on the other way, all the adsorption curves showed good agreement with the Langmuir model; for SY, in particular, both the Freundlich and the Langmuir models were suitable, with the Freundlich correlation coefficient being slightly higher. The hyper-crosslinked particles were able to adsorb RH much more than the other dyes, reaching for RH the equilibrium adsorption capacity of 400 mg/g.

Very interesting were the results obtained for the composite CS-15HR system. By addition of 15 wt% of HR, an outstanding improvement of the RH and SY adsorption capacity were recorded with respect to the plain chitosan hydrogel, respectively more than 400% and 130%. Nevertheless, as the adsorption capacity of chitosan towards IC was higher than that shown by the HR particles, for IC a decrease of about 10% of the equilibrium concentration adsorption was recorded for the composite hydrogel with respect to the plain chitosan hydrogel. As concerning the modalities of adsorption, RH adsorption of the CS-15HR composite was classified as Langmuir type, while IC and SY adsorption as Freundlich type, demonstrating that the adsorption behaviour towards these three dyes was led, respectively, by the most adsorbent component.

All the results obtained by the adsorption tests of the selected dyes demonstrated that the combination of organic polymers characterized by different structure and porosity, hydrophobic/hydrophilic behaviour, and adsorption properties was effective for the realization of broad-spectrum adsorbent materials.

**Table 4.1.** Freundlich and Langmuir fitting parameters for CS, HR and CS-15HR dye adsorption

		Freundlich			Langmuir		
		$K_F$ [(mg/g)(L/mg) <sup>1/n</sup> ]	$n$	$R^2$	$K_L$ (L/mg)	$q_m$ (mg/g)	$R^2$
Indigo Carmine	CS	1.932	1.774	0.9844	-	-	-
	HR	-	-	-	0.040	28.7	0.9962
	CS-15HR	2.128	1.876	0.9909	-	-	-
Rhodamine 6G	CS	0.319	1.691	0.9847	-	-	-
	HR	-	-	-	0.196	408.5	0.9998
	CS-15HR	-	-	-	0.036	70.4	0.9998
Sunset Yellow FCF	CS	0.512	1.675	0.9772	-	-	-
	HR	7.074	3.166	0.9979	0.021	51.4	0.9935
	CS-15HR	0.464	1.341	0.9992	-	-	-

## Conclusions

A new composite hydrogel based on a chitosan matrix containing high surface area hyper-crosslinked styrene-based particles was prepared and characterized for possible application in water purification.

Hyper-crosslinked particles were obtained by a new process, based on the bulk polymerization of a lightly crosslinked styrenic precursor polymer, followed by Friedel-Crafts reaction.

A mechanical treatment based on the use of a planetary ball milling was used and resulted very effective to reduce and homogenise the particle dimensions in view of their embedding in the composite hydrogel. The composite hydrogel was then prepared by dissolution of chitosan in water and contemporary dispersion of the filler, followed by gelation through physical crosslinking of the chitosan phase induced by alkaline solution. During gelation, the hyper-crosslinked particles were effectively embedded in the chitosan matrix. Morphological analysis of the freeze-dried composite hydrogel revealed a good distribution of the particles in the chitosan matrix and a good interfacial adhesion between the two phases.

Compression tests revealed that the filler addition did not affect the mechanical properties of the hydrogel, actually increasing its compression modulus.

Adsorption tests on three different dyes, Indigo Carmine, Rhodamine 6G and sunset yellow FCF showed that, through the realization of the new composite hydrogel, it was possible to effectively combine the adsorption performances of the chitosan matrix and the hyper-crosslinked particles. There is still room for further improvements of the composite performances, for instance by optimizing the hydrogel composition and the mechanical treatment for the size reduction of the hyper-crosslinked particles. Nevertheless, the realized material can be considered the first representative of a new class of broad-spectrum adsorbents for possible applications in water remediation.

## Supplementary information

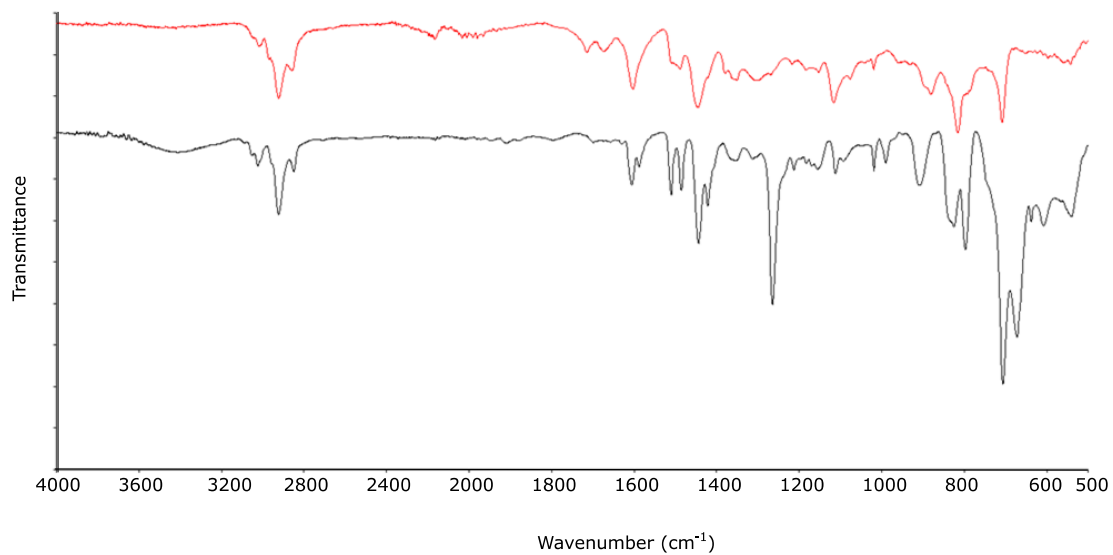


**Figure S4.1** ATR-FTIR spectra of the precursor (DVB-VBC, black curve) and the hyper-crosslinked (HR, red curve) resin

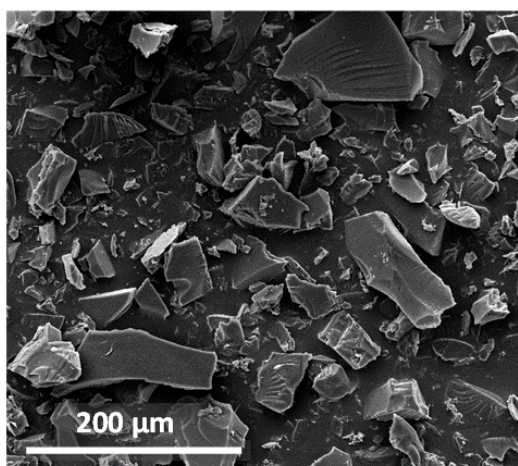


**Figure S4.2** SEM micrograph of the hyper-crosslinked resin HR0

Prior to the composite preparation, the HCL resin was milled to reduce and homogenise its dimensions, aiming to promote a good dispersion of the filler in the chitosan matrix. The milling procedure comported a substantial reduction of the total porosity but not significant lowering in adsorption properties, since they are principally led by the polymer microporosity.

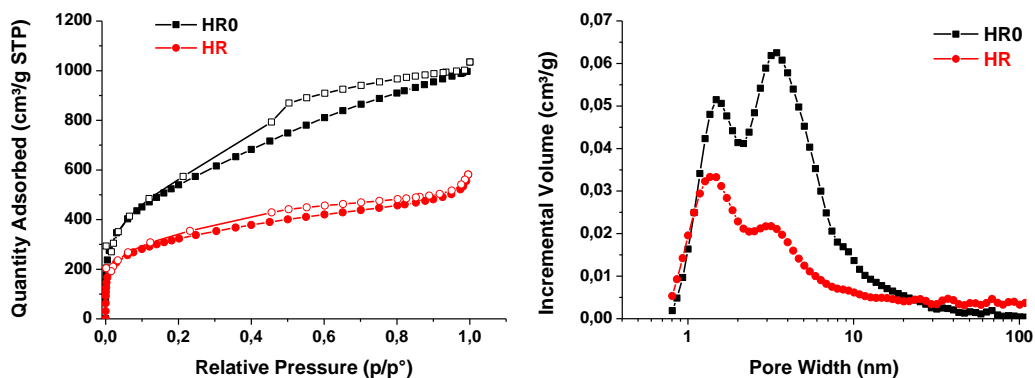


**Figure S4.3** Nitrogen adsorption (filled symbols) and desorption (empty symbols) isotherms at 77 K (left) and DFT pore size distribution (right) of the plain (HR0) and ball-milled (HR) hyper-crosslinked resins

**Table S4.1** Results of SSA and pore size distribution analysis on the plain (HR0) and ball-milled (HR) hyper-crosslinked resins, the chitosan (FD-CS) and composite (FD-CS-15HR) freeze-dried hydrogels

Sample	BET (m <sup>2</sup> /g)	Micro / Total pore volume (%)	Micropore volume (cm <sup>3</sup> /g)	Total pore volume (cm <sup>3</sup> /g)
<b>HR0</b>	1964 ± 9	30	0,42	1,39
<b>HR</b>	1092 ± 19	39	0,31	0,79
<b>FD-CS</b>	8 ± 1	-	-	0,01
<b>FD-CS-15HR</b>	60 ± 1	49	0,02	0,04

## References

- <sup>1</sup> D. Pokhrel and T. Viraraghavan, *Sci Total Environ*, 2004, **333**, 37.
- <sup>2</sup> T. Robinson, G. McMullan, R. Marchant, and P. Nigam, *Bioresour Technol*, 2001, **77**, 247.
- <sup>3</sup> I. M. Banat, P. Nigam, D. Singh, and R. Marchant, *Bioresour Technol*, 1996, **58**, 217.
- <sup>4</sup> G. Crini and P. M. Badot, *Prog. Polym. Sci.*, 2008, **33**, 399.
- <sup>5</sup> S. Karaca, A. Gürses, and R. Bayrak, *Energy Convers. Manage*, 2004, **45**, 1693.
- <sup>6</sup> C. Namasivayam, and S. Sumithra, *J. Environ. Manage*, 2005, **74**, 207.
- <sup>7</sup> M. Alkan, O. Demirbas, S. Celikc, and M. Dogan, *J. Hazardous Mater.*, 2004, **116**, 135
- <sup>8</sup> O. Ozdemir, B. Armagan, M. Turanand M.S. Celik, *Dyes Pigments*, 2004, **62**, 49
- <sup>9</sup> A. Krysztalkiewicz, S. Binkowski, T. Jesionowski, *Appl. Surf. Sci.*, 2002, **199**, 31
- <sup>10</sup> Z. Aksu and S. Tezer, *Proc. Biochem.*, 2005 **40**, 1347
- <sup>11</sup> M. Vakili, M. Rafatullaha, B. Salamatinia, A. Z. Abdullahc, M. H. Ibrahima, K. B. Tanb, Z. Gholamic and P. Amouzgarb, *Carbohydrate Polymers*, 2014, **113**,115
- <sup>12</sup> W.S. Wan Ngah, L.C. Teonga, and M.A.K.M. Hanafiaha, *Carbohydrate Polymers*, 2011, **83**, 1446
- <sup>13</sup> G. Z. Kyzas and D. N. Bikiaris, *Mar. Drugs*, 2015, **13**, 312
- <sup>14</sup> S. Oliveraa, H. B. Muralidharab, K. Venkateshb, V. K. Gunab, K. Gopalakrishnab, and Y. K. Kumar, *Carbohydrate Polymers*, 2016, **153**, 600
- <sup>15</sup> N. A. Travlou, G. Z. Kyzas, N. K. Lazaridis, and E. A. Deliyanni, *Langmuir*, 2013, **29**, 1657
- <sup>16</sup> M. Farzaneh, G. Mehrorang, S. Ardeshir, M. Morteza, and D. Shanaz, *Chemosphere*, 2009, **74**, 583
- <sup>17</sup> M. Kumar, P. T. Bijay, and K. S. Vinod, 2009, **172**, 1041
- <sup>18</sup> S. L. Won, H. C. Lee, Y. G. Jeong, B. G. Min, and S. C. Lee, *Fibers and Polymers*, 2009, **10**, 636
- <sup>19</sup> N. Fontanals, R. M. Marcé, F. Borrulla and P. A. G. Cormack, *Polym. Chem.*, 2015, **6**, 7231
- <sup>20</sup> R.T. Woodward, L.A. Stevens, R. Dawson, M. Vijayaraghavan, T. Hasell, I.P. Silverwood, A.V. Ewing, T. Ratvijitvech, J.D. Exley, S.Y. Chong, F. Blanc, D.J. Adams, S.G. Kazarian, C.E. Snape, T.C. Drage and A.I. Cooper, *J. Am. Chem. Soc.*, 2014, **136**, 9028.
- <sup>21</sup> R. Dawson, A.I. Cooper and D.J. Adams, *Polym. Int.*, 2013, **62**, 345.
- <sup>22</sup> R. Dawson, L.A. Stevens, T.C. Drage, C.E. Snape, M.W. Smith, D.J. Adams and A.I. Cooper, *J. Am. Chem. Soc.*, 2012, **134**, 10741
- <sup>23</sup> J. Germain, F. Svec and J.M.J. Fréchet, *Chem. Mater.*, 2008, **20**, 7069
- <sup>24</sup> V.A. Davankov and M.P. Tsyurupa, *Reactive Polymers*, 1990, **13**, 27
- <sup>25</sup> J.-H. Ahn, J.-E. Jang, C.-G. Oh, S.-K. Ihm, J. Cortez and D. C. Sherrington, *Macromolecules*, 2006, **39**, 627
- <sup>26</sup> B. Li, X. Huang, L. Liang and B. Tan, *J. Mater. Chem.*, 2010, **20**, 7444

- <sup>27</sup> R. Dawson, T. Ratvijitvech, M. Corker, A. Laybourn, Y. Z. Khimyak, A. I. Cooper and D. J. Adams, *Polym. Chem.*, 2012, **3**, 2034
- <sup>28</sup> J. Germain, J. Hradil, J. M. J. Frechet and F. Svec, *Chem. Mater.*, 2006, **18**, 4430
- <sup>29</sup> X. Zhang, A. Li, Z. Jiang and Q. Zhang, *Journal of Hazardous Materials B*, 2006, **137**, 1115
- <sup>30</sup> J.-H. Huang, K.-L. Huang, S.-Q. Liu, A.-T. Wang, C. Yan, *Colloids and Surfaces A: Physicochem. Eng. Aspects*, 2008, **330**, 55
- <sup>31</sup> S. Liu, D. Chen, J. Zheng, L. Zeng, J. Jiang, R. Jiang, F. Zhu, Y. Shen, D. Wu and G. Ouyang, *Nanoscale*, 2015, **7**, 16943
- <sup>32</sup> R. Castaldo, R. Avolio, M. Cocca, G. Gentile, M. E. Errico, M. Avella, C. Carfagna and V. Ambrogio, “A versatile synthetic approach towards hyper-crosslinked styrene-based polymers and nanocomposites”, *under submission*, chapter 3 of this thesis
- <sup>33</sup> S. Ladet, L. David, and A. Domard, *Nature*, 2008, **452**, 76
- <sup>34</sup> K. Yao, J. Li, F. Yao, and Y. Yin, *Chitosan-based hydrogels: functions and applications*, CRC Press, 2001
- <sup>35</sup> P. B. Nagabalasubramanian, S. Periandy and S. Mohan, *Spectrochim. Acta, Part A*, 2010, **77**, 150.
- <sup>36</sup> F. Rouquerol, J. Rouquerol, K.S.W. Sing, P. Llewellyn and G. Maurin. *Adsorption by Powders and Porous Solids Principles, Methodology and Applications. Second edition*, Elsevier, 2014
- <sup>37</sup> F.L. Slejko, *Adsorption Technology: A Step-by-step Approach to Process Evaluation and Application*, Marcel Dekker, New York-Basel, 1985.
- <sup>38</sup> A.M. Li, Q. X. Zhang, J. L. Chen, Z. H. Fei, C. Long and W. X. Li, *React Funct Polym*, 2001, **49**, 225
- <sup>39</sup> D. D. Duong, *Adsorption Analysis: Equilibria and Kinetics*, World Scientific Publishing Co., Singapore, 1998
- <sup>40</sup> A. M. El-Kamash, *J Hazard Mater*, 2008, **151**, 432

# Chapter 5

## Effects of the oxidation degree on the self-assembly and the surface area of graphene oxide

### Authors and affiliations

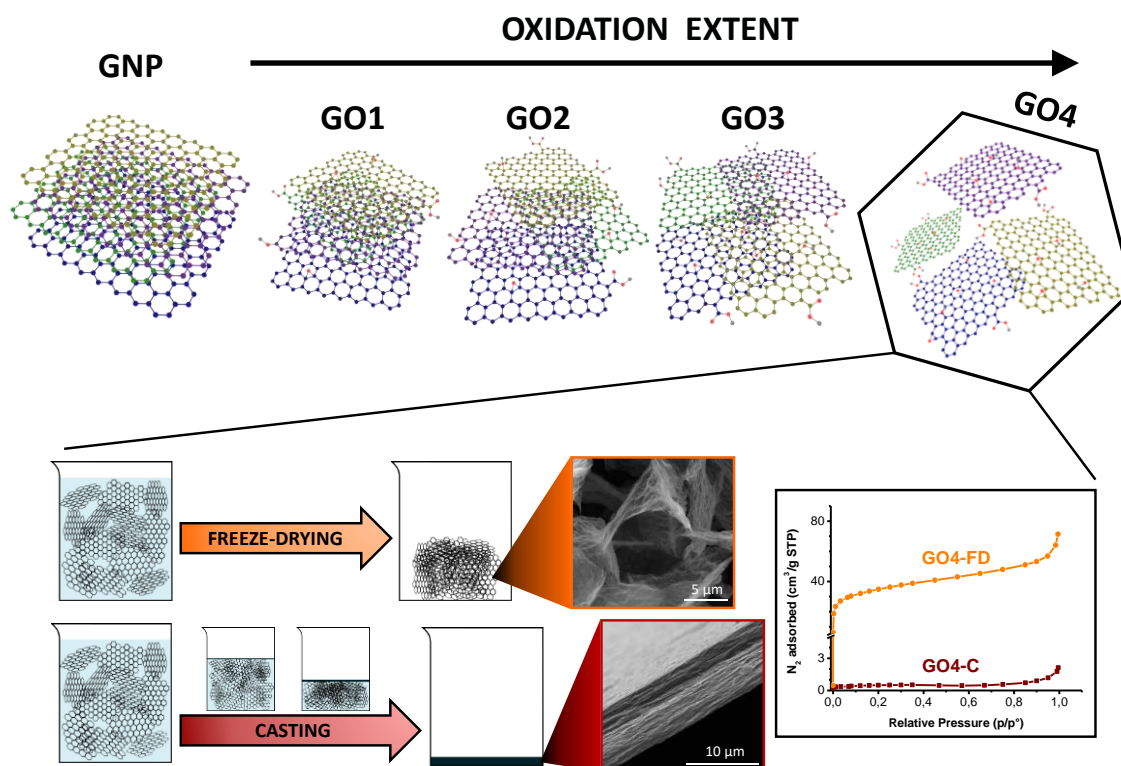
Rachele Castaldo,<sup>a,b,1</sup> Giuseppe Cesare Lama,<sup>a,b,1</sup> Gennaro Gentile,<sup>a</sup> Paolo Aprea,<sup>b</sup> Maurizio Avella,<sup>a</sup> Veronica Ambrogio,<sup>a,b</sup> and Pierfrancesco Cerruti<sup>a</sup>

<sup>a</sup>Institute for Polymers, Composites and Biomaterials, National Research Council of Italy, Via Campi Flegrei 34, 80078 Pozzuoli, Italy.

<sup>b</sup>Department of Chemical, Materials and Production Engineering, University of Naples, Piazzale Tecchio 80, 80125 Napoli, Italy.

<sup>1</sup>These authors contributed equally to this paper.

## Abstract



The effect of the oxidation degree on the self-assembly and surface area of graphene oxide was investigated. FTIR and EDX spectroscopy indicated that the obtained GO samples were characterized by a very low to high level of oxidation. Raman and WAXS analysis showed that increasing the oxidation degree a progressive disruption of the interlayer distance between graphene sheets was obtained. A non-linear dependence of the enthalpy of the process with the amount of oxygen-containing functional groups was revealed by DSC and correlated to the chemistry of the oxidation. Self-assembly processes were used to prepare bulk and porous 3D GO structures, respectively based on water removal by evaporation at the liquid/air interface and by freeze-drying at the dynamic ice/water interface. For both processes, SEM and TEM analysis revealed a dependence of the self-assembly ability of GO with the oxidation degree. Specific surface area (SSA) measurements carried out on water dispersed GO revealed that GO sheets, even at low O/C atomic ratio, were well dispersed and only limited stacking phenomena occurred. BET SSA measurements demonstrated that the self-assembly of highly oxidized GO at the liquid-air interface induced relevant stacking phenomena, while freeze-drying was able to induce the formation of highly interconnected porous structures with reduced interlayer stacking.

## Introduction

Graphene is defined as a flat monolayer of carbon atoms tightly packed into a two-dimensional honeycomb lattice,<sup>1</sup> and is the basis for the realization of several advanced materials and devices, with applications in a large number of sectors that are expected to revolutionize multiple industrial fields.<sup>2</sup>

Key factors for the realization of advanced systems are understanding and controlling the self-assembly process of graphene and graphene derivatives. In particular, the realization of aqueous dispersions of graphene oxide (GO) was already in 2008 presented as an effective method for the processing of graphene.<sup>3</sup> During the last decade, it has been widely demonstrated that the self-assembly of GO, due to its amphiphilic property, can allow the realization of a variety of nanostructured systems with different morphologies. With different approaches free-standing films and membranes, hydrogels, aerogels, crumpled particles, hollow spheres, sack-cargo particles, pickering emulsions have been obtained.<sup>4</sup>

Despite the large scientific interest on this material, a few papers report comprehensive information on the effects of the oxidation degree on GO physico-chemical and structural properties, processability, adsorption properties of gases and organic dyes from water solutions and finally on the available specific surface area of GO in different physical states, such as dry GO self-assembled through different processes, or water dispersed GO.

Dreyer et al.<sup>5</sup> deeply investigated the chemistry of graphene oxide. More recently, Krishnamoorthy et al.<sup>6</sup> detailed the different types of oxygen containing functional groups formed at increased oxidation degrees and how they influence the structural properties of GO. Even if these papers are fundamental for the understanding and for the qualitative and quantitative estimation of the effects of the oxidation process of graphene, they did not deal with the processing and the adsorption properties of the final materials.

As concerning the self-assembly of GO in different conditions, a very broad review<sup>4</sup> discusses the phenomena occurring during the self-concentration of GO at various interfaces, also showing possible applications of the graphene-based systems developed. Amongst the processing methodologies available to tailor graphene-based structures, particularly interesting are the self-assembly at the liquid-air interface<sup>7</sup> and at the ice-water interface<sup>8</sup>, in view of obtaining bulk and porous 3D GO architectures, respectively. On the one hand, the effect of the oxidation degree of GO on the water mediated interlayer interactions has been investigated through molecular dynamics simulations,<sup>9</sup> explaining the mechanism at the basis of self-concentration of GO at the liquid-air interface. On the other, the formation of 3D porous structures has mainly been the object of studies

aimed at tailoring the stability of the GO architectures through effective reduction processes, with only a few information available on the relationships between the oxidation degree of GO and the final morphology of graphene networks.

Another relevant aspect of GO bulk and porous 3D structures is related to their adsorption properties, and to the estimation of the surface area of these systems available to physical and chemical interactions with different adsorbates, such as gases and water-soluble dyes. Gadipelli and Guo<sup>10</sup> well summarized the gas sorption properties of graphene and derivatives, whereas Yan et al.<sup>11</sup> detailed the effect of the oxidation degree of graphene oxide on the adsorption of methylene blue from water solutions.

Nevertheless, further insight on these aspects would be still needed to correlate the adsorption properties of GO to the level of interactions occurring between GO sheets, either in bulk or porous 3D architectures.

Starting from this basis, the work here presented is focused on the effect of the oxidation degree on the self-assembly and the surface area of GO samples, realized by a modified Hummers method from commercial graphite nanoplatelets (GNP) and processed through water casting and freeze-drying. In a first phase, a multi-technique characterization of the realized GO at different oxidation degree was performed to correlate the oxidative conditions adopted to the final oxidation degree of the obtained GO. Then, morphological and structural properties of bulk and porous 3D architectures realized by self-assembly at the liquid-air interface and at the ice-water interface were evaluated and correlated to the different oxidation degree of the starting water-dispersed GO samples. Finally, the specific surface area of the realized systems was evaluated by BET analysis, and the results were discussed in relation to their structural properties and the specific surface area measurements carried out on GO water dispersions by methylene blue adsorption tests.

## **Experimental section**

### **Materials**

Graphite nanoplatelets (GNP) grade C, average lateral dimensions 1-2  $\mu\text{m}$  according to the datasheet provided by the supplier, were purchased from XG Science (Lansing, MI, USA).

Sulfuric acid ( $\text{H}_2\text{SO}_4$ , reagent grade, 96% wt/wt in  $\text{H}_2\text{O}$ ), hydrochloric acid (HCl, reagent grade, 37% wt/wt in  $\text{H}_2\text{O}$ ), potassium permanganate ( $\text{KMnO}_4$ , > 99.0%), hydrogen peroxide solution ( $\text{H}_2\text{O}_2$  30

% wt/wt in H<sub>2</sub>O), methylene blue (MB, > 97%) and all solvents were purchased by Sigma Aldrich (Milan, Italy) and used without further purification.

## Preparation of GO

GO was synthesized by a severe oxidation process of GNP taking inspiration from the Krishnamoorthy's modified Hummers method.<sup>6</sup> GNP (1 g) was stirred in 25 mL of a 96% H<sub>2</sub>SO<sub>4</sub> solution for 30 minutes, keeping the temperature at 0 °C by an ice bath.<sup>12</sup> Then, 0.5, 1, 2 or 3% wt/wt equivalent of KMnO<sub>4</sub> were gradually added, while the solution was kept at room temperature by a water bath. From the reaction between H<sub>2</sub>SO<sub>4</sub> and KMnO<sub>4</sub>, Mn<sub>2</sub>O<sub>7</sub> was formed, that represents the actual oxidating species.<sup>5,13</sup> After completely adding potassium permanganate, the temperature was raised to 35 °C and stirring was held for two more hours. The resulting solution was diluted by gently adding 45 mL of water under vigorous stirring, while keeping the bath temperature at 70 °C. After stirring for 15 more minutes, 100 mL of H<sub>2</sub>O<sub>2</sub> water solution (3% wt/wt) were poured into the mixture, reducing the residual potassium permanganate and manganese oxide into manganese sulfate.<sup>14</sup> The mixture was kept stirring for one more hour and then the resulting suspension was centrifuged. The precipitate was collected and washed with 5% wt/wt HCl water solution. The resulting suspension was centrifuged again and the precipitate was collected in 140 mL of distilled water. Centrifugation and washing of the precipitate with distilled water were repeated until neutrality. Finally, the suspensions were diluted up to a final concentration of GO of about 4 mg/mL and sonicated with a Sonics Vibracell ultrasonic processor (500 W, 20 kHz) at 25% of amplitude, with a 30s/30s ON/OFF cycle, to improve the dispersion of the GO nanosheets. The obtained suspensions were coded as GO1, GO2, GO3, GO4, where the number indicates the degree of oxidation obtained using increasing amounts of KMnO<sub>4</sub>.

## Self assembly of GO

Cast GO samples (thickness about 8 μm) were obtained from water suspensions through an assembly process induced by the self-concentration of GO during water evaporation at the liquid/air interface.<sup>15</sup> In particular, samples were obtained by water casting at room temperature for at least 48h, followed by drying in vacuum oven at 90 °C overnight. Systems were coded as GO1-C, GO2-C, GO3-C, GO4-C.

A further class of GO samples was obtained by assembly at dynamic ice/water interface, realized by freeze-drying from the above described GO water suspensions. GO1, GO2, GO3, GO4 (40 mL) were poured in vials and immersed in liquid nitrogen for 10 min. Therefore, the frozen samples were kept at -20 °C overnight and then freeze-dried at -80 °C and 5x10<sup>-2</sup> torr in a Edwards Modulyo freeze-

drying equipment for 48h. The obtained systems were coded as GO1-FD, GO2-FD, GO3-FD, GO4-FD.

## **Characterization techniques**

Energy Dispersive X-ray (EDX) analysis was performed using a FEI Quanta 200 FEG SEM equipped with an Oxford Inca Energy System 250 and an Inca-X-act LN<sub>2</sub>-free analytical silicon drift detector, on GNP and dried GO samples placed onto aluminium SEM stubs. The analysis was performed at 30 kV acceleration voltage. Average results and standard deviation values are based on three consecutive measurements on different areas of each sample.

Cast GO samples and pristine GNP were analyzed by means of Fourier transform infrared spectroscopy (FTIR) to evaluate the extent of the surface modification. By comparison, FTIR spectra were recorded on pristine GNP. Spectra were recorded with a Perkin Elmer Spectrum One FTIR spectrometer using a resolution of 4 cm<sup>-1</sup> and 32 scan collections.

Confocal Raman spectra were acquired on cast GO samples and GNP by a Horiba-Jobin Yvon Aramis Raman spectrometer operating with a diode laser excitation source limiting at 532 nm and a grating with 1200 grooves/mm. The 180° back-scattered radiation was collected by an Olympus metallurgical objective (MPlan 50X, NA = 0.50) and with confocal and slit apertures both set to 400 μm. The radiation was focused onto a Peltier-cooled CCD detector (Synapse Mod. 354308) in the Raman-shift range 2000-1000 cm<sup>-1</sup>. To separate the individual peaks in unresolved, multicomponent profiles, spectral deconvolution was performed using the software Grams/8.0AI, Thermo Scientific using a Voigt function line shape. By a non-linear curve fitting of the data, height, area and position of the individual components were calculated.<sup>16</sup>

The average size of GO sheets in water suspension was determined through Dynamic Light Scattering (DLS) analysis using a Zetasizer Nano ZS (Malvern Instruments). The analysis was performed at 25 °C at a scattering angle of 173°.

Wide-angle X-ray scattering analysis (WAXS) was carried out on cast GO samples by means of a Rigaku model III/D max generator equipped with a 2D imaging plate detector, using a Ni-filtered Cu K $\alpha$  radiation (wavelength 1.5418 Å) at room temperature. To separate the individual peaks in unresolved WAXS profiles, spectral deconvolution was performed using the above mentioned software Grams/8.0AI, Thermo Scientific using a Lorentzian functions.

Thermogravimetric analysis (TGA) of cast GO samples and GNP was carried out using a Mettler TGA/SDTA851 analyzer. All the samples were analyzed in nitrogen flux (30 mL/min) at 2 °C/min heating rate, from room temperature to 800 °C, using about 3 mg of material for each sample.

Differential scanning calorimeter (DSC) experiments were carried out on cast GO samples and GNP using a TA Instruments DSC Q2000. The analyses were performed under nitrogen flux (30 mL/min) in dynamic mode at a 10 °C/min heating rate from 100 to 400 °C.

Scanning electron microscopy (SEM) of GNP, cast GO and freeze-dried GO samples was performed by means of a FEI Quanta 200 FEG SEM in high vacuum mode. Before SEM observations, samples were mounted onto SEM stubs by means of carbon adhesive disks and sputter coated with a 15 nm thick Au-Pd layer. All the samples were observed at 10-30 kV acceleration voltage using a secondary electron detector.

Bright field Transmission Electron Microscopy (TEM) analysis of GO and GNP was performed on a FEI Tecnai G12 Spirit Twin (LaB6 source) at 120 kV acceleration voltage. TEM images were collected on a FEI Eagle 4k CCD camera. Before the analysis, water dispersed GO samples, diluted at about 1 mg/mL, were collected by immersing TEM copper grids in the suspensions. By comparison, GNP was also analysed after dispersion at about 1 mg/mL in N,N-dimethylformamide (DMF) and collection and drying onto TEM copper grids.

Specific surface area (SSA) of GNP, cast GO and freeze-dried GO samples was determined through N<sub>2</sub> adsorption analysis, performed at liquid nitrogen temperature, by means of a Micromeritics ASAP 2020 analyzer, using high purity gases (> 99.999 %). Prior to the analysis, all the samples were degassed at 150 °C under vacuum (P < 10<sup>-5</sup> mbar) for 10 h. SSA was determined from the linear part of the Brunauer-Emmett-Teller (BET) equation.

SSA of graphene oxide in suspension (MB SSA) was measured through UV-vis spectroscopy with methylene blue (MB) dye as a probe.<sup>17,18,19</sup> GO1, GO2, GO3 and GO4 were diluted to 0.030 mg/mL in order to obtain a stable dispersion of graphene oxide in water, then an amount of MB equal to 1.5 times that required to cover the theoretical surface area of graphene oxide (2630 m<sup>2</sup>/g) was added to the GO suspensions. After mixing for 24h at room temperature, a conjugate structure of GO and MB was formed, due to  $\pi$ - $\pi$  interactions, and a precipitate was visible. The GO/MB mixture was centrifuged at 10000 rpm for 10 minutes by means of a Hermle Labortechnik Z 326 K centrifuge, to induce separation of the smaller sheets from the transparent solution. Then, the MB concentration of the supernatant solution was measured using a Jasco V570 UV spectrophotometer. A calibration curve was built to evaluate the MB concentration from the absorbance of the solution at 664 cm<sup>-1</sup>. Consequently, the mass of MB adsorbed on GO ( $m_{MB}$ ) was calculated and, considering the specific surface area of a MB molecule ( $SSA_{MB} = 2.54 \text{ m}^2/\text{g}$ ),<sup>20</sup>  $m_{MB}$  was correlated to the exposed area of the graphene oxide ( $SSA_{GO}$ ) through the following equation:

$$SSA_{GO} = m_{MB} \cdot SSA_{MB} / m_{GO} \quad (5.1)$$

where  $m_{GO}$  is the mass of GO used in the experiment.

## Results and discussion

### Oxidation process

Quantitative analysis of the GNP oxidation was carried out by EDX analysis, whose results are reported in Table 5.1. As concerning plain GNP, the oxygen/carbon atomic ratio was 0.06. This result showed that even in plain GNP there is a detectable level of oxidation, due to the production process. Increasing the oxidation degree of the realized GO samples, a monotonic increase of the O/C atomic was recorded, with a final value of 0.65 measured for the sample GO4, corresponding to a high oxidation level.<sup>21</sup>

The oxidation process of GNP was monitored by FTIR analysis. FTIR spectra in the range 800-2000  $\text{cm}^{-1}$  of GNP on cast GO samples are reported in Figure 5.1a, showing the presence of convoluted bands in the range 1570-1620  $\text{cm}^{-1}$  attributed to adsorbed water molecules and to C=C stretching vibrations of unoxidized graphitic domains.<sup>22</sup> The band at 1720-1740  $\text{cm}^{-1}$ , whose relative intensity progressively increased with the oxidation degree, was assigned to C=O stretching vibrations of carboxyl edge groups.<sup>23</sup> Absorption bands attributed to C-O stretching vibrations and O-H deformations of carboxyl and hydroxyl groups are centered at 1040-1050  $\text{cm}^{-1}$  and 1360-1370  $\text{cm}^{-1}$ , respectively, whereas the presence of epoxy groups was evidenced by the typical band attributed to the C-O stretching, centered at 1220-1230  $\text{cm}^{-1}$ .<sup>24</sup> As shown in Figure 5.1a, the intensity of the adsorption band attributed to hydroxyl groups was relatively more intense at low oxidation degrees, whereas the adsorption band attributed to epoxies was significantly more intense the highly oxidized GO4-C sample. As concerning the carboxyl groups, their bands slightly increased in intensity with the oxidation degree. These results indicated that the relative amount of the oxygen containing groups generated on graphene sheets changed with the conditions used for the oxidation process, with different species predominating at different oxidation degrees. In particular, OH groups seemed to be more relevant at low oxidation degrees, while epoxy groups prevailed at higher oxidation degrees, both these species being mainly present on the basal plane of graphene oxide sheets.<sup>25</sup> On the contrary, carboxyl groups, generated at the edges of graphene oxide sheets, progressively increased with the dosage of  $\text{KMnO}_4$ .

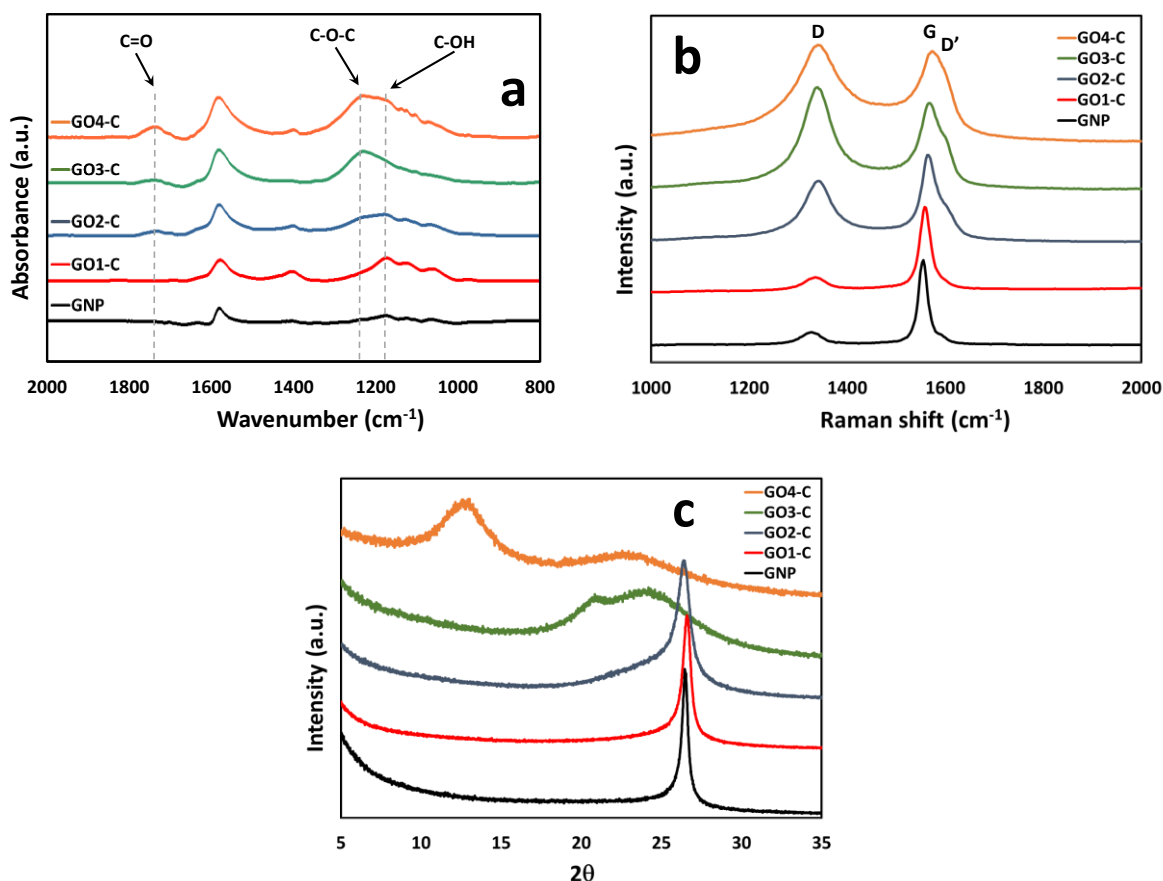


**Figure 5.1** FTIR (a), Raman (b) and WAXS spectra (c) of GNP and cast GO samples

Raman spectra of GNP and cast GO samples in the range 1000-2000 cm<sup>-1</sup> are reported in Figure 5.1b. In each spectrum a band centred at 1326-1343 cm<sup>-1</sup> (D-band) and a complex band with components centred at 1555-1572 cm<sup>-1</sup> (G-band) and 1595-1602 cm<sup>-1</sup> (D'-band) were observed. The D-band is typical of disordered carbon in graphene, and in particular of finite or nanosized graphitic planes, defects, vacancies, heptagon-pentagon pairs, kinks and heteroatoms. The G-band originates from the in-plane tangential stretching of carbon-carbon bonds in graphene sheets. Finally, the D' band, evidenced as a shoulder of the G-band at higher frequencies, is another feature induced by disorder and defects in the graphene structure. By spectral deconvolution, the intensity ratio  $I_D/I_G$ , a parameter indicating the degree of disorder in the graphene structure, was calculated and reported in Table 5.1.

**Table 5.1** Results of EDX, Raman and XRD analysis on GNP and cast GO samples at increasing oxidation degrees

Sample	GNP	GO1-C	GO2-C	GO3-C	GO4-C	
KMnO <sub>4</sub> /GNP wt equivalent	-	0.5	1.0	2.0	3.0	
O/C atomic ratio	0.06 ± 0.01	0.15 ± 0.03	0.24 ± 0.01	0.34 ± 0.03	0.65 ± 0.07	
I <sub>D</sub> /I <sub>G</sub>	0.14	0.16	0.75	1.23	1.11	
Average aromatic cluster size (nm)	11.8	11.3	2.8	2.6	2.0	
WAXS	2θ <sub>1</sub> (degrees)	26.5	26.6	26.4	24.4	23.3
	d <sub>1</sub> (nm)	0.336	0.335	0.338	0.365	0.382
	FWHM <sub>1</sub> (degrees) *	0.51	0.61	0.90	5.1	5.6
	D <sub>1</sub> (nm) **	31.7	26.5	17.9	3.2	2.9
	2θ <sub>2</sub> (degrees)	-	24.7	24.5	20.9	12.7
	d <sub>2</sub> (nm)	-	0.360	0.363	0.425	0.697
	FWHM <sub>2</sub> (degrees) *	-	3.9	5.2	2.6	2.8
	D <sub>2</sub> (nm) **	-	4.1	3.1	6.1	5.9
	I <sub>2</sub> /I <sub>1</sub> ***	0	0.10	0.28	0.48	2.41

\* FWHM = full width at half maximum

\*\* D<sub>i</sub> = mean size of the of the stacked domains in the direction perpendicular to graphene planes, calculated from the reflection i (eq. 3)

\*\*\* Intensity ratio between WAXS reflection 1, centred at higher 2θ values, and reflection 2, centred at lower 2θ values

Results showed that more drastic oxidative conditions induced a progressive increase of I<sub>D</sub>/I<sub>G</sub>, even if a small inversion of the trend was observed for sample GO4, as already reported by Kadam et al.<sup>26</sup> Through the analysis of the Raman spectra, the aromatic cluster size (L) in GNP and in each cast GO sample was calculated applying the empirical equation:<sup>17,27</sup>

$$L \text{ (nm)} = 4 A_G/A_D \quad (5.2)$$

where A<sub>G</sub> and A<sub>D</sub> are the integrated intensities of G and D peaks, respectively.

As shown in Table 5.1, the average aromatic cluster size, related to the size of the extended aromatic system left undamaged upon the oxidation process, monotonically decreased with the increase of KMnO<sub>4</sub> dose, from 11.8 to 2.0 nm.

Nevertheless, as revealed by DLS measurements, even if the oxidation process significantly reduced the aromatic cluster size, it did not affect the average size of the platelets, that remained almost unchanged with respect to those of GNP, irrespectively of the final oxidation extent of GO.

WAXS intensity profiles of GNP and cast GO samples are shown in Figure 5.1c. Results are reported in Table 5.1. For GNP a sharp diffraction peak at 2θ<sub>1</sub> = 26.5° (interlayer distance of 0.336 nm) was observed, which corresponds to a compact stacked planar multilayered carbon structure.<sup>17</sup> Upon mild

oxidation, i.e. in the case of GO1-C and GO2-C, this peak remained sharp and well resolved. However, a broadening effect was observed and quantified through spectral deconvolution. Its full width at half maximum (FWHM) increased from 0.51 (GNP) to 0.90 (GO2-C) due to the early distortion occurring of the AB stacking order of the graphite lattice generated by oxidation. For GO1-C and GO2-C, spectral deconvolution also indicated the presence of a second reflection at lower angles,  $2\theta_2 = 24.7\text{-}24.5^\circ$ , corresponding to an increase of the interlayer distance, up to 0.363 nm. Nevertheless, for these samples, the extent of layer stacking almost unaffected by the oxidation was still high, as indicated by the intensity ratio between the reflection 2 and 1, lower than 0.3.

When higher oxidation levels were reached, for GO3-C, a shift of the peak corresponding to the 002 reflection was recorded, associated to the evidence of a second reflection at lower angles. By deconvolution, the first peak, attributed to a more packed fraction of GO sheets, was centered at  $2\theta_1 = 24.4^\circ$ , with an increase of the corresponding  $d_1$  spacing (0.365 nm) with respect to pristine GNP, while the second peak was centered at  $2\theta_2 = 20.9^\circ$  ( $d_2 = 0.425$  nm). Moreover, for GO3-C, the distortion of the AB stacking order of the graphite lattice was very significant as well as the relative amount of less densely stacked GO sheets, as indicated by the high  $\text{FWHM}_1=5.1$ , and by the  $I_2/I_1$  ratio = 0.48, respectively.

Finally, at high oxidation degrees, for sample GO4-C, an inversion of the intensities of the first and second reflection was observed, in this case the peak at lower angles being much more intense with respect to the broad reflection at higher  $2\theta$  values ( $I_2/I_1 = 2.41$ ).<sup>28</sup> Reflection were centered at  $2\theta_2 = 12.7^\circ$  and  $2\theta_1 = 23.3$ . Therefore, most of the GO sheets for GO4-C were stacked with an average spacing  $d_2 = 0.697$  nm, and a lower fraction with an average spacing  $d_1 = 0.382$  nm. This abrupt change was the consequence of the heterogeneous nature of the oxidized graphene, constituted by graphitic  $sp^2$  domains and by  $sp^3$  domains typical of oxidized graphite.<sup>6</sup>

The average size ( $D$ ) of the stacked domains in the direction perpendicular to the graphene planes was calculated for cast GO samples at different oxidation degrees using the Debye-Scherrer equation:<sup>29</sup>

$$D = k \lambda / \beta \cos \theta \quad (5.3)$$

where  $k$  is a shape factor whose value can be approximated to 0.89, even if it varies with the shape of the crystallites,  $\beta$  is the FWHM in radians of the reflection,  $\lambda$  is the wavelength of the radiation used and  $\theta$  is the Bragg angle of the reflection. As concerning the behavior of the reflection located at higher angles, the average domain size progressively decreased with increasing the oxidation degree, from about 32 nm for GNP, to a final  $D_1$  value lower than 3 nm for GO4-C. Dividing these domain sizes by the calculated  $d_1$  spacing for each sample, the average number of GO sheets can be obtained in each domains. In our case, this average number varied between about 94 GO sheets for GNP, 79 (GO1-C), 53 (GO2-C), and finally 8.6 and 7.5 for GO3-C and GO4-C, respectively, thus

demonstrating that stacking phenomena were progressively inhibited increasing the oxidation degree. In the case of low oxidized samples, a similar data analysis was not very significant for the low intense and high convoluted reflection at lower  $2\theta$  angles, due to uncertainty of the  $\text{FWHM}_2$  values calculated by spectral deconvolution. Nevertheless, for the sample GO4-C, whose reflection centered at  $2\theta_2$  angles was well separated by that centered at  $2\theta_1$ , the calculated average number of stacked GO sheets spaced by about 0.70 nm, was close to 8, this value being comparable to the value found for the more tight GO sheets evidenced by the reflection centered at  $2\theta_1$ . This finding indicated that the highly oxidized sample was constituted by two classes of stacked primary GO sheets, different for their average spacing (0.382 vs. 0.697 nm) and their average dimension in the direction perpendicular to the GO planes (2.9 vs. 5.9 nm), but similar in the average number of their constituting GO flakes.

GNP and cast GO samples with different oxidation degrees were also analysed by TGA in non-oxidative conditions, in order to evaluate their thermal stability. Results are reported in Figures 2a-b and in Table 5.2. At about 150 °C, a relevant mass loss occurred for all the samples, whose extent was directly correlated to their oxidation degree. The maximum rate of degradation occurred between 178 and 190 °C. For the sample GO4-C, the derivative TGA curve also showed, in addition to the main degradation peak, the presence of a shoulder at a higher temperature, as already reported by Kang et al.<sup>30</sup> for GO sample oxidized in comparable conditions. The residual percent weight at 300 °C decreased from 98 wt% for GNP to 85 wt% for GO3-C and to 69 wt% for GO4-C. For all the samples, the mass loss process was attributed to the thermally induced decomposition of labile oxygen-containing groups in GO,<sup>18</sup> producing the formation of carbon monoxide and dioxide, and water. Calorimetric analysis allowed associating this weight loss step in the range 150-300 °C to an exothermic process.

**Table 5.2.** Results of thermogravimetric and calorimetric analysis on GNP and cast GO samples at increasing oxidation degrees

Sample	TGA	DSC	
	Residual weight at 300° C (%)	T <sub>exo</sub> (°C)	ΔH <sub>exo</sub> (J/g)
GNP	98	-	0
GO1-C	94	205	40
GO2-C	93	204	87
GO3-C	85	201	323
GO4-C	69	213	809

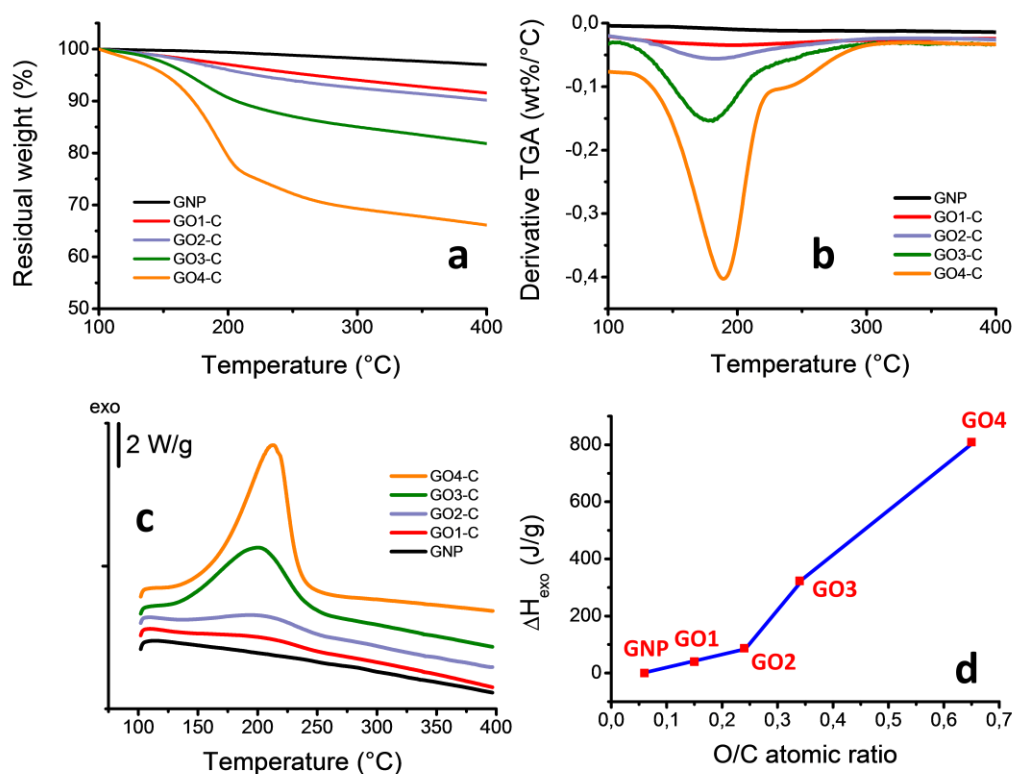


**Figure 5.2** Results of thermogravimetric and calorimetric analysis on GNP and cast GO samples at increasing oxidation degrees: TG and derivative TG curves (a, b); DSC traces (c); enthalpy associated to the thermal decomposition process vs. O/C atomic ratio of cast GO samples

DSC curves of GNP and cast GO samples are reported in Figure 5.2c. The maximum temperature and the enthalpy of the process are reported in Table 5.2. As it can be observed, while the degree of oxidation did not significantly affect the temperature corresponding to the maximum of the exothermic peak, significant changes of the  $\Delta H_{\text{exo}}$  were progressively recorded increasing the oxidation level of the GO samples up to GO2-C, followed by an even more abrupt change starting from GO3-C, up to 809 J/g for GO4-C. Plotting the obtained  $\Delta H_{\text{exo}}$  vs. the oxygen content of GO cast samples, expressed as the O/C atomic ratio (see Figure 5.2d), a change in the slope of the curve was clearly evidenced at medium oxidation levels. To explain this behaviour, it can be considered the structure of GO sheets consisting of unoxidized polyaromatic areas alternate to oxidized clusters containing hydroxyl and epoxide groups and carboxyl groups located at the edges of the GO sheets,<sup>25</sup> and the results obtained by FTIR analysis, that demonstrated that the relative amount of these groups changed with the final oxidation degree of GO. Kang et al.<sup>30</sup> demonstrated that the ratio among different functional groups, especially epoxies and hydroxyls, significantly affected the thermal stability of GO. Recently, Qiu et al.,<sup>31</sup> through theoretical calculations, showed that the decomposition of epoxide groups is significantly exothermic while the thermal decomposition of hydroxyl groups is isoenthalpic or only slightly endothermic. The thermal decomposition of carboxyl

groups, instead, is exothermic, but less than the decomposition of epoxides. All these considerations are consistent with the results that we obtained by FTIR and DSC analysis, confirming that at low oxidation levels the predominant species are carboxyl groups and hydroxyl groups, and progressively increasing their content in GO, their thermal decomposition induced a slow increase of the associated  $\Delta H_{\text{exo}}$ . Increasing the oxidation level, a higher concentration of epoxy groups was generated on graphene, thus making the decomposition of highly oxidized GO samples progressively much more exothermic, with a steeper increase of the associated enthalpy.

### Self-assembly of GO

As above anticipated, in this work the processing of GO was focused on two self-assembly processes. The first one was induced by the self-concentration of GO during water evaporation at the liquid/air interface, and it was aimed at generating cast GO samples (GOX-C, where X indicates different oxidation degrees of GO in water dispersion). The second self-assembly process was realized at the dynamic ice/water interface, and the corresponding GOX-FD samples were obtained by freeze-drying from GO water suspensions. A schematization of the casting and freeze-drying processes is proposed in Figure 5.3 where, for sake of simplicity, typical GO oxygen containing functional groups were omitted and water was represented in light blue.

For what concerns the casting process, it must be considered that GO suspensions are constituted by deprotonated graphene oxide sheets which create a dynamic network through their dipole-dipole interactions. When solvent evaporation is promoted, GO sheets reaching the interface tend to aggregate and, once further sheets reach the upper layer are able to interact with the first layer through van der Waals forces. Therefore, GO tend to self-concentrate at the interface and GO sheets tend to stack, progressively forming a layer-by-layer cast film (steps C-I to C-IV of Figure 5.3).<sup>32</sup>

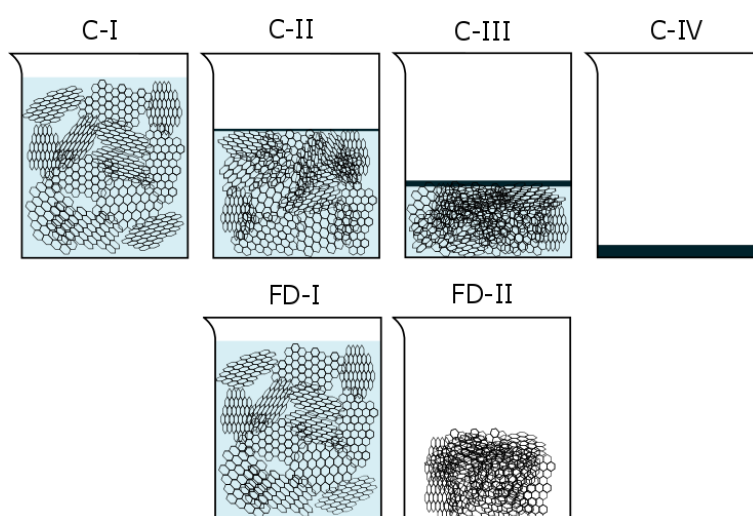


**Figure 5.3** Representation of the drying steps involved in the GO casting (C-I to C-IV) and freeze-drying (FD-I, FD-II)

Even if the mechanism of self-concentration and stacking of GO layers is widely accepted, a few papers concentrated the analysis of the effect of the oxidation degree of GO on the self-assembly, that is the key factor for the formation of GO cast films, also denoted as GO paper-like, papers or composite papers. Medhekar et al.,<sup>9</sup> through molecular dynamics simulations, elucidated the effect of the amount of oxygen containing groups on the interlayer mechanism of formation, structure and mechanical properties of GO papers. While the work was mainly focused on the water mediated interlayer interactions, they also mentioned the possible presence of intra-layer hydrogen bonds. Once again considering that GO sheets consist of unoxidized polyaromatic areas alternate to oxidized clusters containing hydroxyl and epoxide groups, and ionizable carboxyl groups mainly located at the edge,<sup>25</sup> as the interaction amongst ionizable carboxyl edge groups is mainly repulsive,<sup>33</sup> the formation of a self-standing membrane can mainly derive from intra-layer hydrogen bonds involving hydroxyl and epoxide groups. Therefore, the effect of different oxidation degree on the self-assembly process of GO is expected to be relevant.

Indeed, the realization of cast GO films from dispersions containing GO at different oxidation degrees confirmed this hypothesis. In Figure 5.4 results of SEM analysis on GO-C samples are reported. Starting from GO1, GO2 or GO3-C it was not observed the formation of self-standing films. As shown in Figure 5.4a, starting from the low oxidized GO2, the obtained samples were constituted by discontinuous GO islands with average size of hundreds of micrometers. The analysis of the surface of this sample at higher magnifications (Figure 5.4d) confirmed the low level of interaction amongst GO platelets. Very similar results were observed for GO1-C. At higher oxidation levels (GO3-C, see Figure 5.4e) a more pronounced interaction between adjacent GO platelets was observed, single GO sheets were not clearly identifiable and they were crumpled and well linked to each other. Nevertheless, also in this case the investigation of the cast sample at low magnifications revealed the presence of discontinuous fragments of GO with average size of about 250-300  $\mu\text{m}$ . Only further increasing the oxidation level to GO4, a large, self-standing and flexible GO film was obtained. The surface morphology of the GO4-C sample is shown in Figure 5.4b and f. At low magnification, the continuity of the film and the absence of defects was clearly evidenced. At higher magnification the high level of interaction between GO sheets did not allow identifying their original contour and shape, all the sheets resulting merged in a continuous and regular morphology. The cross-sectional structure of the film GO4-C is shown in Figures 4g and 4h. The sample was characterized by a homogeneous thickness, approximately 8  $\mu\text{m}$ , with the presence of almost parallel GO layers along the whole section.

A further insight on the mechanism of self-assembly of GO with different oxidation levels was obtained by TEM analysis, whose results are shown in Figure 5.5. The occurrence of the formation of a self-standing film at the liquid air interface was confirmed by TEM image shown in Figure 5.5a. By immersion of a non coated copper grid within the GO4 dispersion, after water evaporation a self-standing film with lateral dimension larger than 40  $\mu\text{m}$  was observed amongst the mesh grids. At

higher magnification, TEM analysis revealed the fine structure of the film, and it was possible to identify some of the constituting GO sheets. Selected area electron diffraction (SAED) showed that the film was composed by turbostratically stacked multilayer GO sheets, not oriented along preferential directions in the plane.<sup>34</sup> On the contrary, using uncoated TEM grids, it was not possible to collect self-standing films from GO1-3 dispersions. As shown in Figure 5.5d for GO2, GO sheets were not able to give an effective self-assembling and after water evaporation they resulted partially isolated on the carbon support of the carbon-coated copper grid. Similar results were obtained for GO1 and GO3.

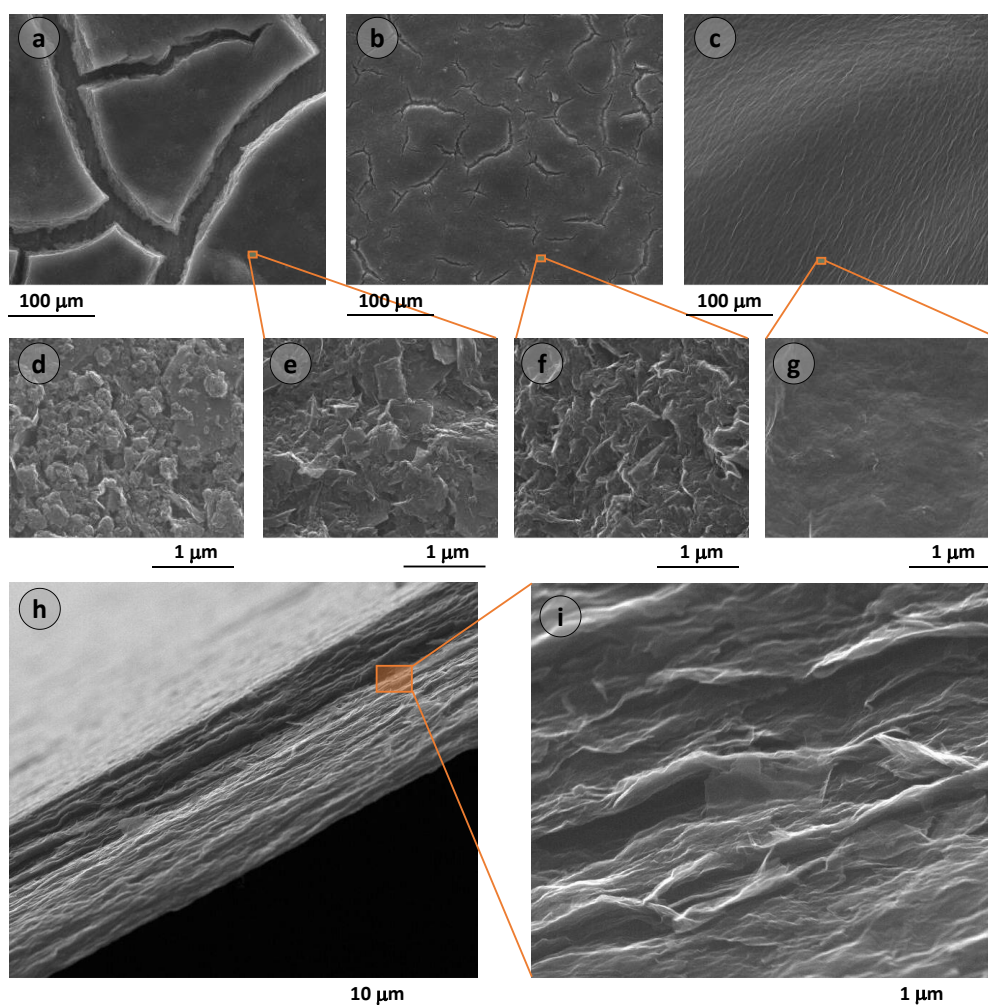


**Figure 5.4** SEM micrographs of: upper surfaces of (a,d) GO2-C; (b,f) GO4-C; (c) GNP, (e) GO3-C; (g,h) cross-sections of GO4-C

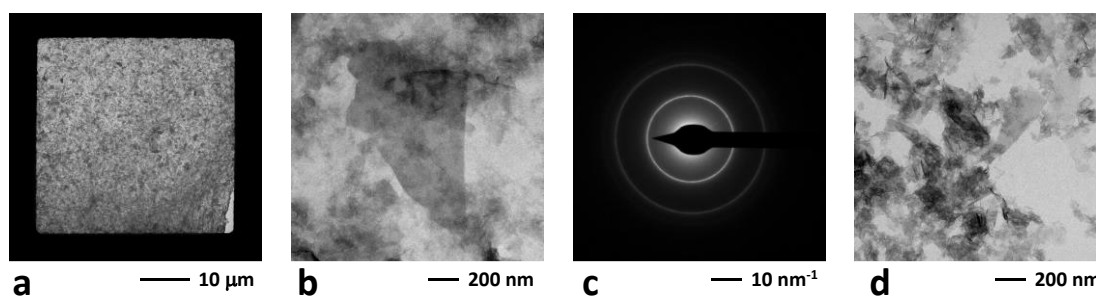


**Figure 5.5** (a,b) TEM micrographs of a self-standing GO film on non-coated copper grid obtained from the water dispersion GO4; c) SAED of (b); d) TEM micrograph of GO sheets collected on a carbon-coated copper grid from the water dispersion GO2

As concerning the freeze-drying process, schematizes in Figure 5.3, second line, it has already allowed realizing hierarchical porous structures starting from GO dispersions.<sup>35,36</sup> The freeze-drying process and the porous structure formation is regulated by the liquid/GO sheets and the GO sheets/GO sheets interactions, both affected by the amount of oxygen-containing groups of GO. Qui et al.<sup>37</sup> obtained graphene cellular monoliths starting from GO dispersions with very high oxidation degree (O/C atomic ratio 0.93), by a preliminary partial reduction, followed by freeze-drying and by a second step of reduction. They evaluated that a partial reduction up to an O/C atomic ratio of about 0.52 was necessary for the realization of stable porous structures. Nevertheless the peculiar multi-step procedure adopted, including a final reduction step up to an O/C atomic ratio of about 0.16, did not allow obtaining general information on the effect of the oxidation degree on the self-assembly of GO occurring during freeze-drying.

Therefore, in our work, a simple one-step freeze-drying procedure was adopted, based on the freezing at  $-20\text{ }^{\circ}\text{C}$  of GO solutions, followed by cryodesiccation. The obtained results were correlated to those obtained by the casting procedure. At the end of the process, samples GO1-FD, GO2-FD and GO3-FD were in powder form, with no macroscopic evidence of formation of a porous structure. On the other hand, for GO4-FD a porous structure was obtained, even if it was very fragile. The difficulty to obtain stable porous structures was a result somehow expected, as a chemical or thermally induced reduction process to obtain reduced GO (rGO) is considered a fundamental step to realize stable low-density porous monoliths starting from GO dispersion. Moreover, a drop of the sample dimension was obtained during the freeze-drying, with an approximate 50 % volume shrinkage with respect to the volume of the frozen dispersion.

SEM analysis on freeze-dried samples confirmed these macroscopic evidences. GO1-FD, GO2-FD and GO3-FD all exhibited similar morphologies, as shown for GO2-FD in Figures 6a-c. The samples were constituted by micrometric particles obtained through agglomeration of GO sheets during the water sublimation process. Particles size approximately ranged between 1 and 60  $\mu\text{m}$ . The surface morphology of these particles showed that the GO sheets were very tightly interconnected, somehow

more than those obtained by the casting procedure (see for instance Figure 5.6c in comparison to Figure 5.4d).

On the contrary, SEM analysis of GO4-FD showed the absence of particle-like agglomerates. The freeze-drying induced the formation of an irregular porous structure (Figure 5.6d) constituted by GO sheets randomly-connected in large stacks, well shown in Figures 6e-f.

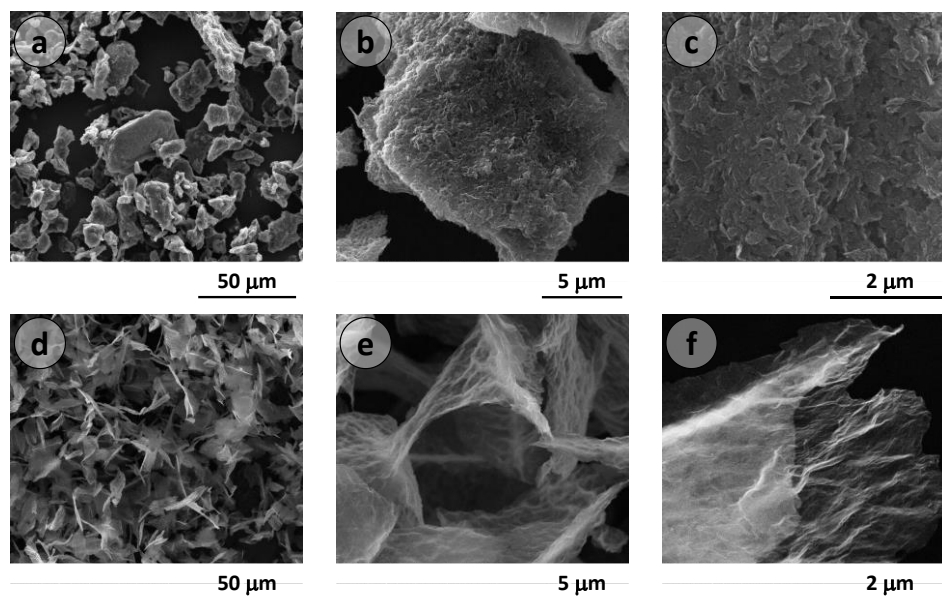


**Figure 5.6** SEM micrographs of GO2-FD (a,b,c) and GO4-FD (d,e,f)

### Surface area of GO

Several studies are focused on the adsorption capacity in water dispersions of methylene blue (MB) by graphene oxide.<sup>38,39,40,41,42</sup> Since the first work of McAllister et al.,<sup>18</sup> with slight change of the protocol, the adsorption of MB has been used to evaluate the SSA of graphene oxide and its derivatives.<sup>19,43,44</sup> The relationship between the oxidation degree of graphene oxide samples and their MB adsorption was already reported by Yan et al.,<sup>11</sup>. In this work, an exponential increase of the dye uptake was obtained with the increase the oxidation degree, attributed to the enhanced exfoliation of highly oxidized GO and to the presence of more active adsorption sites towards the dye. Nevertheless, the authors did not evaluate from the experimental MB uptake the SSA of the samples.

Instead, for our systems, using the MB dye as a probe, the specific surface area (MB SSA) of samples GO1-GO4 was determined on diluted water suspensions, by adding an excess of MB and determining the amount on non-adsorbed dye, as detailed in the experimental. Results are reported in Table 5.3.

Low oxidized GO samples, GO1 and GO2, showed MB SSA values close to 1400 m<sup>2</sup>/g. Considering the theoretical specific surface area of graphene and graphene derivatives (2630 m<sup>2</sup>/g) these results

indicated that, even at low O/C atomic ratio, GO sheets were well dispersed and only limited stacking phenomena occurred in water suspensions. Moreover, by increasing the oxidation degree, the MB SSA monotonically increased, up to a significant value of 1760 m<sup>2</sup>/g for GO4, showing that for this sample, in diluted conditions, only about 33% of the available GO area was masked by stacking and interactions occurring amongst GO sheets.

**Table 5.3** Specific surface area values calculated by methylene blue adsorption (MB SSA) on GO water suspensions and by N<sub>2</sub> adsorption at 77K (BET SSA) on cast and freeze-dried GO samples

Sample	MB SSA (m <sup>2</sup> /g)	BET SSA (m <sup>2</sup> /g)	
		Cast (-C)	Freeze-dried (-FD)
GNP	-	480 ± 5	
GO1	1415 ± 19	346 ± 1	305 ± 1
GO2	1401 ± 79	333 ± 1	264 ± 2
GO3	1700 ± 83	195 ± 1	148 ± 1
GO4	1760 ± 185	1.8 ± 0.1	122 ± 1

Results of the BET SSA of GNP and cast GO samples obtained by GO at different oxidation degree are also reported in Table 5.3 and the nitrogen adsorption isotherms are showed in Figure 5.7.

Gas adsorption properties of graphene and related materials, including graphene oxide, have been comprehensively discussed by Gadipelli and Guo.<sup>10</sup> By N<sub>2</sub> adsorption (77 K, 1 bar), BET SSA value up to about 900 m<sup>2</sup>/g have been reported for thermally exfoliated GO,<sup>45</sup> even if most of the GO samples described in literature showed BET SSA values lower than 500 m<sup>2</sup>/g.<sup>10,46</sup> The low BET SSA values observed for bulk GO samples with respect to the theoretical value of 2630 m<sup>2</sup>/g, are generally explained considering that the bulk material shows large extent of stacking, assumed that the interlayer gallery spaces are inaccessible to the probe molecules used in surface area analysis.<sup>47</sup>

In our case, starting from a BET SSA of 480 m<sup>2</sup>/g for commercial GNP, increasing the oxidation degree of GO, a progressive decrease of the BET SSA was observed, with an approximate 30% decrease of the surface area recorded for GO1-C and GO2-C and 60% decrease for GO3-C (see Table 5.3). Interestingly, a very low surface area was recorded for GO4-C, close to 2 m<sup>2</sup>/g, demonstrating the relevance of stacking phenomena by self-assembly of highly oxidized GO at the liquid-air interface. Moreover, this result also indicated that, despite the wide interlayer spacing calculated by WAXS analysis for GO4-C (about 0.70 nm), these interlayer galleries were inaccessible to the probe nitrogen molecule used in surface area analysis, also as a possible consequence of the high level of interactions amongst oxygen containing functional groups of adjacent graphene oxide sheets.

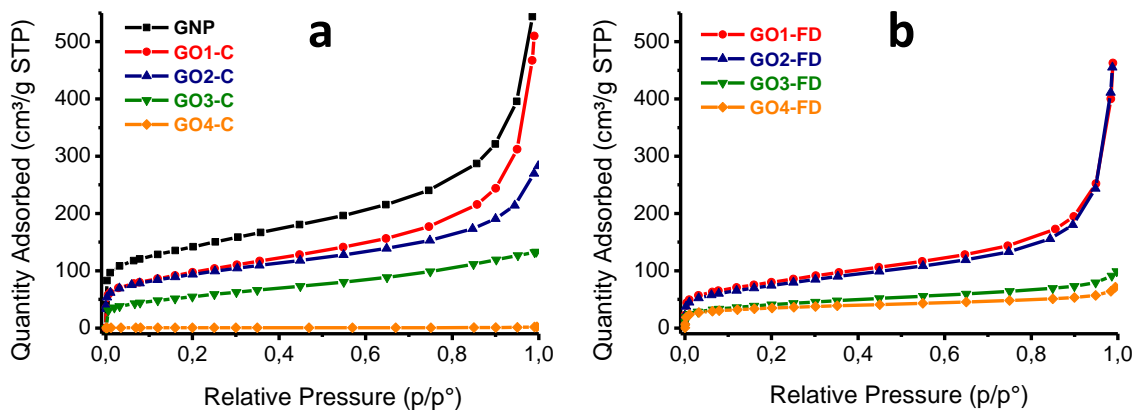


**Figure 5.7** Nitrogen adsorption isotherms at 77 K of GNP and cast GO samples (a) and freeze-dried GO samples (b)

Very interesting results were also obtained by the nitrogen adsorption analysis of freeze-dried GO samples. For GO1-FD, GO2-FD and GO3-FD, BET SSA values were slightly lower than those recorded for the corresponding cast samples GO-C. This finding was well explained taking into account the results of morphological analysis that, for freeze-dried samples obtained from low or medium oxidized GO1-GO3 suspensions, showed the presence of micrometric particles constituted by GO sheets more tightly interconnected than the corresponding cast samples.

On the contrary, BET analysis of GO4-FD showed an opposite behavior in comparison to the corresponding cast sample. In fact, in this case the freeze-dried sample showed an increased BET SSA ( $122 \text{ m}^2/\text{g}$ ) with respect to GO4-C (about  $2 \text{ m}^2/\text{g}$ ), demonstrating that for highly oxidized GO samples, characterized by a high level of exfoliation in water suspension, the freeze-drying process was able to induce the formation of highly interconnected porous structures with reduced interlayer stacking. Even if these porous structures could be further tailored by controlling other parameters such as the average size and size distribution of the GO sheets, and could be stabilized by chemical or thermal reduction processes, the oxidation degree of the starting graphene oxide is a fundamental factor for the obtainment of high surface area graphene based materials.

## Conclusions

This work presents an insight on the effect of the oxidation degree on the self-assembly and surface area of graphene oxide. GO samples were realized from graphite nanoplatelets by a modified Hummers method, using different dosage of  $\text{KMnO}_4$ . The effect of the  $\text{KMnO}_4/\text{GNP}$  ratio on the type and amount of oxygen-containing functional groups generated on the surface of graphene was investigated by FTIR, Raman and Energy dispersive X-ray spectroscopy. Results indicated that the obtained GO samples were characterized by a very low to high level of oxidation. Raman and WAXS analysis allowed obtaining a deep characterization of the structure of GO samples, confirming that increasing the oxidation degree induced a progressive disruption of the graphitic crystalline order and an increase of the interlayer distance between graphene sheets. DLS measurements indicated that, even if the oxidation process significantly reduced the aromatic cluster size of GNP, it did not affect the average size of the platelets.

Thermal and thermogravimetric analysis were proven to be useful tools for the characterization of GO samples. The exothermal thermal decomposition of GO was significantly affected by the oxidation degree, and a non-linear dependence of the enthalpy of the process with type and amount of oxygen-containing functional groups was detected.

Two different self-assembly processes were then used to prepare bulk and porous 3D GO structures, respectively based on the self-concentration of GO during water removal by evaporation at the liquid/air interface, and freeze-drying at the dynamic ice/water interface. SEM and TEM analysis on the obtained samples clearly revealed a dependence of the self-assembly ability of GO with the oxidation degree. As concerning cast samples, only at high oxidation levels large, defect-free, self-standing GO films were obtained, constituted by highly interacting graphene sheets showing also at high magnifications a continuous and regular morphology. Consistent results were also obtained on 3D GO samples obtained by freeze-drying. In this case, only at high oxidation degrees a porous structure was obtained and an approximate 50 % volume shrinkage with respect to the volume of the frozen dispersion was recorded. Freeze-drying on highly oxidized GO induced the formation of an irregular porous structure constituted by GO sheets highly interconnected in large random stacks.

Specific surface area measurements carried out on GO in water dispersions, by using methylene blue as a probe, revealed for low oxidized GO samples MB SSA values close to  $1400 \text{ m}^2/\text{g}$  indicating that, even at low O/C atomic ratio, GO sheets were well dispersed and only limited stacking phenomena occurred in water suspensions. This effect was more pronounced for highly oxidized GO, showing in this case that, in diluted conditions, only about 33% of the available GO area was masked by stacking and interactions occurring amongst GO sheets.

BET specific surface area measurements carried out by nitrogen adsorption at 77 K also gave interesting information on the interaction occurring between graphene sheets at different levels of oxidation. In particular, a progressive decrease of the BET SSA was recorded on cast samples by increasing the oxidation level, with a final SSA of about 2 m<sup>2</sup>/g recorded for the highly oxidized sample. This demonstrated the relevance of stacking phenomena by self-assembly of highly oxidized GO at the liquid-air interface. Moreover, BET analysis of the porous 3D sample obtained by freeze-drying of highly oxidized GO showed an increased BET SSA with respect to the corresponding cast sample. This demonstrated that the freeze-drying process was able to induce the formation of highly interconnected porous structures with reduced interlayer stacking.

As a general conclusion, the oxidation degree of the starting GO is to be considered as a crucial factor to obtain and exploit the potential high surface area of graphene based materials.

## References

- <sup>1</sup> A. K. Geim, K. S. Novoselov, *Nat. Mater.*, 2007, **6**, 183.
- <sup>2</sup> A. C. Ferrari, F. Bonaccorso, V. Falco, K. S. Novoselov et al., *Nanoscale*, 2015, **7**, 4598.
- <sup>3</sup> D. Li, M. B. Muller, S. Gilje, R. B. Kaner, G. G. Wallace, *Nat. Nanotechnol.*, 2008, **3**, 101.
- <sup>4</sup> J.-J. Shao, W. Lv, Q.-H. Yang, *Adv. Mater.*, 2014, **26**, 5586.
- <sup>5</sup> D. R. Dreyer, S. Park, C. W. Bielawski, R. S. Ruoff, *Chem. Soc. Rev.*, 2010, **39**, 228–240
- <sup>6</sup> K. Krishnamoorthy, M. Veerapandian, K. Yun, S.-J. Kim, *Carbon*, 2013, **53**, 38.
- <sup>7</sup> X. Wang, Z. Xiong, Z. Liu, T. Zhang, *Adv. Mater.*, 2015, **27**, 1370.
- <sup>8</sup> Y. Ma, Y. Chen, *Natl. Sci. Rev.*, 2015, **2**, 40.
- <sup>9</sup> N. V. Medhekar, A. Ramasubramaniam, R. S. Ruoff, V. B. Shenoy, *ACS Nano*, 2010, **27**, 2300.
- <sup>10</sup> S. Gadipelli, Z. X. Guo, *Progr. Mater. Sci.*, 2015, **69**, 1.
- <sup>11</sup> H. Yan, X. Tao, Z. Yang, K. Li, H. Yang et al., *J. Hazard. Mater.*, 2014, **268**, 191.
- <sup>12</sup> A. M. Dimiev, J. M. Tour, *ACS Nano*, 2014, **8**, 3060.
- <sup>13</sup> K. R. Koch, P. F. Krause, *J. Chem. Educ.*, 1982, **59**, 973.
- <sup>14</sup> W. S. Hummers Jr., R. E. Offeman, *J. Am. Chem. Soc.*, 1958, **80**, 1339.
- <sup>15</sup> J. J. Shao, W. Lv, Q. Guo, C. Zhang, Q. Xu, Q. H. Yang, F. Kang, *Chem. Comm.*, 2012, **48**, 3706.
- <sup>16</sup> V. Ambroggi, G. Gentile, C. Ducati, M. C. Oliva, C. Carfagna, *Polymer*, 2012, **53**, 291.
- <sup>17</sup> H. Yan, H. Wu, K. Li, Y. Wang, X. Tao, H. Yang, A. Li, R. Cheng, *ACS Appl. Mater. Interfaces*, 2015, **7**, 6690.
- <sup>18</sup> M. J. McAllister, J.-L. Li, D. H. Adamson, H. C. Schniepp, A. A. Abdala, J. Liu, O. M. Herrera-Alonso, D. L. Milius, R. Car, R. K. Prud'homme, I. A. Aksay, *Chem. Mater.*, 2007, **19**, 4396.
- <sup>19</sup> P. Montes-Navajas, N. G. Asenjo, R. Santamaría, R. Menéndez, A. Corma, H. García, *Langmuir*, 2013, **29**, 13443.
- <sup>20</sup> R. S. Rubino, E. S. Takeuchi. *J. Power Sources*, 1999, **81–82**, 373.
- <sup>21</sup> M. Nováček, O. Jankovský, J. Luxa, D. Sedmidubský, M. Pumera, V. Fila, M. Lhotka, K. Klímová, S. Matějková, Z. Sofer, *J. Mater. Chem. A*, 2017, **5**, 2739.
- <sup>22</sup> Y. Wang, J. Liu, L. Liu, D. D. Sun, *Nanoscale Res. Lett.*, 2011, **6**, 241.
- <sup>23</sup> D. C. Marcano, D. V. Kosynkin, J. M. Berlin, A. Sinitskii, Z. Sun, A. Slesarev, L. B. Alemany, W. Lu, J. M. Tour, *ACS Nano*, 2010, **4**, 4886.
- <sup>24</sup> C. Xu, X. Shi, A. Ji, L. Shi, C. Zhou, Y. Cui, B. Xu, *PLoS One*, 2015; **10**, e0144842.
- <sup>25</sup> J. Kim, L. J. Cote, F. Kim, W. Yuan, K. R. Shull, J. Huang, *J. Am. Chem. Soc.*, 2010, **132**, 8180.
- <sup>26</sup> M. M. Kadam, O. R. Lokare, K. V. M. K. Kireeti, V. G. Gaikara, N. Jha, *RSC Adv.*, 2014, **4**, 62737.
- <sup>27</sup> F. Tuinstra, J. L. Koenig, *J. Chem. Phys.*, 1970, **53**, 1126.
- <sup>28</sup> H. K. Jeong, M. H. Jin, K. P. So, S. C. Lim, Y. H. Lee, *J. Phys. D: Appl. Phys.*, 2009, **42**, 065418.

- <sup>29</sup> L. Zhang, F. Zhang, X. Yang, G. Long, Y. Wu, T. Zhang, K. Leng, Y. Huang, Y. Ma, A. Yu, Y. Chen, *Sci. Rep.*, 2013, **3**, 1408.
- <sup>30</sup> J. H. Kang, T. Kim, J. Choi, J. Park, Y. S. Kim, M. S. Chang, H. Jung, K. T. Park, S. J. Yang, C. Rae Park, *Chem. Mater.*, 2016, **28**, 756.
- <sup>31</sup> Y. Qiu, F. Collin, R. H. Hurt, I. K. laotsa, *Carbon*, 2016, **96**, 20.
- <sup>32</sup> C. Chen, Q.-H. Yang, Y. Yang, W. Lv, Y. Wen, P.-X. Hou, M. Wang, H.-M. Cheng, *Adv. Mater.*, 2009, **21**, 3007.
- <sup>33</sup> F. Kim, L. J. Cote, J. Huang, *Adv. Mater.*, 2010, **22**, 1954.
- <sup>34</sup> L. Chen, J. Lei, F. Wang, G. Wang, H. Feng, *RSC Adv.*, 2015, **5**, 40148.
- <sup>35</sup> H. Ham, T. V. Khai, N. H. Park, D. S. So, J. W. Lee, H. G. Na, Y. J. Kwon, H. Y. Cho, H. W. Kim, *Nanotechnology*, 2014, **25**, 235601.
- <sup>36</sup> J. Wang, X. Gao, Y. Wang, C. Gao, *RSC Adv.*, 2014, **4**, 57476.
- <sup>37</sup> L. Qiu, J. Z. Liu, S. L. Y. Chang, Y. Wu, D. Li, *Nat. Comm.*, 2012, **3**, 1241.
- <sup>38</sup> T. Liu, Y. Li, Q. Du, J. Sun, Y. Jiao, G. Yang, Z. Wang, Y. Xia, W. Zhang, K. Wang, H. Zhu, D. Wu, *Colloids Surf. B*, 2012, **90**, 197.
- <sup>39</sup> L. Chen, J. Yang, X. Zeng, L. Zhang, W. Yuan, *Mater. Express*, 2013, **3**, 281.
- <sup>40</sup> W. Zhang, C. Zhou, W. Zhou, A. Lei, Q. Zhang, Q. Wan, B. Zou, *Environ. Contam. Toxicol.*, 2011, **87**, 86.
- <sup>41</sup> S.-T. Yang, S. Chen, Y. Chang, A. Cao, Y. Liu, H. Wang, *J. Colloid Interface Sci.*, 2011, **359**, 24.
- <sup>42</sup> W. Peng, H. Li, Y. Liu, S. Son, *J. Mol. Liq.*, 2016, **221**, 82.
- <sup>43</sup> H. Zhang, X. Han, Z. Yang, J. Zou, *J. Nanomater. Mol. Nanotechnol.*, 2013, **S1**, 003.
- <sup>44</sup> Q. Wu, Y. Sun, H. Bai, G. Shi, *Phys. Chem. Chem. Phys.*, 2011, **21**, 11193.
- <sup>45</sup> K. S. Subrahmanyam, S. R. C. Vivekchand, A. Govindaraj, C. N. R. Rao, *J. Mater. Chem.*, 2008, **18**, 1517.
- <sup>46</sup> V. B. Parambath, R. Nagar, K. Sethupathi, S. Ramaprabhu, *J. Phys. Chem. C*, 2011, **115**, 15679.
- <sup>47</sup> F. Guo, M. Creighton, Y. Chen, R. Hurt, I. Külaots, *Carbon*, 2014, **66**, 476.

# Chapter 6

## Conclusions

In this work are reported for the first time the preparation and characterization of hyper-crosslinked nanocomposites based on a divinylbenzene/styrene/vinylbenzyl chloride (DVB/ST/VBC) matrix and containing modified multi-walled carbon nanotubes (MWCNTs), graphene nanoplatelets (GNP) or modified graphene oxide (GO), as well as results on applicative examples of these materials for water purification applications.

First, the traditional Davankov-type procedure to prepare HCL polymers, based on the suspension prepolymerization of the monomers followed by the Friedel-Crafts hyper-crosslinking step, was applied to the synthesis of HCL nanocomposites. PVBC grafted MWCNTs were dispersed into DVB/ST/VBC monomer mixtures, with molar ratios 2/0/98 or 2/49/49, and then suspension polymerization was promoted. MWCNTs were found to induce a complex morphology of the polymer precursor beads. Moreover, after hyper-crosslinking, they slightly affected the SSA of the nanocomposites, and induced, at low nanofiller contents, an interesting increase in the microporous fraction of the material. The increase in microporous fraction was also accompanied by increase in CO<sub>2</sub>, H<sub>2</sub> adsorption and phenol adsorption from solution. It was noteworthy that the HCL DVB/ST/VBC system, containing low amount of the VBC monomer and characterized by a relatively low degree of hyper-crosslinking, showed, by addition of modified MWCNTs, an increase in CO<sub>2</sub> and phenol adsorption up to the range of adsorption of the highly crosslinked system. The addition of nanotubes also promoted an increase of the CO<sub>2</sub>/N<sub>2</sub> selectivity for all the investigated compositions, thus indicating that the embedding in Davankov-type resins of carbon nanotubes, characterized by their extended  $\pi$ -conjugation, is a promising approach to realize highly selective systems towards CO<sub>2</sub> absorption.

With a second approach to realize high surface area HCL nanocomposites, a suitable synthetic strategy to improve the dispersion of the inorganic nanofillers into the polymeric matrix was set-up. This strategy was based on the bulk polymerization of the precursor monomers, and it was very effective for the embedding and dispersion of modified or even unmodified inorganic nanofillers. This innovative solvent-free and high yielding procedure permitted to obtain HCL polymers characterized by SSA and adsorption properties comparable or even better than those shown by the

corresponding materials prepared by suspension pre-polymerization. Therefore, new HCL nanocomposites containing GNP and surface modified GO nanofillers were prepared. In particular, using surface modified GO, i.e. GO nanoplatelets grafted with PVBC, a polymer phase able to participate to the hyper-crosslinking step through its chloromethyl groups, microporous nanocomposites based on a ST/DVB precursor, i.e. without the chlorinated VBC monomer, were also realized. Their microporosity was only generated during the hyper-crosslinking occurring at the interface between the modified GO nanoplatelets and the styrene based matrix. Despite to their reduced specific surface area with respect to traditional Davankov-type resins, these HCL nanocomposites showed excellent gas adsorption properties and phenol uptake from water solutions.

Through mechanical processes, sizes and shapes of these HCL polymers and nanocomposites were also homogenised, in order to meet the requirements for their use as functional fillers in different polymeric matrices. In particular, polysulfone membranes containing HCL polymers and nanocomposites and chitosan hydrogels containing HCL polymers were prepared. The former were tested to evaluate their phenol uptake from water. HCL materials, used as functional fillers, were found to induce significant improvements of the phenol equilibrium adsorption capacity, up to 67%. Instead, the addition of HCL particles in chitosan hydrogels promoted an increase, up to 400%, of the hydrogel adsorption capacity toward specific dyes.

Therefore, the bulk polymerization coupled to Friedel-Crafts hyper-crosslinking was proven to be a versatile strategy, usable “on demand” to obtain different classes of advanced materials. On the one hand, it allowed to easily embedding, within the final HCL porous structure, different functional nanofillers, thus obtaining a new class of advanced microporous organic polymer nanocomposites. On the other hand, through mechanical processes able to reduce and homogenise the size of the obtained HCL resins and nanocomposites, the obtained microporous particles were effectively used as functional fillers in polymer systems, enhancing the adsorption properties of the matrices.

Finally, an in-depth investigation on graphene oxide was performed, in order to evaluate the effect of the chemistry and the processing conditions on the possible application of this material as a functional filler in microporous high surface area multiphase systems. In particular, the effect of the oxidation degree on the self-assembly and surface area of graphene oxide was explored. GO samples were realized from graphite nanoplatelets by a modified Hummers method, using increasing dosage of  $\text{KMnO}_4$ . The obtained GO samples were characterized by a very low to high level of oxidation. Raman and WAXS analysis showed that increasing the oxidation degree a progressive disruption of the interlayer distance between graphene sheets was obtained. A non-linear dependence of the enthalpy of the process with the amount of oxygen-containing functional groups was revealed by DSC and correlated to the chemistry of the oxidation. Self-assembly processes were used to prepare bulk and porous 3D GO structures, respectively based on water removal by evaporation at the liquid/air interface and by freeze-drying at the dynamic ice/water interface. For both processes, SEM and TEM analysis revealed a dependence of the self-assembly ability of GO with the oxidation

degree. Specific surface area measurements carried out on water dispersed GO revealed that GO sheets, even at low O/C atomic ratio, were well dispersed and only limited stacking phenomena occurred. BET SSA measurements demonstrated that the self-assembly of highly oxidized GO at the liquid-air interface induced relevant stacking phenomena, while freeze-drying was able to induce the formation of highly interconnected porous structures with reduced interlayer stacking.

# Appendix A1

## List of Figures

1.1.	Hyper-crosslinking reaction scheme through external and internal electrophile .....	5
1.2.	Nanosized carbon allotropes .....	11
1.3.	The Lennard-Jones potential .....	16
1.4.	Interaction potential in a slit-shaped pore, simplified to a bi-dimensional system .....	17
1.5.	Classification of adsorption isotherms .....	20
1.6.	Classification of adsorption isotherms hystereses .....	22
1.7.	Molecular structure of methylene blue .....	30
2.1.	Reaction scheme for the two-step synthesis of HCL resins based on DVB, ST and VBC ...	47
2.2.	Results of the characterization of surface modified carbon nanotubes: scheme of the surface modification reaction and FTIR, TGA and TEM analysis results .....	48
2.3.	FTIR spectra of the gel-type precursor resins and the HCL resins and nanocomposites .....	50
2.4.	SEM micrographs of the precursor beads .....	50
2.5.	SEM micrographs of the sections of the precursor nanocomposite beads .....	52
2.6.	Nitrogen adsorption/desorption isotherms at 77K and DFT pore size distribution of the HCL resins and nanocomposites .....	54
2.7.	Phenol adsorption isotherms measured at 298 K of the HCL resins and nanocomposites ...	58
S.2.1.	Inhomogeneous product obtained by the suspension polymerization of 2 mol% DVB, 98 mol% VBC and 3phr of unmodified MWCNT .....	60
S.2.2.	SEM micrographs of the cross-sections of the precursor beads .....	60
3.1.	Innovative systems based on microporous polymers and nanocomposites obtained through bulk prepolymerization followed by Friedel-Crafts hyper-crosslinking .....	73
3.2.	ATR-FTIR spectra of precursor and HCL DVB/VBC resins prepared by bulk and suspension polymerization .....	74
3.3.	<sup>13</sup> C CP/MAS NMR spectra of precursor and HCL DVB/VBC resins prepared by bulk and suspension polymerization .....	74

3.4.	Nitrogen adsorption/desorption isotherms at 77K and DFT pore size distribution of the HCL resins and nanocomposites prepared by bulk prepolymerization .....	76
3.5.	Scheme of the hyper-crosslinking reaction at the interface between the chlorine-free precursor resin and the surface modified graphene oxide (GO-PVBC) .....	78
3.6.	ATR-FTIR spectra of the precursors and HCL materials .....	79
3.7.	Results of TEM and SEM analysis of precursor and HCL nanocomposites .....	80
3.8.	SEM micrographs of the plain and ball-milled HCL resins and nanocomposites .....	84
3.9.	SEM micrographs of polysulfone plain and composite membranes. Upper/lower surfaces and cross-sections .....	86
S.3.1.	GO-PVBC TEM and FTIR analysis results .....	88
S.3.2.	<sup>13</sup> C NMR spectra of the DVB/ST/VBC precursors .....	89
S.3.3.	SEM image of the X_DVB-VBC resin as obtained by suspension prepolymerization followed by the hyper-crosslinking step .....	89
S.3.4.	Nitrogen adsorption/desorption isotherms at 77 K and DFT pore size distribution of the plain and ball-milled HCL resins and nanocomposites .....	90
4.1.	Molecular structure of Indigo Carmine, Rhodamine 6G and Sunset Yellow FCF .....	100
4.2.	Hyper-crosslinked polymers synthesis schematic .....	102
4.3.	SEM micrographs of HR, FD-CS, FD-CS-15HR .....	103
4.4.	Mechanical compression test results of CS and CS-15HR .....	103
4.5.	Nitrogen adsorption/desorption isotherms at 77 K up to 1 bar and DFT pore size distribution of the freeze-dried hydrogels and the hyper-crosslinked resin .....	104
4.6.	CS, HR and CS-15HR equilibrium dye adsorption isotherms .....	105
S.4.1.	ATR-FTIR spectra of the precursor and the hyper-crosslinked resin .....	108
S.4.2.	SEM micrograph of the hyper-crosslinked resin HR0 .....	108
S.4.3.	Nitrogen adsorption/desorption isotherms at 77 K and DFT pore size distribution of the plain and ball-milled hyper-crosslinked resins .....	109
5.1.	FTIR, Raman and WAXS spectra of GNP and cast GO samples .....	120
5.2.	Results of thermogravimetric and calorimetric analysis on GNP and cast GO samples at increasing oxidation degrees: TG and derivative TG curves; DSC traces; enthalpy associated to the thermal decomposition process vs. O/C atomic ratio of cast GO samples .....	124
5.3.	Representation of the drying steps involved in the GO casting and freeze-drying .....	125
5.4.	SEM micrographs of GO and GNP samples .....	127
5.5.	TEM micrographs and SAED of GO samples .....	128
5.6.	SEM micrographs of GO2-FD and GO4-FD .....	126
5.7.	Nitrogen adsorption isotherms at 77 K of GNP, cast and freeze-dried GO samples .....	131

# Appendix A2

## List of Tables

2.1. Results of SSA and pore size distribution analysis, CO <sub>2</sub> and H <sub>2</sub> uptake, CO <sub>2</sub> /N <sub>2</sub> selectivity	.54
2.2. Freundlich parameters and correlation coefficients of the fitting of the phenol adsorption curves .....	58
3.1. Codes and compositions of the precursor resins and nanocomposites prepared .....	67
3.2. Results of SSA and pore size distribution analysis, CO <sub>2</sub> uptake, and H <sub>2</sub> uptake .....	76
3.3. Results of phenol adsorption tests from water solutions performed on HCL resins and nanocomposites and on mixed matrix membranes .....	83
4.1. Freundlich and Langmuir fitting parameters for the dye adsorption .....	106
S.4.1. Results of SSA and pore size distribution analysis on the plain and ball-milled hyper-crosslinked resins, the chitosan and composite freeze-dried hydrogels .....	109
5.1. Results of EDX, Raman and XRD analysis on GNP and cast GO samples at increasing oxidation degrees .....	121
5.2. Results of thermogravimetric and calorimetric analysis on GNP and cast GO samples at increasing oxidation degrees .....	123
5.3. Specific surface area values calculated by methylene blue adsorption on GO water suspensions and by N <sub>2</sub> adsorption at 77K on cast and freeze-dried GO samples .....	130

# Appendix B

## Publications

- Synthesis and adsorption study of hyper-crosslinked styrene-based nanocomposites containing multi-walled carbon nanotubes  
R. Castaldo, R. Avolio, M. Cocca, G. Gentile, M. E. Errico, M. Avella, C. Carfagna and V. Ambrogi, *RSC Advances*, 2017, 7, 6865, DOI: 10.1039/c6ra25481k
- Plasticization of poly(lactic acid) through blending with oligomers of lactic acid: Effect of the physical aging on properties  
R. Avolio, R. Castaldo, G. Gentile, V. Ambrogi, S. Fiori, M. Avella, M. Cocca and M. E. Errico, *European Polymer Journal*, 2015, 66, 533, DOI:10.1016/j.eurpolymj.2015.02.040
- Hyper-crosslinked resins filled with multiwalled carbon nanotubes  
R. Castaldo, V. Ambrogi, R. Avolio, C. Cocca, M. E. Errico, G. Gentile, M. Avella, and C. Carfagna, *AIP Conference Proceedings* 1736, 020063 (2016); DOI: 10.1063/1.4949638
- Effect of physical ageing on properties of PLA plasticized with oligomeric esters of lactic acid  
R. Castaldo, V. Ambrogi, M. Avella, R. Avolio, C. Carfagna, M. Cocca, M. E. Errico, G. Gentile, *AIP Conference Proceedings* 1599, 138 (2014); DOI: <http://dx.doi.org/10.1063/1.4876797>

# Appendix C

## Meeting Contributions

- A new synthetic way to hyper-crosslinked polymers and nanocomposites  
*Materials 2016*, Catania, Italy, 2016. Oral contribution
- Hyper-crosslinked resins filled with multiwalled carbon nanotubes  
*8th International Conference Times of Polymers & Composites*, Ischia, Italy, 2016. Oral contribution
- Effect of multiwalled carbon nanotubes on structure, morphology and adsorption properties of hyper-crosslinked resins  
*12<sup>th</sup> FOA – International Conference on the Fundamentals of Adsorption*, Friedrichshafen, Germany, 2016. Poster presentation
- Adsorption study of hyper-crosslinked nanocomposites filled with multi-walled carbon nanotubes  
*Macrogiovani – AIM*, Catania, Italy, 2016. Oral presentation
- High surface area hyper-cross-linked resins containing GNP or MWCNT  
*GraphITA 2015*, Bologna, Italy, 2015. Poster presentation
- High surface area hyper-cross-linked resins containing multi-walled carbon nanotubes  
*EPF 2015 - European Polymer Federation*, Dresda, Germany, 2015. Oral contribution
- Effect of physical ageing on properties of PLA plasticized with oligomeric esters of lactic acid  
*7<sup>th</sup> International Conference Times of Polymers & Composites*, Ischia, Italy, 2014. Oral contribution